Gas Diffusion Layer Characterization and Microstructural Modeling in Polymer Electrolyte Fuel Cells

by

Zahra Tayarani Yoosefabadi

M.Sc., Amirkabir University of Technology, 2009

B.Sc., University of Tehran, 2006

Thesis Submitted in Partial Fulfillment of the

Requirements for the Degree of

Doctor of Philosophy

in the

School of Mechatronic Systems Engineering

Faculty of Applied Sciences

SIMON FRASER UNIVERSITY

Spring 2021

Declaration of Committee

Name:	**Zahra Tayarani Yoosefabadi**
Degree:	**Doctor of Philosophy**
Title:	**Gas Diffusion Layer Characterization and Microstructural Modeling in Polymer Electrolyte Fuel Cells**
Examining Committee:	**Chair:** Mohammad Narimani Lecturer, Mechatronic Systems Engineering
	Erik Kjeang Supervisor Associate Professor; Mechatronic Systems Engineering
	Gary Wang Committee Member Professor, Mechatronic Systems Engineering
	Woo Soo Kim Committee Member Associate Professor, Mechatronic Systems Engineering
	Sami Khan Examiner Assistant Professor, Sustainable Energy Engineering
	Mina Hoorfar External Examiner Professor, School of Engineering University of British Columbia

Abstract

Polymer electrolyte fuel cells (PEFCs), as promising clean energy power sources, are potential substitutes not only for stationary power generation but also for mobile applications specifically in transportation due to their high power density and performance as well as lack of pollutants. PEFC vehicles are at the dawn of commercialization, but still, cost, performance, and durability of current PEFCs need to be further improved to facilitate vast market integration especially under high current density conditions. Pursuant to this goal, comprehensive multidisciplinary understanding of multiphase transport of mass, heat, and electricity in the PEFC constituents including the gas diffusion layer (GDL), as the centerpiece of this thesis, will help to make progress towards material optimization and subsequently fuel cell performance improvements. The GDL transport capability is determined by its effective transport properties which are strongly dependent on its morphological, microstructural, and physical characteristics. Therefore, accurate knowledge regarding the correlation between the GDL microstructure and its transport properties is essential for improving the performance and durability of PEFCs as well as for material optimization, fuel cell design, and prototyping in the area of fuel cell development and manufacturing. In this context, this thesis aims to develop a fast and cost-effective design tool for GDL microstructural modeling and transport properties simulation.

Given the limitations of experimental, analytical, and tomographic techniques, stochastic microstructural model development to retrieve the heterogeneous GDL microstructure is a more reliable and flexible tool for GDL material design and prototyping assignments to reduce cost and time of the design cycle. Inspired by the randomness of the GDL porous media structure and its fabrication process, the GDL microstructure is virtually reconstructed as a collection of stochastic processes to provide a robust representation of the structure. The technique of stochastic microstructural reconstruction relies on statistical correlation functions which describe the probabilities of the porous media constituents' distribution and aim to encompass all the details of the porous media. The obtained 3D digitized realizations of the stochastic model are then used as a domain for numerical computation of transport properties. In this thesis, a unique stochastic GDL microstructural modeling framework inspired by manufacturing information and characterization data is developed in which all GDL substrate and MPL components are resolved, and thoroughly validated with literature and measured data for a variety of MPL-coated GDLs. The effects of PTFE loading and liquid water saturation on the GDL substrate anisotropic transport properties for both gas and liquid phases are found to be highly coupled and are therefore simulated and analyzed jointly. Furthermore, a parametric study is conducted to investigate the effect of MPL pore morphology composition on the MPL and MPL-coated GDL transport properties. The validated stochastic design tool can be used as a fast and accurate framework for reconstructing GDL porous materials and understanding the correlation between the GDL morphology and transport properties. This paves the way for development of improved GDL materials with desired transport properties in modern PEFCs.

Keywords: PEFC; GDL; MPL; stochastic modeling; transport properties; PTFE; saturation; morphology; GDL design tool

To my beloved parents

and

my best friend and love, Ali.

Acknowledgments

I would like to express my sincere gratitude to my supervisor Dr. Erik Kjeang for his immense knowledge, invaluable guidance, insightful discussions, steady encouragement, inspiration, and support throughout my PhD. It was a privilege for me to work with him and learn from his experience.

I greatly appreciate the efforts of my committee members, Prof. Gary Wang and Dr. Woo Soo Kim, who contributed their valuable time to scrutinize my work and helped me to improve my work by providing valuable feedbacks and comments.

I would also like to thank our colleagues at Ballard Power Systems as our industrial collaborator; specifically, Dr. David Harvey, Julie Bellerive, Shanna Knights, and Dr. Silvia Wessel; for their time, help, and kind cooperation.

This research was supported by the Natural Science and Engineering Research Council of Canada (NSERC), Ballard, Mercedes-Benz Canada Fuel Cell Division, and Simon Fraser University. The research made use of facilities at SFU Fuel Cell Research Laboratory (FCReL), 4D LABS as well as Ballard.

Last but not least, my thanks go to my family specially my parents that have endlessly encouraged and supported me through all stages of my life. No achievement was possible in my life without their presence and support. Finally, special thanks to my love and best friend, Ali Shagerdmootaab, for his kind companionship, understanding, and devotion.

Table of Contents

List of Tables

List of Figures

List of Acronyms

Symbol	Description
AB	Acetylene Black
AFC	Alkaline Fuel Cell
AFM	Atomic Force Microscope
BEV	Battery Electric Vehicle
BFM	Binary Friction Model
BP	Black Pearls
BPS	Ballard Power Systems
BSE	Backscattered Electrons
CL	Catalyst Layer
CLSM	Confocal Laser Scanning Microscope
CNP	Carbon Nanoparticle
CNT	Carbon Nanotube
CVF	Cumulative Volume Fraction
DEM	Discrete Element Methods
DOE	Department of Energy
DVF	Differential Volume Fraction
EDS	Energy Dispersive X-ray Spectroscopy
EDS	Energy Dispersive Spectroscopy
EGN	Electrochemically Exfoliated Graphene
EMT	Effective Medium Theory
FCEV	Fuel Cell Electric Vehicle
FCReL	Fuel Cell Research Laboratory
FEP	Fluorinated Ethylene Propylene
FFP	Flow Field Plate
FGP	Flake Graphite Particle
FIB-SEM	Focused Ion Beam-Scanning Electron Microscopy
GDL	Gas Diffusion Layer
GHG	Greenhouse Gas

HOR	Hydrogen Oxidation Reaction
HS	Hashin-Shtrikman
ICE	Internal Combustion Engine
IP	In-plane
LAC	Library and Archives Canada
MEA	Membrane Electrode Assembly
MG	Maxwell-Garnett
MIP	mercury Intrusion Porosimetry
MPL	Microporous Layer
MSP	Method of Standard Porosimetry
NSE	Navier-Stokes Equation
NWP	Non-wetting Phase
ORR	Oxygen Reduction Reaction
PAFC	Phosphoric Acid Fuel Cell
PAN	Polyacrylonitrile
PEFC	Polymer Electrolyte Fuel Cell
PEM	Polymer Electrolyte Membrane
PFA	Perfluoroalkoxy
PFSA	Per-Fluorinated Sulfonic Acid
PLP	Poisson Line Process
PLT	Poisson Line Tessellation
PPP	Poisson Point Process
PSD	Pore Size Distribution
PTC	Parallel Thermal Conductance
PTFE	Polytetrafluoroethylene
PTL	Porous Transport Layer
PVDF	Polyvinylidene Fluoride
Redox	Reduction–Oxidation
RVE	Representative Volume Element
SE	Secondary Electrons
SE	Structuring Element

SEM	Scanning Electron Microscope
SFU	Simon Fraser University
SOFC	Solid Oxide Fuel Cell
TCR	Thermal Contact Resistance
TP	Through-plane
WP	Wetting Phase
XCT	X-ray Computed Tomography

Nomenclature

A	Surface Area (m^2)
A'	Surface Area Per Unit Volume (m^{-1})
BW	Basis Weight ($kg\ m^{-2}$)
c_p	Specific Heat Capacity ($J\ K^{-1}\ kg^{-1}$)
C	Constant
C_i	Gas Species i Concentration ($mol\ m^{-3}$)
$\|d\|$	Distance (m)
d	Diameter (m)
$\bar{d}$	Mean Diameter (m)
D	Diffusion ($m^2\ s^{-1}$)
$D50$	Median Pore Diameter (m)
D_{Kn}	Knudsen Diffusion ($m^2\ s^{-1}$)
$\vec{e}$	Unit Vector
E	Electric Voltage Difference (V)
f	Phase Function
h	Thickness (m)
H	Heat (Enthalpy) of Evaporation ($J\ kg^{-1}$)
i_e	Current Density ($A\ m^{-2}$)
I	Electrical Current (A)
j	Superficial Heat Flux (W)
J_i	Gas Species i Superficial Flux ($mol\ m^{-2}\ s^{-1}$)
k	Permeability (m^2)
k_I	Inertial Permeability (m)
K	Thermal Conductivity ($W\ m^{-1}\ K^{-1}$)
Kn	Knudsen Number
l_c	Characteristic Length Scale (m)
L_D	Domain Length (m)
m	Mass (kg)

m'	Mass Fraction
M_i	Diffusing Species i Molecular Weight (mol)
n	Constant
N	Molar Flux (kg s^{-1} m^{-2})
N_l	Number of Random Lines
N_v	Number of Voxels
p	Probability Density Function
$P( )$	Cumulative Probability Distribution Function
P	Pressure (Pa)
PV	Pore Voxel
q	Heat Flux (W m^{-2})
Q	Volumetric Flow Rate (m^3 s^{-1})
Q'	Heat Source Term (W)
r	Radius (m)
$\vec{r}$	Position Vector (m)
R	Resistive Property
R_g	Gas Constant (J mol^{-1} K^{-1})
R^2	Coefficient of Determination
Re	Reynolds Number
s	Liquid Water Saturation
S_e	Energy Source Term (W m^{-3})
S_i	Gas Species i Source Term (mol s^{-1} m^{-3})
S_m	Mass Source Term (kg s^{-1} m^{-3})
S_V	Momentum Source Term (N m^{-3})
$S_{\phi s}$	Potential Source Term (V S m^{-3})
SS_{tot}	Total Sum of Squares
SS_{err}	Error Sum of Squares
SV	Solid Voxel
SVP	Solid Volume Percentage (%)
T	Temperature (K)

$\vec{V}$	Velocity (m s^{-1})
VP	Volume Percentage
X	Inverse Cumulative Density Function
Y	Cumulative Probability Distribution Function

Greek Letters

α	Phase-Change (Condensation/Evaporation) Coefficient (kg m^{-2} s^{-1})
β	Anisotropy Parameter
γ	Surface Tension (N m^{-1})
δ	Constant
Γ	Transport Coefficient
ε	Porosity
θ	Latitude Angle (°)
θ_c	Contact Angle (°)
λ	Mean Free Path (m)
Λ	Intensity Parameter
μ	Dynamic Viscosity (Pa s)
ρ	Density (kg m^{-3})
ρ_i	Polar Distance (m)
σ	Electrical Conductivity (S m^{-1})
φ	Longitude Angle (°)
φ_i	Polar Angle (°)
ϕ	Electric Potential (V)
ψ	Potential
ω	Weight Percentage
Ω	Volume (m^3)

Subscripts

B	Binder
BS	Binder Space
c	Capillary
C	Carbon Particles
CS	Carbon Agglomerate Space
eff	Effective
f	Fluid
F	Fiber
g	Gas Phase
int	Intruded
$interm$	Intermediate
IP	In-Plane
K	Kapton
l	Liquid
m	Mercury
$meas$	Measured
NWP	Non-Wetting Phase
o	Open Space
p	Penetrometer
pen	MPL Penetration
psm	Penetrometer-Sample-Mercury
PLB	Polymeric Binder
PPB	Papermaking Binder
rel	Relative
s	Sample
sat	Saturation
sub	GDL Substrate
S	Solid Phase
SS	Sphere (Pore) Space

T	Hydrophobic Agent (e.g. PTFE)
TP	Through-Plan
TS	Hydrophobic Agent Space
WP	Wetting Phase
ϑ	Solid or Pore Phase

Superscripts

eff	Effective

Chapter 1.

Introduction

1.1. Research Background and Motivation

By definition, a fuel cell is an electrochemical device producing electricity by converting the chemical energy of a fuel, *e.g.*, hydrogen, and an oxidizing agent, *e.g.*, oxygen, through a pair of reduction–oxidation (redox) reactions. Fuel cells unlike batteries can continuously produce electrons as long as fuel and oxidizing agent are supplied. There are many types of fuel cells and they all consist of anode and cathode electrodes and an electrolyte in which positively charged ions are allowed to move from anode to cathode. A stream of hydrogen is delivered into the anode in which a catalyst facilitates the hydrogen oxidation reaction (HOR) to split hydrogen into protons (positively charged hydrogen ions) and electrons. The newly formed protons permeate through the electrolyte to the cathode while the electrons are impeded and, hence, travel along an external circuit to the cathode electrode, thus generating useful electrical current. At the cathode, another catalyst facilitates the oxygen reduction reaction (ORR) between the protons, electrons, and a stream of oxygen (usually in air) to generate water and heat as the only by-products.

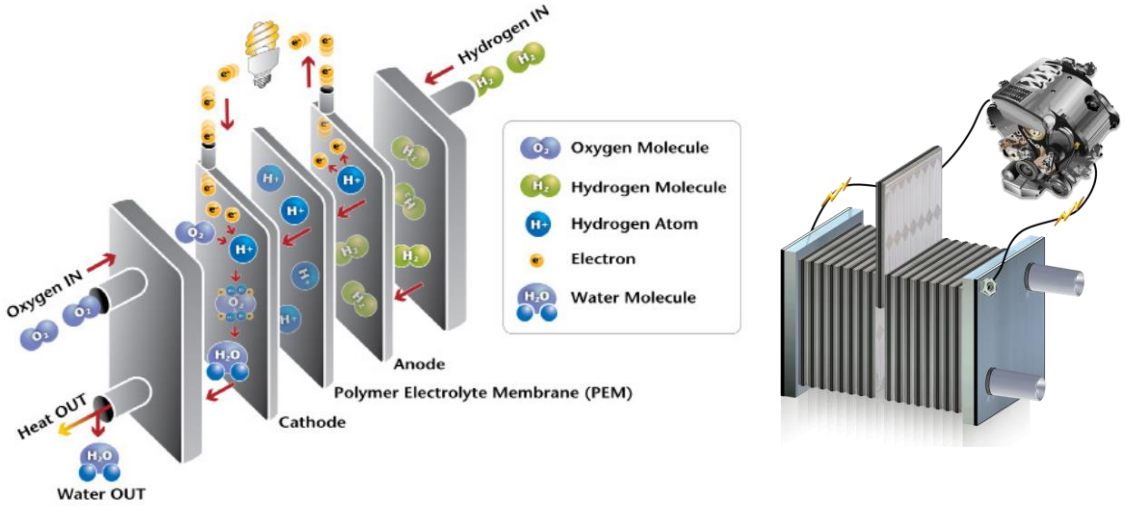

(a) (b)

Figure 1.1. Schematic of a polymer electrolyte fuel cell: (a) a unit cell depicting the operating principle; and (b) a fuel cell stack, adapted from U.S. Department of Energy [1].

Figure 1.1(a) depicts the operating principle schematic of a fuel cell unit. Individual fuel cells produce relatively small electric potentials, less than 1 V in realistic operating conditions, so, cells are "stacked" or placed in series to create sufficient voltage to meet an application's requirements as illustrated in Figure 1.1(b). Fuel cells are primarily classified by the type of the electrolyte they use, *i.e.*, polymer electrolyte fuel cell (PEFC), phosphoric acid fuel cell (PAFC), solid oxide fuel cell (SOFC), and alkaline fuel cell (AFC). For PEFCs, a proton conducting polymer membrane (typically Nafion from DuPont®) contains the electrolyte solution that separates the anode and cathode electrodes.

To achieve global ambitions for greenhouse gas (GHG) emissions reduction to curb climate change, fuel cells and PEFCs, in particular, as clean energy solutions are potential substitutes for internal combustion engines (ICEs) due to their high power density and low operating temperature. Their superiorities include significantly higher theoretical efficiency compared to ICEs, potential of reduced GHG emissions power generation, less challenging maintenance due to compact, modular designs with few moving parts, scalable power output from mW to MW, and rapid start-up [2,3]. The wide range of applicability and prominent features make PEFCs promising power sources not only for stationary power generation but also for mobile applications specifically in transportation as a replacement for ICEs.

As of 2018, a suite of preliminary, commercial hydrogen-fed PEFC vehicles are available on the market. Indeed, cost, performance, and durability of current vehicles are still impeding market growth and need to be further improved for mass market adoption. Table 1.1 depicts the US Department of Energy (DOE) key technical attributes status and targets for an 80 kW_{net} integrated transportation PEFC system operating on direct hydrogen with their graphical representation where the green line indicates the status of the key attributes in 2017 as a percentage of the 2025 targets [4–7]. PEFC systems must be demonstrated with long-term durability target of 8,000 hours equivalent to 150,000 miles of driving in different operating conditions with less than 10% loss of performance. That being said, the projected durability in 2017 was 4,100 hours which is approaching the 2020 target of 5,000 hours but significantly lower than the 2025 target of 8,000 hours. Besides, system specific power must also increase to be competitive with ICEs with the ultimate

target of 900 W kg^{-1}. Moreover, the DOE estimated system cost in 2015 and 2017 was \$53 and \$45 kW^{-1} with high-volume production of 500,000 units/year which shows a significant gap with its target system cost of \$40 and \$35 kW^{-1} for 2020, 2025, and an ultimate cost target of \$30 kW^{-1} beyond 2030, at the same production volume. Note that, the cost estimates are still far from reality in terms of production volumes and therefore more realistic values must be provided. Referring to the DOE report, the expected cost of automotive PEFCs based on technologies in 2017 was ~\$280 kW^{-1} for 20,000 units/year [4]. According to McKinsey & Company study, a cost reduction of roughly 70-80% for fuel cell vehicles would be possible mainly by industrialization of the PEFC system given an annual production volume of 150,000 vehicles [8].

Figure 1.2 illustrates the total cost of ownership (TCO) trajectory of fuel cell electric vehicles (FCEV), battery electric vehicles (BEV), and ICE vehicles under the

Table 1.1. DOE key technical attributes status and targets for an 80 kW_{net} integrated transportation PEFC power system operating on direct hydrogen with its graphical representation from U.S. Department of Energy where the green line indicates the status in 2017 as a percentage of the 2025 targets [4–7].

Key Technical Attributes	2015 Status	2017 Status	2020 Targets	2025 Targets	> 2030 Targets
Peak energy efficiency (%)	60	60	65	65	70
Power density (W L^{-1})	640	650	650	650	850
Specific power (W kg^{-1})	650	650	650	850	900
Cost (\$ kW^{-1})	53	45	40	35	30
Durability in automotive drive cycle (h)	3,900	4,100	5,000	8,000	8,000

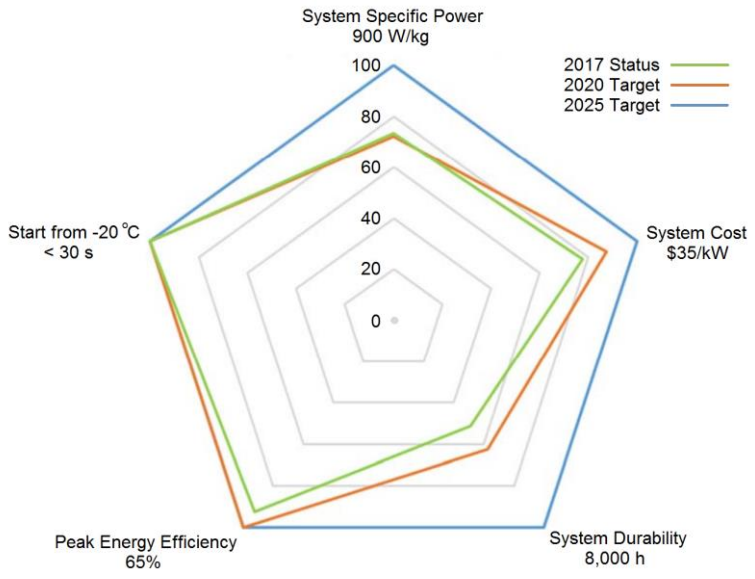

assumed scenario of high-production volume with different tank range by 2050 conducted by McKinsey center for future mobility. The cost analysis trajectory of passenger vehicles show that the attractiveness of FCEVs varies across use cases and will outcompete BEVs by circa 2025, 2030, and 2040 for large (650 km), medium (600 km), and small (200 km) range tank vehicles, respectively, thereby, fuel cell vehicles are more competitive in segments with heavier use and longer-range requirements. Yet, to reach this scale, there is a need for investment, policy alignment, and demand creation [8].

It is also worth noting that, hydrogen production is another impediment to fuel cell technology commercialization and the overall challenge is the production cost. The DOE target is to develop technologies to produce, deliver, and dispense hydrogen at the cost of less than $4/kg. To reach these goals, a wide portfolio of processes over a range of time frames and production scales are considered as schematically depicted in Figure 1.3. Hydrogen production by natural gas reforming is an established technology which is able to reach the cost targets in the near-term. Technologies based on renewable resources such

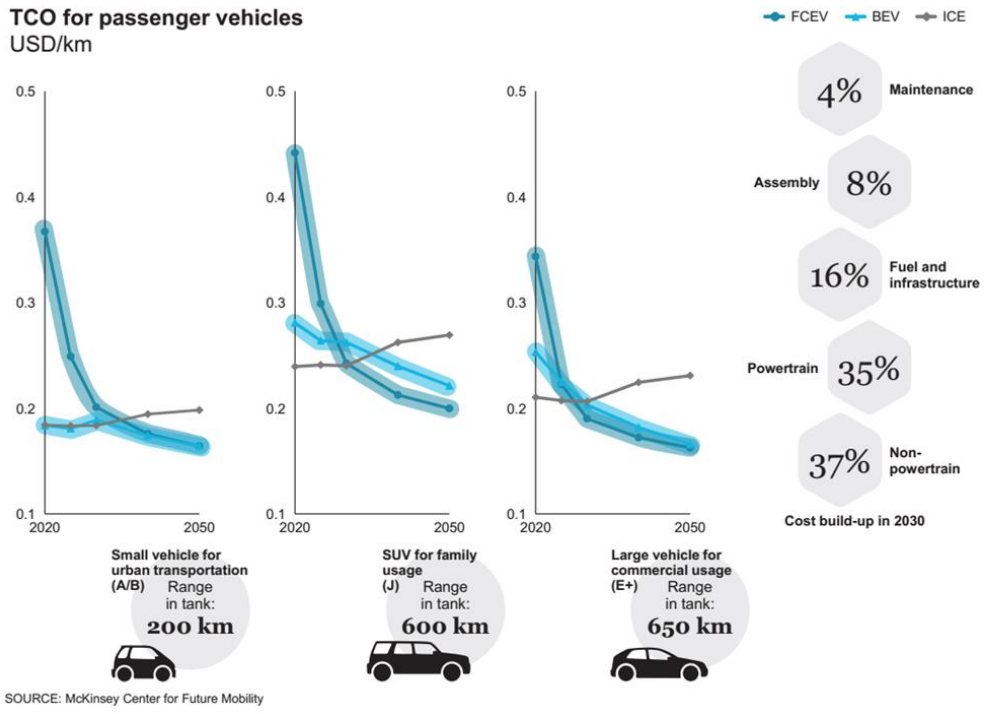

Figure 1.2. Total cost of ownership trajectory of passenger fuel cell electric, battery electric, and internal combustion engine vehicles with different tank range by 2050 reported by McKinsey center for future mobility [8].

as biomass and wind-generated electricity, in the mid-term, and technology pathways with near-net zero carbon emissions such as those based on solar energy, in the longer term, are anticipated to reach the cost targets. This goal is based on thorough research with stakeholders, academia, and national labs [1].

The current PEFCs performance and durability owe their entity to numerous investigations performed by various researchers and developers all around the world. Nevertheless, to-date, a wide variety of industrial and academic research is still outstanding in order to achieve the far-reaching targets of PEFC performance and durability at low system cost. In a report released by McKinsey, Hydrogen Council estimated the investments of $280 billion are required through 2030 to accelerate the development and commercialization of hydrogen and fuel cell technology to foster the energy transition [9]. To this end, comprehensive multidisciplinary understanding on materials of PEFC constituents and their properties will help to make progress towards material optimization and subsequently fuel cell performance improvements.

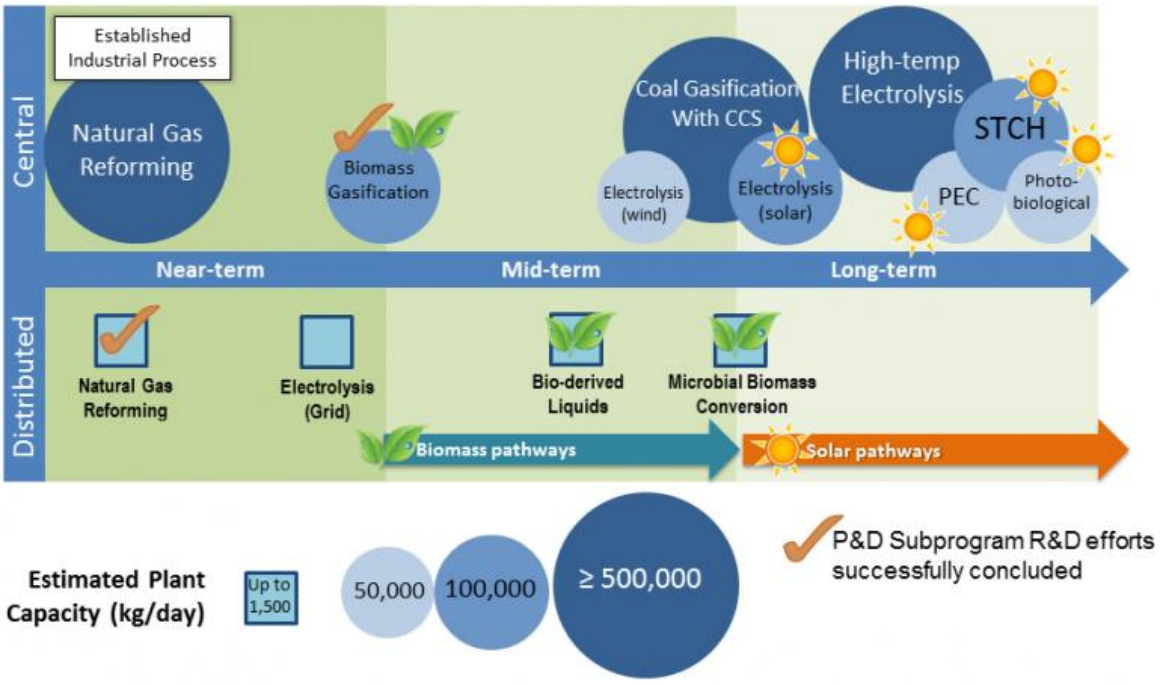

Figure 1.3. A wide portfolio of processes for hydrogen production over a range of time frames and production scales, adapted from U.S. Department of Energy [1].

Figure 1.4[1] illustrates a schematic of a PEFC stack which is composed of multiple cells of repeating membrane electrode assemblies (MEAs) and flow field plates (FFPs) that are backed up with end FFPs on both ends. FFPs are designed to perform several roles simultaneously in PEFCs. They not only distribute fuel and oxidant within the cell but also separate the reactant gases from adjacent cells, connect the cells electrically, carry water away from each cell, act as a support structure, and keep the cells cool. Commonly used FFP designs include straight, parallel, inter-digitated, serpentine, or pin-type flow field channels which propound the possibility to facilitate one transport mode over the other. The goal of all different designs is to provide uniformly distributed mass transfer to and from the MEA while ensuring that the pressure of the reactants does not drop dramatically.

As depicted in Figure 1.5, MEA is the core component of a cell which is typically composed of polymer electrolyte membrane (PEM), catalyst layers (CL), and gas diffusion layers (GDL) on both sides of a cell called 5-layer MEA. The GDL, aka porous transport layer (PTL), is a bi-layer graded porous structure which is composed of a macroporous GDL substrate and a thin delicate catalyst-backing layer called microporous layer (MPL). The figure also summarizes the characteristics of MEA constituents particularly thickness, composition, porosity, and pore diameter, although, there might be a slight difference in

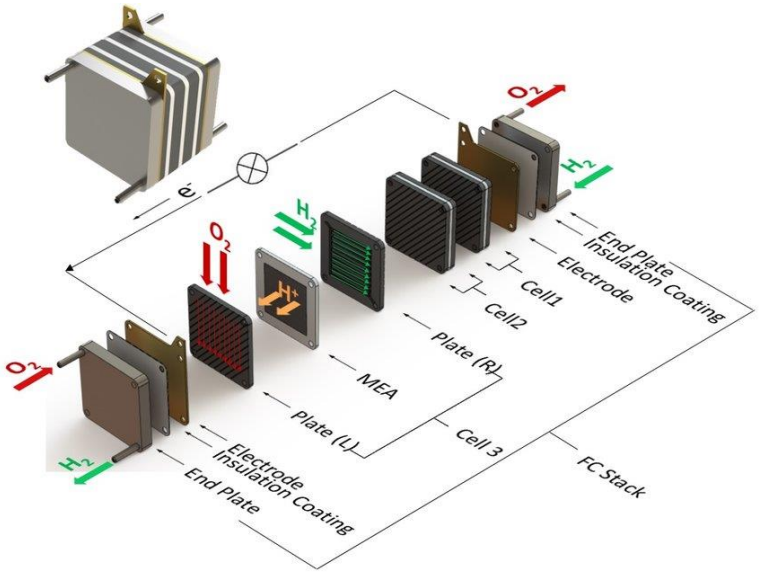

Figure 1.4. Schematic of a fuel cell stack operation and components [10].

[1] Reprinted from Renewable and Sustainable Energy Reviews, 75, Thamo *et al.*, A review on prognostics and health monitoring of proton exchange membrane fuel cell, 440-450, 2017, with permission from Elsevier.

characteristics of the layers in the anode and cathode electrodes. Nevertheless, the functions and transport phenomena of the MEA constituents are schematically shown and briefly summarized in Table 1.2. Indeed, accurate knowledge on the subject of gas and water transport properties in different MEA constituents is absolutely essential.

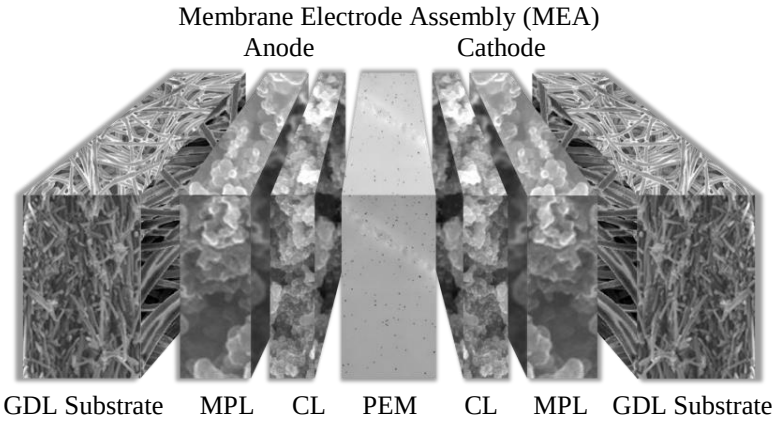

Layer	Thickness (µm)	Porosity (%)	Pore Diameter (µm)	Composition
GDL Substrate	180 – 400	70 – 90	1 – 100	Carbon Fiber, Binder, PTFE
MPL	10 – 100	40 – 60	0.02 – 0.2	Carbon Powder and PTFE
CL	6 – 25	40 – 50	0.04 – 0.07	Carbon, Platinum, PFSA (Nafion®)
PEM	25 – 125	–	–	PFSA (Nafion®)

Figure 1.5. Membrane electrode assembly constituents of a PEFC with their characteristics [11,12].

Table 1.2. Functions and transport phenomena of a PEFC Membrane Electrode Assembly [3].

Layer	Functions and Transport Phenomena	Schematic of Transport Phenomena
GDL	• Gas reactant porous media flow • Water evaporation and condensation • Liquid water porous media flow • Electron transport • Heat transfer	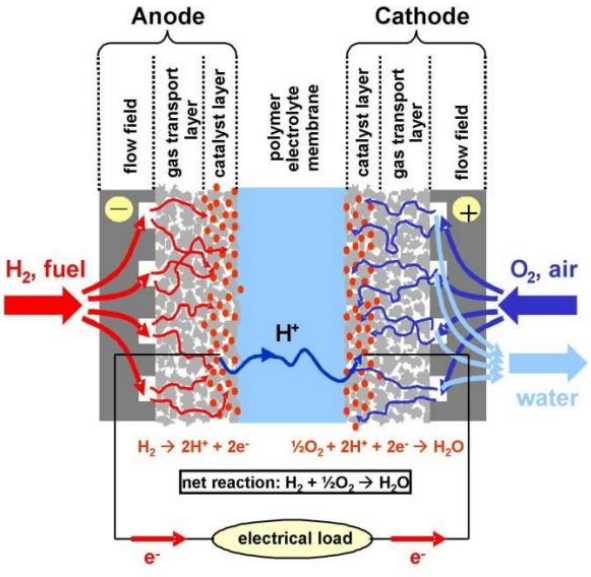
CL	• Electrochemical reactions • Gas reactant porous media flow • Water evaporation and condensation • Liquid water porous media flow • Membrane (dissolved) water transport • Membrane water sorption/desorption • Electron transport • Proton transport • Heat transfer	
PEM	• Repelling electrons • Impermeable barrier to gas reactants • Membrane (dissolved) water transport • Proton transport • Heat transfer	

The GDL, as the centerpiece of this thesis, is a bi-layer carbon-based conductive porous material functioning as a core component of the MEA for reactant and water transport. Its characteristic structure is illustrated by the measured SEM images shown in Figure 1.6. The GDL functions include reactant gases and two-phase mass transport along with electrical charge transfer between catalyst layers and flow field plates, as well as thermal management and mechanical stability. GDL substrate features primary pore sizes in the range of 1 – 100 µm and usually contains carbon fibers, carbonaceous binder, and hydrophobic agent such as polytetrafluoroethylene (PTFE), while the MPL features primary pore sizes in the range of 20 – 200 nm and is usually made of carbon nano-particle agglomerates and PTFE. Other types of additives may also be added to the two layers to improve their functionality. The GDL transport capability is the mechanisms of how gases, liquid, charges, and heat are transported in the porous structure of the GDL, *i.e.*, gas

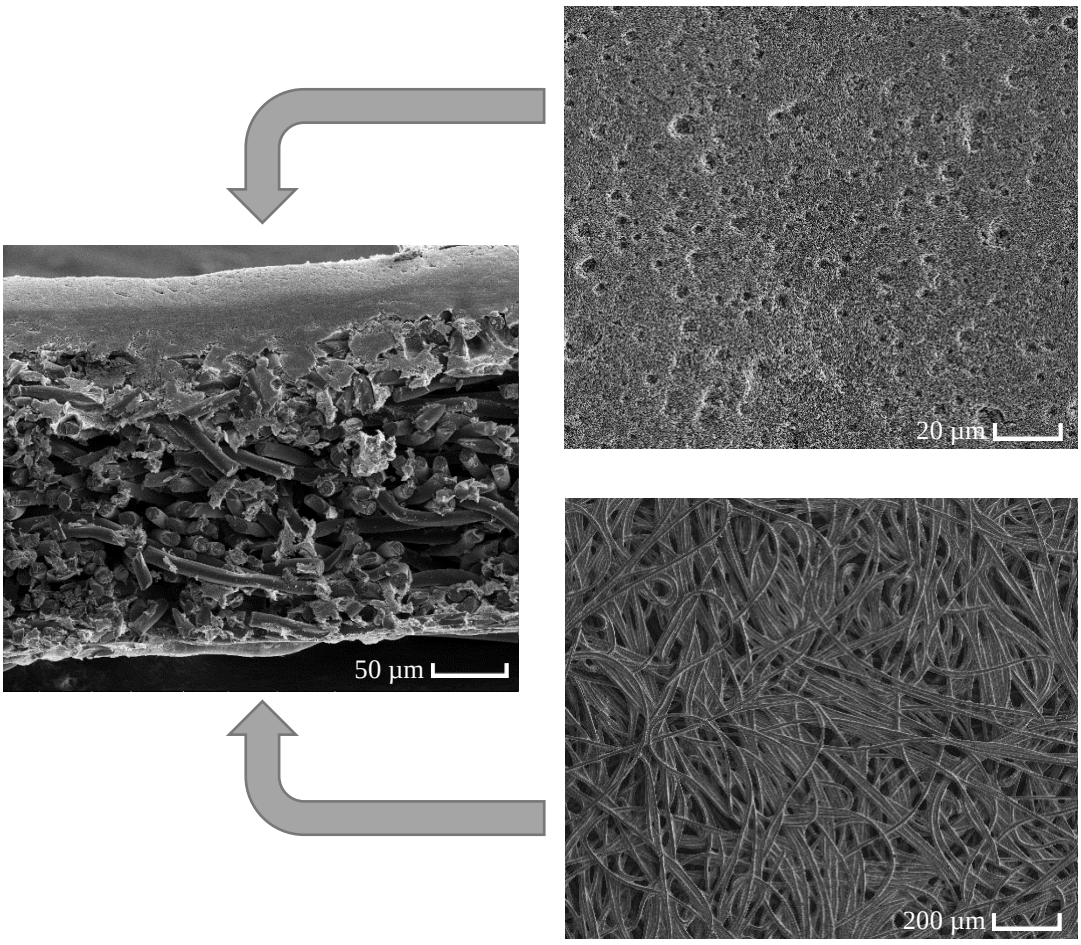

Figure 1.6. Measured cross-sectional, top, and bottom view SEM images of a GDL (MPL-coated GDL) taken at SFU 4D LABS.

diffusivity, permeability, and thermal and electrical conductivity, which is highly dependent on its real pore morphology that will ultimately affect the fuel cell performance [3,13].

MPL, as a recent but essential addition to the MEA, is a smooth transitional layer between the macroporous GDL substrate and nanoporous CL [2,13,14] and it is unlikely to find a modern PEFC that does not have this layer. It has been experimentally and numerically proven that coating the MPL on GDL substrate facing the CL, to form a porosity-graded GDL structure, enhances the fuel cell performance particularly at high power densities. The MPL tends to penetrate into the GDL substrate and thus, forming a compact composite-like GDL structure. Indeed, the MPL improves the interfacial properties and assists the liquid water management during fuel cell operation. It is discussed in [11] that MPL increases the chemical and mechanical stability by avoiding the entrenching of CL to the carbon paper GDL substrate, especially on compression conditions. It also improves the current collection and reduces the thermal and electrical resistance between CL and GDL substrate [15,16]. In terms of water management, it enhances mass transport limitations by reducing the number of injection sites and successively reduces the overall saturation and flooding at high current density conditions specifically at the cathode electrode [17]. In addition, the MPL cracks and pores can provide proper routes for evacuation of liquid water; thus, avoid the flooding at high current density conditions. Moreover, the hydrophobic agent in the MPL allows the CL and membrane to retain sufficient liquid water at low current density conditions and suppresses water accumulation thus improves start-up performance. Hence, due to crucial MPL effect on fuel cell functionality, the MPL pore morphology composition, *i.e.*, particle type, size, loading (thickness), and PTFE content are identified as the key MPL characteristics that influence the GDL transport properties and ultimately fuel cell performance. However, while implementing the MPL increases the overall fuel cell performance, the exact phenomena of the underlying mechanisms are yet to be elucidated.

Motivation: Accurate knowledge regarding transport properties of gas, water, electrons, and heat in the bi-layer GDL is essential for improving the performance and durability of PEFCs as well as for material specifications, design, and prototyping in the

area of fuel cell development and manufacturing. Moreover, reliable assessment of the MPL structure and its properties is a major challenge, and literature data are scarce. In this context, this thesis aims to develop novel tools for MPL and GDL substrate characterization, microstructural modeling, transport properties simulation, and analysis. Furthermore, understanding the correlation between the GDL substrate and MPL real pore morphology composition and GDL transport properties provides important information for material optimization and fuel cell design which is the focus of the thesis. There have been rare investments on providing a design tool to meet the demand on the GDL transport properties for different applications by altering the MPL and GDL substrate design and composition. Microstructural model development on the scale of the pore system is a feasible tool to derive this correlation which will be extensively elaborated in this thesis.

1.2. Literature Review

There are several experimental techniques for GDL morphology and pore structure characterization and variety of established experimental, theoretical, analytical, and

Table 1.3. Imaging techniques for GDL substrate and GDL morphology and microstructure characterization [11].

Apparatus	Imaging Type	Usage Scope
SEM	2D	**Strength:** Commonly used apparatus. **Weakness:** Limited capability in providing information on surface perturbations from 2D images, *e.g.*, surface roughness.
SEM together w/ EDS	2D	**Strength:** Identify the fluorine content and distribution with EDS analysis, hence, a measure for the PTFE presence in the GDLs. **Weakness:** The same as SEM.
Optical Microscope	2D	**Strength:** Cheaper and faster 2D imaging; applicable to samples with any surface roughness. **Weakness:** Limited focus depth and resolution capabilities, hence, poor quantitative surface information compared to SEM.
AFM	2D	**Strength:** More accurate quantitative information on surface roughness, conductive regions, and adhesion force distributions from surface scans. **Weakness:** Limited scanning area and measurement speed.
CLSM	2D or 3D	**Strength:** 3D structure reconstruction from 2D images captured at different depths; deeper information of morphological details, *e.g.*, physical interactions between binder and fiber in GDL substrates.
3D Surface Profiler	2D or 3D	**Strength:** 2D or 3D characterization of the entire surface profile of the structure; ability to depict the highest and lowest points on a surface and the regions in between, hence, the thickness uniformity.

numerical techniques for transport properties determination which will be extensively discussed in the following subsections.

1.2.1. GDL Morphology and Pore Structure Characterization

In terms of qualitative pore characteristics and morphology, Table 1.3 summarizes the commonly used 2D and 3D imaging apparatuses, the imaging type, and usage scope for GDL morphology and microstructure characterization. The apparatuses include scanning electron microscope (SEM), SEM with energy dispersive X-ray spectroscopy (EDS), optical microscope, atomic force microscope (AFM), confocal laser scanning

Table 1.4. Measurement techniques for GDL substrate and GDL pore structure characterization, *e.g.*, porosity and pore size distribution [11].

Technique	Measuring Method
Standard Porosimetry	Determining the curve of capillary pressure vs saturation of a test sample by utilizing known capillary pressure curves of two standard samples with equal capillary potentials. **Strengths** • Non-destructive and simple-to-perform. • Characterization of porous media with the pore diameter of 0.3 nm - 100 μm. • Can be employed with various working fluids under room conditions.
Mercury Intrusion Porosimetry	Utilizing the magnitude of the pressure required to overcome the surface tension to determine the pore characteristics. **Strengths** • Robust characterization of porous medium with the pore diameter of 3 nm - 100 μm. • Mercury as the working fluid since it is non-wetting for most surfaces. • Applicable for porous media containing both hydrophobic and hydrophilic pores. **Weakness** • Destructive. • Back streaming of the extruded mercury preventing accurate detection of pore characteristics of porous materials with small pore sizes. • Mercury is toxic.
Capillary Flow Porometry	It is based on the principle similar to that of MIP. **Strengths** • Non-destructive and relatively faster method and uses a wetting fluid. • Working fluid selection based on porous material specification.
Water Intrusion Porosimetry	It is based on the principle similar to that of MIP. **Strengths** • Non-toxic working fluid (water), hence, low risk of sample damage and less-complex equipment and a lower imposition pressure. **Weakness** • Unsuitable for characterization of hydrophobic pores.

microscope (CLSM), and three-dimensional surface profiler. With regard to quantitative and more precise information on GDL pore structure, Table 1.4 summarizes the popular techniques, the measuring method, and the usage scope for GDL characterization as a complement to qualitative pore morphology characterization. The techniques include method of standard porosimetry (MSP), mercury intrusion porosimetry (MIP), capillary flow porometry, and water intrusion porosimetry [11]. By considering the usage scope, the appropriate pore morphology and structure characterization technique can be adopted to meet the application's requirements.

1.2.2. GDL Transport Properties Determination

There have been several methods in the literature to determine the GDL substrate and GDL transport properties of effective permeability coefficient, effective diffusion coefficient, effective thermal and electrical conductivity; based on experimental techniques [18–21], theoretical and analytical approaches, and numerical simulations which will be summarized in the following subsections.

i. Experimental Techniques

The following subsections are allocated to reviewing the most frequently used techniques and apparatuses in the open literature for GDL transport properties measurements.

Absolute Permeability Coefficient: There have been several *ex-situ* experimental techniques with well-established principles, to determine the in-plane (IP) and through-plane (TP) absolute permeability coefficients for GDLs [20–25]. Hence, the employed experimental equipment is similar with slight architectural differences as schematically shown in Figure 1.7[2]. The fundamental concept behind the absolute permeability measurements is to measure the pressure drops between the two edges of the porous media at different working-fluid flow rates. Air in humidified form, as the working-fluid, is

[2] Reprinted from Progress in Energy & Combustion Sci., 74, A. Ozden, S. Shahgaldi, X. Li, F. Hamdullahpur, A review of gas diffusion layers for proton exchange membrane fuel cells - With a focus on characteristics, characterization techniques, materials and designs, 50-102, 2019, with permission from Elsevier.

generally used to mimic the actual cell operation conditions. The measured flow rates and pressure drops are converted to absolute permeability coefficients by solving the Darcy's law in one dimension with the assumptions that the velocity of the working-fluid is sufficiently small, and the pressure drop across the sample is predominantly caused by viscous drag. Indeed, by altering the working-fluid flow direction, the pressure drops in both the IP and TP directions and that being so the IP and TP absolute permeability coefficients can be determined.

Relative Permeability Coefficient: There are rare experimental data for the relative permeability measurement as a function of liquid water saturation through the GDL due to its moderately challenging procedure, thus, the reliability of the measurement procedures has not yet been established [11]. Penn State method as a steady-state flow measurement technique is probably the only available experimental procedure for GDL relative permeability measurement adopted by Sole *et al.* [26]. With accurate knowledge on water saturation and flow rates of water and gas phases, the relative permeability of each phase can be calculated through simple Darcy's correlations [26]. This method was also used to measure the water relative permeability of Toray TGP-090 carbon paper [27] and Toray TGP-H-060, TGP-H-090, TGP-H-120, and E-TEK carbon cloth [28].

Effective Diffusion Coefficient: There are several *in-situ* [29–31] and *ex-situ* [30,32–36] techniques in the literature to determine the effective diffusion coefficient more commonly oxygen diffusion resistance through the GDL. Regarding the *ex-situ* techniques,

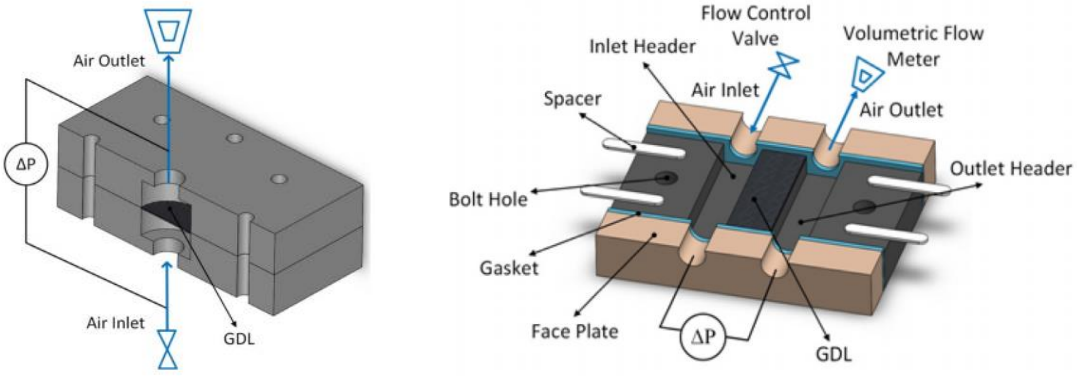

Figure 1.7. Schematic of the experimental setup for the (a) through-plane and (b) in-plane (section view) absolute permeability measurements of the GDL [11,20,25].

a Loschmidt cell is utilized to perform the effective diffusion coefficient measurement which is based on a closed-tube method developed by Loschmidt in the late 1800s. The Loschmidt cell, as a closed-tube schematically depicted in Figure 1.8[3], consists of top and bottom chambers, which can be connected or separated via a sliding gate as part of the bottom chamber in position (5a) or (5b), respectively, and a specimen mounted between the chambers. The specimen is mounted on the top surface of sliding gate which is aligned to the center of the cell marked as x = 0 on the coordinate system. The cell is equipped with inlet and outlet flow controllers to control the gas flow rates, oxygen sensor to monitor the oxygen concentration variations, and humidity sensors to measure the relative humidity. The apparatus is engineered in a way that diffusion process follows a one dimensional Fick's law of diffusion [37]. The overall diffusion coefficient is calculated by fitting of one dimensional diffusion process to the data recorded for the concentration variation with respect to time. By considering the diffusion resistance network built up inside the chambers, which consists of both specimen and chamber resistances, the specimen diffusion coefficient can be calculated.

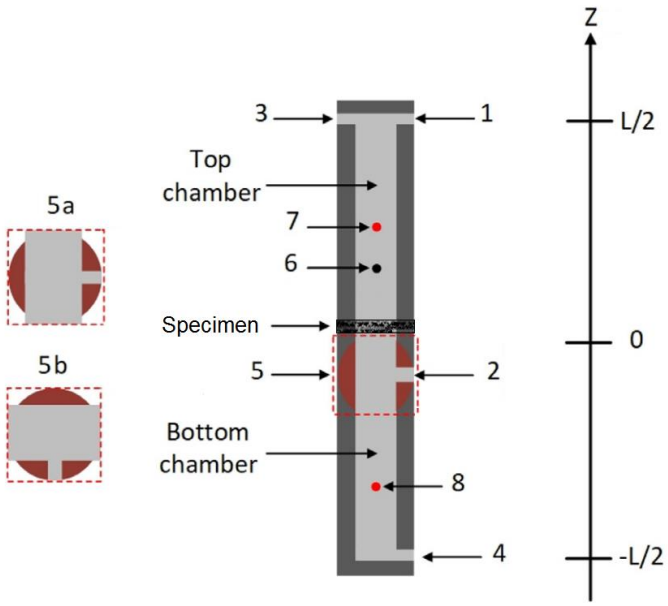

Figure 1.8. Schematic of the Loschmidt cell for through-plane diffusion coefficient measurements. 1 and 2: gas inlets; 3 and 4: gas outlets; 5: sliding gate, (5a): open position, (5b): closed position; 6: oxygen sensor; 7 and 8: humidity sensors [11,25].

[3] Reprinted from [11] with minor modifications with permission from Elsevier.

Effective Electrical Conductivity: The IP electrical conductivity of the GDL can be measured by the four-probe method [25,38]. To do so, a GDL sample is mounted on an insulation plate and two conductive electrodes are attached to each end of the sample as schematically illustrated in Figure 1.9[4]. The two electrodes are connected to the outer probes from which the supplied electrical current I is flowing through the GDL sample. Subsequently, the corresponding voltage difference E of the two inner probes attached to the sample is measured and thus the resistance R of the path between the two inner probes is calculated according to Ohm's law. Thereafter, the resistivity of the GDL, can be calculated by taking the geometry-dependent correction factor into account whose value depends on the distance between the inner probes as well as the sample dimensions. In the final step, the electrical conductivity σ_{eff} can be obtained as an inverse of the resistivity.

Similarly, the four-probe method is utilized to measure the TP electrical conductivity with a slight architectural apparatus difference to mimic the GDL condition in an actual cell operation [38]. In this method, a disc-like GDL sandwiched between two stainless steel discs is placed between two conductive electrodes. The whole setup is mounted in a clamp by which the experiment can be performed under different clamping

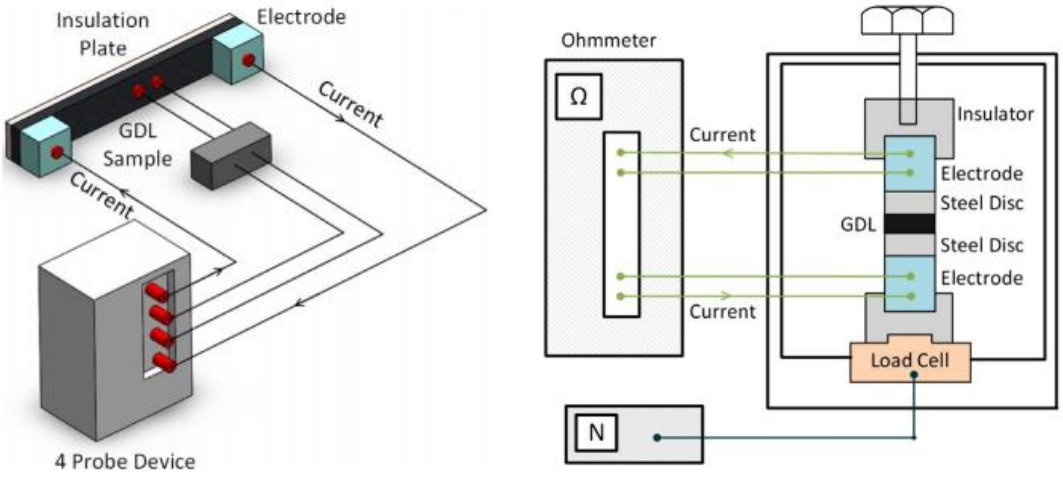

(a) (b)

Figure 1.9. Schematic of the experimental setup for the (a) in-plane and (b) through-plane electrical conductivity measurements of the GDL[11,25,38].

[4] Reprinted from [11], with permission from Elsevier.

pressures. The outer and the inner probes are connected to the electrodes on each side and the resistance calculated by the Ohm's law is the total bulk resistance of the GDL, steel discs, electrodes, and interfacial contact resistances between the compartments.

Effective Thermal Conductivity: Several experimental techniques have been developed to measure the effective thermal conductivity of GDLs including steady-state and quasi-steady-state methods. As a steady-state technique of TP GDL thermal conductivity measurements, a guarded heat flux meter is used in [25] for which the sample setup and apparatus details are schematically illustrated in Figure 1.10[5]. The apparatus is designed to allow one dimensional heat transfer in the axial direction. Heat flux originated from the temperature difference between the hot and cold plates generates a temperature gradient along the highly conductive rods which is measured with a set of thermocouples in the same intervals between the plates in steady-state conditions. Heat flux is calculated utilizing the temperature gradient and the thermal conductivity of the rods governed by the conduction equation. Hence, by analogy with Ohm's law, the total thermal resistance is achieved by considering the temperature difference as the voltage and heat flux as the current. The total resistance includes the sample resistance as well as the contact resistance between the sample and the top and bottom rods. Therefore, the contact resistance as a

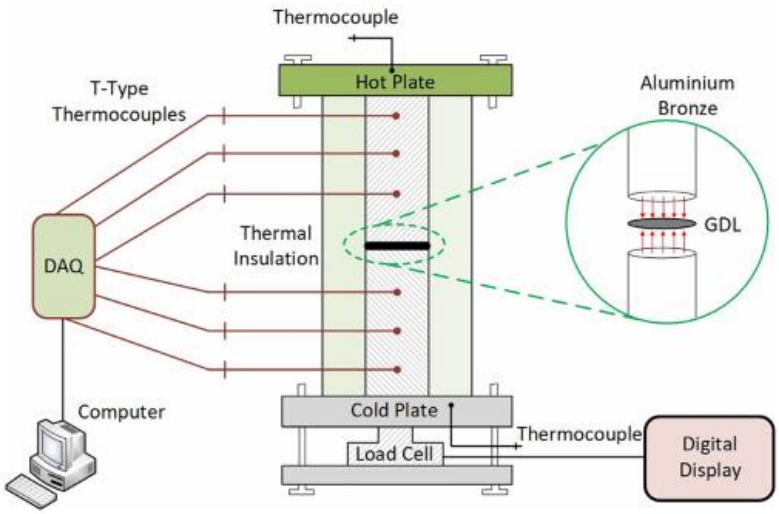

Figure 1.10. Schematic of the experimental setup for the through-plane thermal conductivity measurements of the GDL [11,25].

[5] Reprinted from [11], with permission from Elsevier.

function of sample and the rods surface characteristics should be calculated to derive the GDL sample thermal resistance. To do so, the potential approach is to conduct several experiments with the stack of samples to estimate the resistances which is a fairly challenging task. Other steady-state methods for TP GDL thermal conductivity measurements have also been developed to investigate the changes in the TP GDL thermal conductivities under various saturation levels and mechanical compressions [39]. The method is practical for understanding the thermal transport phenomena in an actual operating cell conditions and providing experimental data for modeling studies [11].

Regarding the steady-state IP GDL thermal conductivity measurements, two methods have been developed, so far [40,41]. The apparatus utilized in [40], is fairly similar to the one for the TP thermal conductivity measurements as explained before and the schematic of the experimental setup is depicted in Figure 1.11[6]. A one-dimensional conduction heat transfer through the axis of the upper and lower fluxmeters is a must for which the apparatus needs to be placed inside a vacuum chamber. The other steady-state

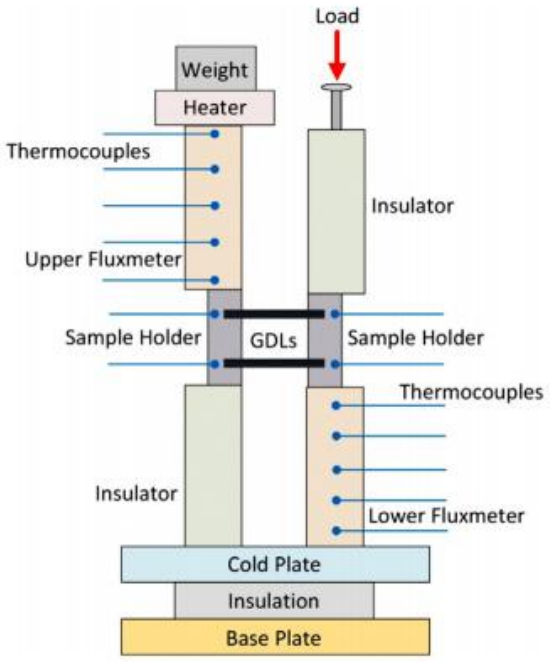

Figure 1.11. Schematic of the experimental setup for the in-plane thermal conductivity measurements of the GDL [11,25].

[6] Reprinted from [11], with permission from Elsevier.

method in [41] known as parallel thermal conductance (PTC) method offers the advantage of fast data collection due to two consecutive simple-to-perform steps in the measurements and quick sample preparation. Moreover, in contrary to [41], the technique provides high measurement accuracy with no need of further assumption or thermal contact resistance measurements.

Concluding Remarks: For material optimization in modern PEFCs design and development process, analysis of a wide range of GDL samples with experimental techniques are substantially costly in terms of time and resources which is not feasible in a design cycle with iterative nature. Furthermore, it is hypothesized that MPL is the most delicate layer among other MEA components and cannot be fabricated as a discrete layer with realistic thicknesses. Indeed, direct experimental measurement methods of MPL transport properties are not reliable and accurate enough to provide a solid understanding of its properties. MPL transport properties are evaluated by comparing the overall changes in the measured properties of GDL (MPL-coated GDL) and GDL substrate [32,41–46] which are underestimated due to penetration of MPL into GDL substrate. As a conclusion, theoretical and numerical approaches as an alternative provide more reliability and flexibility for GDL material prototyping assignments to reduce the cost and time of the design cycle. Nevertheless, the design cycle involves a degree of uncertainty, hence, experimental techniques should be utilized as complimentary approaches to shed light on GDL transport properties understanding.

ii. Theoretical and Analytical Techniques

A variety of theoretical and analytical methods have been developed in the open literature to estimate the transport properties of general porous media for which the details will be briefly discussed in the following paragraphs. Indeed, the obtained mathematical models, which are widely used to estimate the GDL transport properties, are commonly employed in macroscopic PEFC modeling and analysis [40,47,48].

Effective Diffusion Coefficient: As summarized in Table 1.5, several mathematical models have been developed to estimate the diffusion coefficient of general porous media composed of spherical particles [49–53]. Reliability and accuracy of the models for the

application of GDL diffusion coefficient estimation will be extensively elaborated in section 2.3 to contextualize the simulated data of the current work. Briefly saying, the models provide inaccurate data for estimation of GDL diffusion coefficients which are inherently made of cylindrical carbon fibers or cloths. The mathematical models merely depend on the porosity of the porous media as a fundamental characteristic of GDL structural parameters. However, not only porosity but also other key structural parameters, *e.g.*, tortuosity, pore size distribution (PSD), and mean pore radius, which are ignored in the models, have a strong influence on GDL diffusion. For instance, tortuosity as a measure of diffusion path complexity through interconnected pores is neglected in the models.

Effective Permeability Coefficient: Several mathematical models have been developed to estimate the intrinsic and relative permeability coefficients of general porous media based on their pore structural characteristics where the common correlations are summarized in Table 1.6 [48,54–57]. As a recent advancement in analytical approaches, a mathematical model is developed in [47] in which the permeability of the ordered fibrous porous media towards normal and parallel flow is determined by employing an integral technique solution. In their work, the fibrous porous media are simplified as repetitive solid matrix of fibers parallel to each other, but randomly distributed in the volume. Several

Table 1.5. Summary of common correlations for the prediction of diffusion through porous media [49–53].

Ref.	Model		Type / Material
[49]	$\frac{D_{eff}}{D_{bulk}} = \varepsilon^{1.5}(1-s)^{1.5}$	(1-1)	Effective medium approximation / A porous media composed of uniformly distributed spherical particles
[50]	$\frac{D_{eff}}{D_{bulk}} = (1-s)^{1.5}(1-(1-\varepsilon)^{0.46})$	(1-2)	Multi length scale / Spherical particle based porous media
[51]	$\frac{D_{eff}}{D_{bulk}} = \varepsilon(1-s)^{2}\left(\frac{\varepsilon-0.11}{1-0.11}\right)^{0.785}$	(1-3)	Percolation theory / Randomly 2D network of stacked fibers
[52]	$\frac{D_{eff}}{D_{bulk}} = \varepsilon(1-s)^{1.5}\left(\frac{\varepsilon-0.037}{1-0.037}\right)^{0.661}$	(1-4)	Percolation theory / A porous media composed of freely overlapping random fibers oriented in different directions
[53]	$\frac{D_{eff}}{D_{bulk}} = 1+\frac{3\left(1-\varepsilon(1-s)\right)}{\varepsilon(1-s)-3}$	(1-5)	Effective medium approximation / An isotropic porous media composed of uniformly distributed spherical particles

touching and non-touching fiber arrangements are considered. Hence, analytical permeability relationships are developed for variety of touching fiber arrangements as a function of fibers diameter and medium porosity.

Even though researchers have put forth extensive efforts to develop mathematical models for GDL permeability coefficient estimation, the proposed models are not yet accurate enough. It is due to the fact that the GDL permeability is highly interlinked to structural characteristics of porosity, pore size distribution, and fiber diameter. Moreover, the other weakness of the proposed models for the application of MPL-coated GDL permeability estimation comes from the fact that the MPL complex structure has not been taken into consideration for model development. Considering all the limitations for GDL permeability estimations, the mathematical models are still widely used for liquid water transport investigation due to lack of reliable experimental data. It is noteworthy that numerical GDL microstructural methods are accurate alternatives to estimate the GDL permeability.

Table 1.6. Summary of common correlations for permeability of porous media [48,54–57].

Ref.		Model		Type / Material
[54]	Intrinsic Permeability	$k = \frac{\varepsilon^{n+1}}{C(1-\varepsilon)^n}$ $n = 2$ for carbon paper GDL substrate	(1-6)	Kozeny-Carman A semi-empirical formula for beds of particles n and $\boldsymbol{C}$: Kozeny-Carman constants depending on structure
[48]		$k = r^2 \frac{\varepsilon(\varepsilon - 0.11)^{\delta+2}}{8(Ln\varepsilon)^2(1-\varepsilon)^{\delta}[(\alpha+1)\varepsilon - 0.11]^2}$ $\delta = 0.521$ for the IP $\delta = 0.785$ for the TP	(1-7)	Tomadakis & Robertson Percolation theory for randomly overlapping fibrous porous structures δ: a constant depending on structure & flow direction
[55]	Relative Permeability	$k_{rel,WP} = s_{WP}^n$ $k_{rel,NWP} = (1 - s_{NWP})^n$	(1-8)	Power Law n: fitting constant depending on structure
[56]		$k_{rel,WP} = s_{WP}^{3+2/n}$ $k_{rel,NWP} = (1 - s_{WP})^2\left(1 - s_{WP}^{1+2/n}\right)$	(1-9)	Brooks-Corey n: a constant describing pore distribution
[57]		$k_{rel,WP} = s_{WP}^{\delta}\left(1 - \left(1 - s_{WP}^{1/n}\right)^n\right)^2$ $k_{rel,NWP} = (1 - s_{NWP})^{\delta}\left(1 - s_{WP}^{1/n}\right)^{2n}$	(1-10)	Van-Genuchten n and δ: constants depending on structure (fitting parameter) and pore tortuosity, respectively

Effective Electrical Conductivity: The effective medium approximation theory (EMT) is usually used in the literature to derive approximations of effective electrical conductivity of homogeneous porous structures consisting of spherical/ellipsoidal particles as summarized in Table 1.7 [49,53,58]. In this theory, the properties and relative fractions of the porous structure components are often used to describe the effective conductivity of the medium. While the widely-used Bruggeman and Looyenga approximations [49,58] for modeling electron transports in PEFCs are based on the EMT, Das *et al.* [53] developed an expression for GDL effective electrical conductivity by utilizing another form of the EMT which is the generalized Maxwell-Garnett (MG) equation normally applied to multiphase mixtures. The MG states that the effective property is a function of the bulk property of the inclusions and the matrix as well as the volume fraction of the embedded material. Das approximation utilized the Hashin bounds, where these bounds have been developed for a homogeneous mixture of coated sphere assemblage, in which the effective property of a porous material will obey the following relation:

$$\Gamma_2 + \frac{3\Gamma_2(VP_1)(\Gamma_1 - \Gamma_2)}{3\Gamma_2 + (VP_2)(\Gamma_1 - \Gamma_2)} \leq \Gamma_{eff} \leq \Gamma_1 + \frac{3\Gamma_1(VP_2)(\Gamma_2 - \Gamma_2)}{3\Gamma_1 + (VP_1)(\Gamma_2 - \Gamma_1)} \qquad (1\text{-}11)$$

where Γ_1 and Γ_2 are the bulk properties and VP_1 and VP_2 are the volume fractions of phases 1 and 2, respectively, with Γ_{eff} being the effective property of the homogeneous mixture. The drawback of the EMT approximations in estimating the GDL effective electrical conductivity is in underestimating the structural parameters of the medium.

Table 1.7. Summary of common correlations for the prediction of effective electrical conductivity through porous media.

Ref.	Model		Type / Material
[49]	$\sigma_{eff} = \sigma_S(1-\varepsilon)^{1.5}$	(1-12)	Effective medium approximation / A porous media composed of uniformly distributed spherical particles
[60]	$\sigma_{eff} = \sigma_S(1-\varepsilon)^{3}$	(1-13)	Effective medium approximation / A porous media composed of uniformly distributed spherical particles
[53]	$\sigma_{eff} = \sigma_S\left(\frac{2-2\varepsilon}{2+\varepsilon}\right)$	(1-14)	Hashin-Shtrikman (HS) bounds / A homogeneous mixture of coated sphere assemblage

Effective Thermal Conductivity: In theory, the effective thermal conductivity of the porous media is a function of porosity and bulk thermal conductivities of solid and fluid phases. In contrast to the effective diffusion coefficient and permeability, there are no specific correlations for effective thermal and electrical conductivities of carbon paper diffusion media. However, an averaged value that lies between the maximum and minimum material properties is sometimes used. This averaging approach considers the conductivity of the different regions of the porous medium with respect to their volume fractions and is hence referred to as mixing law models. A summary of the available mathematical models utilized for the bounds of GDL effective thermal conductivity estimation are listed in Table 1.8 [59–61]. Hashin–Shtrikman (HS) as the most widely used bounds have been developed for a homogeneous mixture of coated sphere assemblage and stated that the effective properties of a porous material must lie between upper and lower bounds.

GDL thermal conductivity is a directional-dependent transport property and its estimation is quite challenging due to complex and anisotropic microstructure of GDL as well as apparent differences in the bulk thermal conductivities of the solid and fluid phases. In many analytical analyses, thermal conductivity has been predicted by combining series and parallel models and/or by taking the mean geometric average of the thermal conductivities of solid and liquid phases [11]. A very few analytical and empirical studies have been developed in the literature to consider the anisotropy of the GDL in thermal

Table 1.8. Summary of common correlations for thermal conductivity of porous media [72, 76-77].

Ref.	Model		Type / Material
[59] [60]	$K_{max}^{eff} = \varepsilon K_f + (1-\varepsilon)K_S$	(1-15)	Kaviany & Abdulagatova K_S and K_f are the solid and fluid thermal conductivities. K_{max}^{eff}, K_{min}^{eff} and K_{interm}^{eff} are the maximum, minimum and intermediate effective thermal conductivities.
	$K_{min}^{eff} = \left[\frac{(1-\varepsilon)}{K_S} + \frac{\varepsilon}{K_f}\right]^{-1}$	(1-16)	
[61]	$K_{interm}^{eff} = {K_f}^{\varepsilon} {K_S}^{(1-\varepsilon)}$	(1-17)	Hashin-Shtrikman (HS) bounds / A composite system composed of a large number of coated spheres.
	$K_{min}^{eff} = K_f + \frac{3(1-\varepsilon)K_f(K_S - K_f)}{3K_f + \varepsilon(K_S - K_f)}$	(1-18)	
	$K_{max}^{eff} = K_s + \frac{3\varepsilon K_S(K_f - K_S)}{3K_S + (1-\varepsilon)(K_f - K_S)}$	(1-19)	

conductivity estimation and its impact on polarization behavior but yet as simplified methods [40,62–66]. In an analytical approach, the effective GDL thermal conductivity is estimated by approximation of the GDL geometrical structure as cylindrical carbon fibers which are equally spaced horizontally and stacked vertically to form mechanical contacts [40,62]. They used the Hertzian theory to evaluate the contact area between the overlapping fibers. In [66], using statistically-based unit cell model, they demonstrated that the structural parameters of angle distribution and aspect ratio are as important as porosity for the prediction of conduction through GDLs. Moreover, in [63], using fractal model, other structural parameters including shape and size of solid phase as well as PSD have been approximately incorporated to investigate their effects on heat transfer phenomena.

Concluding Remarks: All the above-mentioned conventional mathematical models for the GDL transport properties estimation have not been developed based on the real GDL 3D microstructural information. Moreover, the MPL complex morphology and structure has not been taken into consideration for model development for the application of MPL-coated GDL transport property estimation. Therefore, it is a considerable challenge to rigorously determine GDL transport properties without access to the real 3D morphological and microstructural characteristics and, correspondingly, the resulting estimations of transport properties and predictions of fuel cell performance have a high degree of uncertainty in the proposed analytical methods [67]. For example, it is nearly impossible to have an accurate knowledge regarding tortuosity and PSD without having realistic GDL 3D microstructural information. Given these limitations, a shift towards developing more comprehensive numerical techniques, which consider the realistic pore characteristics of GDLs, provides an opportunity to precisely estimate the effective transport properties.

iii. Numerical Techniques

Due to the challenges and limitations of the aforementioned experimental and theoretical approaches, clear representation of the GDL and MPL structure with numerical microstructural methods and consequently effective transport properties numerical simulation can offer complementary capabilities. There are several numerical microstructural modeling techniques such as pore network, tomographic reconstruction

from measured images [68–70], and virtually reconstructed stochastic methods [71–77] to reconstruct the GDL microstructure that acts as a 3D microstructural computational domain for numerical modeling of transport properties.

Pore Network Microstructural Modeling: The first attempt to deploy pore network modeling for the study of multiphase transport in GDLs was introduced by Gostick *et al.* [78]. In the pore network model, which is a developing method to elucidate the pore-scale physics of liquid water transport, the GDL pore space continuum is considered as a geometrical model of regular or irregular lattice of pores interconnected via throats [78–86]. Simplifying assumptions regarding the shape of pores and throats are invariably made to facilitate the computation of capillary and transport characteristics of the pore network elements. The model is then used to calculate unknown saturation dependent transport properties after calibrating to real materials using measured material properties such as porosity or permeability. While these models can provide substantial insight to the pore-scale liquid water transport and can address the effect of mixed wettability on liquid water distribution, they rely on generalized structures to match the average properties of the GDL, such as porosity and permeability, which are insufficient to define a unique pore structure in addition to their dependency on appropriate and accurate calibration data [87].

Tomographic Microstructural Modeling: Tomographic image-based micro-structural reconstruction techniques such as X-ray computed tomography (XCT) [88,89] and focused ion beam-scanning electron microscopy (FIB-SEM) can be used to obtain detailed 3D digital image representation of the GDL and MPL microstructures [90–96].

XCT has recently shown good prospects for analyzing GDL and MPL internal microstructures due to its non-invasive and non-destructive imaging technique and its ability to differentiate between different phases of the porous structure. A set of 2D images of the porous media are captured from different incident angles, thereby, generating projections of the structure in different planes. The projections are combined using a computerized tomographic reconstruction algorithm to generate consecutive 2D cross-section images of the porous media. In this way, different cross-sectional images can be combined to attain a 3D reconstruction of the original structure. Depending on the desired

image resolution for the porous media under study, either micro-XCT (pixel resolution 1–5 μm) for GDL substrate or nano-XCT (pixel resolution 10–20 nm) for MPL can be employed to reconstruct the 3D microstructure. Moreover, XCT enables fuel cell researchers to investigate the two-phase flow in the GDL substrate and MPL efficiently [97]. In addition, FIB-SEM as a destructive technique utilizes a dual-beam device for repetitive milling with focused ion beam (FIB) and high-resolution imaging with scanning electron microscopy (SEM) of nanoscale materials in three dimensions followed by image processing to reach the real 3D morphology of the structure.

Although, the tomographic methods provide accurate and realistic reconstruction of the GDL 3D microstructure and insight of the internal structure, extensive sample preparation steps and difficulty in preparing thin samples due to soft nature of the MPL material in NXCT and the inability to differentiate carbon and PTFE phases throughout the GDL in FIB-SEM due to limited precision of the physical rendering are the major limiting factors of these methods. More importantly, analysis of a wide range of GDL samples is substantially costly in terms of time and resources which is not feasible in a design cycle for performing extensive parametric studies [98]. These methods are also not well-suited to capture the stochastic behavior exhibited by the GDL and MPL structures, as they only provide a single realization of the material. Finally, these methods do not mathematically parametrize the structure, and therefore, combined with the time and cost issues, make it difficult to characterize, manipulate, and optimize the structure. Hence, a fast and cost-effective design tool for virtual model reconstruction of real GDL materials is crucial [68,70].

Stochastic Microstructural Modeling: Inspiring the randomness of GDL porous media structure and its fabrication process, the GDL microstructure can be virtually reconstructed as a collection of stochastic processes. The technique of stochastic microstructural reconstruction relies on different statistical correlation functions which describe the probabilities of the porous media constituents' distribution and aim to encompass all the details of the porous media structure [99]. For instance, the statistical n-point matrix correlation functions, which are defined as the probability of finding n number of random points in a given phase, are used to retrieve the heterogeneous GDL

microstructure via the process of stochastic reconstruction. The obtained 3D digitized realizations of the stochastic model are then used as a domain for numerical computation of transport properties. The general approach with low cost and high speed of data generation makes it reliable and flexible enough to be considered as a virtual design tool for material prototyping assignments. However, validation is a challenging task in order to ensure a correct representation of the physical structure. There has been few studies on 3D GDL substrate [69,71–74,76,77,100–106] and MPL [107–109] virtual stochastic micro-structural modeling as an alternative to tomographic reconstruction techniques.

- **GDL Substrate Stochastic Microstructural Modeling:** For GDL substrates, random digital microstructural models of non-woven carbon fibers are stochastically generated by a macroscopically homogeneous random system of infinitely long straight cylinders. Indeed, the method inputs are based on known structural parameters, namely, fiber diameter, fiber orientation, porosity, and binder or/and PTFE fractions which are obtained from images of the actual GDL material captured from electron microscopy (*e.g.* SEM) and/or tomographic imaging methods (*e.g.* XCT).

There are two main methods for carbon fiber stochastic reconstruction modeled by a stationary random system of intersecting lines, known as Poisson line process (PLP) as a modeling element, dilated by a sphere to realize the cylindrical carbon fibers. The process of randomly adding cylindrical fibers is continued until the desired porosity is reached. These methods include:

Method 1: Overlapping cylindrical fibers are randomly placed in 3D space with a constant overall porosity where the method is originally stemmed from Schladitz *et al.* [105]. This general method is applicable to variety of GDL substrates with different anisotropy parameters. The anisotropy in the *z*-direction is described by a one-parametric directional distribution of the fibers. The groups at the Fraunhofer Institute for Industrial Mathematics (Fraunhofer ITWM) at Kaiserslautern are instrumental contributors to the development and use of such GDL models in the fuel cell community [69,74,105].

Method 2: Overlapping intersecting lines are randomly placed in a 2D horizontal Euclidean plane, aka planar Poisson line tessellations (PLT), dilated with a sphere with respect to 3D

to obtain a thin layer of cylindrical fiber structure. The independently distributed layers with constant and identical porosity are stacked together to construct the 3D model. This method is a special case of the first method which is applicable for the commercially available GDL substrates in which carbon fibers have high anisotropy fiber alignment in horizontal direction [71,72]. The groups at the Institute of Stochastics at Ulm University are the contributors of the proposed technique [71].

GDL substrate fibrous porous media are often more complex than a collection of randomly distributed carbon fibers in which binding material(s) is commonly added as a thermoset resin in the manufacturing process. Most previous literature on the GDL substrate stochastic microstructural modeling neglected the presence of binder and PTFE and the structure was generated by only an assembly of overlapping carbon fibers [74,76]. Although the skeleton and alignment of the fibers are sufficient for first-order analysis, the binder is a non-negligible portion of the solid phase which physically connects the fibers and thus has an influential impact on the solid phase transport properties including thermal and electrical conductivities.

In general, binder is often assumed to be attached to the fibers as a highly wetting fluid with respect to carbon fibers. Thus, the binder materials recede into the smaller pores or tight crevices near fiber intersections with relatively low static contact angle due to capillary forces. Indeed, it has been a common practice to fill the pore space of the generated fiber skeleton with binder using various approaches until the desired porosity is reached. The approaches include stochastic methods with predefined probability functions [71,72] or image processing operations such as morphological opening of the fibrous pore space [69,74,76,101] or morphological closing of the fibrous skeleton [73,103] which is briefly explained in the following.

In the Bernoulli-filling technique proposed in [71,72] as a stochastic binder generation method, the binder is treated as thin films bounded by polygons (cells) generated by random intersecting fibers. In this technique, each cell of the 3D-dilated PLT in any given thin layer is independently filled with a certain filling probability $p \in [0,1]$, which describes the amount of binder, whether or not the other cells of the layer are filled.

Neglecting the wetting property of the binder material (thermoset resin) is the downside of this method. For image processing operations, the wetting property of the binder accumulated at small crevasses near the fiber intersections is closely mimicked to digitally generate the binder with 3D morphological closing of the fiber skeleton in the method proposed by Daino *et al.* [73]. The desired wetting fluid morphology of the digital binder is retained by utilizing a spherical structuring element (SE) for the morphological closing. The volume of binder added to the fibrous skeleton is proportional to the SE's diameter [73,102,103]. On the other hand, in the method proposed by Becker *et al.* [69], the morphological opening of the pore space with SE spheres of increasing diameter, known as Granulometry, is used to determine the pore size of the 3D geometry. Indeed, binder is added to the fibrous skeleton by filling the pores, starting from the smallest pores, until the desired binder weight percentage is reached [69,74,76].

Despite the fact that carbon fiber GDL substrates are the promising candidates for handling mass, heat, and species transport during cell operation, they must still undergo an additional microstructure enhancement in the manufacturing process, *i.e.*, hydrophobic treatment via hydrophobic agents. The hydrophobic agents include but are not limited to polyvinylidene fluoride (PVDF), fluorinated ethylene propylene (FEP), perfluoroalkoxy (PFA), and polytetrafluoroethylene (PTFE) [11] as the most commonly used hydrophobic agent in the open literature. Hence, PTFE treatment is an ultimate but important procedure of the GDL substrate manufacturing process that renders more uniform hydrophobic characteristics which aids liquid water expelling and facilitates gas transport through the GDL substrate [110].

Although hydrophobic treatment in the GDL substrate mainly enhances the water management within the cell, its impacts on other GDL substrate characteristics should also be considered for an appropriate cell design. Experimental studies have shown improving hydrophobicity but decreasing bulk porosities, pore sizes, permeability, electrical and thermal conductivity due to PTFE application on carbon fiber GDL substrates [90,93,111,112]. Indeed, optimizing the PTFE treatment parameters, *e.g.*, PTFE loading, to have an optimized balance between water generation and water removal is a key challenge that must be overcome to minimize the ohmic losses and mass transport

limitations. However, certain discrepancies exist in the understanding to optimize the PTFE loading. Some works confirmed through measurement of capillary pressure curves that increasing the PTFE application above 5% wt. did not affect liquid water wetting and this small amount of PTFE was nearly sufficient for complete coverage of the carbon fibers [113]. Discrepancies also exist in the literature as to whether thicker [114] or thinner [115] GDL substrates with PTFE treatments result in improved water management and PEFC performance.

There are rare studies in the open literature to model both binder and PTFE in a digitally reconstructed GDL substrate [73,102]. Nevertheless, almost all of them reconstructed the PTFE with the same methodology as the binder as a wetting fluid residing in small pores and crevices of fiber intersections. For instance, in the model proposed by Daino *et al.* [73], PTFE was digitally added to the GDL substrate after application of the binder through an additional morphological closing with a spherical SE of a larger radius than was used for the binder addition. The volume fraction of PTFE added to the digital GDL substrate was controlled by the difference in SE radii between the binder and PTFE additions.

- **MPL Stochastic Microstructural Modeling:** The MPL is commonly composed of nano carbon black particles held together by PTFE yielding the porosity between 0.35 to 0.65 [94,109]. There has been limited studies on the conventional MPL stochastic microstructural modeling as an alternative approach to tomographic reconstruction [107–109]. Moreover, the difference in length scales between the MPL and the GDL substrate make it challenging to model a representative volume consisting of both materials, concurrently. The first major step forward to develop such models was conducted by Zamel *et al.* [108] and Becker *et al.* [109]. They developed stochastic modeling methods to reconstruct the MPL as carbon particle agglomerates without considering the PTFE phase where hydrophobicity is a key requirement to prevent flooding of the channels and manage the water content of the MEA. The 3D virtual MPL structure is used to obtain MPL bulk properties in the framework of a multi-pore-scale approach to compute the GDL (MPL-coated GDL) transport properties.

Becker *et al.* [109] used a multi-pore-scale approach to determine the diffusivity of the GDL by reconstructing the GDL substrate and MPL microstructures. They used an algorithm to reconstruct the MPL based on adding connected agglomerates of n slightly overlapping spheres until the desired porosity is achieved. They developed a mathematical formulation to take into account the Knudsen diffusion in the small pores of the MPL. Zamel *et al.* [108] reconstructed the MPL with the similar approach as [109] to investigate the effect of MPL porosity, thickness, and penetration into the GDL substrate on GDL diffusion coefficient and thermal conductivity using multi-pore-scale approach. The MPL structure is reconstructed as a network of large pores and agglomerates of particles glued together [108]. This follows the algorithm of generating the large pores represented by large overlapping spheres and then adding the carbon particles outside of the pore space. Finally, the small particles are glued together by filling the small pores between them which is the superiority of this algorithm relative to the MPL reconstruction presented by Becker *et al.* [109]. Whereas, Hannach *et al.* [107] developed a 3D stochastic MPL model to capture the real morphology of the MPL by distinguishing carbon nanoparticles and PTFE which is superior relative to the two others due to considering the PTFE particles. In their proposed stochastic algorithm, three structural parameters were used to control the internal composition of the MPL which are the fraction of seed particle, the degree of overlap between connected particles, and the connectivity of particles. As a conclusion, there is a scarcity of literature available for establishing the best practices for creating realistic MPLs and GDLs with different pore morphology compositions and evaluating their accuracy.

1.3. Research Objectives

This thesis aims to develop a comprehensive design tool for 3D GDL stochastic microstructural model development and transport properties simulation which is a reliable and flexible virtual design tool for GDL material design and prototyping assignments and can potentially reduce time and cost of the fuel cell design cycle. The following steps are taken to achieve this aim.

- The GDL substrate/MPL/MPL-coated GDL morphology and pore structure for variety of structures are qualitatively and quantitatively characterized.

- A novel stochastic microstructural modeling framework is developed to reconstruct the heterogeneous microstructure of GDL substrate/MPL/MPL-coated GDL components.

- A detailed qualitative and quantitative validation for the structural characteristics of the reconstructed microstructures is conducted to satisfy the measured SEM images, porosity, thickness, PSD, and particle size distribution. The obtained 3D digitized realizations of the stochastic models are then used as a computational domain for numerical modeling of transport properties.

- The algorithms and partial differential equation solvers in both macroscopic and microscopic levels derived by governing conservation equations describing concentration, flow, and conduction are employed to simulate the effective transport properties of effective diffusivity, tortuosity, permeability, and thermal and electrical conductivities.

The intent of the following studies is to validate the reliability of the proposed design tool algorithm in order to have a well-established algorithm for design and prototyping assignments of hypothetical materials for next-generation fuel cells:

- The GDL substrate stochastic modeling framework is employed to reconstruct a commercially available GDL substrate over a range of PTFE loadings and their anisotropic transport properties are simulated in both dry and partially saturated conditions in order to determine the structure-property relationships for PTFE treated GDL substrates in different liquid water saturation levels.

- The stochastic MPL and MPL-coated GDL modeling framework is employed to reconstruct variety of existing MPL materials with different particle type and size to investigate the effect of MPL pore morphology composition on the MPL and MPL-coated GDL transport properties.

The validated stochastic design tool can be used as a fast and cost-effective framework for reconstructing GDL porous materials and understanding the correlation between the GDL morphology and transport properties.

1.4. Thesis Structure and Contributions

The structure of the dissertation is as follows:

Chapter 2 proposes a unique stochastic GDL substrate microstructural modeling framework which is developed and thoroughly validated for variety of carbon-paper GDL substrates. Subsequently, various numerical algorithms are employed to simulate the effective transport properties. A complete set of anisotropic transport properties for both gas and liquid phases is determined over a range of PTFE loadings under both dry and partially saturated conditions. The publications of research in Chapter 2 are listed as below:

1. **Z. Tayarani-Yoosefabadi**, D. Harvey, J. Bellerive, E. Kjeang, "*Stochastic microstructural modeling of fuel cell gas diffusion layers and numerical determination of transport properties in different liquid water saturation levels*", Journal of Power Sources 303 (2016) 208-221

2. **Z. Tayarani-Yoosefabadi**, D. Harvey, E. Kjeang, "*Numerical Determination of Transport Properties of Gas Diffusion Layers in Wet Conditions*", Pacific Rim Meeting on Electrochemical and Solid-State Science (PRiME 2012) & 222nd Meeting of the Electrochemical Society, Oct. 2012, Honolulu, HI

3. **Z. Tayarani-Yoosefabadi**, D. Harvey, E. Kjeang, "*Numerical Determination of Transport Properties of PEFC Gas Diffusion Layers*", 10th Fuel Cell Science, Engineering and Technology (ASME) Conference, Jul. 2012, San Diego, CA

In Chapter 3, a novel stochastic MPL microstructural modeling tool is proposed to generate a three-dimensional reconstruction of MPLs in different pore morphology structures. A parametric study is conducted to investigate the effect of MPL structure on its transport properties, *i.e.*, diffusion coefficient, permeability, and electrical and thermal conductivities.

The focus of Chapter 4 is to numerically model the GDL transport properties by using pore-scale models for the reconstructed GDL microstructure that is composed of MPL models established in Chapter 3 coated on GDL substrate model developed in Chapter 2. The effects of MPL compositions on the GDL transport properties are thoroughly elaborated. The publications of research in Chapter 3 and Chapter 4 are listed as below:

1. **Z. Tayarani-Yoosefabadi, J. Bellerive, E. Kjeang,** "*Microstructural modeling of microporous layers and bi-layer gas diffusion media for polymer electrolyte fuel cells; the effect of MPL structural parameters on MPL and MPL-coated GDL transport properties*", Manuscript will be submitted soon.
2. **Z. Tayarani-Yoosefabadi**, M. El Hannach, M. Andisheh-Tadbir, E. Kjeang, "*Effect of fuel cell manufacturing process on MPL structure and properties*", Confidential Technical Report for an NSERC Engage Project in collaboration with Mercedes-Benz Canada, Fuel Cell Division, Mar. 2014.
3. **Z. Tayarani-Yoosefabadi**, M. El Hannach, M. Andisheh-Tadbir, E. Kjeang, *Characterization of Microporous Layer Structure and Properties*, 226th Meeting of the Electrochemical Society, Oct. 2014, Cancun, Mexico; ECS Meeting Abstract 21 (2014) 1232.
4. M. Andisheh-Tadbir, **Z. Tayarani-Yoosefabadi**, M. El Hannach, E. Kjeang, "*Impact of MPL properties on fuel cell performance*", 226th Meeting of the Electrochemical Society, Oct. 2014, Cancun, Mexico; ECS Meeting Abstract 21 (2014) 1231.
5. **Z. Tayarani-Yoosefabadi**, D. Harvey, E. Kjeang, "*Simulation of effective transport properties of GDLs coated with MPLs in dry and wet conditions*", Hydrogen & Fuel Cells 2013 Conference, Jun. 2013, Vancouver, BC.

Chapter 5 summarizes the contributions and accomplishments of this research. Based on theoretical studies and simulation and experimental results, a conclusion addressing the motivations of this research is presented. Finally, suggestions about potential research opportunities are provided to enlighten the path for future work.

Chapter 2.

Macroporous Gas Diffusion Layer Substrate Characterization and Stochastic Microstructural Modeling

In this chapter, a fast and cost-effective GDL substrate stochastic microstructural modeling framework is developed inspired by the manufacturing and pore structure characterization. The developed framework is a collection of stochastic processes including digital reconstruction of non-overlapping graphitized carbon fibers, carbonaceous binder, and PTFE. After through validation, the digital realization of the GDL substrate microstructure is used as a computational domain for material transport properties determination. The effects of PTFE loading and liquid water saturation on the GDL transport properties are found to be highly coupled and are therefore analyzed jointly in this work. Thereby, a complete set of anisotropic transport properties for both gas and liquid phases is determined over a range of PTFE loadings under both dry and partially saturated conditions. The framework algorithm has been conducted to stochastically reconstruct variety of Ballard Power Systems (BPS) material products and simulate their transport properties. However, due to confidentiality of the BPS materials, the commercially available Toray TGP-H GDL substrate is considered as a case study in this thesis.

This chapter is structured as follows: In section 2.1, GDL substrate manufacturing process steps as well as SEM as a qualitative and MIP as a quantitative characterization techniques are introduced at length and interpretation of the measured data is elaborated in the Model Validation section. In section 2.2.1, a novel GDL substrate stochastic microstructural modeling framework is extensively elaborated with the algorithm diagrammatically illustrated in subsection 2.2.1iv. The qualitative and quantitative microstructural validation is conducted with literature and measured data for Toray TGP-H carbon paper as a case study in section 2.2.2. Section 2.2.3 describes the algorithms and partial differential conservation equations in both macroscopic and microscopic level to numerically model the effective GDL substrate transport properties of effective diffusivity, permeability, and thermal and electrical conductivity as a measure of their respective

phenomenon. Upon microstructural validation, the transport properties in the solid and pore phases of the untreated GDL substrate are simulated and compared to measured experimental data to extend the validation in section 2.3. Subsequently, the transport properties of the wetting and non-wetting phases are simulated under a range of PTFE loadings and liquid water saturation levels and the results are thoroughly analyzed and new correlations for the liquid water-saturation-dependent transport properties are proposed.

2.1. GDL Substrate Morphology and Pore Structure Characterization

Carbon-fiber-based GDL substrates usually made of non-woven carbon fiber papers or woven carbon cloths are the most promising candidates for use as diffusion media due to their high porosity and good electrical conductivity. A carbon-paper-based GDL substrate identified as a carbon-carbon composite is made of graphitized carbon fibres with 6–9 μm fiber diameter which are chemically and mechanically bound into a web-like matrix by a carbonized polymeric-based binder. They usually contain graphitized carbon fibers, carbonaceous binder, and hydrophobic agent. The GDL substrate sheets are typically 180–400 μm thick and possess a highly porous morphology with porosities of 70-90% such that a majority of pores are macro-scale pores in the range of 1–100 μm [3,11,110].

This unique architecture is formed in a manufacturing process as graphically illustrated in Figure 2.1[7] with Polyacrylonitrile (PAN)-precursed-carbon fiber as the most common choice for the production of carbon-paper-based GDL substrates, for which the starting fiber is a co-polymer comprising more than 90% PAN. The carbon-fiber paper manufacturing steps include: a) fiber stabilization to transform the fiber from thermoplastic to thermoset material by heating in air at ~230°C; b) carbonization by heating to 1200-1350°C in nitrogen, yielding enhanced fiber properties; c) chopping the tows into 3-12 mm fiber lengths in preparation for papermaking; and d) papermaking using a wet-laid process, which results in a highly porous mat of non-overlapping fibers with very high aspect ratio

[7] Reprinted from [11] with minor modifications with permission from Elsevier.

(length/diameter) and predominantly planar orientation. During this process, the chopped carbon fibers are dispersed in an aqueous binder, typically polyvinyl alcohol or styrene binder, followed by the drying procedures. The papermaking binder content is typically 5–15% of the total weight [13,110,116].

In continuation of the manufacturing process, the carbon fibers are chemically and mechanically bound together to provide an approximately 180-400 µm thick sheet with sufficient mechanical integrity. To this end, the process includes e) continuous impregnation of the rolls of carbon-fiber paper with a thermoset resin-based binder in order to mold the paper to a desired thickness and density. The resin-based binder suspension includes but is not limited to polymeric binder (typically thermoset resin due to their carbon yield and low cost), pore former, and graphite particles in a methanol-based (typically methylcellulose) solvent.; and f) heating to ~150°C in air for solvent evaporation and resin oligomerization. The resin-based binder is mainly accumulated at fiber intersections due to its relatively low static contact angle on the fibers during solvent evaporation. Typically, the resin-based binder constitutes around 45% of the solid phase volume. g) consecutive

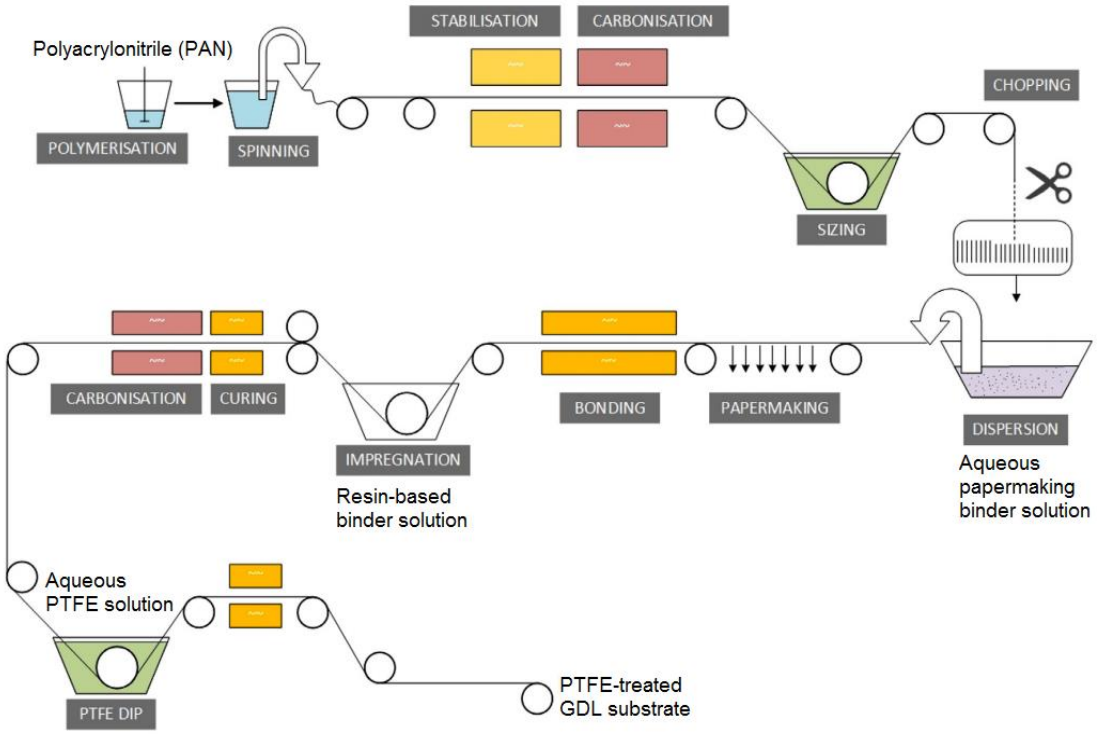

Figure 2.1. Graphical illustration of the manufacturing process for roll-to-roll production of PEFC gas diffusion layer substrate materials using PAN-based carbon fibers [11,110,116].

carbonization and graphitization of stacked carbon fiber sheets in horizontal or vertical batch furnaces. On completion of these stages, the resulting microstructure contains carbon fibers with high anisotropy alignment in horizontal direction in which carbon fibers acquire graphite-like properties while the resin-based binder remains as amorphous carbon [11,13,110,116].

In the final manufacturing step, the GDL substrate is generally treated with a hydrophobic agent to increase the hydrophobicity for better liquid water transport within the GDL to make the pathways available for gas-phase reactant transport. The hydrophobic agents are including but not limited to polyvinylidene fluoride (PVDF), fluorinated ethylene propylene (FEP), perfluoroalkoxy (PFA), and polytetrafluoroethylene (PTFE) as the most commercially available hydrophobic agent. The PTFE treatment also serves to stabilize this property, since the surface chemistry and hydrophobicity of untreated carbon-fiber paper may change during fuel cell operation [110]. To this end, the GDL substrate is commonly dipped into an aqueous PTFE suspension followed by drying and sintering (heating above 350°C) processes at stepwise elevated temperatures to achieve a homogeneous PTFE particles distribution throughout the surface which is fairly critical for uniform surface hydrophobicity. The drying process in the PTFE treatment step of the dipping technique plays a key role to control the PTFE distribution through the GDL substrate thickness as illustrated in Figure 2.2. The figure proves the effect of drying rate

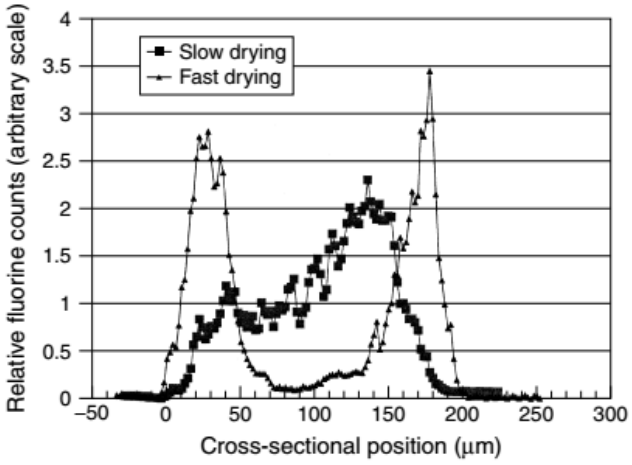

Figure 2.2. Cross-sectional fluorine maps produced by Energy Dispersive Spectroscopy technique across Toray TGP-H GDL substrate. The PTFE distribution through the paper depends heavily on drying conditions [110].

on the PTFE distribution as illustrated in cross-sectional fluorine distribution maps produced by Energy Dispersive Spectroscopy (EDS) technique which will be introduced later in this section [110]. For instance, rapid drying in a convective oven tends to result in PTFE concentration on the GDL substrate's top and bottom exposed surfaces. On the contrary, slow diffusive drying results in PTFE distributed more evenly through the thickness. Note that, submersion under vacuum conditions is necessary to ensure full penetration of the PTFE dispersion into the substrate, which is generally not the case for industrial teflonation processes. Indeed, industrial PTFE dispersion results in non-uniform distribution throughout the thickness with higher concentration at the GDL substrate's top and bottom surfaces [90]. PTFE can also be deposited by other well-suited coating techniques namely spraying and brushing, specifically, when attempting to coat one side of the diffusion media.

In summary, a thorough understanding of the manufacturing techniques provides useful insight into how the GDL substrate constituents are arranged [13,110]. Note that, the engineering parameters of the manufacturing process directly or indirectly influence the resulting morphological, microstructural, and physical GDL substrate characteristics, and hence overall cell performance, durability, and stability.

Most of the GDL substrate characteristics are determined based on the constituent materials and their associated specifications. However, morphological, microstructural, and physical GDL substrate characteristics such as porosity, pore size distribution, thickness, compressibility, and effective diffusion pathway length are generally analyzed via concise qualitative and quantitative characterization techniques and apparatuses as summarized in section 1.2.1. As a qualitative characterization technique, scanning electron microscopy (SEM) is utilized in this work to characterize the surface topography and composition of fabricated GDL substrate samples. SEM is a type of electron microscope that produces images of a sample by scanning the surface with a high-energy focused beam of electrons in a raster scan pattern. The electrons interact with the sample atoms producing signals; low energy more surface sensitive secondary electrons (SE) and high energy backscattered electrons (BSE); that contains information about the samples' surface topography [117]. SEM instruments are typically equipped with an EDS system to allow

for the chemical analysis of materials being observed by SEM. X-ray signals produced in EDS are used to identify chemical composition as well as quantify elements distribution at detectable concentrations by providing compositional maps. Simultaneous SEM/EDS

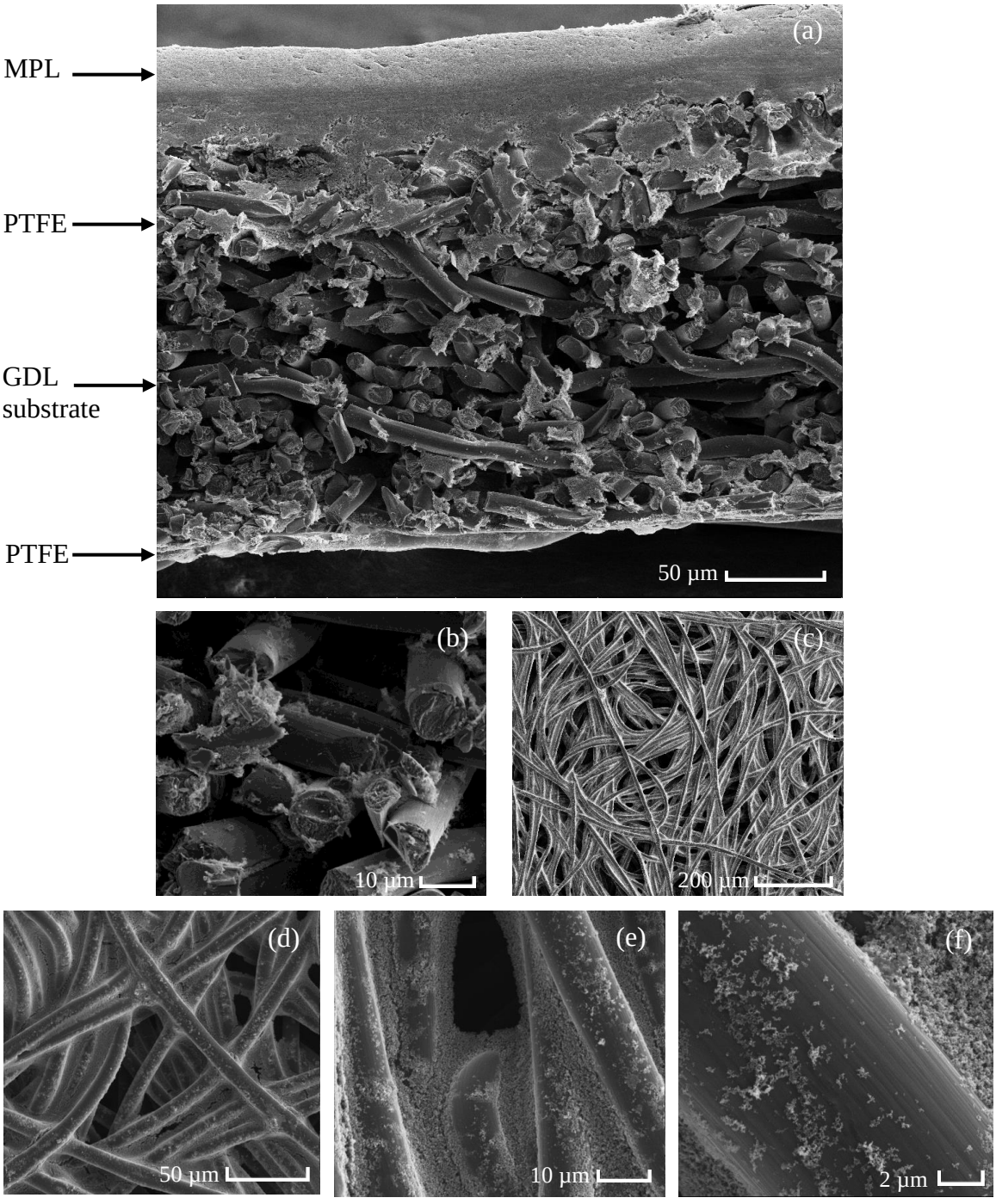

Figure 2.3. Measured SEM images of a GDL substrate coated with MPL; cross-sectional view in (a) 900x and (b) 5kx and bottom view in (c) 350x, (d) 1.5kx, (e) 5kx, and (f) 25kx magnifications.

analysis is advantageous in providing semi-quantitative analysis of materials [117,118]. The measured surface and cross-sectional SEM images of a GDL (MPL-coated on GDL substrate) are shown in Figure 2.3. It is evident from the figure that the GDL substrate contains open pores in the range of tens of micrometers formed by the interconnected network of non-overlapping randomly distributed carbon fibers. Indeed, the carbon fibers are positioned arbitrarily in the IP direction yielding anisotropic microstructural characteristics. Furthermore, PTFE treatment is observed in the images as white homogeneous interconnected network of PTFE particles distributed throughout the surface with higher concentration at the GDL substrate's top and bottom surfaces as illustrated in Figure 2.3. The carbonaceous binder is also present throughout the fibrous structure, in particular at fiber contact points.

As a quantitative and more precise characterization, the porosity, pore shape, size, connectivity, distribution, density, and other porosity-related characteristics of the GDL substrate is characterized via porosimetry techniques, specifically, mercury intrusion porosimetry (MIP; Micromeritics®) which has been conducted in this work. MIP as a destructive but simple-to-perform method is capable to characterize porous materials containing pores in the range of 3nm-150µm [119,120]. It is the non-wetting property of the mercury combined with its high surface tension (γ = 486.5 mN m^{-1}), that uniquely qualifies it for use in porosimetry for probing both the hydrophobic and hydrophilic pore spaces [120]. MIP is the progressive intrusion of mercury into a porous material under stringently controlled applied pressures. Indeed, mercury does not wet most materials and will not spontaneously penetrate pores by capillary action, *cf.* Figure 2.4. Thereby, during MIP, the sample is immersed in mercury which must be forced to intrude the internal pores under applied external pressures. By measuring the intruded mercury volume into the sample material by a mercury penetrometer with each pressure change, the PSD, *i.e.*, volume of pores in the corresponding pore size class, is determined. Albeit, the required equilibrated pressure is inversely proportional to the pore size governed by the Washburn equation, Eq. (2-1), which describes the equilibrium between the intrusion pressure P_{int} and the resisting force:

$$d_{pore} = -4\gamma_m \cos\theta_{c,m} / P_{int} \qquad (2\text{-}1)$$

where γ_m is the mercury surface tension, d_{pore} is the pore diameter, and $\theta_{c,m}$ is the mercury contact angle which is considered as 145°. In other words, only slight pressure is required to intrude the mercury into large macropores, whereas, much greater pressures are required to force the mercury into comparatively smaller pores [119–122]. Figure 2.5 schematically illustrates the mercury filling of a penetrometer with the immersed sample and cross-sectional view of the penetrometer.

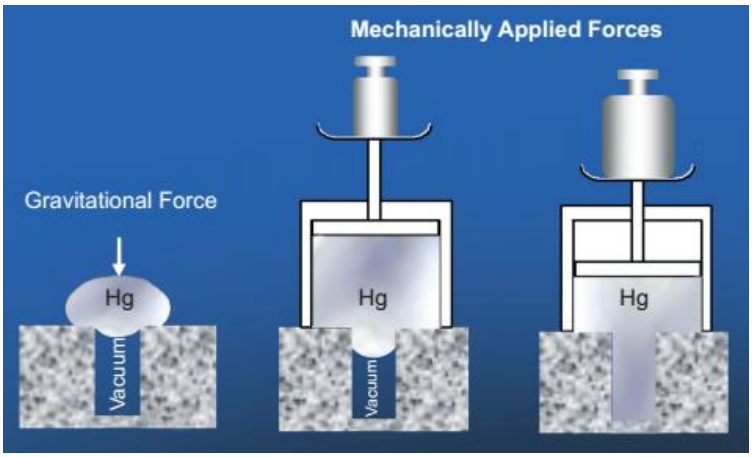

Figure 2.4. Schematic illustration of non-wetting property of mercury in which an external force is a must to intrude the mercury into the open pores [122].

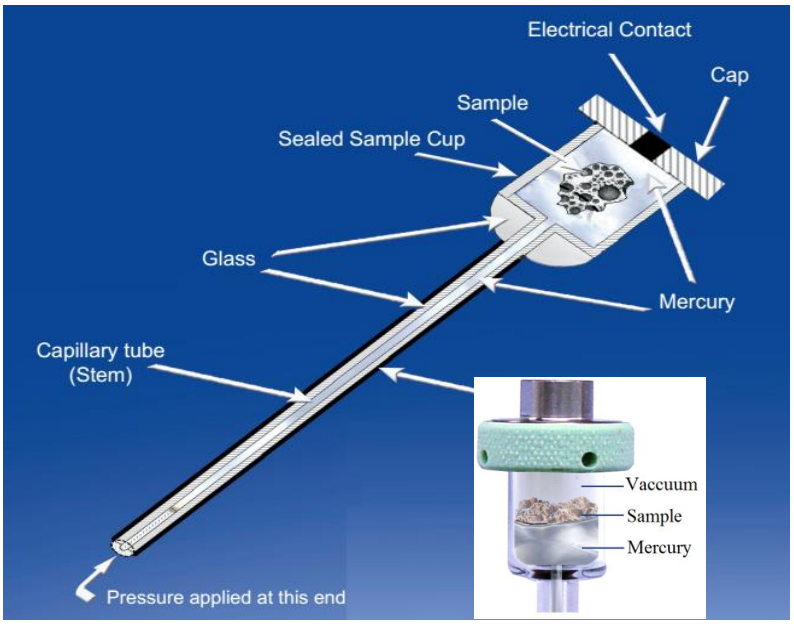

Figure 2.5. Illustration of mercury filling the penetrometer volume with the sample present and cross-sectional view of a mercury penetrometer [122].

The measured PSD can be depicted by differential volume fraction (DVF) ($\mathrm{d}\Omega/\mathrm{d}d$) as a bell-shaped curve and its integration to derive cumulative volume fraction (CVF) ($C_\Omega(d)$) as a sigmoidal curve, both of which are weighted by the pore volume. The reliability and accuracy of the MIP method for carbon-paper GDL substrates is established, as the material has high porosity with high connectivity pores and is relatively rigid, although the method assumes cylindrical pores and does not capture closed pores (which are uncommon in carbon paper) [121,123]. The MIP-measured PSD of a GDL substrate will be expounded in the Model Validation section. The GDL substrate and GDL pore sizes are classified as follows which facilitates the description of different pore characteristics to gain a better understanding of the mass transport capabilities of different porous microstructures [11,124]:

- Micropores: pores with radius smaller than 50 nm.
- Mesopores: pores with radius between 50 nm and 10 μm.
- Macropores: pores with radius larger than 10 μm.

2.2. Numerical Formulation

2.2.1. GDL Substrate Stochastic Microstructural Modeling

In this section, a novel GDL substrate stochastic microstructural modeling framework is extensively elaborated. Inspired from GDL substrate manufacturing and pore morphology and structure characterization described in section 2.1, the developed framework is a collection of stochastic processes including digital reconstruction of graphitized fiber, carbonized binder, and PTFE. Thereupon, after thorough validation of the digital realization of the GDL substrate microstructure, it will be used as a computational domain in the following subsection for material transport properties determination.

The GDL substrate is digitally reconstructed in three steps: i) Reconstruction of Fibrous Skeleton; in which non-overlapping infinitely long cylindrical carbon fibers are digitally deposited in a discrete 3D domain utilizing a stationary Poisson line process (PLP) with one-parametric directional distribution stemmed in-part from Schladitz *et al.* [105];

followed by ii) Reconstruction of Binder; including *papermaking binder* as a thin film binder with 3D morphological closing operation of the fiber skeleton targeting the shape of a concave meniscus and/or *resin-based binder* as agglomerates of disc-shaped graphite particles receded in small pores near the fiber intersections by utilizing Sphere Packing method along with a thin film polymeric binder modeled with 3D morphological closing operation; and ultimately, iii) Reconstruction of PTFE Treatment; as a solid binder with properties similar to the real porous PTFE component concentrated in two thin layers near the top and bottom surfaces of the substrate utilizing an additional morphological closing operation.

Finally, the new underlying modeling framework is implemented for the Toray TGP-H GDL substrate as a case study to digitally reconstruct the microstructure in the Case Study subsection. The modeling framework developed and validated in this work is expected to become a reliable and versatile tool for hypothetical GDL substrate materials design and prototyping assignments for next-generation fuel cells for which the algorithm flowchart is briefly described in the GDL Substrate Design Tool Algorithm subsection.

i. Reconstruction of Fibrous Skeleton

A closer investigation of GDL substrate structure as well as manufacturing process leads to the impression to develop a manageable stochastic fibrous skeleton model with as few parameters as possible with the following reasonable assumptions:

1. The fibers are straight with negligible curvature, cylindrical with the same diameter, infinitely long compared to the modeling domain size, and not allowed to overlap.

2. The fiber system is macroscopically homogeneous in which the microstructural characteristics are independent of the location from where the representative volume element (RVE) is extracted.

3. The fiber system is isotropic in the material plane (*xy*-plane) which implies that the distribution properties of the stochastic model are invariant with respect to translations as well as rotations about the pressing direction (*z*-axis).

These assumptions justify the stochastic fiber generation utilizing a spatial stationary random system of intersecting lines, known as stationary Poisson line process (PLP). It is a Poisson point process on the space of one-directional affine subspaces of $\mathbb{R}^3$ described by the expected total length per unit volume and the distribution of the directions of lines. To this end, a basic knowledge of the PLP in $\mathbb{R}^2$ as the modeling element of the fiber generation is useful in understating of the developed model which will be provided in the following.

Poisson Line Process in $\mathbb{R}^2$***:*** A PLP is a process of generating a random collection of intersecting lines $L_1, L_2, \dots, L_n$ scattered in $\mathbb{R}^2$. Any line L_i, $i = 1,2, \dots, n$ in this plane can be uniquely characterized by its perpendicular distance ρ_i from origin o and angle φ_i to the positive x-axis in counter clockwise direction, as shown in Figure 2.6 (a). The pair of random values (ρ_i, φ_i) are understood as realizations of certain pair of random variables (P, Φ). The values of the random distances P can be arbitrary real positive numbers, whereas the random angles Φ take values between 0 and 2π. Indeed, any line in $\mathbb{R}^2$ is represented by the coordinate of a point on a representation surface $C \equiv [0, 2\pi) \times [0, \infty)$, as illustrated in Figure 2.6 (b). Therefore, there is a one-to-one correspondence between lines in $\mathbb{R}^2$ and points on the surface C. A random collection of intersecting lines in $\mathbb{R}^2$, which is called Poisson line tessellation (PLT), can be constructed from a set of random independent points on C generated by Poisson point process. As the GDL substrate is

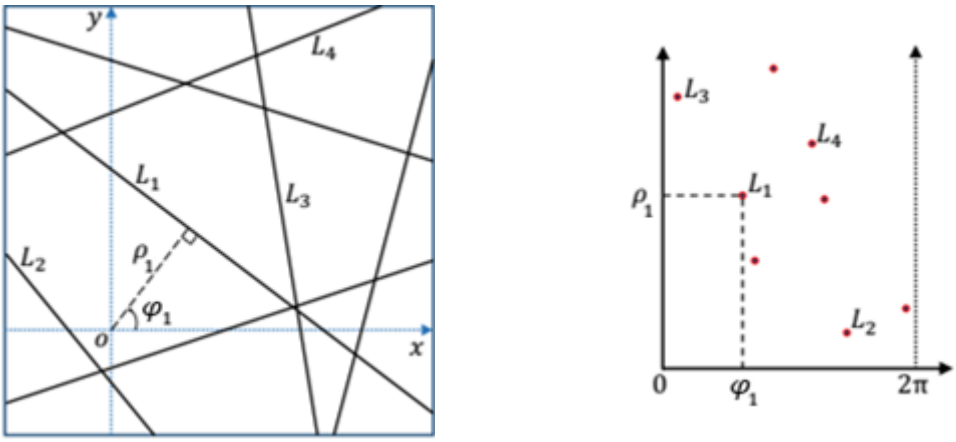

(a) (b)

Figure 2.6. Illustration of (a) Poisson line process in $\mathbb{R}^2$ and (b) Poisson point process on representation surface.

isotropic in the *xy*-plane, the PLP is stationary, *i.e.*, the distribution of lines is invariant with respect to translations and rotations around the origin. To do so, a PLT can be generated as an independently marked Poisson point process with a sequence of $(\rho_1, \varphi_1), (\rho_2, \varphi_2), \ldots, (\rho_n, \varphi_n)$ in which the random polar distances $\rho_1, \rho_2, \ldots, \rho_n$ should form a homogeneous Poisson point process on the positive real line with intensity parameter $\Lambda > 0$, where Λ is the expected number of points per unit length. While the random polar angles $\varphi_1, \varphi_2, \ldots, \varphi_n$ are independently and uniformly distributed random values in the interval $[0, 2\pi)$. The PLP is perfectly controlled by Λ which can also be interpreted as the mean total edge length per unit area of the PLT in the sense that there are on average more lines for larger values of Λ [125–127].

In the developed method, the non-overlapping infinitely long (fiber length >> domain size) cylindrical fibers with a given diameter and orientations that follow certain probability distributions are randomly deposited in a discrete 3D domain of size ${L_D}^3$ until the desired porosity is reached, as schematically illustrated in Figure 2.7. The digital reconstruction algorithm for the formation of fibrous skeleton is based in-part on the stochastic modeling procedure of Schladitz *et al.* [105], using the above-described Poisson line process in $\mathbb{R}^3$. Indeed, the projection of the fibers' principal axis are randomly distributed in the *xy*-plane while their directional distribution in *z*-axis obeys a one-parametric probability density function where the parameter enforces the anisotropy of

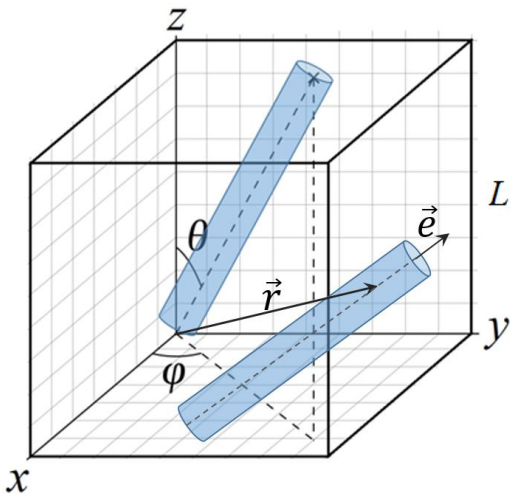

Figure 2.7. Placing fibers into a discrete 3D representative volume element domain of size L^3.

carbon fibers. The proposed fibrous skeleton generation algorithm steps are as follows:

Step 1: Generate N_l number of random lines corresponding to the principal axes of cylindrical fibers according to their probability distribution functions.

Step 2: Discretize the domain in ${N_v}^3$ cubic voxels to determine voxels' phase and dilation of the lines with a sphere with radius r to model the profile of the fibers.

Step 3: Determine the porosity and if necessary, adjust r or/and N_l to satisfy the required fiber skeleton porosity ε_F.

The three fibrous skeleton generation algorithm steps are thoroughly elaborated as follows:

Step 1: In the proposed algorithm, each cylindrical fiber is characterized by a random point along its principal axis with position vector $\vec{r} = (x, y, z)$ and a unit vector $\vec{e} = (e_x, e_y, e_z)$ parallel to the fiber's principal axis as depicted in Figure 2.7. The unit vector can be expressed by a set of angles (θ, φ) in a spherical coordinate system as:

$$\begin{aligned} e_x &= \sin\theta \cos\varphi \\ e_y &= \sin\theta \sin\varphi \\ e_z &= \cos\theta \end{aligned} \tag{2-2}$$

where $\varphi \in [0, 2\pi)$ and $\theta \in [0, \pi)$ are the longitude and latitude angles, respectively.

By imposing the directional distribution conditions of the cylindrical fibers, the fibers' orientations and positions follow certain probability density functions as per below:

1. The probability density function of each vector component for position vector $\vec{r} = (x, y, z)$, which is a random point on the principal axis of each cylindrical fiber, is given by:

$$p(x) = p(y) = p(z) = \frac{1}{L_D} \tag{2-3}$$

2. The GDL substrate is isotropic in the *xy*-plane, hence, the direction of the fibers' principal axis is uniformly distributed in this plane. Since longitude angle φ is chosen uniformly in the range of $[0,2\pi)$, the probability distribution is given by:

$$p_{xy}(\varphi) = \frac{1}{2\pi} \tag{2-4}$$

3. The fibers' directional distribution in the *z*-axis (latitude angle θ) obeys the following probability density function stemmed from Schladitz *et al.* [105]:

$$p_z(\theta) = \frac{\beta sin\theta}{2[1 + (\beta^2 - 1)\cos^2\theta]^{3/2}} \tag{2-5}$$

Hence, the total probability distribution which is only a function of latitude angle is defined as follows:

$$p(\theta,\varphi) = p_z(\theta)p_{xy}(\varphi) = p(\theta) = \frac{\beta sin\theta}{4\pi[1 + (\beta^2 - 1)\cos^2\theta]^{3/2}} \tag{2-6}$$

where the anisotropy parameter β controls the anisotropy of the structure, latitude angle $\theta \in [0,\pi)$ represents the TP elevation of the fibers, and longitude angle $\varphi \in [0,2\pi)$ corresponds to their IP orientation [105]. If β = 1, the material is isotropic in 3D space and by increasing its value, the fibers tend to be more parallel to the *xy*-plane as depicted in Figure 2.8.

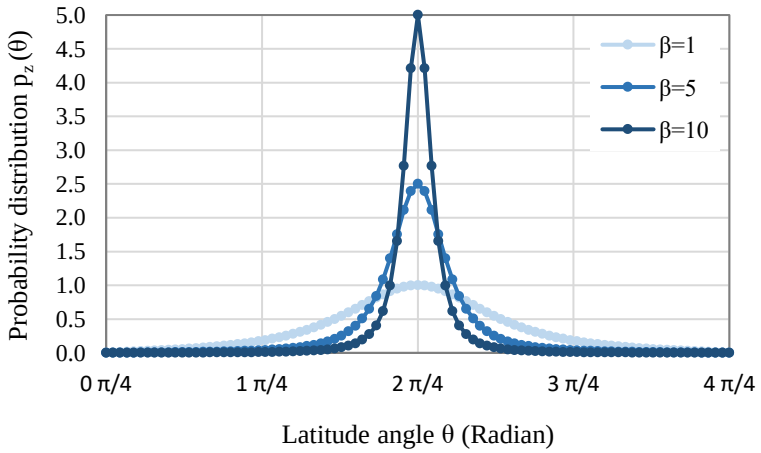

Figure 2.8. Theoretical probability distribution p(θ) of carbon fibers for different values of the anisotropy parameter β = 1, 5, 10.

For the stochastic fiber generation using the Poisson process, generation of random variables X that follow the aforementioned probability density functions for x, y, z, φ, and θ can be achieved using the inverse transform theorem [128]. Generally, this method is for generating random variables following any probability distribution $p(X)$ by computing its cumulative probability distribution function $Y = P(X)$ as follows:

$$Y = P(X) = \int_{a}^{X<b} p(X')dX' \tag{2-7}$$

which maps a random variable $X \in (a, b)$ to a probability $Y \in (0,1)$. This method produces a sequence of uniform random values Y between 0 and 1 using a pseudo-random number routine which are used as inputs for the inverse cumulative density function $X = P^{-1}(Y)$ to produce the required random X values as shown in Figure 2.9. In conclusion, the X values obtained with the above method follow the probability density function, $p(X)$.

Applying the inverse transform theorem for the generation of random values for x, y, z, φ, and θ following their probability density functions are as follows:

1. Computing the cumulative probability distribution for the components of position vector $\vec{r}$ as $\big(P(x), P(y), P(z)\big) = \left(\frac{x}{L_D}, \frac{y}{L_D}, \frac{z}{L_D}\right)$ and subsequently their inverse functions, the random numbers of the vector components can be obtained by:

$$(x, y, z) = \big(L_D Y_x, L_D Y_y, L_D Y_z\big) \tag{2-8}$$

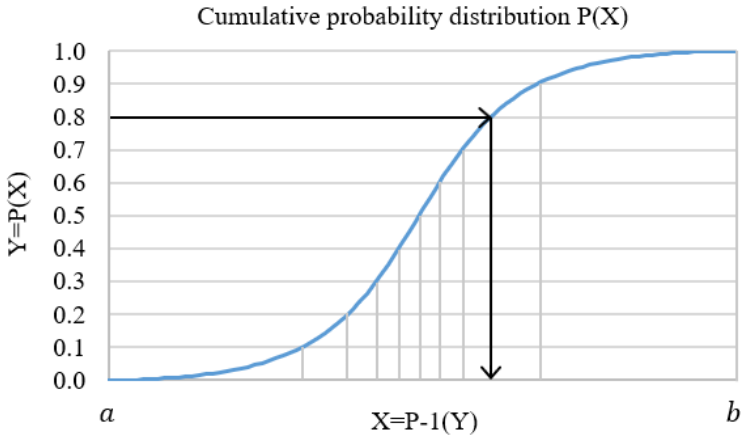

Figure 2.9. Inverse transform theorem for the generation of random values X from cumulative probability distribution P(X).

2. Similarly, the cumulative probability distribution of the longitude angle φ is computed as $P_{xy}(\varphi) = \frac{1}{2\pi}\varphi$ and subsequently using the inverse function, the random value of the longitude angle can be obtained by:

$$\varphi = 2\pi Y_{\varphi} \tag{2-9}$$

3. Furthermore, the random values of the latitude angle are obtained by first deriving the cumulative probability distribution as follows:

$$P_z(\theta) = \int_0^{\theta} \frac{\beta \sin\theta'}{2[1-(\beta^2-1)\cos^2\theta']^{3/2}} d\theta' = \frac{1}{2} - \frac{\beta\cos\theta}{2\sqrt{(\beta^2-1)\cos^2\theta+1}} \tag{2-10}$$

and second, calculating the inverse function $P_z^{-1}(Y_\theta)$ as:

$$\theta = P_z^{-1}(Y_\theta) = \pm\cos^{-1}\left[\frac{1}{\sqrt{(\beta/(1-2Y_\theta))^2-\beta^2+1}}\right] \tag{2-11}$$

where $Y_x, Y_y, Y_z, Y_\varphi, Y_\theta \in (0,1)$ are the random values that follow a uniform distribution obtained by a pseudo-random number routine. Following the above algorithm, a sequence of straight lines corresponding to the principal axes of the cylindrical fibers can be generated characterized by the position vector $\vec{r}$ and a parallel unit vector $\vec{e}$.

***Step 2*:** The above-described PLP generates random intersecting lines. Hence, dilation of the lines with a sphere as a structuring element is required to model the profile of the fibers as extensively elaborated in [71,126]. To this end, the continuous domain ${L_D}^3$ is discretized into ${N_v}^3$ cubic voxels with the dimensions $\delta x = \delta y = \delta z = \frac{L_D}{N_v}$. The center

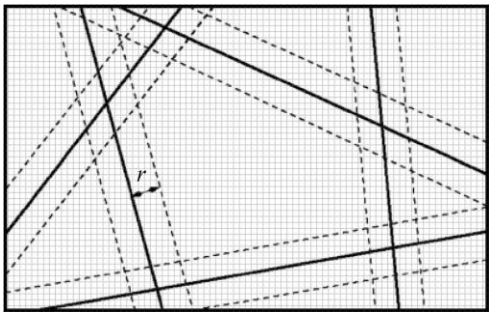

Figure 2.10. A 2D view of a PLT dilation in a discritized domain in which |d| should satisfy the condition |d| ≤ r.

coordinate of each voxel is given by $\vec{r}_{ijk} = \left((i-1/2)\delta x, (j-1/2)\delta y, (k-1/2)\delta z\right)$ in which $i, j, k = 1,2,\dots,N$. Assuming that we have M such lines with $\vec{r}_m$ and $\vec{e}_m$, where $m = 1,2,\dots,M$, the solid phase can be defined through the voxel position vector $\vec{r}_v = (x_v, y_v, z_v) \in (0, L_D)^3$ whose distance $|d|$ from at least one principal axis of the above series of lines satisfies the condition $|d| \leq r$ as depicted in Figure 2.10, or equivalently:

$$|d| = |(\vec{r}_v - \vec{r}_m) \times \vec{e}_m| \leq r \tag{2-12}$$

otherwise, the voxel is considered as a void phase.

***Step 3*:** In the developed algorithm, we add cylindrical fibers with a fixed diameter in a 3D digital domain until the desired porosity for the fibrous skeleton prior to resin impregnation, ε_F, is reached. To do so, the produced digitized domain can be described by the phase function $f(\vec{r})$, defined as:

$$f(\vec{r}) = \begin{cases} 0, & if\ \vec{r}\ belongs\ to\ the\ void\ phase \\ 1, & if\ \vec{r}\ belongs\ to\ the\ solid\ phase \end{cases} \tag{2-13}$$

where $\vec{r}$ is the position vector of the voxel center from an arbitrary origin. The fiber skeleton porosity, ε_F, can be defined as:

$$\varepsilon_F = 1 - \langle f(\vec{r}) \rangle \tag{2-14}$$

where $\langle \cdot \rangle$ gets the mean value.

ii. Reconstruction of Binder

GDL substrate fibrous porous media are often more complex than a collection of randomly distributed carbon fibers in which binding materials are commonly added as a papermaking binder and/or a resin-based binder in the manufacturing processes. The binder is a non-negligible portion of the solid phase which physically connects the fibers and thus has an influential impact on the solid phase transport properties including thermal and electrical conductivities. By investigating the GDL substrate structure as well as manufacturing processes, the binder material is generally observed to be receded into the smaller pores or tight crevices at fiber intersections with relatively low static contact angle

[69,73,110]. This is due to high wetting fluid property of the binder solution with respect to the carbon fibers as this property is schematically shown in Figure 2.11.

Referring back to the GDL substrate manufacturing in section 2.1, carbon fiber paper is made of chopped carbon fibers held together by a papermaking binder which is usually polyvinyl alcohol or styrene binder. The papermaking binder content is typically 5–15% of the total weight [13,110]. In continuation of the manufacturing process, adding a carbonizable thermoset resin-based binder allows the carbon-fiber paper to be molded to a desired thickness and density. In the final treatments for stabilization; curing, carbonization and graphitization processes; the styrene binder, pore former, and methanol-based solvent are evaporated, and the graphitized resin binder is cross-linked while bonding the fibers and graphite particles. Typically, the resin-based binder constitutes around 35-45% of the solid phase volume [110]. Therefore, the proposed binder model is representative of common manufacturing techniques, *cf.* Figure 2.1, and digitally represents the physical interaction of binder material with carbon fiber skeleton.

Reconstruction of papermaking binder: As previously noted, the papermaking binder material is generally accumulated as a thin film at small crevasses near the fiber intersections due to high wettability of the binder. This property is closely mimicked to digitally generate the binder with 3D morphological closing operation of the fiber skeleton targeting the shape of a concave meniscus[8] as a thin binder film [73,102,103]. The closing

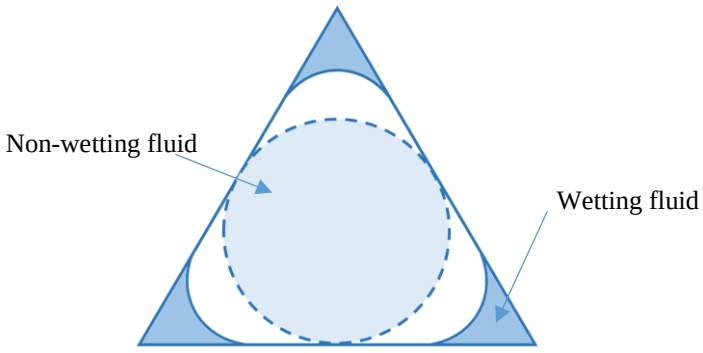

Figure 2.11. Wetting property compared to non-wetting property of fluids at fiber intersections.

[8] The free surface of a liquid-vapor boundary near the walls of the containing vessel (a pore or capillary) and which assumes a curvature due to surface tension.

operation is implemented as a two-step procedure, which is schematically illustrated in Figure 2.12, including dilation followed by erosion of the fiber skeleton utilizing a spherical structuring element (SE). In the first step, a dilation operation is performed on the fiber skeleton by a spherical SE in which the fibers are dilated by a thin binder film. This is represented by Minkowski sum $\oplus$ between the fiber skeleton A and the SE which is mathematically defined as:

$$B = A \oplus SE = \{a + se | a \in A, se \in SE\} \tag{2-15}$$

where B is the dilated carbon fiber skeleton. The result is the thickened fiber bundle which may overlap in areas where the fibers are close together as depicted in Figure 2.12 (b). In the second step, an erosion operation is conducted on the dilated structure by the SE in which the structure is diminished by a given number of voxels as illustrated in Figure 2.12 (c). This is explained by Minkowski difference $\ominus$ of B with the reflected set of SEs which is mathematically defined as $B \ominus SE$. The result is a reduction on B whereby the pores that are smaller than the SE are filled as thin concave meniscus at fiber intersections. Note that the two morphological operators of dilation and erosion are not inverse to each other as follows:

$$(A \oplus B) \ominus B \neq A \tag{2-16}$$

The weight fraction of the papermaking binder added to the fibrous skeleton is proportional to the SE's diameter. Hence, the morphological closing operation is repeated with a different SE diameter if the required binder weight fraction is not met. The diameter of the dilation and erosion SE's determines the concrete shape of the binder meniscus. In

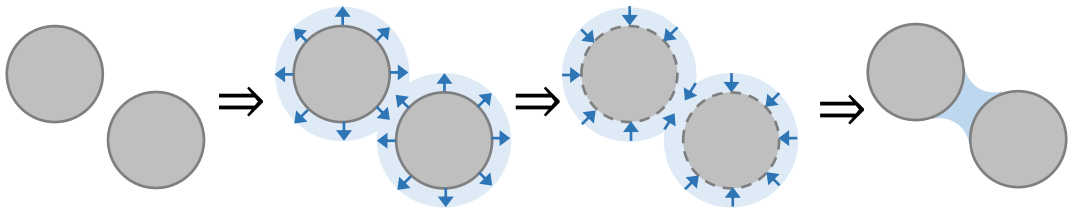

(a) Carbon fiber cross-section | (b) Dilation | (c) Erosion | (d) Carbon fiber cross-section bounded with papermaking binder

Figure 2.12. Schematic illustration of the binder generation between carbon fibers.

the developed model, the dilation and erosion SE diameters are considered the same, which leads to a minimal contact angle between the solid fibrous structure and the binder corresponding to a thin papermaking binder film with high wettability. This step is optional for GDL substrates with styrene binder as the papermaking binder due to its evaporation in the carbonization process.

Reconstruction of resin-based binder: Inspired by the manufacturing process as well as the SEM image characterizations of GDL substrate structure, it is revealed that the resin-based binder material in the impregnation step is generally accumulated in the small pores due to high wettability of its suspension. Indeed, it is in the form of graphite particles receded in the small pores near fiber intersections along with a thin film polymeric binder which bonds the carbon fibers and graphite particles. The resin-based binder suspension may include graphite particles, polymeric (resin) binder, pore former, and other materials in a liquid solvent. The resin-based binder property that forms the composite nature of the GDL substrate is closely mimicked and digitally modeled in two steps until the desired porosity is reached, as follows:

Step 1: The graphite particles are added to the fibrous skeleton as an agglomerate of disc-shaped particles with different sizes accumulating in small pores where the density of fibers is higher.

Step 2: The polymeric binder added as a thin film to the uniformly distributed graphite particles is modeled with 3D morphological closing operation of the fiber skeleton and graphite particles, as per the methodology explained in the Reconstruction of papermaking binder subsection, to assure inter-particle and particle-fiber bonding is achieved.

To model the agglomerates of disc-shaped graphite particles added to the fibrous skeleton in *Step 1*, the following algorithm is applied:

1. First, the void space between the fibers needs to be divided into *pore space*, VP_{SS}, and *binder space*, VP_{BS}. Briefly saying, the pores are randomly generated in the domain by distributing solid spheres, which are allowed to overlap, within a range of diameters until a desired volume percentage of the void space is filled. To this end, first, loosely

packed solid spheres are randomly generated in the void space of the reconstructed fibrous skeleton through a series of steps utilizing a multi-sized random loose sphere packing method [129–131]. The spheres represent the pore former and restrict the spreading of the binder material. The fixed spheres are successively added with the following conditions until a desired volume percentage of the void space VP_{SS} is filled:

- Fixed solid spheres are allowed to overlap with each other but not with the fibers.
- Spheres are within a certain range of diameters greater than graphite particles' diameter and less than the maximum applicable diameter (usually 99 µm).
- Spheres are added starting with largest spheres and continues with smaller ones.

Thereafter, the structure is inverted, such that the solid spheres and fibrous skeleton are transformed into *pore space* and the remaining void space converts to *binder space* to prepare for the resin-based binder generation. Henceforth, the spheres act as fixed pores.

2. Next, the binder space is randomly filled by distributing the graphite disc-shaped particles of different lengths and diameters until the desired binder volume percentage SVP_B is reached. Nevertheless, if the binder space is fully filled with the graphite particles, it does not satisfy the GDL substrate porosity and PSD requirements. As an evidence, measured MIP data of commercially available GDL substrates, e.g., AvCarb EP40 and Toray TGP-H GDL substrates, show that around 20-25% of the pore space is made up of pores smaller than 20 µm mostly near fiber intersections where the density of fibers is higher. For this reason, reconstructing a GDL substrate that satisfies both its high porosity (>75%) and small pore size (<20 µm) conditions can only be achieved by generating the resin-based binder as a porous material consisting of graphite particles with porosity of approximately 60-80%. Hence, the volume percentage of binder space VP_{BS} for generating the porous binder with ε_B should be more than the binder volume percentage SVP_B considering the binder porosity. Fiber skeleton and binder solid volume percentage SVP_F and SVP_B can be obtained using known GDL substrate components' characteristics such as fiber and binder basis weights and densities from materials data sheets as detailed in GDL Substrate Design

Tool Algorithm subsection. Therefore, the stopping criterion of the Sphere Packing in *Step 1* is determined by:

$$VP_{SS} = 1 - (SVP_F + \frac{1}{1-\varepsilon_B} SVP_B) \quad (2\text{-}17)$$

3. Last, the fibrous skeleton and graphite disc-shaped particle distribution are merged into a united GDL substrate structure.

It is worth mentioning that the binder is only modeled as a thin film in the open literature and there has been no study to model the graphite particles which is a non-negligible component of the resin-based binder solution. Hence, this is one of the noticeable prominent features in this work. The image processing operations such as morphological closing of the fibrous skeleton [73,103] or morphological opening of the pore space [69,74,76,101] has been developed in the literature to model the binder as a thin film. The morphological closing of the fibrous skeleton which is extensively explained above is employed in this work to model the papermaking and polymeric binder. On the other hand, in the method proposed by Becker *et al.* [69], the morphological opening of the pore space with spherical SE of increasing diameter, known as Granulometry [132], is used to determine the pore radius threshold of the 3D geometry. The binder is added by filling the pores, starting from the smallest ones and finishing once the desired binder weight percentage is reached. As a note, the first step of the graphite particle modeling algorithm of the resin-based binder can be implemented by the morphological opening method as an alternative approach to Spherical Packing method. There is no available evidence for the superiority of one method over the other but that could be investigated as a suggested future work.

iii. Reconstruction of PTFE Treatment

Despite the fact that carbon fiber GDL substrates are promising candidates for handling mass, heat, and species transport during cell operation, they must still undergo an additional microstructure enhancement process, *i.e.*, hydrophobic treatment via hydrophobic agents such as PTFE. Bearing in mind that a certain humidification level is a must to have an efficient proton transport through the membrane as well as the catalyst

layer considering that the proton transport governing mechanisms function adequately in the presence of sufficient water. However, excess water should also be effectively removed from the cell to make the pathways available for gas-phase reactant transport especially in high current density operating conditions. Hence, PTFE treatment is an ultimate but important procedure of the GDL substrate manufacturing process that renders more uniform hydrophobic characteristics which aid liquid water expelling, *i.e.*, reduce water accumulation to prevent cell flooding, and provide more reactant pathways to facilitate gas transport through the GDL towards the catalyst layer [110].

The rational PTFE modeling methodology is inspired by the GDL substrate cross-sectional BSE SEM imaging and EDS analysis as well as surface BSE SEM imaging and manufacturing processes. Note that, BSE is preferred to SE SEM imaging by highlighting the PTFE distribution as white areas due to higher fluorine atomic density compared to carbon. Cross-sectional SEM imaging, *cf.* Figure 2.3, and EDS analysis, *cf.* Figure 2.2, is advantageous in providing information about the PTFE distribution throughout the GDL substrate thickness. As elaborated in EDS analysis in section 2.1, the manufacturing process plays a key role to control the PTFE distribution with non-uniform distribution with higher concentration at the top and bottom surfaces in rapid drying, as the most common industrial PTFE treatment, versus more even distribution throughout the thickness in slow drying. Moreover, the behavior and intended location of the PTFE particles on the GDL substrate surface can be inspired by the PTFE treatment process. Note that the aqueous PTFE suspension is comprised of PTFE resin particles with ~0.5 µm diameter. During the sintering step, the temperature exceeds the melting point of the PTFE particles that enables coalescence of adjacent PTFE particles and random distribution in conglomerated regions between carbon fibers which is also confirmed by BSE SEM imaging in the literature [90].

Hence, PTFE improves the GDL substrates hydrophobicity as well as the mechanical strength by acting as a porous binder between carbon fibers with submicron-sized pores. Thereafter, the PTFE modeling as a porous binder is not feasible due to limited modeling resolution (1 voxel=0.5 µm) in which submicron-sized (less than 0.5 µm) PTFE and micron-sized (~20-100 µm) GDL substrate pore structures cannot be resolved at the

same time. Therefore, the PTFE is incorporated as a solid binder with properties similar to the real porous component distributed through the substrate thickness by morphological closing operation explained in the Reconstruction of papermaking binder in subsection 2.2.1ii. The process steps of PTFE distribution throughout the substrate thickness for a bimodal TP distribution, as the most common industrial PTFE distribution, concentrated in two thin layers near the top and bottom surfaces of the substrate is illustrated in Figure 2.13. The process starts with (1) cropping the PTFE thickness h_T from top and bottom of the reconstructed substrate structure. Note that PTFE distribution does not have a uniform pattern along the surface, thus, the average is considered as h_T; (2) subtract the cropped structure from the initial GDL substrate structure; (3) add ω_T PTFE to structure 2 as a solid binder by morphological closing to reach the PTFE-treated substrate porosity $\varepsilon_{sub,PTFE}$; and (4) merge structures 1 and 3. Note that all reconstruction process steps are conducted in the TP direction. For the case of slow drying of PTFE treatment process where the PTFE penetrates throughout the domain, ω_T consists of ω_{T1}, PTFE weight percentage at top and bottom surfaces of the substrate, added to structure 2 and ω_{T2}, PTFE weight percentage throughout $(h_{sub} - 2h_T)$, added to structure 1.

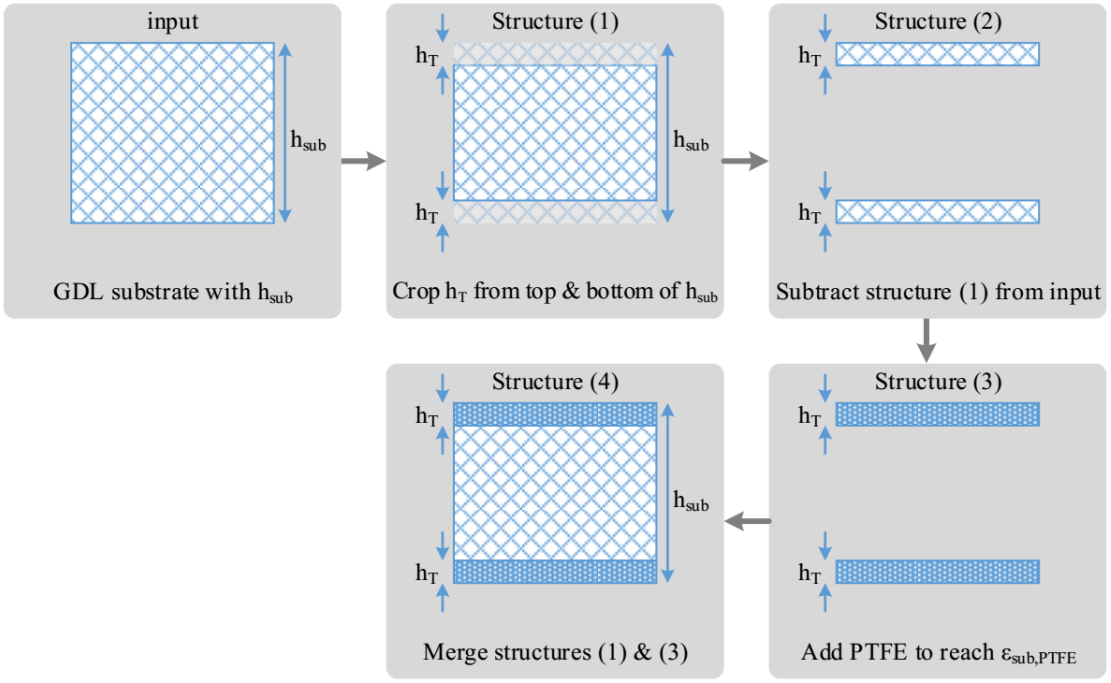

Figure 2.13. Graphical illustration of process steps for bimodal TP PTFE distribution concentration at the top and bottom surfaces of the substrate.

Although hydrophobic treatment in the GDL substrate mainly enhances the water management within the cell, its impact on other characteristics should also be considered for an optimized cell design. Experimental studies have shown that an increase in the electron insulating PTFE loading improves the hydrophobicity but may also deteriorate the electrical and thermal conductivities to a certain extent as well as bulk porosities, pore sizes, and permeability [90,93,111,112]. Indeed, optimizing all these parameters for a specific fuel cell is rather difficult due to their antagonistic relationship with each other. Generally speaking, PEFC diffusion media have been treated with a wide range of loadings from 5 to 40% wt. PTFE. In fact, the PTFE loading is controlled by either the dipping time or concentration of the aqueous suspension in the manufacturing process. Therefore, understanding to optimize the hydrophobic agent loading is a pressing need in the fuel cell community that should be overcome to minimize the ohmic losses and mass transport limitations which is one of the main intents of this work. The developed design tool is capable to model the GDL substrate transport properties in different PTFE loadings by reconstructing the structures. The transport properties are then utilized as inputs for performance modeling and optimization purposes.

The other challenge in hydrophobic agent loading optimization is that the expectations from the GDL substrate characteristics may vary depending on the fuel cell operating conditions. As an example, the GDL substrate is expected to retain as much water as possible for the membrane humidification under dry conditions, whereas, the water is expected to be expelled to avoid cell flooding under wet conditions. Nevertheless, most of the proposed designs have met the performance expectations under only a very limited range of operating conditions which identifies a crucial need for GDL substrates versatility under a wider range of operating conditions in fuel cell development and manufacturing. This need highlights another potential of the developed design tool for GDL substrate prototyping assignments of more advanced designs.

iv. GDL Substrate Design Tool Algorithm

The algorithm flowchart for the proposed GDL substrate microstructural modeling framework which is extensively described in subsections i to iii is diagrammatically illustrated in Figure 2.14. The algorithm was implemented in GeoDict using the following

known input parameters from manufacturer's datasheet and observation from SEM images characterization. After thorough validation, the framework is expected to become a reliable and versatile tool for hypothetical GDL substrate materials design and prototyping assignments to reduce the cost and time of the design cycle.

Input parameters from datasheet:

- ρ_F Fiber density
- ρ_B Binder density (papermaking and resin-based)
- ρ_T Hydrophobic agent density
- d_F Fiber diameter
- h_{sub} GDL substrate thickness
- ε_{sub} GDL substrate porosity
- ρ_{sub} GDL substrate bulk density
- BW_{sub} GDL substrate basis weight (grammage or areal weight)
- BW_F Fiber basis weight; typically, 45-70 g m^{-2}
- ω_{PPB} Papermaking binder weight percentage; typically, 5-15% wt.
- ω_{PLB} Polymeric binder weight percentage
- ω_T Hydrophobic agent weight percentage as $\omega_{T1} + \omega_{T2}$
- ω_{T1} PTFE weight percentage at top and bottom surfaces of the substrate
- ω_{T2} PTFE weight percentage throughout $(h_{sub} - 2h_T)$

Note that, GDL substrate thickness, porosity, bulk density, and basis weight are related as follows where SVP is the GDL substrate solid volume percentage:

$$SVP_{sub} = 1 - \varepsilon_{sub} = \frac{BW_{sub}}{\rho_{sub} h_{sub}} \tag{2-18}$$

Input parameters from SEM images characterization of existing materials:

- β Fibrous skeleton anisotropy parameter; typically, 1-1000
- ε_B Porosity of graphite particles distribution in resin-based binder
- h_T Hydrophobic agent penetration thickness

Using the abovementioned input parameters, other input parameters can be calculated as per below:

$$SVP_F = \frac{\Omega_F}{\Omega_{Domain}} = \frac{BW_F}{\rho_F h_{sub}} \tag{2-19}$$

$$SVP_B = \frac{\Omega_B}{\Omega_{Domain}} = \frac{BW_B}{\rho_B h_{sub}} \tag{2-20}$$

$$VP_{BS} = \frac{\Omega_{BS}}{\Omega_{Domain}} = \frac{1}{1-\varepsilon_B} SVP_B \tag{2-21}$$

$$VP_{SS} = \frac{\Omega_{SS}}{\Omega_{Domain}} = 1 - (SVP_F + VP_{BS}) \tag{2-22}$$

where Ω_F, Ω_B, and Ω_{Domain} are the fiber, binder, and domain volumes and binder basis weight can be obtained by $BW_B = BW_{sub} - BW_F$.

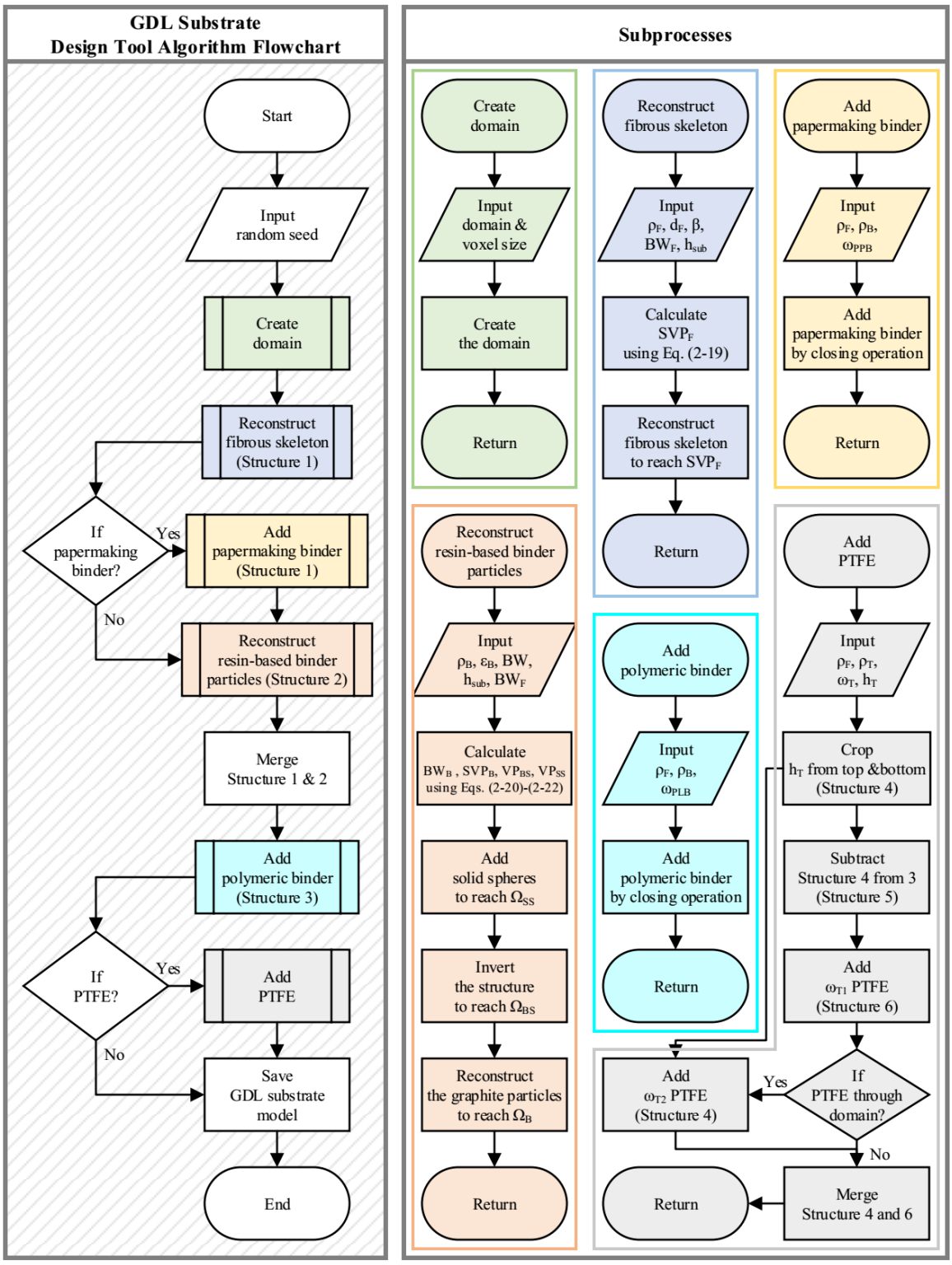

Figure 2.14. The GDL substrate design tool algorithm flowchart (left-side block) and its subprocesses (right-side block). Subprocesses color coding: - Create domain in green, - Reconstruct fibrous skeleton in blue, - Add papermaking binder in yellow, - Reconstruct resin-based binder particles in orange, - Add polymeric binder in phosphoric blue, and – Add PTFE in grey.

v. Case Study

This section is devoted to a case study on the developed stochastic microstructural modeling design tool, diagrammatically illustrated in Figure 2.14, using Toray TGP-H GDL substrate as a reference standard to validate and analyze the new underlying framework. Toray TGP-H has been chosen as a commonly used and commercially available GDL substrate for which many comparisons with the literature are available. According to material datasheet, the Toray TGP-H product implemented here has a 170 µm nominal thickness, 78% porosity, 75 g m^{-2} basis weight, and ~30 µm average pore size. Other known GDL substrate parameters such as material composition including fiber, binder, and PTFE with densities of 1.76, 2.25, 2.15 g cm^{-3} and binder and PTFE weight percentages can be obtained from material datasheet. These values are used as input parameters for the microstructural reconstruction algorithm as follows:

- ***Reconstruction of Fibrous Skeleton*:** Initially, a set of cylindrical fibers are randomly generated across a 3D modeling domain of 200×200×170 μm^3 dimensions following the three steps of fibrous skeleton algorithm in the Reconstruction of Fibrous Skeleton subsection. The domain width is chosen with the same order of magnitude as the thickness to provide a reasonable statistical representation of the GDL substrate. The fibers are stochastically generated under the constraint of fixed fiber solid volume percentage SVP_F and are represented as infinitely long (fiber length >> domain size) and non-overlapping circular cylinders of 7 µm diameter which are approximately oriented towards the *xy*-plane. To this end, the anisotropy parameter of the probability density function $\beta = 20$ in Eq. (2-6) due to predominant alignment of carbon fibers in the *xy*-plane which is observed through captured SEM images. Note that the constraint of SVP_F is derived from Eq. (2-19) using fiber basis weight BW_F, density ρ_F, and domain thickness h_{Domain} inputs obtained from material datasheet where $BW_F = \rho_F \Omega_F / A$. The domain is segmented into small voxelized cubes, where each cube represents solid or pore phase. A maximum voxel (volume pixel) size of 0.5 µm is required for sufficient resolution of the fiber geometry which results in approximately 54 million voxels per domain. For this purpose, a grid independence study was performed on a dummy fibre structure to determine a suitable voxel size by which

consistent material property simulations with less than 10% tolerance was achieved. An example of the obtained fiber structure is illustrated in Figure 2.15(a) where the positioning of the fibers defines the overall fibrous skeleton of the GDL substrate structure. Provided the small domain size relative to a realistic GDL substrate sheet size, multiple randomized models with different random seeds using the stochastic approach are necessary to create a statistical sample set representative of a larger sheet. The random seed is a non-negative integer number that defines the random initial position of the fibers where changing its value generates different sequences of random numbers and, hence, different realizations of the reconstructed structure with the same properties.

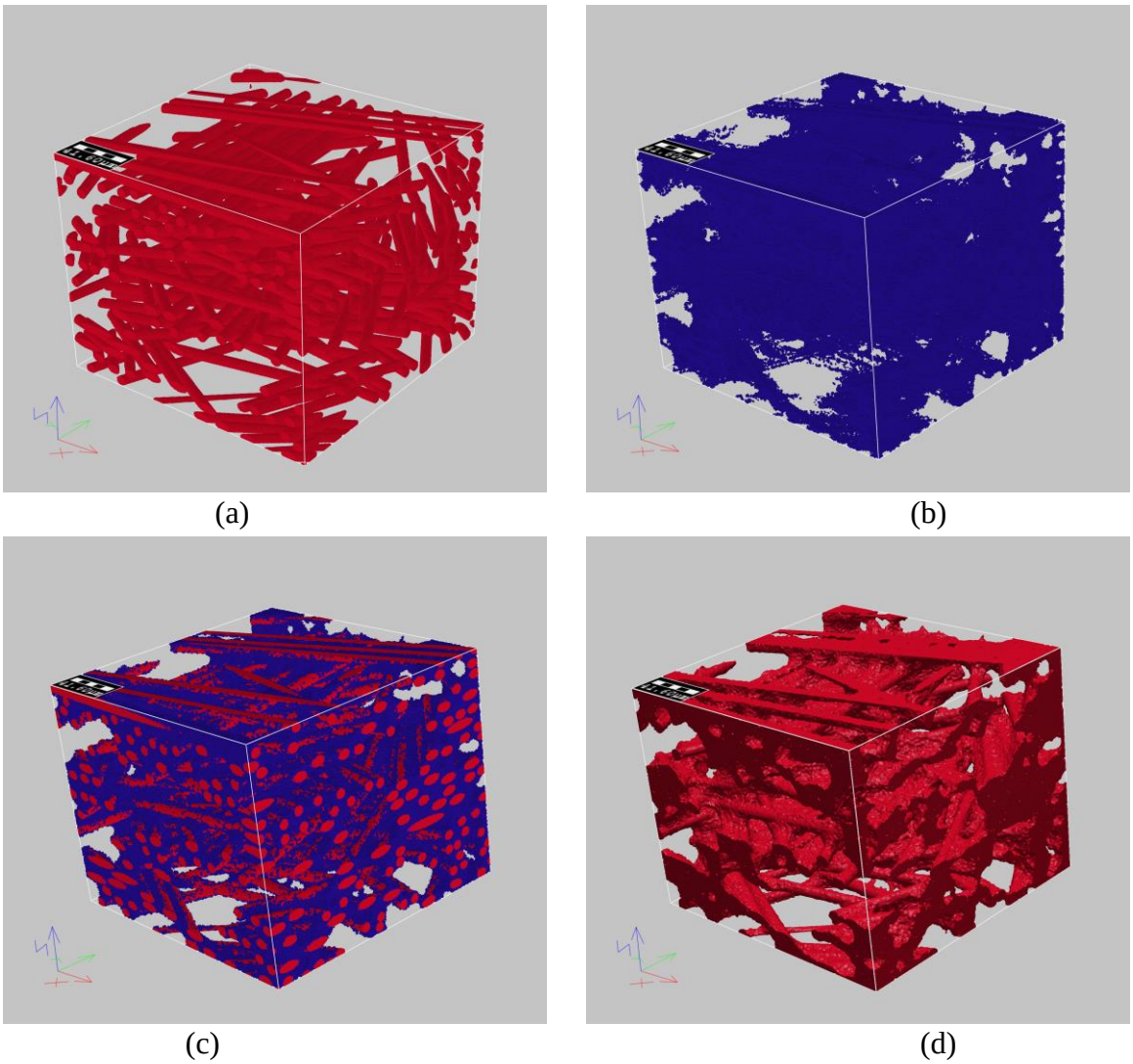

(a) (b)

(c) (d)

Figure 2.15. 3D stochastic microstructural model of (a) graphitized carbon fibers, (b) graphite particles of the resin-based binder, (c) completed view, and (d) smooth view of Toray TGP-H GDL substrate.

- ***Reconstruction of Binder:*** The second step in the GDL substrate structure creation is the generation of resin-based binder as an agglomerate of small disc-shaped graphite particles with different lengths and diameters and polymeric binder, known to be accumulated in small pores near the fiber intersections and thereby connect the fibers physically, thermally, and electrically. To this end, the two-step resin-based binder reconstruction algorithm in the Reconstruction of Binder subsection is followed until the desired binder solid volume percentage, obtained in Eqs. (2-20)-(2-22), is reached. Figure 2.15(b) illustrates the disc-shaped graphite particles of the resin-based binder randomly distributed across the inverted solid phase. Thereafter, the polymeric binder added to the merged fibrous skeleton and graphite particles structure is depicted in Figure 2.15(c) as a complete Toray TGP-H GDL substrate structure with the smooth view shown in Figure 2.15(d).

- ***Reconstruction of PTFE Treatment:*** The PTFE coating is generated via an optional, final step. Four PTFE loadings are considered in the present work (0, 10, 20, and 30% wt.), as illustrated in Figure 2.16. The procedure for the PTFE implementation is guided by cross-sectional SEM images of GDL substrate material samples, indicating two thin PTFE layers near the top and bottom surfaces resulting from the drying and sintering steps of the manufacturing process [90]. Hence, two layers at the top and bottom of the GDL substrate model are selected for randomized PTFE generation using the same generation scheme as for the papermaking binder thoroughly explained in the Reconstruction of PTFE Treatment subsection. The thickness of these layers is considered as 20, 25, and 30 μm for a desired PTFE loading of 10, 20, and 30% wt., respectively, while the PTFE penetration throughout the whole thickness is considered for 30% wt. PTFE with higher concentration near the surfaces, in accordance with the SEM images.

In order to ensure the realisticity of the real Toray TGP-H GDL substrate microstructural implementation, a comprehensive qualitative and quantitative validation is conducted and elaborated in the Model Validation subsection.

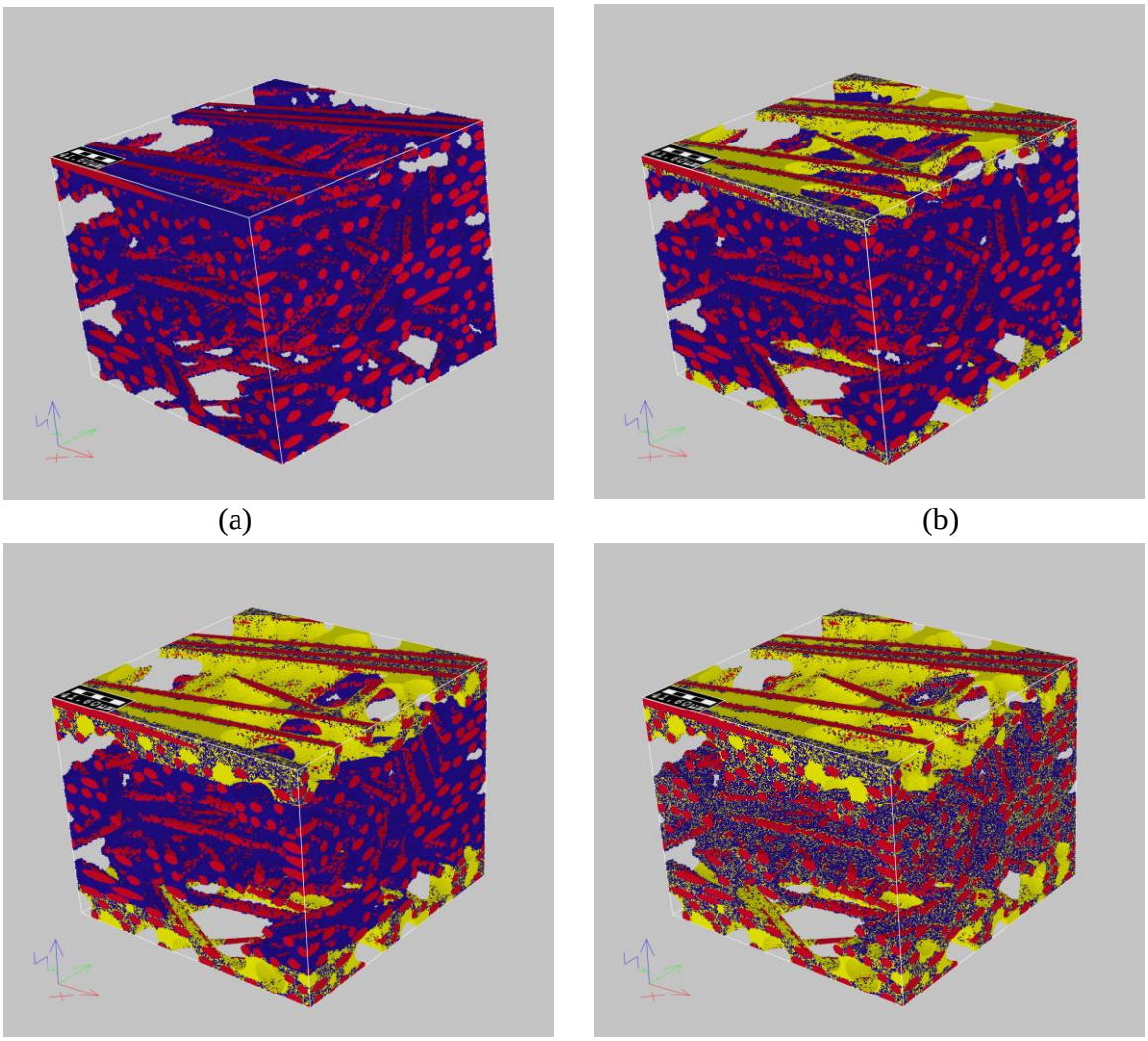

Figure 2.16. 3D illustration of the microstructural Toray TGP-H GDL substrate model for (a) 0% wt., (b) 10% wt., (c) 20% wt., and (d) 30% wt. PTFE.

2.2.2. Model Validation

Virtual reconstruction of the GDL substrate requires thorough model validation to ensure accurate representations of the real structural characteristics. The structural characteristics of the models are validated according to the material specifications for GDL substrate thickness, basis weight, and porosity as well as measured mercury intrusion porosimetry (MIP; Micromeritics) data. In addition, a collection of SEM images are captured to support the model validation. These characteristics are strictly monitored after each part of the model generation. Figure 2.17 diagrammatically illustrates the validation algorithm for microstructural reconstruction of pre-existing material or design of new GDL substrate/MPL/GDL porous material.

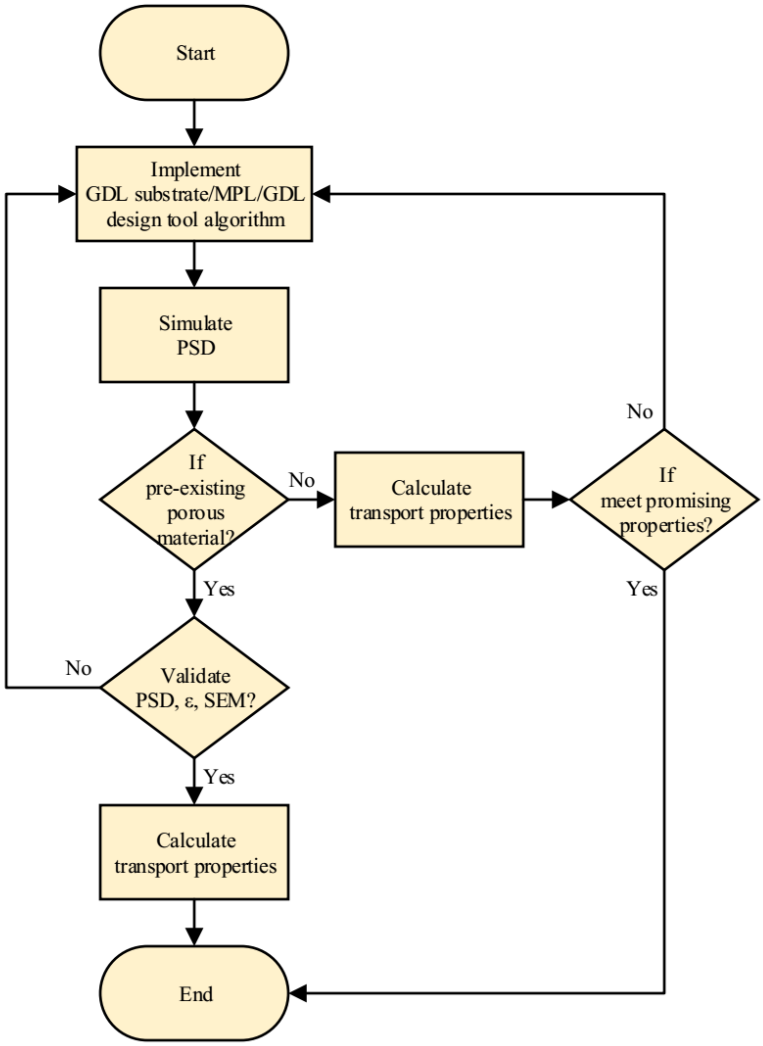

Figure 2.17. The flowchart of validation algorithm for GDL substrate/MPL/GDL stochastic micro-structural reconstruction of pre-existing material or design of new material.

The results of the qualitative and quantitative validation of Toray TGP-H in our case study are elaborated in the following. For the qualitative validation, Figure 2.18 compares selected SEM images to the model structure in the cross-sectional and top-down orientations. The obtained images demonstrate the accuracy of the reconstructed GDL substrate models. As a quantitative validation, the PSD of the reconstructed Toray TGP-H GDL substrate model is analyzed via a simulated intrusion porosimetry method with the top and bottom faces in contact with a virtual non-wetting fluid reservoir by closely mimicking the MIP experiment as the methodology is explained in section 2.1. This is algorithmically accomplished by a stepwise procedure that erodes the pore space by fluid spheres of radius r, discards the pores not connected to the reservoir, and calculates the volume of the remaining fluid connected to the reservoir for each choice of r. The simulated PSD results for 0 and 30% wt. PTFE are compared to MIP-measured PSD data

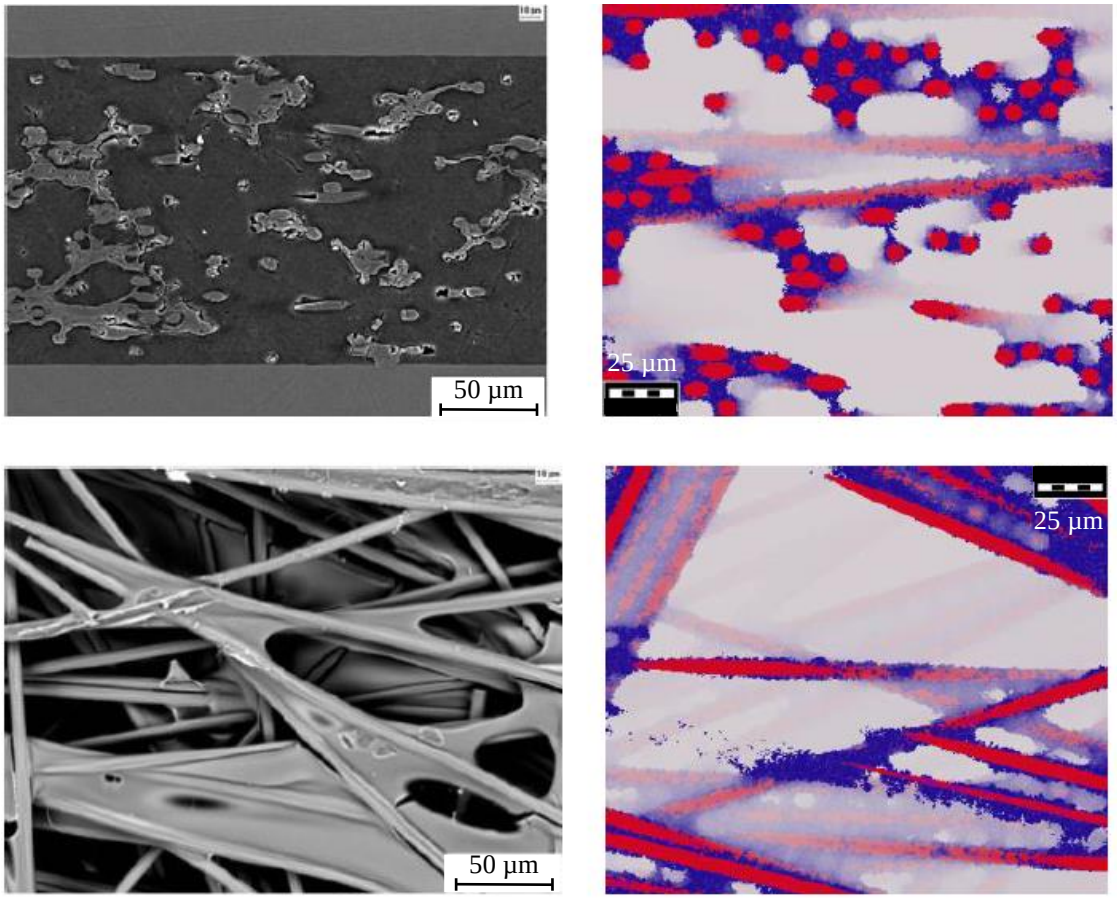

Figure 2.18. Microstructural non-teflonated Toray TGP-H GDL substrate stochastic model (right) compared to measured (left) cross-sectional view and top view SEM images (back-scattered electron mode).

in Figure 2.19. In all four cases, the dominating pore sizes are about 30 µm, where 14.3% reduction is observed in measured median pore diameter (D50) with 2.1% error for the model (Table 2.1). Indeed, the small differences between the curves are not statistically significant. Hence, the simulated PSD shows the same trend with measured data for both PTFE levels, and the minor deviations are likely associated with material variability. Detailed information for porosity, basis weight, and median pore diameter is provided in Table 2.1. Figure 2.20 illustrates the log-normal PSD measured by MIP, showing a reduced pore volume and marginally reduced pore sizes with increasing PTFE loading. Moreover, as shown in Figure 2.21, the Toray TGP-H GDL substrate open porosity decreases substantially with increased PTFE loading due to the constant thickness before and after teflonation. This trend is well captured by the model, in agreement with the specification, literature [115], and porosity data. However, porosity of the substrate batch used in the measurements is ~3% below specification, presumably due to batch-to-batch variability.

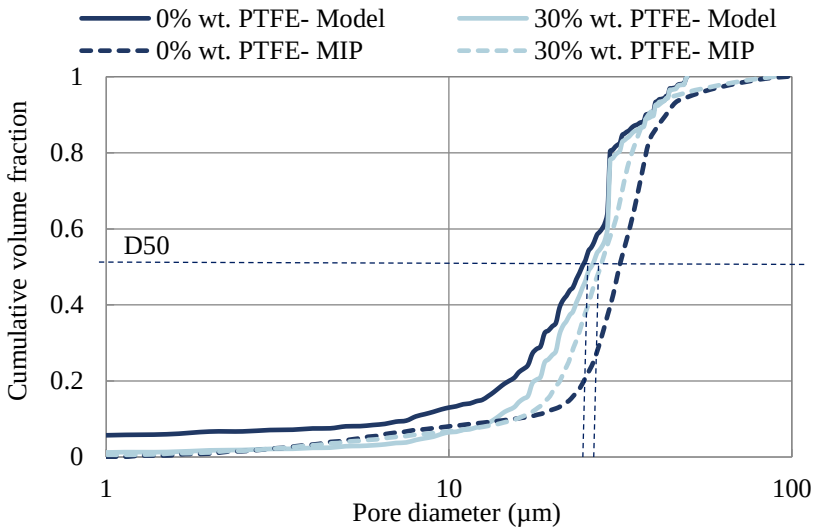

Figure 2.19. Cumulative volume fraction of the modeled Toray TGP-H GDL substrate compared to in-house MIP data in 0% and 30% wt. PTFE.

Table 2.1. Properties of the reconstructed Toray TGP-H GDL substrate model in different % wt. PTFE compared to in-house measured MIP data.

		0%	10%	20%	30%
Porosity (%)	Model	78	76.4	73.1	70
	MIP	74.8	72	67.4	63.7
Basis weight (g m^{-2})	Model	75	83.3	93.7	107.1
	MIP	75	82.1	94.5	108.3
Median pore diameter (µm)	Model	34.2	31.8	29.5	29.3
	MIP	32.9	30.6	28.7	28.1

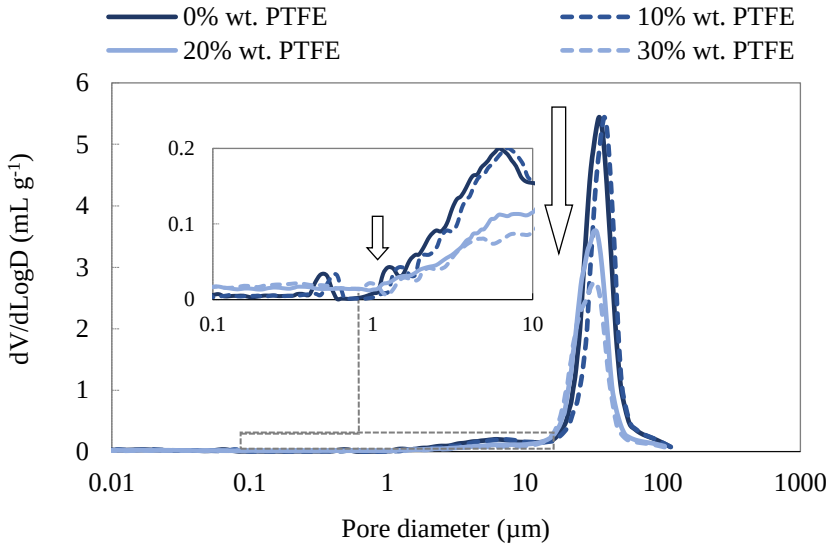

Figure 2.20. MIP-measured differential pore size distribution of the Toray TGP-H GDL substrate in different % wt. PTFE.

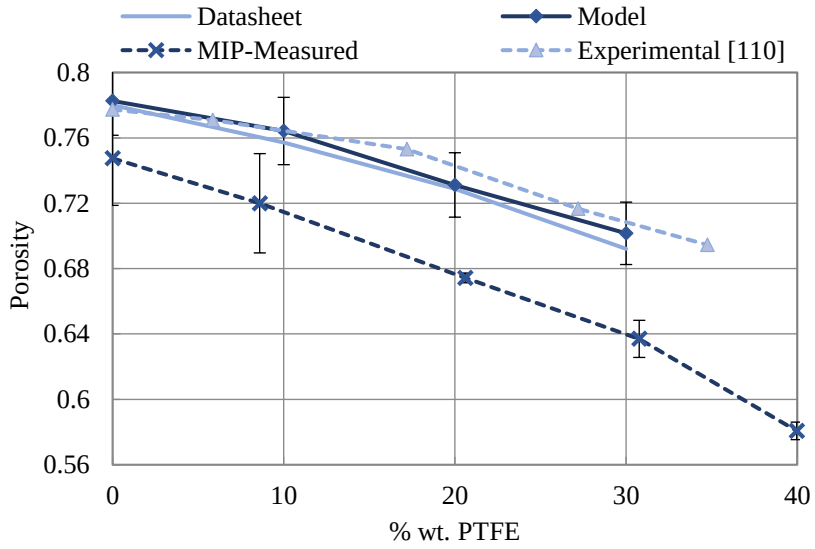

Figure 2.21. Toray TGP-H GDL substrate average bulk porosity of the model and MIP-measured data compared to experimental data [111].

2.2.3. Effective Transport Properties Modeling

The rate of reaction in the catalyst layer is influenced by various transport phenomena occurring throughout the GDL allowing species transport to and from the catalyst surface. There are four key transport phenomena in the GDL, namely, species diffusion, mass convection, thermal conduction, and electrical conduction. Each of these processes are primarily driven by their pertinent potential difference, *i.e.*, concentration,

pressure, temperature, and electrical potential gradients, respectively. The GDL transport processes are described by solving the conservation equations of species, mass and momentum, energy, and charge, correspondingly. This section describes the algorithms and partial differential conservation equations used to numerically simulate the GDL transport properties of effective diffusivity, permeability, and thermal and electrical conductivities as a measure of their respective phenomenon for the 3D virtually reconstructed GDL models. The explicit jump finite volume solver is applied, and simulations are conducted in all three principal directions of the domain which is segmented into small voxelized cubes. Each cube represents either solid or pore phase that is used as the voxel mesh to serve as the mesh for numerical modeling. The algorithms and partial differential equation solvers in both the macroscopic and microscopic levels used to simulate the GDL transport properties are described in detail in the following subsections [133]. The flux associated with each of the GDL transport processes depends on the gradient of the relevant potential and the effective transport properties as follows:

$$Flux = \Gamma_{eff} \nabla \psi \tag{2-23}$$

The flux is represented by Fick's law in the field of diffusion, Darcy's law in the field of mass convection, Fourier's law in the field of heat conduction, and Ohm's law in the field of electrical current conduction as summarized in Table 2.2.

This section is structured as follows: first, the assumptions made for the GDL transport properties numerical modeling are provided followed by the conservation equations of the relevant key GDL transport phenomena. Thereafter, based upon the 3D virtually created models, the numerical determination of the effective transport properties of diffusivity, permeability, and thermal and electrical conductivities are extensively elaborated. Finally, the process for adding liquid water to the models is also described.

Table 2.2. Key GDL transport phenomena and their corresponding flux, transport coefficient, potential, and conservation law.

Transport Process	Flux	Transport Coefficient	Potential	Conservation Law
Species Diffusion	J_i (mol m^{-2} s^{-1})	D_{eff} (m^2 s^{-1})	C_i (mol m^{-3})	Species
Mass Convection	$\vec{V}$ (m s^{-1})	k_{eff}/μ (m^2 Pa^{-1} s^{-1})	P (Pa)	Mass & Momentum
Heat Conduction	q (W m^{-2})	K_{eff} (W m^{-1} K^{-1})	T (K)	Energy
Electrical Conduction	i_e (A m^{-2})	σ_{eff} (S m^{-1})	ϕ_S (V)	Charge

Making the reasonable assumptions helps to understand the numerical model limitations for accurate interpretation of the results. In this study, the main assumptions made for the mathematical model to make the numerical modeling more manageable are as follows:

- No gravity effects
- Ideal gas properties for the gas reactants
- Ideal gas mixtures
- Incompressible flow
- Laminar flow
- No contamination effects (pure hydrogen in the cell)
- Newtonian fluids (constant viscosity)

It is also worth mentioning that the numerical modeling of GDL transport phenomena can be classified based on the application as follows:

- Dependency on time, *i.e.*, transient versus steady state
- Dependency on temperature, *i.e.*, isothermal versus non-isothermal
- Incorporating of water presence, *i.e.*, single-phase versus multi-phase

i. Conservation Equations

Conservation of Mass: All the processes inside a fuel cell such as fluid flow, diffusion, phase change, and electrochemical reactions has to satisfy the conservation of mass. In GDL, the continuity equation for the gas phase in which the gas phase density, ρ_g, is related to the superficial gas velocity, $\vec{V}_g$, entails:

$$\frac{\partial}{\partial t}\left(\varepsilon_{eff}\rho_g\right) + \nabla.\left(\rho_g\vec{V}_g\right) = S_m \tag{2-24}$$

where $\varepsilon_{eff} = \varepsilon(1-s)$ is the effective porosity with bulk GDL porosity, ε, and liquid water saturation, s, and $\vec{V}_g = \varepsilon_{eff}\vec{V}_{physical}$ with $\vec{V}_{physical}$ as the physical velocity based on volumetric flow rate. The mass source term S_m has different values depending on the cell region where in GDL, S_m is equal to zero for all gases except for water vapor. Indeed, S_m

is the amount of change in water mass due to phase change from vapor to liquid or vice versa. The left side of Eq. (2-24) is the material derivative of mass for a moving fluid. The first term in the left, which is called the local derivative, represents the accumulation of mass over time and the second term, which is called the convective derivative, represents the change in mass flux from one location to another in the flow field [134–137].

Conservation of Momentum: The convective transport of any individual phase in the GDL has to satisfy the conservation of momentum which is described as follows for the gas phase.

$$\frac{\partial}{\partial t}\left(\frac{1}{\varepsilon_{eff}}\rho_g\vec{V}_g\right)+\nabla.\left(\frac{1}{\varepsilon_{eff}^2}\rho_g\vec{V}_g\vec{V}_g\right)=-\nabla P_g+\nabla.\left(\frac{1}{\varepsilon_{eff}}\mu_g\nabla\vec{V}_g\right)+S_V \qquad (2\text{-}25)$$

where P_g and μ_g are the gas phase pressure and viscosity, respectively. The left side of Eq. (2-25) is the material derivative of momentum for a moving fluid. The first term in the left represents the accumulation of momentum with time and the second term describes advection momentum flux. The first two terms on the right side represent the momentum imparted due to pressure and viscosity, respectively. The momentum source term S_V has different values depending on the fuel cell regions, *i.e.*, in GDLs, S_V is defined as:

$$S_V=-\frac{\mu_g}{k}\vec{V}_g \qquad (2\text{-}26)$$

which represents a pressure drop arising from Darcy's drag force imposed by the pore walls on the fluid where k is the GDL permeability [134–137].

Conservation of Species: In addition to convective gas transport, the diffusive transport of gaseous species such as hydrogen, oxygen, nitrogen, and water vapor as the main four species of a cell through the void region of the GDL should be taken into account and the conservation of gaseous species is as follows:

$$\frac{\partial}{\partial t}\left(\varepsilon_{eff}C_i\right)+\nabla.\left(\vec{V}_gC_i\right)+\nabla.\left(-D_{eff}\nabla C_i\right)=S_i \qquad (2\text{-}27)$$

where C_i and D_{eff} are the concentration and effective diffusion coefficient of the gaseous species i. The first two terms on the left represents species accumulation and advection

terms and the third term represents Fickian diffusion of species in a porous medium. The species source term S_i accounts for the consumption or production of species due to electrochemical reactions or phase changes. In GDL, S_i is equal to zero for all gas species except for water vapor. Indeed, S_i is the amount of change in water molecular weight due to phase change from vapor to liquid or vice versa. Furthermore, the continuity equation and the species transport equation are correlated through the following relations [134–137].

$$S_m = \sum_{i=1}^{N} S_i \tag{2-28}$$

$$\rho_g = \sum_{i=1}^{N} M_i C_i \tag{2-29}$$

Conservation of Energy: In GDL, heat transfer processes are governed via conduction, convection, and heat generation as the conservation of energy is given by:

$$\frac{\partial}{\partial t}\left(\left(\rho c_p\right)_{eff} T\right) + \nabla.\left(\left(\rho c_p\right)_{eff} \vec{V}_g T\right) = \nabla.\left(K_{eff} \nabla T\right) + S_e \tag{2-30}$$

where T is the temperature, K_{eff} is the effective thermal conductivity of the porous medium, and

$$\left(\rho c_p\right)_{eff} = (1-\varepsilon)\rho_S c_{p,S} + \varepsilon \rho_g c_{p,g} \tag{2-31}$$

in which ρ_S and $c_{p,S}$ are the density and specific heat capacity of the solid matrix and ρ_g and $c_{p,g}$ are the gas density and specific heat capacity. In fuel cell components, energy source term S_e may include heat from electrochemical reactions, Joule (ohmic) heating, and/or heat of evaporation or condensation in case there is a phase change. In GDLs, the S_e is due to Joule heating S_{Joule}, the heat produced by transferring electrons through the ohmic-resistive solid matrix of the GDL, as well as and the phase-change heating $S_{Phase-Change}$, the heat exchanged in the water phase change (condensation/evaporation) through the pores, as follows:

$$S_e = S_{Joule} + S_{Phase-Change} = \frac{i_e^2}{\sigma_{eff}} - \alpha_{pc} A'_{pc}\left(m'_{sat} - m'_{H_2O,g}\right)\Delta H_{pc} \tag{2-32}$$

where i_e is the current density and σ_{eff} is the GDL effective electrical conductivity in the Joule heating source term and α_{pc} is the phase-change coefficient, A'_{pc} is the phase-change surface area per unit volume, m'_{sat} is the maximum mass fraction of water vapor in dry gas at saturation, $m'_{H_2O,g}$ is the fraction of water vapor in dry gas, and ΔH_{pc} is the Enthalpy of evaporation/condensation [134–137].

Conservation of Charge: The transport of electrons is described by a governing equation for conservation of charge:

$$\nabla.\left(-\sigma_{eff}\nabla\phi_S\right) = S_{\phi S} \tag{2-33}$$

where ϕ_S is the solid phase potential. In the gas diffusion layer, electrons are not produced or consumed; thus, the potential source term $S_{\phi S}$ is equal to zero [134–137].

ii. Effective Diffusivity

In order to conquer the performance losses associated with mass transport limitations in modern PEFCs operating at high current density conditions, a thorough understanding of the gaseous species mass transport through the void region of the GDL porous transport layer is fundamental. The mass transport through the GDL is primarily driven by convective-diffusive transport mechanisms, *i.e.*, convection due to pressure gradient and diffusion due to concentration gradient where the latter constitutes the significant portion of the overall mass transport. Indeed, diffusional mass transport should be optimized to establish a delicate balance between gas species transport and water management. Due to the tortuous structure of a porous medium, the gas molecules inevitably diffuse by following a convoluted route to traverse the void region. Hence, the dimensionless effective bulk diffusivity D^*_{bulk} is defined as the rate of diffusion in a porous medium in relation to the rate of free bulk diffusion in open space as given by $D^*_{bulk} = D_{bulk}/D^o_{bulk}$ [138]. In case of a unary gas, the free bulk diffusion is defined as:

$$D^o_{bulk} = \frac{1}{3}\lambda v_T \tag{2-34}$$

with the thermal velocity $v_T = \sqrt{8R_gT/\pi M}$ where T is the temperature, R_g is the gas constant, and M is the molar mass of the diffusing species. In case of a binary gas mixture,

e.g., O_2 in N_2, D^o_{bulk} is the measurable binary diffusion coefficient. Thereby, the inherent macroscopic effective bulk diffusivity is a geometrical property and is independent of the nature of the gas [77].

Diffusional gas transport through porous medium attributed to a gradient in gas species concentration is microscopically defined as a gradual dispersion of concentration within the porous material which occurs due to internal collisions of gas molecules referred to as continuum (bulk) diffusion and collisions of gas molecules with the pore walls known as Free molecule (Knudsen) diffusion. Herein, determining the porous medium pore size range offers an opportunity to understand which diffusion type has the dominant effect on the overall gas reactant diffusion transport. For instance, the bulk diffusion is dominant through relatively large pores whilst the Knudsen diffusion is the effective gas diffusion mechanism through the nano-scale pores. The contribution of each type of diffusion to the overall diffusion is described by Knudsen number; the ratio of mean free path of gas molecules to the system length scale; as a dimensionless diffusion type metric given by:

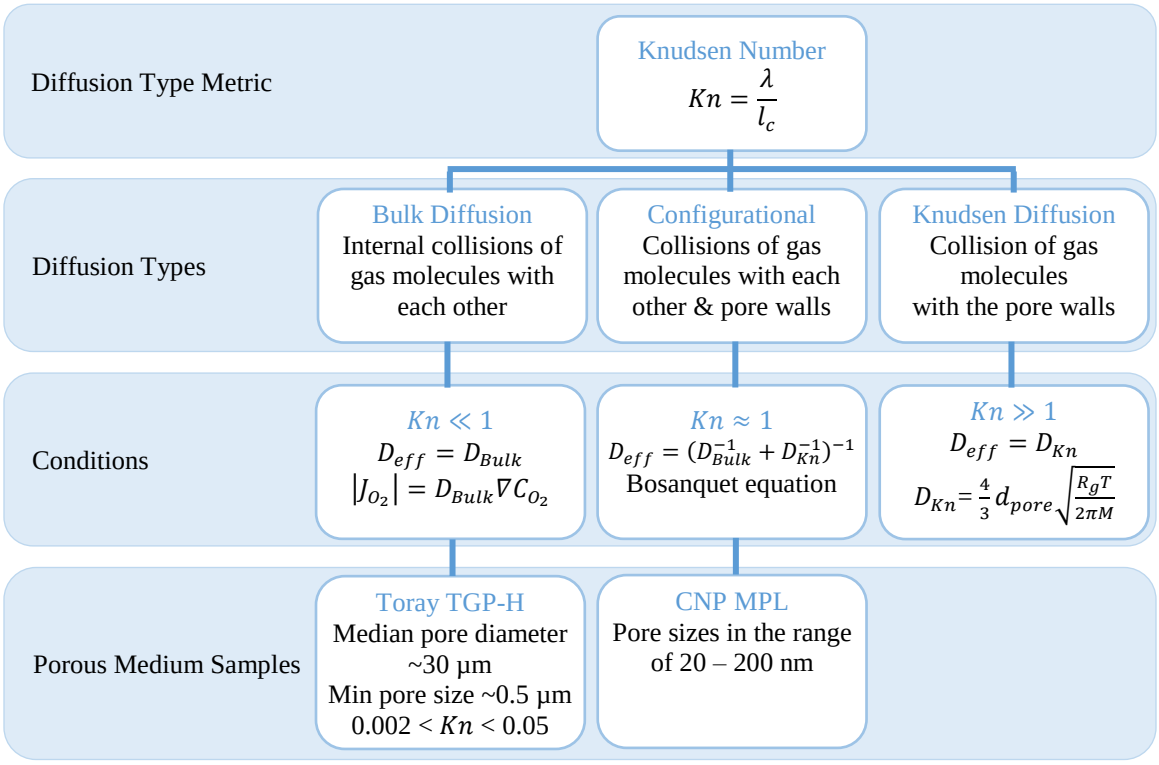

Figure 2.22. Graphical illustration of diffusion types metrics, diffusion types, conditions, and porous medium samples.

$$Kn = \frac{\lambda}{l_c} \tag{2-35}$$

where λ is the gas reactants mean free path and l_c is the mean pore diameter as the characteristic length scale of the porous structure. Therefore, the total gas diffusion is a combination of bulk diffusion D_{bulk} and Knudsen diffusion D_{Kn} interactions as follows:

$$D_{eff} \approx \begin{cases} D_{bulk}, & Kn \ll 1 \\ (D_{bulk}^{-1} + D_{Kn}^{-1})^{-1}, & Kn \approx 1 \\ D_{Kn}, & Kn \gg 1 \end{cases} \tag{2-36}$$

In the case of Knudsen regime, the diffusion is mathematically modeled using a random walk Monte Carlo approach based on the mean square displacement (MSD) of the diffusing molecules. The Knudsen diffusion is proportional to the mean square displacement of a large number of gas particles in three dimensions, which relies on the basic principles of the Brownian movement formulated by Einstein [109]. Due to the tortuous structure of the porous media, the dimensionless effective Knudsen diffusivity is defined as $D_{Kn}^{*} = D_{Kn}/D_{Kn}^{o}$ with D_{Kn}^{o} as the Knudsen diffusion in a capillary tube quantified by [139]:

$$D_{Kn}^{o} = \frac{1}{3} l_c v_T = \frac{4}{3} d_{pore} \sqrt{\frac{R_g T}{2\pi M}} \tag{2-37}$$

where d_{pore} is the mean pore diameter, R_g is the gas constant, T is the temperature in Kelvin, and M is the molecular weight of the diffusing species.

The mean free path of the key GDL gas reactants such as hydrogen, nitrogen, and oxygen are estimated in the range of 65-75 nm at atmospheric temperature and pressure conditions. Hence, the gas reactant transport through bulk diffusion is dominant where the diameter of the pores is generally two orders of magnitude higher than the gas reactant mean free path (pore diameter ~10 μm), whereas in pores with diameters less than one-tenth of the mean free path (pore diameter ~10 nm), the Knudsen diffusion becomes dominant. For any other pore diameters lie between the above limits, both diffusion types are taken into effect. The relationship used for mixed diffusion for which $Kn \approx 1$ is a series network resistance model known as the Bosanquet equation [139–141]. This theory is

firmly entrenched in chemical engineering literature and is widely used in practice to calculate the diffusion coefficient in micro- and meso-porous materials. The degree of validity of the Bosanquet equation is investigated by carrying out molecular dynamics simulations of diffusivities in one-dimensional mesoporous channels with well-defined sizes. For molecules such as hydrogen and oxygen with poor adsorption strength at pore walls, the Bosanquet equation is of reasonable accuracy for a wide range of pore concentrations, which is the case for the present application [139].

In the GDL substrates such as Toray TGP-H, the characteristic pore sizes are much larger than the mean free path of the gas molecules, considering that the average pore diameter is ~30 µm (macropores) and the minimum pore sizes are ~0.5 µm. Diffusion is therefore substantially driven by internal collisions of gas molecules, which is referred to as bulk diffusion and governed by the classical continuum mechanics approach, thus facilitating gas reactants mass transport. Knudsen diffusion, *i.e.*, collisions of gas molecules with the pore walls, is negligible in this case. The average Knudsen number, Kn, is 0.002 with the maximum value of 0.05, which supports the assumption of continuum mechanics valid for $Kn \ll 1$ [142]. In contrast to the GDL substrate, the pore diameter of conventional MPLs lie in the range of 20-200 nm (mesopores) which is in the same range as the mean free path of gas reactants; therefore, both diffusion mechanisms (Bosanquet equation) must be considered. The summary of diffusion types metrics, diffusion types, conditions, and porous medium samples is graphically depicted in Figure 2.23.

In order to numerically determine the bulk effective diffusivity of the reconstructed GDL models, first, the concentration distribution is numerically determined by solving the conservation of species on the microscopic level in the void space as given in Eq. (2-27). In this equation, the species accumulation and advection terms are considered as zero in the steady-state operating conditions. In addition, the species source term S_i is null since the gas species are not produced nor consumed in the GDL. Hence, the conservation of species equation is simplified to Laplace equation for the molecular diffusion as follows:

$$\nabla(D_\vartheta \nabla C_\vartheta) = 0 \tag{2-38}$$

where ϑ represents either solid or void space in the domain Ω in which D_ϑ is equal to D_{O_2} in the void space and zero in the solid space. This equation is numerically solved using Neumann boundary conditions on the internal gas-solid interfaces, periodic boundary conditions on the side walls, and a Dirichlet-based concentration drop in the principal direction of diffusion. The explicit jump finite volume solver [143] is applied, and simulations are conducted in all three principal directions. The residual value of 10^{-8} is conducted for proper convergence of the iterative solution. The unique solution of the Laplace equation is a concentration potential field. Second, the bulk diffusion of a porous medium is macroscopically described by Fick's first law of diffusion as follows [138]:

$$\left|J_{O_2}\right| = D_{eff}\nabla C_{O_2} \tag{2-39}$$

where C_{O_2} is the oxygen concentration, J_{O_2} is the superficial species flux, and D_{eff} is the effective diffusivity tensor averaged over the domain. Having solved Eq. (2-38), the components of the averaged effective diffusivity tensor are computed by integrating the inner product of the evaluation direction i against the flux term in Fick's law and vector in direction j.

$$\left(D_{ij}\right)_{eff} = \frac{1}{\Omega}\int_{\Omega} \vec{e}_i \,.\left(D_\vartheta\left(\nabla C_j + \vec{e}_j\right)\right) d\Omega \tag{2-40}$$

It is worth mentioning that, the bulk effective diffusivity will be anisotropic due to anisotropy of the GDL microstructure, thus, it is fully described by the second-order effective diffusivity tensor by solving for the concentration drops in each space direction.

$$D_{eff} = \begin{bmatrix} D_{xx} & D_{xy} & D_{xz} \\ D_{yx} & D_{yy} & D_{yz} \\ D_{zx} & D_{zy} & D_{zz} \end{bmatrix} \tag{2-41}$$

In the presence of liquid water, Eq. (2-38) is solved for each capillary pressure in the space occupied by the gas phase while the solid and liquid phases are both treated as passive phases with Neumann boundary conditions applied at the gas-solid and gas-liquid interfaces.

iii. Permeability

The permeability of a porous medium quantifies the ability of the material to transmit pressure driven flow of gas and liquid. In fuel cells, this is a critical property that indicates the GDL's capability of convection-governed mass transport for both reactant gas transport from the flow field channels into the catalyst layer and product water transport in the opposite direction. It is particularly important for capillary flow of liquid water away from the catalyst layer in order to prevent flooding.

Permeability has been traditionally defined by Darcy's law of convection to macroscopically study convective flow of a fluid in porous media, *cf*. Eq. (2-42), which reveals the linear proportionality between the flow rate and applied pressure gradient in the seepage velocity [54]:

$$Q = \frac{kA}{\mu}\nabla P \tag{2-42}$$

where Q is the volumetric flow rate across the cross-sectional area A which is calculated by integrating the velocity field V over A, P is the pressure, k is the intrinsic viscous permeability tensor, and μ is the dynamic viscosity. The equation in three dimensions is generalized as:

$$V = -\mu^{-1}\begin{bmatrix} k_{xx} & k_{xy} & k_{xz} \\ k_{yx} & k_{yy} & k_{yz} \\ k_{zx} & k_{zy} & k_{zz} \end{bmatrix}\nabla P \tag{2-43}$$

Darcy's law, which was first experimentally determined by Henry Darcy, is an approximation of the Navier–Stokes equation via homogenization methods in which a net flow equation is obtained by volume averaging over a representative elementary volume of the porous media. Darcy's law is applicable to sufficiently low velocity fluid flow which is generally the case in the GDL substrate pores where the viscous resistance between the fluid and the porous solid are the dominant source of pressure drop in the creeping flow regime. The viscous permeability is an intrinsic property mainly governed by GDL structural characteristics but is independent of the nature and velocity of the fluid since the assumption of continuum fluid mechanics, *i.e.*, $Kn \ll 1$, is valid in the pores. Since GDL

materials are highly anisotropic, the permeability is a symmetric positive-definite second-order tensor represented in Eq. (2-43). The diagonal permeability components translate into IP (x and y) and TP (z) permeability. For the case of an isotropic medium, the permeability remains a scalar.

The validity of conventional Darcy's law to estimate the permeability of PEFC porous media is of concern at high fluid flow velocities or in nanoporous structures, thus, certain corrections should be made. Some extensions are available by analogy with the Navier-Stokes equation for higher velocities called Darcy-Forchheimer equation; taking into consideration of Knudsen effect in nanoporous structures; and the conditions where wall shear is important namely Brinkman extension [54,59]. In some applications, the employment of both Brinkman and Forchheimer equations are obligatory for a more complete momentum equation.

At high fluid flow velocities, the linearity between pressure gradient and flow rate breaks down when the Reynolds number of the flow through the porous medium representing the ratio of inertial to viscous forces based on a typical pore or particle diameter, exceeds the order of unity as given by:

$$Re = \frac{\rho V k^{0.5}}{\mu} \tag{2-44}$$

where ρ is the fluid density. In porous media with higher fluid flow velocities as Re is increased to the range of 1-10, the inertial resistance becomes significant. Hence, the Darcy's equation is modified by adding a nonlinear Forchheimer term to account for the inertial effects to give the Darcy- Forchheimer equation as below:

$$\nabla P = -\frac{\mu}{k} V - \frac{\rho}{k_I} V^2 \tag{2-45}$$

where k_I is known as the inertial permeability. The transition from Darcy to Darcy-Forchheimer is not one from laminar to turbulent flow, since at such comparatively small Reynolds numbers the flow in the pores is still laminar. Rather, the linearity between the pressure gradient and velocity is deteriorated since the quadratic drag due to solid obstacles is now comparable with the surface drag due to friction [54]. Accordingly, with not very

high TP velocities throughout the fuel cell electrodes, neglecting the inertial permeability is a reasonable approach in GDL substrates and MPLs. For GDL substrates with pore size in the range of 1-150 µm, Mukherjee *et al.* [100] stated the negligible effect of inertial forces compared to viscous and surface forces in their mesoscopic modeling formalism and estimated the Reynolds and Capillary numbers to be ~10^{-4} and ~10^{-6}, respectively. In addition, Gostick *et al.* [20] concluded that Darcy's law is accurate within 5% for TP flow through the GDL substrate. Therefore, the assumption of a negligible inertial term compared to the viscous pressure loss is acceptable and the fluid flow in the GDL substrate is expected to exhibit creeping flow characteristics. In contrary, the velocities in MPLs is dependent on viscous permeability and Knudsen diffusivity due to their higher Knudsen effects compared to inertial effects unless very high fluid velocities are encountered [44].

The fluid flow in nanoporous structures with small characteristic lengths such as conventional MPLs with pore sizes in the range of 2-200 nm experience the transitional flow regime, *i.e.*, $0.1 < Kn < 10$, in which the continuum assumption breaks down and Darcy's law is not able to predict the permeability accurately. Thus, the molecule-wall interactions become important and consequently the Knudsen resistance should be incorporated into the convective transport, *cf.* Table 2.3. Experimental studies have been conducted in the literature that proves Darcy's law deviates to predict the pressure drop across the MPL-coated GDL samples due to Knudsen effects [44,144].

To account for both viscous and Knudsen effects together in order to accurately predict the permeability of nanoporous MPL structures, both transport mechanisms are assumed to be in parallel as proposed by Kast and Hohenthanner [145] or are combined using binary friction model (BFM) proposed by Kerkhof [146] valid for fine porous media as follows:

Table 2.3. Different flow models in different flow regimes based on Knudsen number [44,147]**.**

Knudsen Number	Flow Model
$Kn < 0.001$	Continuum region; Navier-Stokes Valid with no-slip boundary condition
$0.001 < Kn < 0.1$	Continuum-transition region; Navier-Stokes Valid only with slip boundary condition
$0.1 < Kn < 10$	Transition region; Navier-Stokes not valid, moment equations or Burnett equation with slip boundary condition.
$Kn > 10$	Free molecule flow No continuum model valid.

$$\frac{\partial P}{\partial x} = -R_g T \left(\frac{kP}{\mu} + D_{Kn}\right)^{-1} N \tag{2-46}$$

where N is the molar flux. The equation can be rearranged using the definition of molar flux as follows:

$$Q = -\frac{kA}{\mu}\left(1 + \frac{\mu D_{Kn}}{k}\frac{1}{P}\right)\frac{\partial P}{\partial x} \tag{2-47}$$

By analogy of Eq. (2-47) with conventional Darcy's law, *cf.* Eq. (2-42), the apparent permeability with the nonlinear term attributed to the Knudsen diffusivity is given by:

$$k_{apparent} = k\left(1 + \frac{\mu D_{Kn}}{k}\frac{1}{P}\right) \tag{2-48}$$

The validity of the apparent permeability in MPLs is assessed in [44] for all PEFC working fluids. Due to low fluid velocities and small porous media pore radii, it is experimentally proved that the inertial permeability is not able to account for the nonlinear effects while the Knudsen diffusivity takes into account the nonlinearity quite accurately for different gases. It highlights the fact that Knudsen diffusivity is the dominant factor that contributes to the nonlinear nature of the pressure vs. velocity profiles.

In order to numerically determine the permeability of the reconstructed GDL models, first, the velocity distribution is numerically determined by solving the conservation of momentum on the microscopic level in the void space as given in Eq. (2-25). For steady-state, creeping, and incompressible flow, the momentum accumulation and advection terms are considered as zero and the Navier-Stokes equation is linearized to Stokes equation for conservation of momentum and the continuity equation for conservation of mass as follows [54]:

$$-\mu\nabla^2\vec{V} + \nabla P = 0 \tag{2-49}$$

$$\nabla \cdot \vec{V} = 0 \tag{2-50}$$

In PEFC porous electrodes, the convection velocities are low, hence the Stokes flow assumption can be applied where advective inertial forces are small compared with viscous forces. No slip on the internal fluid-solid interfaces, periodicity on the side walls, and a

pressure drop in the principal flow direction are applied as boundary conditions. The explicit jump finite volume solver [143] is applied to solve Eqs. (2-49) and (2-50) to derive the mean velocity in which simulations are conducted in all three principal directions. The residual value of 10^{-8} is conducted for proper convergence of the iterative solution. Second, the permeability is macroscopically determined by solving the Darcy's law or its extensions.

While the absolute intrinsic permeability is independent of the fluid, the relative permeability of a phase is defined as the ratio of the phase permeability at a given liquid water saturation to the porous medium intrinsic permeability, thereby, a strong function of porous media microstructural characteristics and fluid properties. In the presence of liquid water, the phase distributions calculated with the pore morphology approach are assumed to be quasi-static as will be described in the Liquid Water Saturation subsection.

iv. Conductivity

Heat transfer through porous materials is a complex simultaneous process of conduction, convection, and radiation. Radiation heat transfer occurs as heat is emitted by the walls of the pores, which requires temperatures greater than 600°C and is hence neglected in thermal analysis of PEFCs operating in low temperatures (<100°C). In addition, convection heat transfer has been proved to be more dominant in pores larger than 100 μm and in temperatures higher than 100°C, which is not the case for the PEFC GDLs, so as to be neglected. Thereby, heat transfer in PEFC GDLs is dominated by conduction, which occurs through solid phase, fluid phase, and interconnected fibers and particles. Temperature gradient, which is a strong function of the cell components' thermal conductivities, is a critical parameter that impacts both water and heat transport mechanisms, and consequently the durability of the cell components. Therefore, detailed thermal analysis and subsequently accurate knowledge on thermal conductivity of cell components, particularly the GDL, is crucial. The GDL thermal conductivity is generally represented by effective thermal conductivity, *i.e.*, a thermo-physical property that takes the contribution of each species' thermal conductivity into effect.

The effective thermal conductivity K_{eff} is macroscopically determined by Fourier's law and by the heat conduction equation in the microscopic space. Heat is transferred through the GDL by conduction in both the solid and pore phases microscopically [55] as follows:

$$\nabla \cdot (K_\vartheta \nabla T_\vartheta) = Q' \tag{2-51}$$

where K_ϑ, T_ϑ, and Q' are the thermal conductivity, temperature defined locally in each phase, and heat source term, respectively. The local thermal conductivities considered for amorphous carbon, graphite, and PTFE are 10.5, 24, and 0.25 W m^{-1} K^{-1} while the values for air and liquid water in the pore space are 0.0262 and 0.606 W m^{-1} K^{-1}, respectively. The source term is taken as zero and only heat transport through conduction is considered to estimate K_{eff}. Hence, Eq. (2-51) is solved for the whole domain in both the IP and TP directions. The temperature and heat flux at the internal interfaces between different materials and phases are continuous and mathematically defined as:

$$T_1 = T_2 \tag{2-52}$$

$$-K_1 \nabla T_1 = -K_2 \nabla T_2 \tag{2-53}$$

The temperature is specified at the two external surfaces in the principal heat flux direction and symmetry boundary conditions are applied at the other four surfaces of the domain. On the macroscopic level, K_{eff} is calculated by solving Fourier's law with known temperature distribution derived from the heat transport equation [55]:

$$j = -K_{eff} \nabla T = \frac{1}{A} \iint_A -K \nabla T \cdot dA \tag{2-54}$$

where j is the superficial heat flux. In the presence of liquid water, the local thermal conductivity of liquid water is added to solve Eq. (2-51).

The PEFC as an electric power source should be engineered with minimum ohmic losses associated with the successive transport of electrons and protons, which are generated within the anode catalyst layer, flowing throughout the cell components. The ohmic losses due to electronic conduction in a fuel cell are a combination of the internal

electrical resistances, which are related to the intrinsic (bulk) characteristics of each individual cell component, and the interfacial electrical resistances, due to the differences in the structural, morphological, and chemical properties of the cell components in contact. GDL as a key component of a unit cell should have high internal electrical conductivity for an efficient electron transport between catalyst layer to flow-field plates and vice versa. Indeed, GDL pore morphology, composition, thickness, and uniformity are the fundamental parameters affecting the GDL internal electrical conductivity. The effective electrical conductivity (σ_{eff}) is calculated by Ohm's law on the macroscopic level and the electric current is governed by Poisson's equation microscopically. The same approach as for K_{eff} is employed. The local electrical conductivity of the amorphous carbon, graphite, and PTFE are 58800, 16667, and 0 S m^{-1}. As both the air and liquid water have negligible electrical conductivity, the pore space is not conducting and considered passive. PTFE is also considered as an insulator.

v. Liquid Water Saturation

In the GDL, the effect of liquid water on the capillary pressure, relative permeability, diffusivity, and conductivity are of particular interest. The quasi-static phase distribution of water and air is evaluated in this work as a function of capillary pressure using the pore morphology approach [148,149]. In the pore morphology model, the stationary distribution of the wetting phase (WP) and non-wetting phases (NWP) is calculated using the capillary pressure defined by the Young-Laplace equation:

$$P_c = \frac{2\gamma cos\theta_c}{r} \tag{2-55}$$

where γ is the surface tension, r pore radius, and θ_c contact angle. Initially, the entire GDL is filled with the WP (air) and the capillary pressure is zero. The pore volume is then eroded by NWP spheres with increasing radius, starting from the smallest radii, while the Young-Laplace equation is used to calculate the corresponding capillary pressure in each step. It is assumed that the interface between the WP and NWP is of spherical shape or by a superposition of spheres. In the case of a simulated drainage experiment, one surface of the GDL is connected to a NWP reservoir and the opposite surface to a WP reservoir. In order for a pore to be filled with NWP at a specific capillary pressure, it must have a pore size

larger than $2\gamma cos\theta_c {P_c}^{-1}$ and a continuous NWP filled pathway to the NWP reservoir. Meanwhile, in the case of imbibition, NWP may imbibe any pore that is large enough to satisfy the first criterion. Considering that the pore morphology method is based on a quasi-static two-phase gas-liquid distribution, the static contact angle expressed in Eq. (2-55) is an important parameter indicating the surface wettability characteristics of a porous medium. Static contact angle is the angle formed at the interfaces of solid, liquid, and gas phases under static conditions which is a strong function of the medium's surface roughness and energy. Therefore, the surfaces are categorized into hydrophobic surfaces with low wettability and contact angle higher than 90° and hydrophilic surfaces with high wettability and contact angle lower than 90°. Noting that, the Young correlation, by which the static contact angle is determined, is ideally derived for smooth surfaces even though the surface roughness has a significant impact on the static contact angle of unsmooth surfaces [3,11,13]. Measured values for θ_c vary significantly for different experimental techniques, including sessile drop, MIP, and capillary rise (Wilhelmy) methods [18,113,150–152]. Mortazavi *et al.* [151] observed that applying 10% wt. PTFE on a raw GDL substrate increases the contact angle from (130±10)° to (150±5)° based on the sessile drop method. Other measurements indicate that the contact angle does not change considerably between a low PTFE loading of 5-10% and a high loading of 30-40% [113,152]. Notably, however, the GDL substrate features mixed wettability after PTFE treatment which impacts liquid water transport and cannot be observed with the aforementioned experimental methods. Sinha *et al.* [80] found that liquid water flows through a connected hydrophilic network and thereby suppresses the finger like morphology observed in a wholly hydrophobic GDL substrate in their pore network model. In the present work, a fully hydrophobic structure is assumed which is consistent with the choice of the pore morphology method. A comprehensive sensitivity study is conducted to observe the effect of contact angle on capillary pressure, *cf.* section 2.3.2. In this case, static contact angle is taken as 130° and 150° for untreated and PTFE treated Toray TGP-H GDL substrate, respectively. Figure 2.23 shows the simulated distribution of liquid water in non-teflonated GDL substrate model obtained by imbibition for different saturation levels of 0.35 and 0.78. Imbibition is expected to be the most relevant liquid water saturation

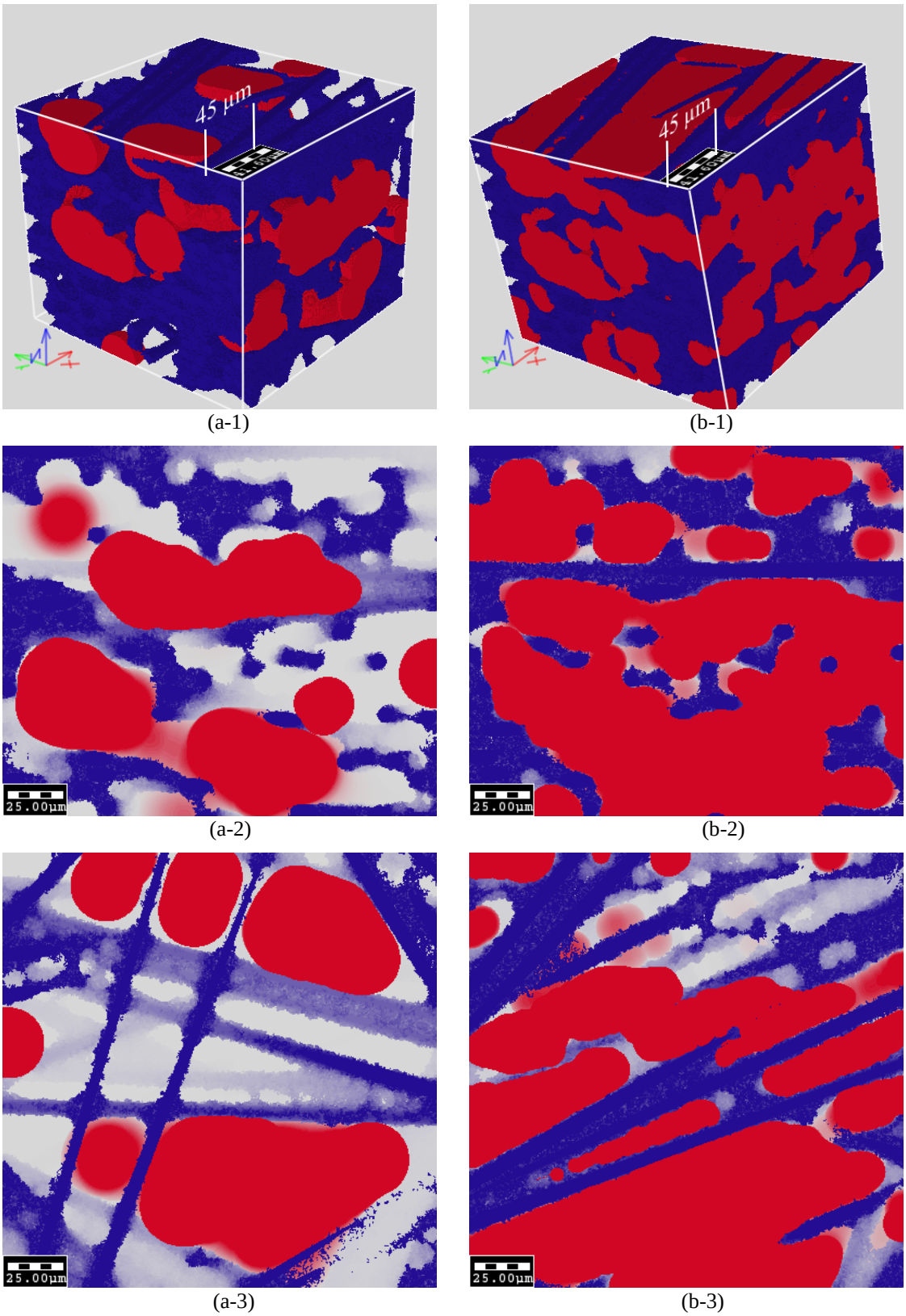

(a-1) (b-1)

(a-2) (b-2)

(a-3) (b-3)

Figure 2.23. Simulated liquid water distribution of non-teflonated Toray TGP-H GDL substrate model at (a) 0.35 and (b) 0.78 saturation levels in (1) 3D, (2) cross-sectional, and (3) top views.

process for GDLs considering that water is imbibed into it via the cathode catalyst layer and/or may condense due to vapor transport from the same.

Considering the mobility of water droplets during cell operation, it is worth mentioning that the wettability characteristics of the surfaces should be determined where the droplets are in motion, *i.e.*, dynamic wettability. The dynamic wettability is quantitatively measured by sliding contact angle which represents the critical surface angle at which the droplet on the surface starts sliding down. A lower sliding angle indicates a more-hydrophobic surface at which a liquid droplet is more likely to slide down at a lower sliding angle [3,11,13].

2.3. Results and Discussion

Microstructural GDL substrate models are stochastically generated and validated using the framework described in subsection 2.2.1 for a standard Toray TGP-H carbon paper at four typical PTFE loadings, *i.e.*, 0, 10, 20, and 30% wt. Upon structural validation, the transport properties in the solid and pore phases of the untreated GDL substrate are simulated and compared with in-house experimental data to extend the validation. Subsequently, the anisotropic transport properties are simulated under a range of liquid water saturation levels, *i.e.*, 0, 20, 40, 60, 80, and 100% non-wetting phase and the results are thoroughly analyzed and applied to develop new transport property correlations. The simulated data reported here are averages of ten stochastic structures and the variability is indicated by 95% confidence intervals.

2.3.1. Dry Conditions

i. Effective Diffusivity

The variation of effective diffusivity in the present model versus the porosity as a result of adding PTFE to the bare GDL substrate is illustrated in Figure 2.24 and compared with empirical correlations available in the literature; as summarized in Table 1.5; and in-house measured data. Both through-plane (TP; z) and in-plane (IP; x and y) properties are considered in the three principal directions of diffusion. As anticipated, increasing the

PTFE content decreases the average porosity of the GDL substrate by covering areas that were previously available for gas diffusion, and the effective gas diffusivity is consequently reduced in all three principal directions. The trends exhibited by the simulated data are in good agreement with the corresponding *ex-situ* measured TP data, although the measured GDL substrate batch had lower porosity than the Toray specification of 78% used for the model. The simulated results reveal that the preferential IP orientation of the fibers results in IP-oriented connected pores with enhanced diffusive capabilities. On average, the IP diffusivities are ~50% larger than the TP diffusivities due to the dominant IP fiber orientation. In addition, the reduction of TP diffusivity as a result of adding PTFE is higher compared to the IP direction. This is a direct result of increased tortuosity, which is less significant in the IP direction. Thus, PTFE mainly reduces the TP interconnectivity of the pores and magnifies the diffusional anisotropy of the material. Overall, although PTFE treatment is essential for water management, it may also interfere with the diffusion and increase gas transport losses in GDL substrates. Accurate information on diffusive properties is therefore important when selecting PTFE loading for GDL substrate prototyping assignments and optimization studies.

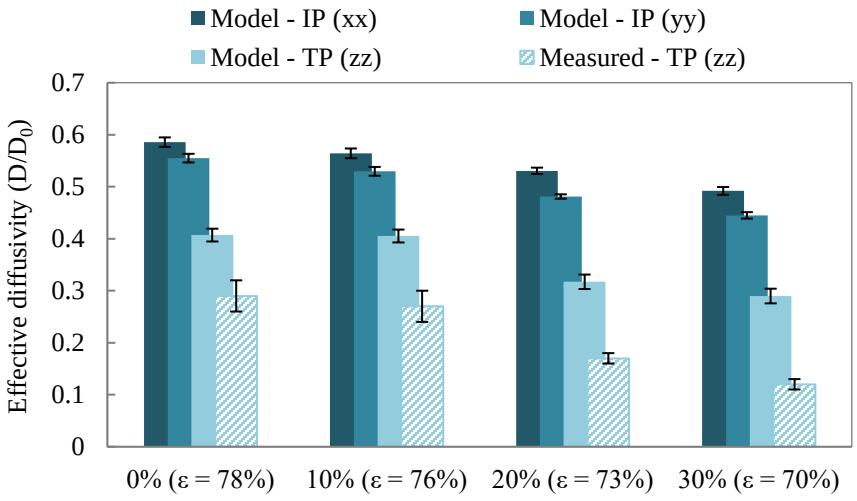

Figure 2.24. Simulated IP and TP effective diffusivity of Toray TGP-H GDL substrate stochastic model compared with measured TP data in different % wt. PTFE.

Table 2.4. Simulated effective diffusivity of Toray TGP-H GDL substrate stochastic model compared with empirical correlations [49,50,52] in different % wt. PTFE.

	Ref. [49]	Ref. [50]	Ref. [52]	Model	Direction
ε = 0.78 (0%)	0.68	0.5	0.67	0.57±0.008	IP
			0.62	0.41±0.013	TP
ε = 0.76 (10%)	0.65	0.47	0.64	0.55±0.009	IP
			0.59	0.40±0.012	TP
ε = 0.73 (20%)	0.62	0.45	0.60	0.51±0.005	IP
			0.54	0.31±0.013	TP
ε = 0.70 (30%)	0.57	0.41	0.55	0.47±0.007	IP
			0.49	0.29±0.014	TP

Established empirical correlations; summarized in Table 1.5; are compared with the numerical data in Table 2.4 in order to put the simulated and measured results into context; however, none of the empirical correlations account for binder or PTFE influences. It can be seen that the spherical agglomerate model by Bruggeman [49] predicts the highest diffusivity while the more realistic fiber model of Tomadakis and Sotirchos [52] results in smaller, anisotropic values. Mezedur *et al.* [50] fitted their lattice network to experimental data, and the results are comparable to the present IP diffusivity results. However, it is noteworthy that the present microstructural modeling results, when compared to commonly employed empirical correlations, are considerably more accurate with the detailed results (TP, IP, binder, PTFE impact) more closely resembling the physical materials and measured data.

ii. Intrinsic Permeability

The effect of PTFE loading on the simulated intrinsic, single phase IP and TP viscous permeability and comparison with the corresponding in-house measured *ex-situ* data are shown in Figure 2.25. As expected, the permeability decreases slightly with increasing PTFE loading due to the filling of pores originally available to participate in convective transport. This implies that the flow resistance of the gas phase increases as the porosity decreases. Similar to the diffusivity results, the permeability is higher in the IP direction than the TP direction due to the preferential fiber alignment in the *xy*-plane and larger connected pathways for the flow. Both simulated and measured data are approximately a factor of three higher in the IP direction than TP. Although the measured TP data are in some cases restricted by the maximum flow rate of the measurement tool, the observed values and trends are consistent with the simulated results. The small

deviations are likely a result of the material variability and lower overall porosity of the physical samples used for the measurements. Overall, the simulated results are in good agreement with the measured data, and the modeling framework again demonstrates higher accuracy and versatility in relation to existing empirical correlations for the intrinsic and relative permeability of porous media as summarized in Table 1.6. For instance, the permeability obtained using the Kozeny-Carman [54] and Tomadakis-Robertson [48] correlations was 7.47 and 12.41 darcy, respectively, which does not capture the large differences observed between the IP and TP directions. A sensitivity study is conducted to observe the accuracy of the model by considering the Navier-Stokes equation as the flow field and assuming a pressure drop of 1 kPa across the GDL substrate. The IP (*xx*), IP (*yy*), and TP (*zz*) permeability of the untreated GDL substrate is derived as 17, 19, and 8 darcy which verifies the accuracy of using Stokes equation for creeping flow within 5-7% error.

iii. Thermal Conductivity

Heat transfer through porous materials is a complex process comprising conduction, convection, and radiation. However, heat transfer in GDLs is presumed to be dominated by conduction, which occurs in both solid and pore phases. As shown in Figure 2.26, the simulated effective thermal conductivity (K_{eff}) of the non-teflonated GDL

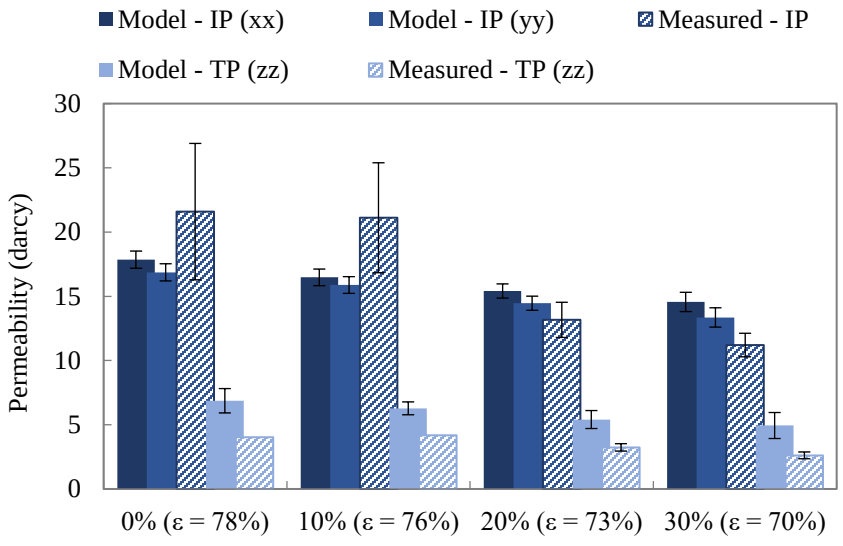

Figure 2.25. Simulated IP and TP permeability of Toray TGP-H GDL substrate stochastic model compared with measured data in different % wt. PTFE.

substrate model is about 5.3 and 18 W m^{-1} K^{-1} in the TP and IP directions, respectively, and increases marginally with PTFE loading. The specific thermal conductivity of PTFE (0.25 W m^{-1} K^{-1}) is higher than air but low relative to carbon and graphite materials (10.5 and 24 W m^{-1} K^{-1}, respectively), and the small increase can therefore be attributed to replacing air with PTFE in the stochastic model. Again, K_{eff} is highly dependent on the fiber distribution, and the IP value is approximately 3-4x higher than the TP value, which is an important consideration for both GDL and MEA design. The present results are in good agreement with analytical data [40] in the IP direction; however, the results are 2-3x higher than the Toray specification and measured data [153] in the TP direction. The difference between the simulated and measured TP results is attributed to thermal contact resistance (TCR), which can contribute up to 65-90% of the measured thermal resistance of the GDL substrate [154] but is not captured by the present model. TCR studies involving porous materials can be relatively complex and are beyond the scope of this work. The simulated IP K_{eff} results are comparable to the maximum and minimum K_{eff} of the empirical correlations developed by Hashin and Shtrikman [61] and Kaviany *et al.* [55] which are 15.8 and 18.3 W m^{-1} K^{-1}. A summary of the available correlations is provided in Table 1.8. However, in contrast to the present modeling approach, the empirical correlations are not capable of capturing the strong anisotropy of the GDL substrate.

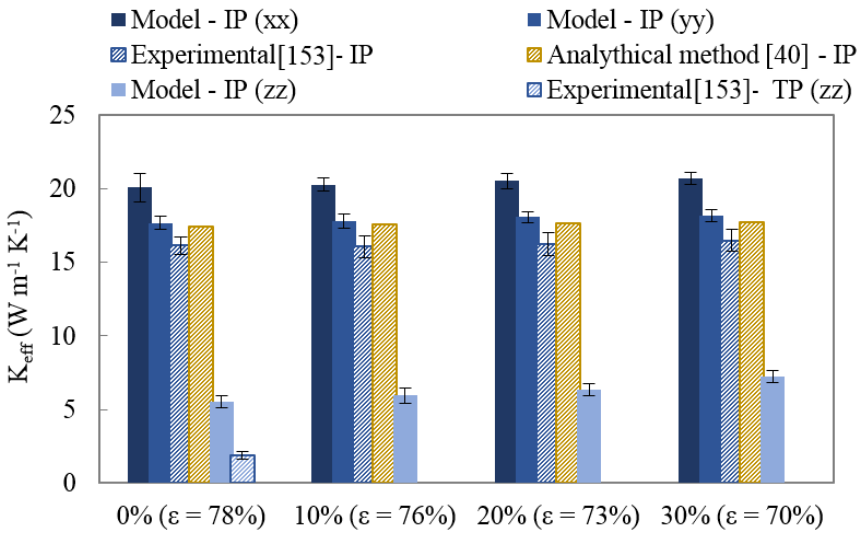

Figure 2.26. Simulated IP and TP effective thermal condictivity of Toray TGP-H GDL substrate stochastic model compared with literature data [40,153] in different % wt. PTFE.

iv. Electrical Conductivity

The effective electrical conductivity σ_{eff} of the GDL substrate is estimated by simulation of steady state electrical conduction in the solid phase of the microstructural models. Figure 2.27 illustrates the obtained σ_{eff} as a function of PTFE loading. The simulated TP electrical conductivity is approximately 600 S m^{-1} and the IP property is 4x higher due to the anisotropic fiber alignment. As a result of the low electrical conductivity of PTFE, the simulated results are essentially independent of PTFE loading. The in-house measured TP data are significantly lower as a consequence of contact resistance between the tool and the sample. Although there is limited experimental verification of anisotropic σ_{eff} in the literature [155], it has been demonstrated that the IP electrical conductivity is about an order of magnitude higher than the TP conductivity [110]. High IP conductivity is essential to achieve a uniform current density distribution in the catalyst layers relative to the land/channel and along-the-channel directions [156].

2.3.2. Wet Conditions

The simulated GDL substrate transport properties presented in the previous section are relevant for fuel cell operation at dry conditions. However, provided that PEFCs

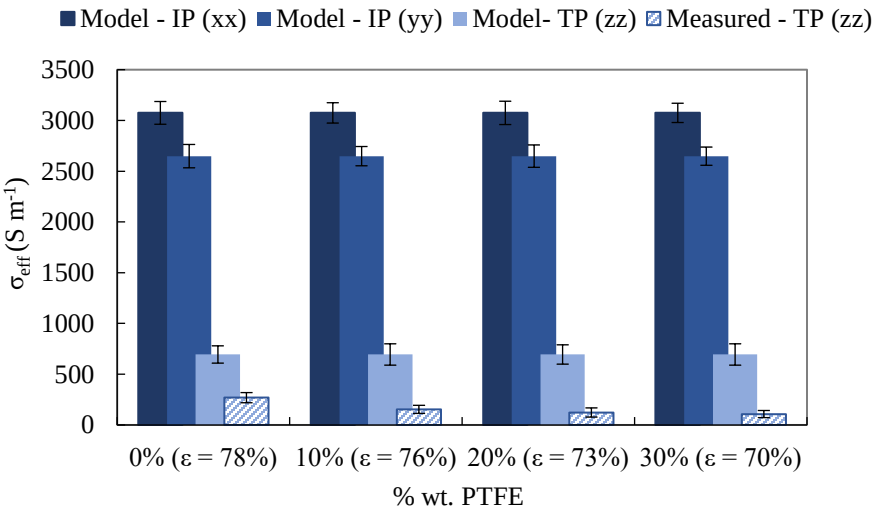

Figure 2.27. Simulated IP and TP effective electrical conductivity of Toray TGP-H GDL substrate stochastic model compared with measured data in different % wt. PTFE.

produce water during operation and typically run at low temperature and fully humidified conditions, the presence of liquid water in the GDL substrate must also be considered. This section therefore presents a complete set of simulated GDL substrate transport properties as a function of PTFE content and liquid water saturation for the Toray TGP-H GDL substrate that can be used more generally in the context of GDL and MEA design for fuel cell operation under wet conditions.

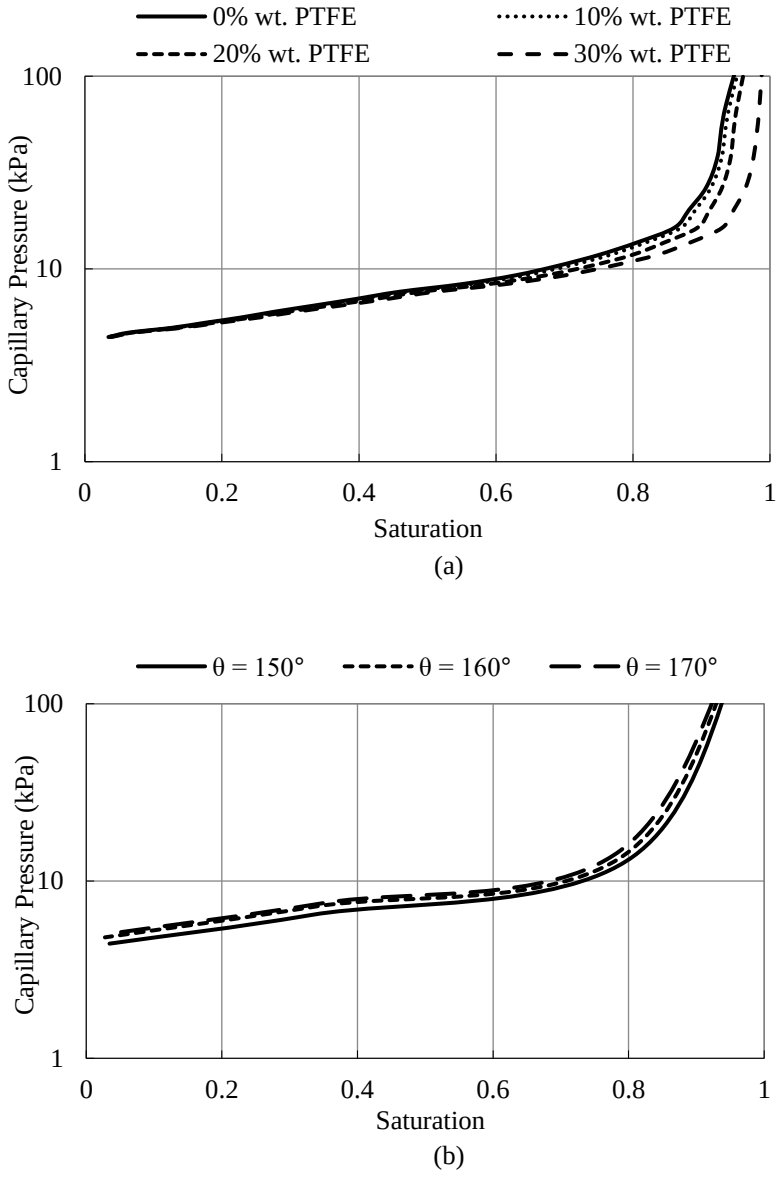

Figure 2.28. Simulated capillary pressure curves as a function of liquid water saturation of Toray TGP-H GDL substrate stochastic model for different (a) % wt. PTFE and (b) contact angles.

i. Capillary Pressure

Figure 2.28(a) presents the simulated capillary pressure variation in the GDL substrate versus the liquid water saturation in the case of imbibition. The simulated percolation path diameter for the non-teflonated GDL substrate model is approximately 20 µm and equivalent to a TP tortuosity of ~2. Simulations for larger contact angles (160° and 170°; Figure 2.28(b)) for the case of 30% PTFE yield similar results albeit higher capillary pressures are required to reach the same saturation level. The overall impact of PTFE loading and contact angle on the capillary pressure curves appears to be minor except at very high saturation levels above 80%.

ii. Relative Diffusivity

The relative gas diffusivity is an important transport property that demonstrates the capability of the GDL to support reactant gas transport to the active sites in the presence of liquid water. The water situated in (or moving through) the GDL limits the rate of gas diffusion compared to dry conditions. Therefore, the amount of water should be controlled for optimum reactant diffusion through the GDL. The simulated relative diffusivity of the non-teflonated GDL substrate is illustrated in Figure 2.29 as a function of liquid water saturation. As can be expected, the relative diffusivity decreases with increasing saturation as the pores available for gas diffusion are gradually filled with liquid water. The simulated results are consistent with previously established empirical correlations for diffusion as a function of porosity in the IP direction; however, a notable difference is found in the TP direction.

As briefly discussed for diffusion under dry conditions (subsection 2.3.1), while the empirical correlations are reasonably accurate for IP properties, the present model is expected to provide considerably more realistic results in the TP direction. In addition, the relative diffusivity is more significantly reduced in the TP direction compared with the IP direction due to the higher tortuosity in the presence of water. A saturation of 0.5, for instance, is found to reduce the diffusivity by more than 80% from approximately 0.4 in the dry state to 0.08, which is of great significance in the context of fuel cell design and operation. Unfortunately, relative diffusivity is challenging to measure, and scarce

experimental data are available for comparison [34]. The TP data obtained by Hwang and Weber [34] using an electrochemical limiting-current method are used to evaluate the modeling results in Figure 2.30. Overall, the simulated results are shown to be in good agreement with the measured data, which validates the present approach. At the same time, the lack of data further justifies the usefulness and application of the present stochastic modeling approach and results. A new correlation is therefore proposed in Eq.(2-56) based on the present numerical data to estimate the TP effective gas diffusivity of carbon paper based GDL substrate as a function of saturation s and % wt. PTFE ω_T as follows:

$$D_{eff,TP} = (23.65\omega_T + 5.17)s^2 + (-6.77\omega_T - 4.25)s - 0.23\omega_T + 0.88 \qquad (2\text{-}56)$$

The correlation represents the trends observed in the numerical data with the coefficient of determination R^2 of 0.96 as follows:

$$R^2 = 1 - \frac{SS_{err}}{SS_{tot}} \qquad (2\text{-}57)$$

where SS_{err} is the error sum of squares and SS_{tot} is the total sum of squares.

The hydrophobic treatment which is necessary to improve the water management can also impede gas diffusion by reducing the porosity and increasing the tortuosity of the GDL substrate. Figure 2.30 determines the combined effect of PTFE loading and liquid water saturation on relative TP gas diffusivity. Decreasing the porosity by adding PTFE results in even lower gas diffusivity than for the non-teflonated material under wet conditions and must also be taken into account for accurate predictions of effective diffusivity during fuel cell operation. Furthermore, the obtained curves are found to be nonlinear functions of saturation; *i.e.*, the diffusivity drops more rapidly than the gas phase porosity at low saturation levels. Overall, the simulated results are expected to provide a reasonable estimation of the true gas diffusivities in wet conditions during fuel cell operation and can be used as a guide for GDL and MEA design.

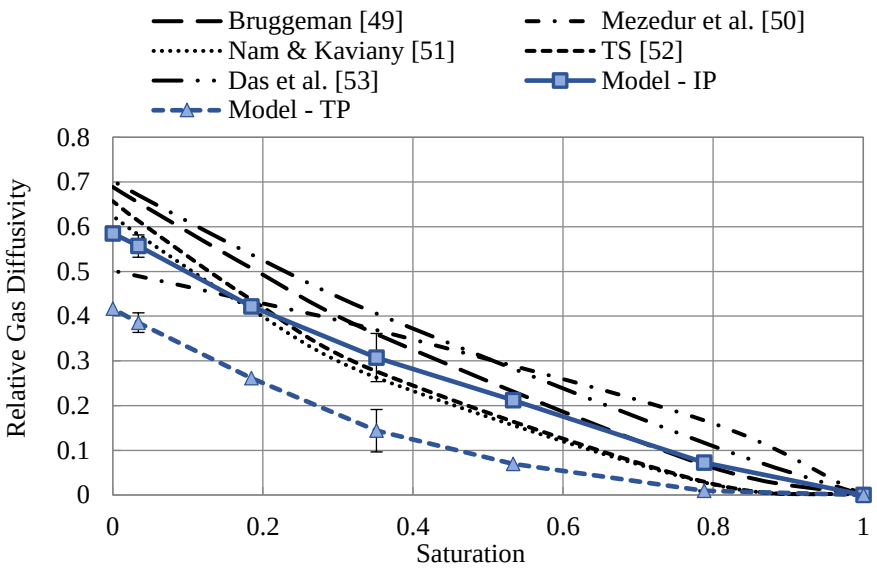

Figure 2.29. Simulated relative IP and TP gas diffusivity for the non-teflonated Toray TGP-H GDL substrate as a function of liquid water saturation compared to empirical correlations [49–53].

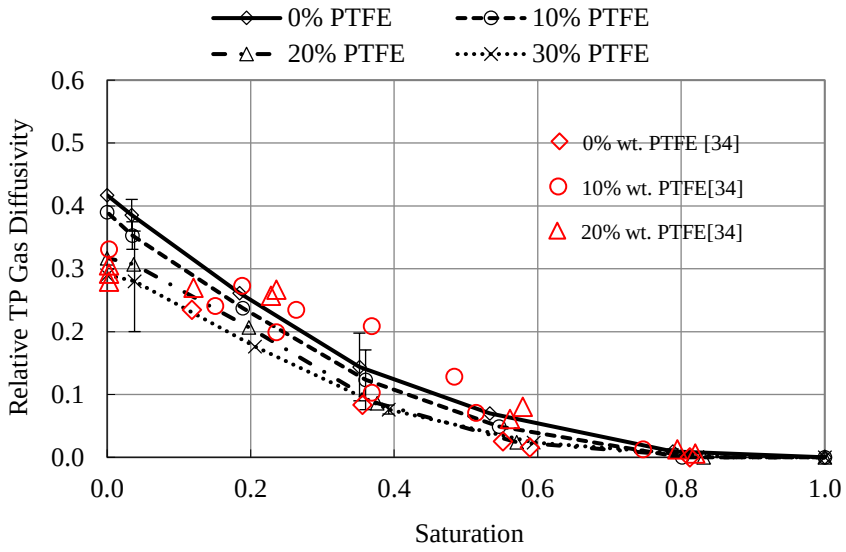

Figure 2.30. Simulated relative TP gas diffusivity for the Toray TGP-H GDL substrate as a function of liquid water saturation in different % wt. PTFE compared to experimental data [34].

iii. Relative Permeability

The oversaturated condition usually occurs in cathode electrode under normal fuel cell operation in which liquid water generation exceeds the vapor saturation. Therefore, water management is crucial which requires low resistive-to-flow or high gas-permeable porous electrodes, more importantly in modern automotive PEFCs operating at high

current density conditions. Indeed, an effective water management happens when the positive pressure gradient or the capillary pressure, which results in the counter-flow liquid water transport, prevails over the negative pressure gradient, which leads the convection gas-phase transport, between the two sides of the cathode electrode. In case of low GDL gas permeability, a high negative pressure gradient is induced across the electrode based on Darcy's law of convection in porous media, which results in high saturation levels within the GDL. It consequently causes water flooding which hinders the oxygen transport by blocking the pathways from the cathode channels to the catalyst layer. Therefore, in the presence of liquid water in the GDL, the need for estimation of gas and liquid phase pressures leads to calculation of the relative permeability of both phases.

The simulated relative permeability of the NWP (water) and WP (gas) of Toray TGP-H GDL substrate as a function of saturation and PTFE loading is given in Figure 2.31. Decreasing WP permeability and increasing NWP permeability with increasing saturation is demonstrated, and order-of-magnitude changes in permeability are readily seen due to the competition for pore space available for the flow. The relative permeability is found to be zero under certain conditions, indicating that no continuous percolation path exists for the given phase due to the prevalence of the opposite phase. This occurs in the gas phase

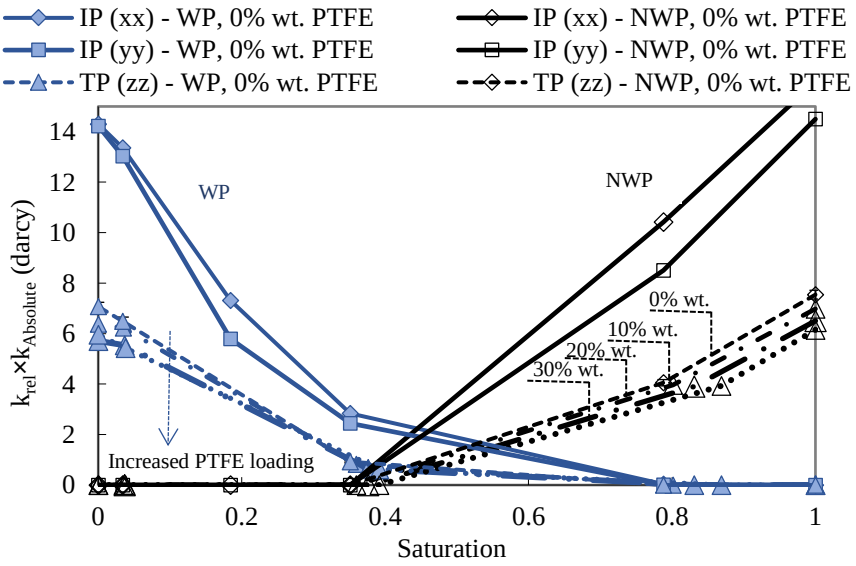

Figure 2.31. Simulated relative IP and TP permeability of the Toray TGP-H GDL substrate as a function of liquid water saturation in different % wt. PTFE for the wetting (WP) and non-wetting (NWP) phases.

when the saturation level reaches 0.8 and in the liquid phase for saturations less than 0.3. The effect of PTFE loading on the TP relative permeability of liquid and gas phases for the Toray TGP-H GDL substrate is also illustrated in Figure 2.31. The relative permeability decreases overall when PTFE is added and the sensitivity to saturation is moderately reduced. New correlations are proposed based on these data for the TP relative permeability of the WP and NWP in Eqs. (2-58) and (2-59), respectively:

$$k_{rel,WP,TP} = (16.95\,\omega_T - 15.26)s^3 + (-33.97\omega_T + 36.66)s^2 + (21.23\omega_T - 28.52)s + (-4.16\omega_T + 7.13) \quad (2\text{-}58)$$

$$k_{rel,NWP,TP} = (-3.97\omega_T + 11.48)s^2 - (1.162\omega_T + 3.99)s + (0.11\omega_T + 0.05) \quad (2\text{-}59)$$

Figure 2.32 depicts a comparison of the predictions using the present approach, the experimental data reported in the literature [78,157–162], and the empirical correlations of Power law [55], Brooks Corey (BC) [56], and Van-Genuchten (VG) [57]. The good agreement between the data verifies the validity of the model for gas and water relative permeabilities of carbon-paper GDL substrates.

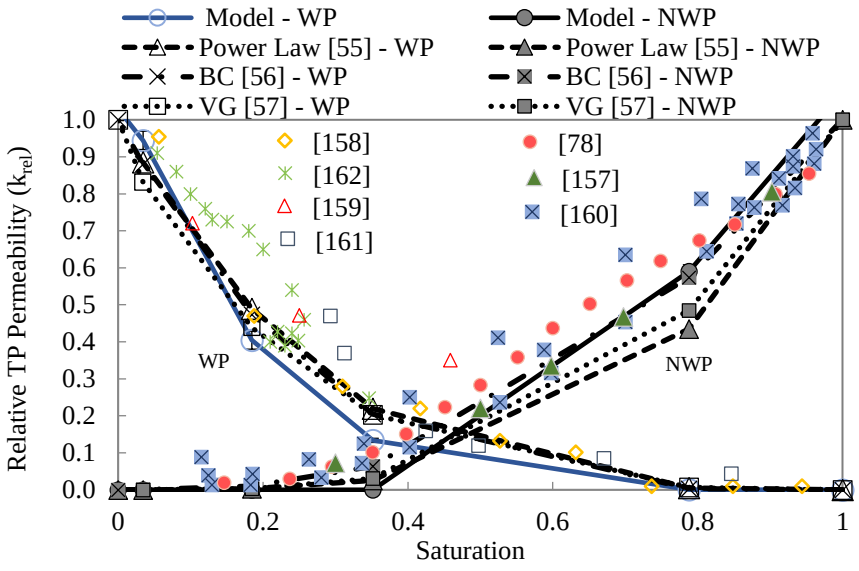

Figure 2.32. Simulated relative TP permeability of the non-teflonated Toray TGP-H GDL substrate as a function of liquid water saturation compared to empirical correlations [55–57] and experimental data [78,157–162].

iv. Thermal Conductivity

While the electrical conductivity of the GDL substrate is independent of liquid water saturation, it is interesting to evaluate the effective thermal conductivity under wet conditions due to the relatively high thermal conductivity of liquid water. Figure 2.33 presents the numerical results for the TP thermal conductivity as a joint function of liquid water saturation and PTFE loading and a new correlation is proposed in Eq. (2-60) based on these data for the TP thermal conductivity:

$$K_{eff,TP} = (-0.162\omega_T + 0.422)s^2 + (-0.287\omega_T + 0.525)s + (0.234\omega_T + 0.477) \quad (2\text{-}60)$$

The rise in K_{eff} obtained by increasing the water saturation is significant. The present results indicate that the TP property in the fully saturated state is nearly 3x higher than in dry conditions. The liquid water is found to decrease the thermal resistance between the fibers and hence increase the rate of heat conduction. Scarce literature data are available for the effect of liquid water on the K_{eff} of GDL substrates. Burheim *et al.* [163] measured the TP K_{eff} of a similar carbon paper having a liquid water saturation of 0.26 to be 0.57 ± 0.06 W m^{-1} K^{-1}. The present results are in good agreement with this measurement as the simulated K_{eff} at 0.26 saturation is approximately 0.6 W m^{-1} K^{-1}, which is within the

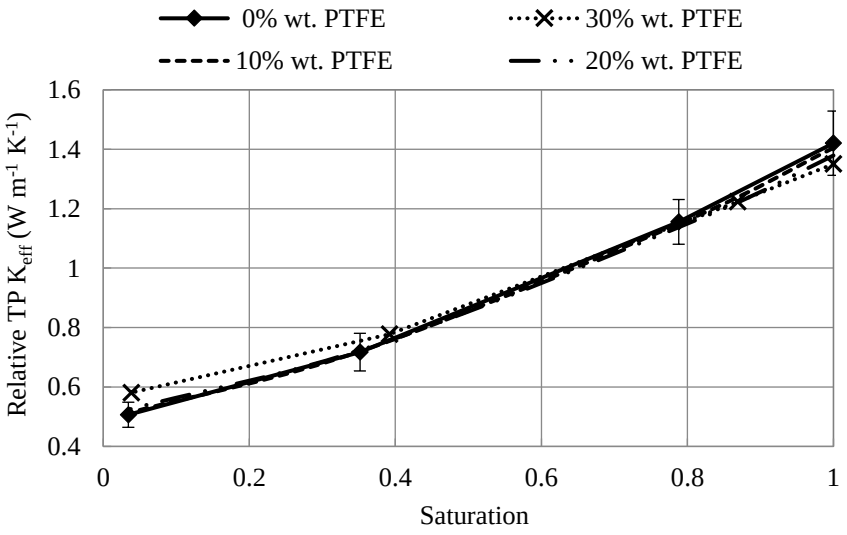

Figure 2.33. TP effective thermal conductivity of the Toray TGP-H GDL substrate as a function of liquid water saturation in different % wt. PTFE.

measured uncertainty range. The coupled effect of adding PTFE and liquid water is also noteworthy: at low saturation levels, the PTFE loading has a positive effect on K_{eff}, while at high saturation levels, the effect is opposite. Overall, the effect of liquid water is much more significant due to its higher thermal conductivity, and the simulated K_{eff} trend with saturation is an important contribution of the present work that may have significant impact on the thermal engineering of fuel cells.

2.4. Summary

A unique stochastic microstructural GDL substrate modeling framework was developed and thoroughly validated for carbon-paper GDL substrates. The modeling framework utilized manufacturing information and a virtual stochastic modeling scheme to provide an accurate realization of carbon fibers, binder, and PTFE components and subsequently employed various numerical algorithms for the simulation of effective transport properties in all three principal axes. A complete set of anisotropic transport properties for both gas and liquid phases was determined over a range of PTFE loadings under both dry and partially saturated conditions. The simulated properties were validated using measured *ex-situ* data and discussed with consideration given for existing theoretical formulations and literature data. The overall trends predicted by the simulations are in good agreement with the measured data and the modeling framework was found to accurately represent the transport characteristics of the physical GDL substrate porous material.

The numerical results of the developed modeling framework were used to examine the capabilities of established theoretical and empirical approximations for diffusivity, permeability, and thermal conductivity. However, while most diffusion correlations are reasonable in the in-plane direction, they are relatively unreliable for through-plane diffusion in anisotropic materials such as GDL substrates. Here, the present microstructural modeling framework was more reliable and capable of simulating properties that more closely resemble those of the actual material. New correlations were hence proposed for carbon-paper GDL substrates by considering the simulated data as a function of saturation and PTFE.

The presence of liquid water was determined to act as a barrier to gas diffusion and affected the gas phase porosity of the GDL substrate. Interestingly however, liquid water was also found to reduce the thermal resistance between the fibers and significantly increase the effective thermal conductivity. The new saturation dependent correlations proposed for these transport properties are therefore an important contribution of this work, as previous empirical correlations were either nonexistent (thermal conductivity) or shown to be inaccurate in the critical through-plane direction (diffusivity). With regards to the PTFE loading, the simulated results demonstrated an important trade-off between enhanced hydrophobicity and reduced gas diffusivity and permeability which must be considered and optimized in the GDL substrate design and manufacturing processes. In closing, the microstructural modeling framework developed and validated in this work is expected to become a reliable and versatile tool for GDL substrate design and prototyping assignments and can potentially reduce the time and cost of the MEA and fuel cell design cycles for future applications.

Chapter 3.

Microporous Layer Characterization and Microstructural Modeling

In modern automotive PEFCs operating at high current density conditions, the concurrent needs for water management and gas diffusion drive the design of the porous materials in the MEA. The presence of an MPL is critical in this context for satisfactory fuel cell performance at high current densities. This highlights the need for a comprehensive design tool to reconstruct a variety of MPLs with different pore morphology compositions, *i.e.*, particle type, size, thickness, PTFE content, and the number of MPLs, to study the influence of MPL morphology on GDL transport properties and ultimately fuel cell performance. For this purpose, a comprehensive stochastic microstructural modeling design tool is developed in this chapter inspired by manufacturing information and characterization data to reconstruct the MPL microstructure by distinguishing between carbon or graphite particles and PTFE for different MPL compositions. Furthermore, a parametric study is conducted to investigate the effect of MPL compositions on the transport properties, *i.e.*, effective diffusivity, permeability, and electrical and thermal conductivities. Since the delicate MPL layer is not a stand-alone layer and hence difficult to characterize experimentally, the numerical modeling is a compelling approach to obtain a comprehensive understanding of these properties. This serves as a reliable tool to correlate between the MPL real pore morphology composition and transport properties for material optimization and fuel cell design.

This chapter is structured as follows. Firstly, the MPL-coated GDL manufacturing process steps as well as extensive qualitative and quantitative characterization of MPL pore morphology with SEM images, particle size distribution with laser diffraction measurement, and pore structure with MIP are described in section 3.1 for the MPLs under study. Furthermore, considering that the MPL is not a stand-alone layer, a technique is developed in this section to extract the MPL MIP PSD data. Section 3.2.1 establishes a novel framework to stochastically reconstruct the microstructure of the MPLs under study

and the algorithm is diagrammatically illustrated in subsection 3.2.1v. In section 3.2.2i, a detailed qualitative and quantitative microstructural validation of MPLs under study is conducted with measured SEM images, porosity, and pore and particle size distributions. To further validate the pore structure of the MPL models, a customized 3D morphological MPL characterization framework developed by FCReL featuring a customized FIB-SEM imaging reconstruction technique is conducted in subsection 3.2.2ii. The effect of MPL particle type and size on its transport properties, *i.e.*, diffusivity, tortuosity, permeability, and thermal and electrical conductivities, are investigated and thoroughly elaborated in detail later in section 4.3 of Chapter 4.

3.1. MPL Morphology and Pore Structure Characterization

A conventional MPL is a porous carbon-based material typically comprised of carbon and hydrophobic agent agglomerates. The distribution of carbon agglomerates and hydrophobic agent, which directly affects the MPL pore shape, size, and wettability, strongly depends on the MPL manufacturing and heat treatment processes [110,164]. The conventional MPL manufacturing process involves three consecutive steps including: a) preparation of the homogeneous slurry by *mixing and stirring* the MPL ink components and subsequently; b) *coating* the ink on a GDL substrate followed by; c) *sintering* and other heat-treatment processes as graphically depicted in Figure 3.1[9]. The MPL ink is typically made of carbon or carbon-like materials, *e.g.*, acetylene black (AB) (42 nm, 51 m^2 g^{-1}) [109], Vulcan XC-72R (30 nm, 250 m^2 g^{-1}) [165,166], or black pearls 2000 (BP2000) (15 nm, 475 m^2 g^{-1}) [167] and hydrophobic agent, *e.g.*, PTFE or Polyvinylidene Fluoride (PVDF) [168,169] dispersed in an alcohol-based solution. Other types of carbon particles such as pelletized carbon black [170], carbon nanotubes (CNTs) [171], amorphous or flake graphite [172], commercial graphene[10] [173,174] or synthetic electrochemically exfoliated graphene (EGN) [175] can also be used as alternatives to conventional MPLs for next-generation fuel cells. Due to vulnerability of most of these materials to oxidative corrosion, graphitized particles are also used as promising alternatives where graphitization changes

[9] Reprinted from [11] with minor modifications with permission from Elsevier.

[10] Graphene: a monolayer of carbon atoms arranged in a two-dimensional honeycomb lattice.

the amorphous carbon structure to crystalline lamellar graphite, resulting in higher oxidative resistance relative to amorphous carbon [110,176]. Spraying and screen-printing methods are the most widely used MPL coating techniques in the GDL manufacturing process [11,110,164]. In the final step, the MPL-coated GDL is sintered at stepwise elevated temperature to uniformly distribute the PTFE inside the MPL porous structure and adhere the MPL material to the GDL substrate; a crucial step for imparting homogeneous surface characteristics. Not only the manufacturing and heat treatment processes but also the MPL composition, *i.e.*, carbon particle and hydrophobic agent type, size, and weight fraction, directly affect the MPL morphology and pore structure and consequently the MPL-coated GDL transport properties which thereby influence the overall fuel cell performance [13,164]. For instance, the MPL thickness shows a great variation, typically between 10 and 100 μm, depending on the manufacturing process and the aforementioned parameters [11].

The MPL morphology can be determined utilizing qualitative characterization techniques with the commonly used 2D and 3D imaging apparatuses as summarized in Table 1.3. In this work, the MPL morphology is observed by utilizing optical microscopy and scanning electron microscopy as the measured cross-sectional and surface view SEM images of an MPL-coated GDL are illustrated in Figure 3.2 and Figure 3.3, respectively. It is perceived that the MPL has distinctively dissimilar morphology and microstructure compared to the GDL substrate, *i.e.*, a more compact porous structure with no visible open pores as well as interconnected surface cracks ranging from 5 to 15 μm in width. Thereby,

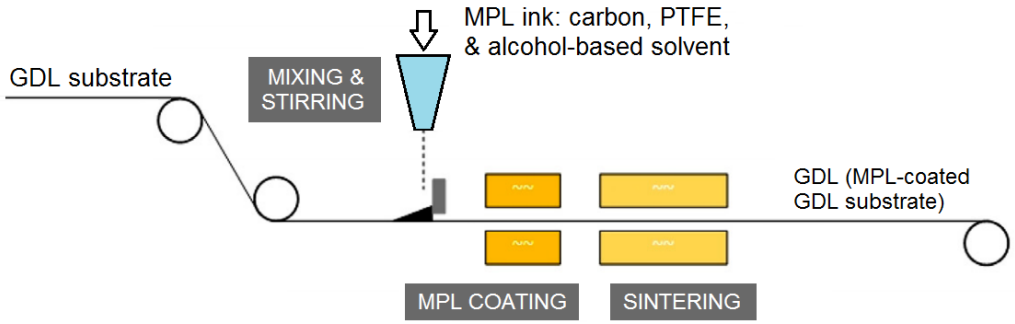

Figure 3.1. Graphical illustration of manufacturing process route for producing PEFC gas diffusion layer (MPL-coated GDL) in continuation of the GDL substrate manufacturing process in Figure 2.1 adapted from [11,110].

the MPL compact porous structure diminishes the electrical interfacial resistance by providing enhanced mechanical support for the catalyst layer. According to the literature, localized thinning of the CL was observed where it is in direct contact with the carbon fibers which leads to MEA degradation, hence, the MPL may also enhance durability compared to the MEA with no MPL [176]. Furthermore, as stated before, the MPL structure is comprised of small-scale carbon powder and hydrophobic agent agglomerates several orders of magnitude smaller than the open pores of the GDL substrate. Thereby, during the MPL coating, which in most cases is a wet coating process [110], the MPL is observed to form a distinct layer on the GDL substrate that also partially penetrates its comparatively larger pores, thus, forming an uneven MPL-penetrated layer profile. As a result, the GDL substrate architecture is modified by lessening the volume of the

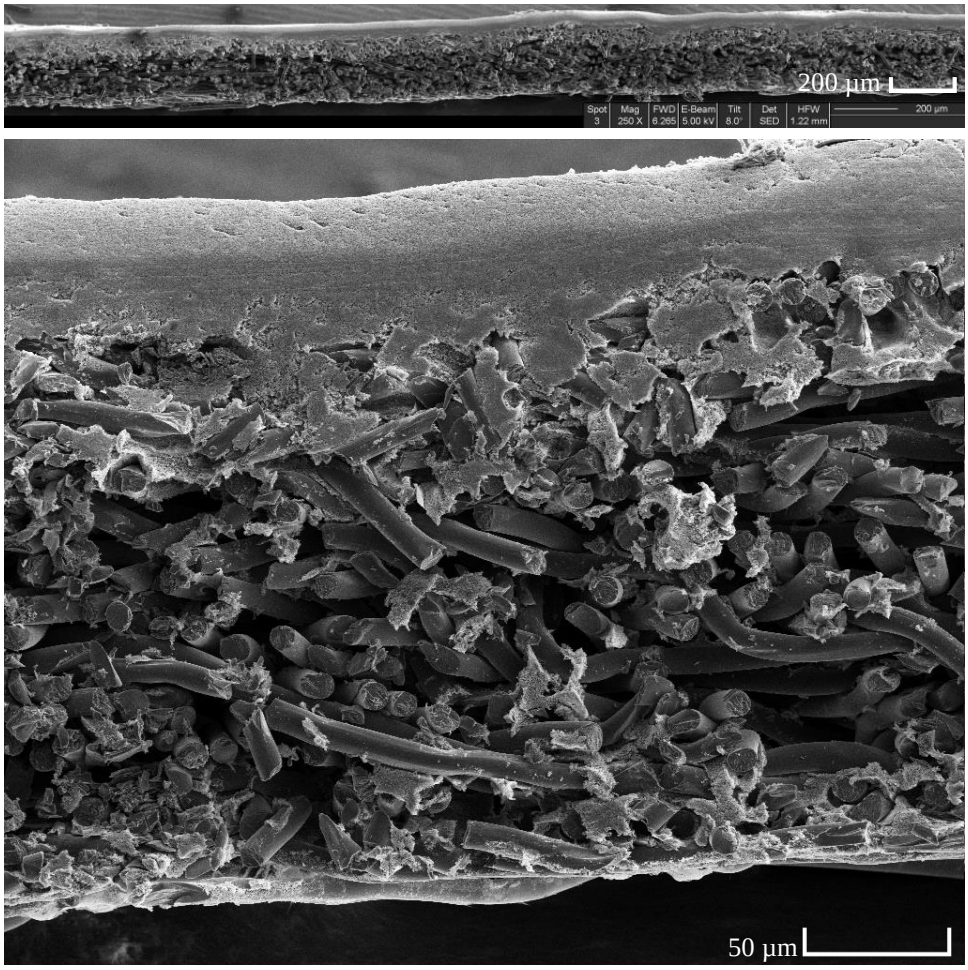

Figure 3.2. Measured cross-sectional view SEM image of a CNP MPL-coated GDL in (a) 250x and (b) 900x magnifications.

macropores and consequently altering its IP and TP transport properties. The MPL-penetrated layer profile is influenced by several parameters including carbon particle and hydrophobic agent type, size, and weight fraction.

The MPLs studied in this work are carbon nanoparticle (CNP) MPL with approximate median particle size (D50) of 40 nm and flake graphite particle (FGP) MPLs with median particle sizes of roughly 2, 6, 8, 11, 18, and 23 μm. The MPLs contain PTFE loading of 40% wt. for the CNP MPL and 18% wt. for FGP MPLs as hydrophobic agent. Based on the SEM images depicted in Figure 3.4(a), the CNP MPL with base material of acetylene black (AB) consists of carbon nanoparticle agglomerates with isotropic alignment, which are roughly of spherical shape with equal size, and PTFE which is less

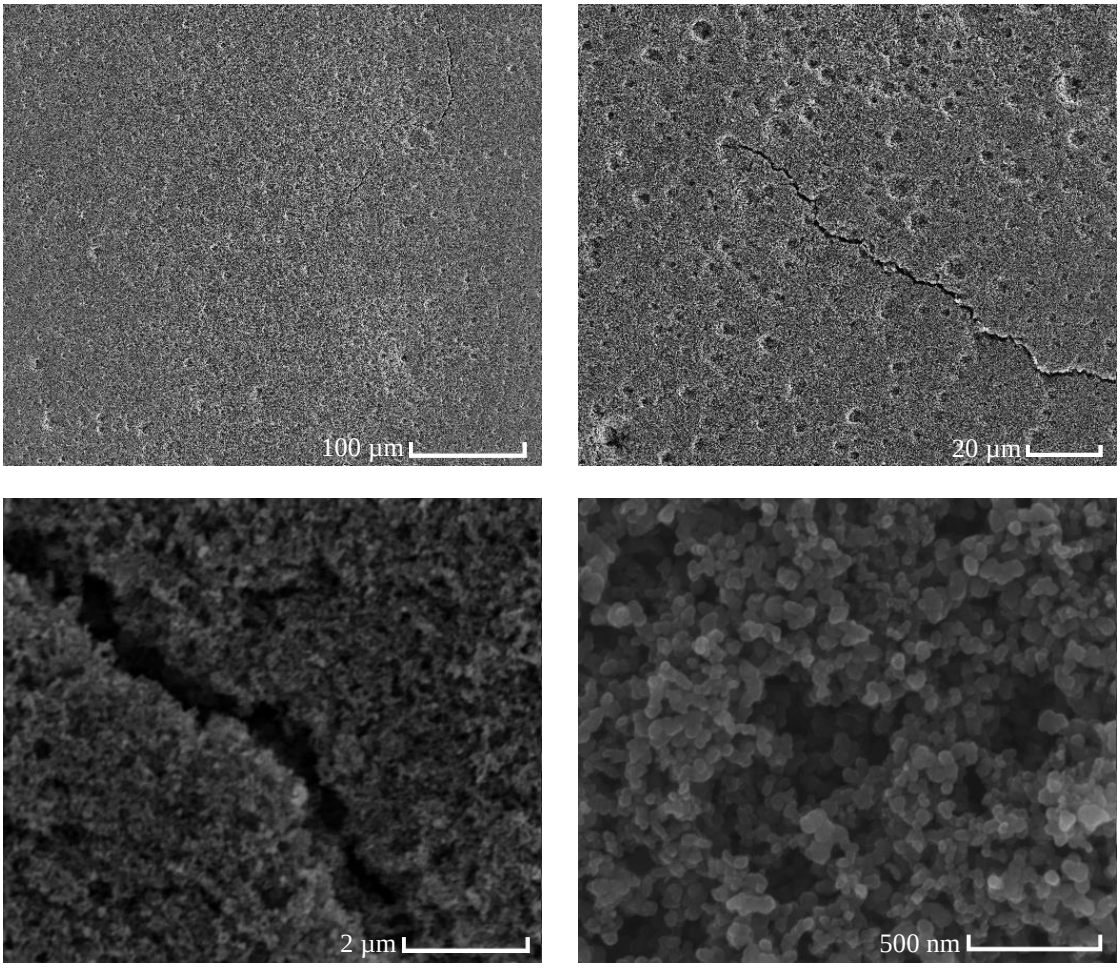

Figure 3.3. Measured surface view SEM image of a CNP MPL-coated GDL in (a) 650x, (b) 2kx, (c) 35kx, and (d) 150kx magnifications.

visible. Due to non-uniform distribution of particles, the solid structure forms an intricate network of pores and agglomerates with approximate median particle size of 40 nm. Moreover, Figure 3.4(b) illustrates SEM images of an FGP MPL with D50 ≈ 11 µm which consists of roughly circular disc-shaped graphite particles and PTFE with predominant alignment of the graphite particles in the in-plane (*x*, *y*) direction.

As a quantitative characterization, PSD of the fabricated MPLs are characterized in this work via MIP using the measurement technique elaborated in section 2.1. However,

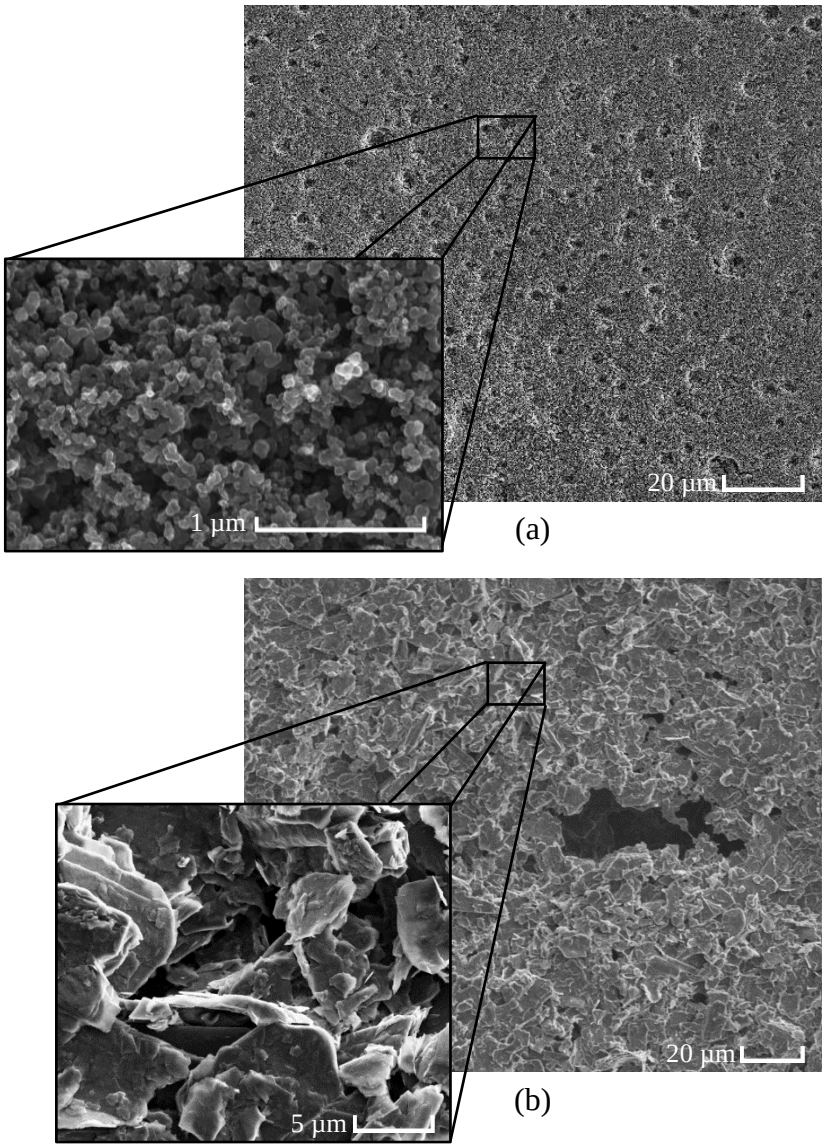

Figure 3.4. Measured back-scattered top view SEM images of (a) a carbon nanoparticle MPL in 2 kx and 80 kx magnification and (b) a flake graphite particle MPL (D50 ≈ 11 µm) in 1.5 kx and 12 kx magnification using an FEI™ DualBeam Strata 235 at SFU 4D LABS.

due to MPL penetration into the GDL substrate during the GDL manufacturing process, which is likely associated with the filling of open non-planar features at the surface of the substrate, interpretation of the GDL MIP results may not be possible to accurately extract the MPL PSD data. Alternatively, to specifically extract the MPL MIP PSD data in this work, a sample is prepared by coating the MPL on a non-porous substrate, *i.e.*, Kapton® polyimide solid film, followed by the regular heat-treatment process of the GDL fabrication protocol. The sample is subsequently analyzed by MIP provided that the presence of the non-porous substrate is correctly accounted for, as detailed in the following.

Figure 3.5 illustrates the mercury filling of a penetrometer and its cross-sectional view with the sample present. For calibration purposes, an MIP experiment is performed with blank Kapton film. Despite the Kapton film being a non-porous solid substrate, mercury intrusion of 7.2 mL m^{-2} is measured due to irregular edges from sample cutting and space created between layers. The MPL porosity in the MIP experiment is defined as:

$$\varepsilon = \frac{\Omega_{m,MPL-int}}{\Omega_{MPL}} \tag{3-1}$$

where $\Omega_{m,MPL-int}$ is the MPL-intruded mercury volume and Ω_{MPL} is the MPL volume. Thereby, the MPL porosity and PSD data are adjusted for mercury intrusion into the Kapton film and its associated edge effect. Moreover, the sample volume must be adjusted for the volume fraction displaced by the Kapton film. Ultimately, the MPL porosity is obtained as follows:

$$\varepsilon = \frac{\Omega_{m,s-int} - \Omega_{m,K-int} - \left(\Omega_{s,MIP} - \Omega_s\right)}{\Omega_s - \Omega_K} \tag{3-2}$$

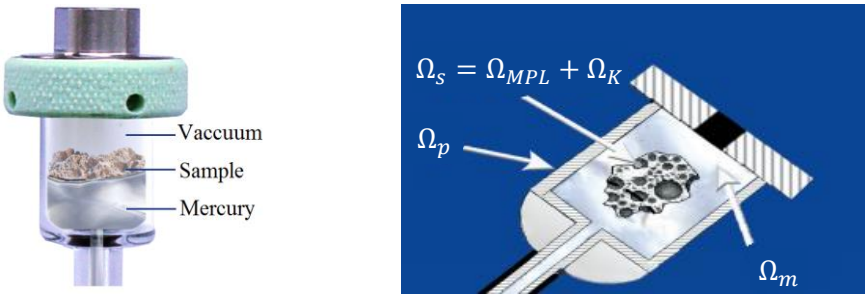

Figure 3.5. (a) Illustration of mercury filling the penetrometer volume with the sample (MPL-coated Kapton film) present and (b) cross-sectional view of a mercury penetrometer [121].

Table 3.1. MIP-measured porosity of the CNP MPL with D50 ≈ 40 nm and the FGP MPLs with D50 ≈ 8 and 23 µm coated Kapton film and their respective MPL porosities after adjustment made in Eq. (3-2).

Porosity (%)	CNP MPL (D50 ≈ 40nm)	FGP MPL (D50 ≈ 8µm)	FGP MPL (D50 ≈ 23µm)
MPL-coated Kapton film	48.6	47.2	62.3
MPL	61.6	56.6	70.5

where $\Omega_{m,s-int}$ and $\Omega_{m,K-int}$ are the measured sample-intruded and Kapton-intruded mercury volumes, respectively. The sample (MPL-coated Kapton film) volume measured by MIP is calculated by:

$$\Omega_{s,MIP} = \Omega_p - \Omega_m \tag{3-3}$$

where Ω_p is the penetrometer volume and Ω_m is the volume of mercury before the intrusion process that can be obtained by:

$$\Omega_m = \frac{m_{psm} - m_p - m_s}{\rho_m} \tag{3-4}$$

where m_{psm}, m_p, and m_s are the measured penetrometer-sample-mercury mass, penetrometer mass, and sample mass, respectively, and ρ_m is the mercury density. Alternatively, the sample volume can also be calculated by $\Omega_s = m_s/\rho_s$ in which the sample density is obtained by:

$$\rho_s = \frac{BW_{s,meas}}{h_{s,meas}} \tag{3-5}$$

where $BW_{s,meas}$ and $h_{s,meas}$ are the measured sample basis weight and thickness, respectively. In the final step, the MPL volume is derived as:

$$\Omega_{MPL} = \Omega_s - \Omega_K \tag{3-6}$$

where the Kapton volume, Ω_K, is calculated with the same strategy as the sample volume. Table 3.1 illustrates the MIP-measured porosity of MPL-coated Kapton film and MPL porosities for CNP and FGP MPLs after adjustment made in Eq. (3-2).

Figure 3.6 depicts the measured differential and cumulative pore volume versus the pore diameter for the CNP and FGP MPLs that are coated on a Kapton film. An increasing pore size trend is observed with the MPL particle size where the pores are ranging from

0.01 μm to 100 μm. The FGP MPLs have two separate peak pore sizes for small (peak 1) and large (peak 2) pores. The large pores are associated with the effective particle spacing of the MPL microstructure which shows an increasing trend with the MPL graphite particle size. In contrast, the small pores are likely a consequence of solvent evaporation during drying and sintering processes in which the integrated pore volume under peak 1 is roughly the same for all particle sizes.

Furthermore, the particle size distribution can be analyzed by laser diffraction measurement technique using diluted ink sample as part of the quantitative characterization of fabricated MPL samples. This is a widely used particle sizing technique for porous materials ranging from hundreds of nanometers up to several millimeters in size. It extracts

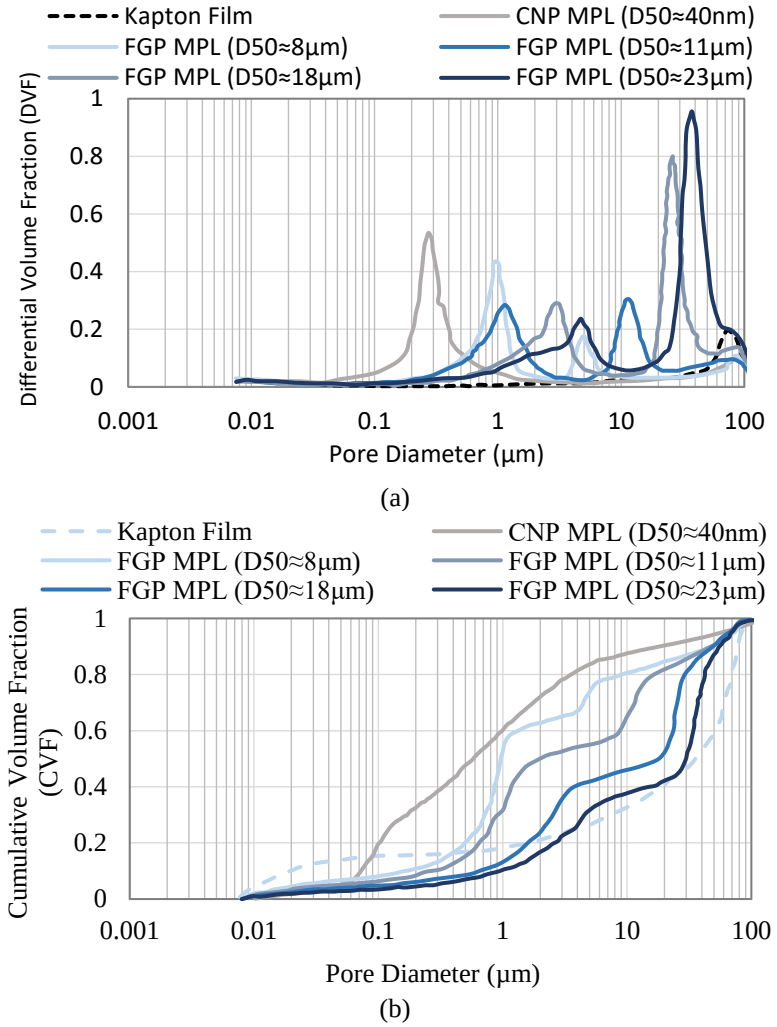

Figure 3.6. Measured (a) differential and (b) cumulative volume fraction MIP data for CNP and FGP MPLs in different median particle sizes coated on Kapton film.

the particle size distribution by measuring the angular variation in intensity of light scattered as a laser beam passes through the sample. The Mie theory of light scattering is utilized to analyze the angular scattering intensity data to calculate the size of particles [177,178]. Large particles scatter light at small angles relative to the laser beam and small particles scatter light at large angles, as schematically illustrated in Figure 3.7 [179].

Figure 3.8 shows the particle size distribution of four different FGP materials measured in-house by laser diffraction. The measured FGP particle size distributions are generally consistent with the D50 values specified by the manufacturer, as noted on the legend. Moreover, the particle size distribution of a blank PTFE dispersion is also

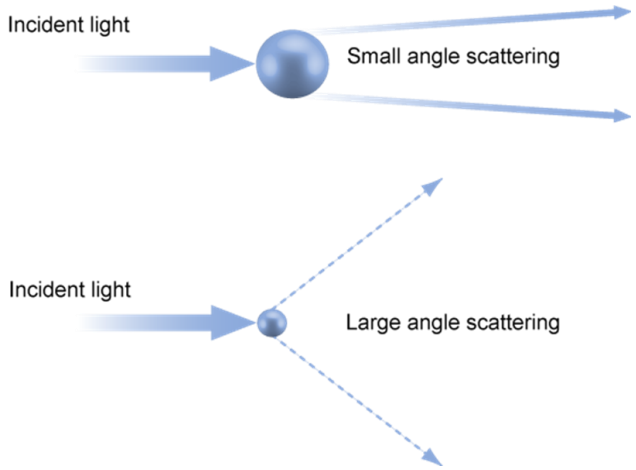

Figure 3.7. Scattering of light from large and small particles as a laser beam passes through a sample [179].

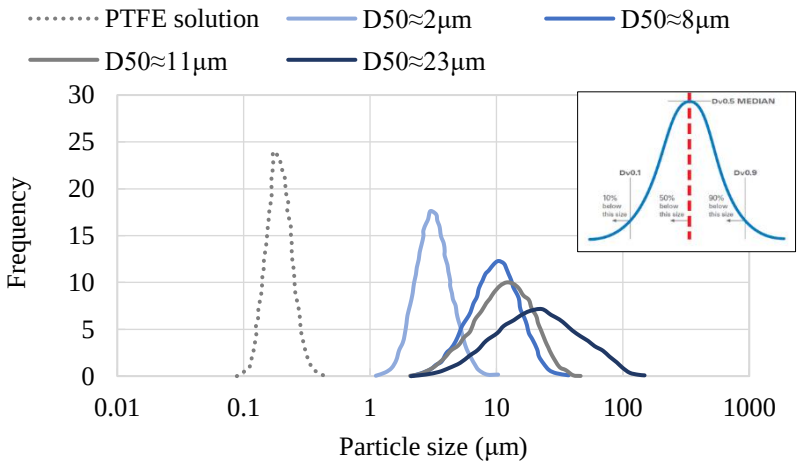

Figure 3.8. Particle size distributions of PTFE and flake graphite particles with different median particle sizes (D50) measured in-house by laser diffraction.

measured, *cf*. Figure 3.8**,** which shows that the PTFE particles are considerably smaller than all FGP particles under study and therefore should not affect the overall solid particle size of the resulting MPL.

3.2. Numerical Formulation

3.2.1. MPL Stochastic Microstructural Modeling

In this section, a novel methodology for MPL stochastic microstructural modeling framework is extensively elaborated. Inspired from MPL manufacturing and pore morphology and structure characterization described in section 3.1, the developed framework is a collection of stochastic processes including digital reconstruction of carbon agglomerates and PTFE. Thereupon, after thorough validation of the digital realization of the MPL microstructure, it will be used as an input in the following subsection for material transport properties determination.

Table 3.2. Required and optional (validation) MPL input parameters for stochastic microstructural modeling.

MPL Input Parameters		Unit	Characterization Method	Influenced By
Required	Basis Weight (BW)	g m^{-2}	Data Sheet	Composition
	Porosity (ε)	%	Data Sheet / MIP	Composition / Manufacturing Process
	Carbon Type	-	Data Sheet	Composition
	Carbon Density (ρ_C)	kg m^{-3}	Data Sheet	Composition
	Hydrophobic Agent Type	-	Data Sheet	Composition
	Hydrophobic Agent Density (ρ_T)	kg m^{-3}	Data Sheet	Composition
	Hydrophobic Agent Weight Fraction (ω_T)	% wt.	Data Sheet	Composition
Optional (Validation)	Pore Size Distribution (PSD)	µm	SEM Image / MIP	Composition / Manufacturing Process
	Particle Size Distribution	µm	SEM Image / Laser Diffraction / Data Sheet	Composition / Manufacturing Process
	Particle Alignments	-	SEM Image	Manufacturing Process

A reliable implementation of the stochastic microstructural MPL model requires comprehensive information about the MPL parameters as listed in Table 3.2. There are two scenarios; reconstructing existing MPLs or creating hypothetical MPL materials. The intent of studying existing MPLs is to validate the reliability of the proposed MPL design tool algorithm in order to have a well-established algorithm for design and prototyping assignments of hypothetical materials for next-generation fuel cells. Whilst the required input parameters of the existing MPLs under study are determined based on the constituent materials and their associated specifications, the optional validation parameters are determined via the characterization techniques of the MPLs at hand described at length in section 3.1. To create hypothetical materials, the MPL input parameters are determined in an iterative study to optimize the required GDL transport capabilities, *e.g.*, mechanical stability, ohmic resistance, diffusivity, *etc*.

The MPLs under study are CNP MPL as a conventional MPL with median particle size of 40 nm and FGP MPLs as promising alternatives for next-generation fuel cells with median particle sizes of roughly 2, 6, 8, 11, 18, and 23 μm [176]. The MPL is digitally reconstructed in four steps: i) Creating a Domain; in which the rectangular cuboid computational domain is algebraically determined using known required MPL input parameters; followed by ii) Reconstruction of Large Pores; by distributing solid large spheres which are allowed to overlap utilizing a multi-sized random loose sphere packing method and inverting the domain structure such that the solid spheres are transformed into large pore space; subsequently, iii) Reconstruction of Carbon Particle Agglomerates; by randomly distributing carbon particle agglomerates with the specified particle type, size, and alignment in agglomeration with each other and with the reconstructed large pores; and ultimately, iv) Reconstruction of PTFE Agglomerates; as a porous binder by randomly distributing cylindrical PTFE particle agglomerates within the narrow pore spaces between the carbon agglomerates. The stochastic MPL microstructural modeling framework developed and validated in this work is expected to become a reliable and versatile tool for MPL design and prototyping assignments for which the flowchart is briefly described in the MPL Design Tool Algorithm subsection.

i. Creating a Domain

A rectangular cuboid computational domain, Ω_{MPL}, which consists of solid material and pore space, is considered as follows:

$$\Omega_{MPL} = \Omega_{solid} \cup \Omega_{pore} \tag{3-7}$$

The solid material in the MPL porous structure considered in this work consists of carbon particles (spherical nanocarbon or flake graphite agglomerates; index C) and PTFE (index T) as follows:

$$\Omega_{solid} = \Omega_C \cup \Omega_T = (1 - \varepsilon)\Omega_{MPL} \tag{3-8}$$

where ε is the porosity.

Referring to Figure 3.6 and Figure 3.8, the particle size and consequently the pore size of CNP (micropores) and FGP (mesopores) MPLs differ by one order of magnitude. This implies that, a single pore-scale model cannot resolve the pore structure of CNP MPL and reconstruct the FGP MPLs with the same voxel size. Therefore, two different modeling scales are reconstructed; the high-resolution model with 20 nm voxel length reconstructs the CNP MPL while the low-resolution model with 0.5 µm voxel length reconstructs the various FGP MPLs. Note that, a grid independence study was performed on a dummy MPL structure to determine a suitable voxel size by which consistent material property simulations with less than 10% tolerance was achieved.

Using known required MPL input parameters such as basis weight and porosity in addition to carbon and PTFE densities and their weight fractions, that can be obtained from materials datasheets, the volume fraction of carbon particles and PTFE phases and subsequently the domain thickness can be determined algebraically. By using the density definition as $\rho = m/\Omega$ and by having the weight fractions of carbon particles and PTFE, the relation between the carbon particles volume, Ω_C, and PTFE volume, Ω_T, is given by:

$$\frac{\Omega_T}{\Omega_C} = \frac{\omega_T}{1 - \omega_T} \times \frac{\rho_C}{\rho_T} \tag{3-9}$$

where ρ_C is carbon particle density and ρ_T and ω_T are PTFE density and weight fraction, respectively. By using Eqs. (3-8) and (3-9), the carbon particles and PTFE volumes can be obtained as:

$$\Omega_C = \frac{(1-\omega_T)\rho_T}{(1-\omega_T)\rho_T + \omega_T\rho_C}(1-\varepsilon)\Omega_{MPL} \tag{3-10}$$

$$\Omega_T = \frac{\omega_T\rho_C}{(1-\omega_T)\rho_T + \omega_T\rho_C}(1-\varepsilon)\Omega_{MPL} \tag{3-11}$$

The basis weight in a porous material is defined as the domain mass, m, over the domain surface area, A, and is be given by:

$$BW = \frac{m}{A} = \frac{\rho_C\Omega_C + \rho_T\Omega_T}{A} \tag{3-12}$$

By substituting Eqs. (3-10) and (3-11) into Eq. (3-12) and considering $\Omega = Ah$, the domain thickness h can be obtained as:

$$h = \frac{BW}{1-\varepsilon}\left[\frac{1-\omega_T}{\rho_C} + \frac{\omega_T}{\rho_T}\right] \tag{3-13}$$

The domain width is chosen with the same order of magnitude as the thickness to provide a reasonable representation of the whole MPL structure.

ii. Reconstruction of Large Pores

Inspired by the SEM characterization of fabricated MPLs, *cf.* Figure 3.4, the MPL structure forms an intricate network of agglomerates and comparatively large pores due to non-uniform distribution of carbon particles. In MPL manufacturing, the small pores are created as a result of solvent evaporation during the heat treatment process and the large pores are associated with the effective particle spacing of the MPL structure. Hence, the reconstruction process continues by creating large pores in the selected domain which is initially filled with void space as extensively elaborated in the following:

The domain is divided into *large pore space*, VP_{SS_C}, and *carbon agglomerate space*, VP_{CS}. Briefly saying, the large pores are randomly generated in the domain by distributing solid large spheres, which are allowed to overlap, within a range of diameters until a desired volume percentage of the void space is filled. To this end, first, loosely

packed solid spheres are randomly generated in the void space through a series of steps utilizing a multi-sized random loose sphere packing method. Common packing methods to simulate random loose sphere packing are Monte Carlo and discrete element methods (DEM) with the packing density of around 0.6 [130,131,180]. The fixed solid spheres are successively added with the following conditions until a desired volume percentage of the void space VP_{SS_C} is filled:

- Allowed to overlap with each other.
- Generated within a certain range of diameters representing the range of large pores.
- Added starting with largest spheres and continues with smaller ones.

Thereafter, the process is followed by inverting the domain structure such that the solid spheres are transformed into *large pore space* and the remaining void space converts to *carbon agglomerate space* to prepare for the carbon agglomerate generation. Henceforth, the spheres act as large pores.

To digitally reconstruct the existing MPL materials, the size and volume fraction of the large pores can be inspired by differential volume fraction (DVF) and cumulative volume fraction (CVF) PSD data, respectively. Measured DVF for most MPLs under study have one or two characteristic pore sizes as illustrated by separate peaks in Figure 3.6 from uniform pore distribution to more complicated networks of pores. The range of diameters is originated from pore diameters span[11] around the large pore peak (peak 2) of a bell-shaped DVF PSD, *i.e.*, D10 to D90, and is mapped to the sigmoidal CVF distribution to find the volume fraction of the large pores. To explore the hypothetical MPL materials with no explicit knowledge of the measured PSD, a fraction of the void space is set aside for large pores and the range of large pores diameters are determined based on the fuel cell operating conditions and inherent characteristics of the cell components. This is an iterative study to optimize the range of large pores diameters as one of the input parameters to meet the required GDL transport capabilities. For instance, in modern automotive PEFCs operating at high current density conditions, higher diffusive MPL material is superior,

[11] Span is an indication of how far the 10 percent (D10) and 90 percent (D90) pore diameters are apart in the differential pore volume distribution.

hence, the large pores diameters are greater than the ones in applications where the mechanical support is the main function of the MPL.

iii. Reconstruction of Carbon Particle Agglomerates

By SEM characterization of MPLs under study, *cf*. Figure 3.4, it is perceived that the MPL structure forms an intricate network of carbon agglomerates and comparatively large pores. In MPL manufacturing, carbon agglomeration is the process of amassing carbon particles into cohesive units like pellets or granules. Simply put, carbon agglomeration is the phenomena of sticking carbon particles together to form particulate solid material. While carbon agglomeration results in particles that look visibly different, the original carbon particles are still present in the structure; often with completely unaltered shape and size the same as before they were agglomerated; and are held together by binding mechanisms. The agglomerated carbon particles feature porosity which leaves void spaces between the agglomerate-forming particles characterized as small to medium pore diameters with span around the small pore peak (peak 1) of a bell-shaped DVF PSD of the MPL under study, *cf*. Figure 3.6.

Thereby, the reconstruction process continues by randomly distributing carbon particle agglomerates with the volume Ω_C derived in Eq. (3-10) in the *carbon agglomerate space* with the volume VP_{CS} in agglomeration with each other and with the reconstructed large pores. The randomness of the carbon agglomerate distribution is controlled by the location of the reconstructed large pores (two-fold randomness) while the center of a given particle is not allowed to fall into the large pores. Since the agglomerated carbon particles leave void spaces between the agglomerate-forming particles, $\Omega_C < VP_{CS}$, where the difference is associated with the volume percentage of the small to medium pores.

Based on MPL material characterization, the type of carbon agglomerates studied in this work are roughly spherical carbon nanoparticles with isotropic distribution or disc-shaped graphite particles with predominant in-plane alignment. Moreover, the particle diameter probability distribution of carbon particles is approximated by discrete probability distribution with 20% from the midpoint of each quintile as illustrated in Figure 3.9(a). To ensure flawless carbon particle agglomeration, thus avoiding particles isolation with no

contact with other solid phase, a certain degree of carbon particle overlap is allowed with at least one adjacent particle. This warrants that the reconstructed MPLs are thermally and electrically conductive. As a limitation of permissible overlap, the center of a newly generated particle is not allowed to be placed within an adjacent, pre-existing particle. Moreover, the distance between the centers of any two adjacent particles has to be less than the sum of their radii. To fulfill these conditions, the distance, $|d|$, between the centers of two adjacent particles with r_1 and r_2 radii shown in Figure 3.9(b) should meet the following criteria:

$$\max(r_1, r_2) < |d| < r_1 + r_2 \tag{3-14}$$

iv. Reconstruction of PTFE Agglomerates

The current state-of-the-art MPLs are made of carbon particle agglomerates surrounded by a hydrophobic agent such as PTFE. The PTFE serves as a porous binder to maintain the structural integrity of MPL carbon particles and provide adequate hydrophobicity to aid effective water management, that is, to keep the membrane hydrated under dry conditions and avoid liquid water flooding under wet conditions. The optimum PTFE content reported in the literature varies between 5% and 35% wt. Although common

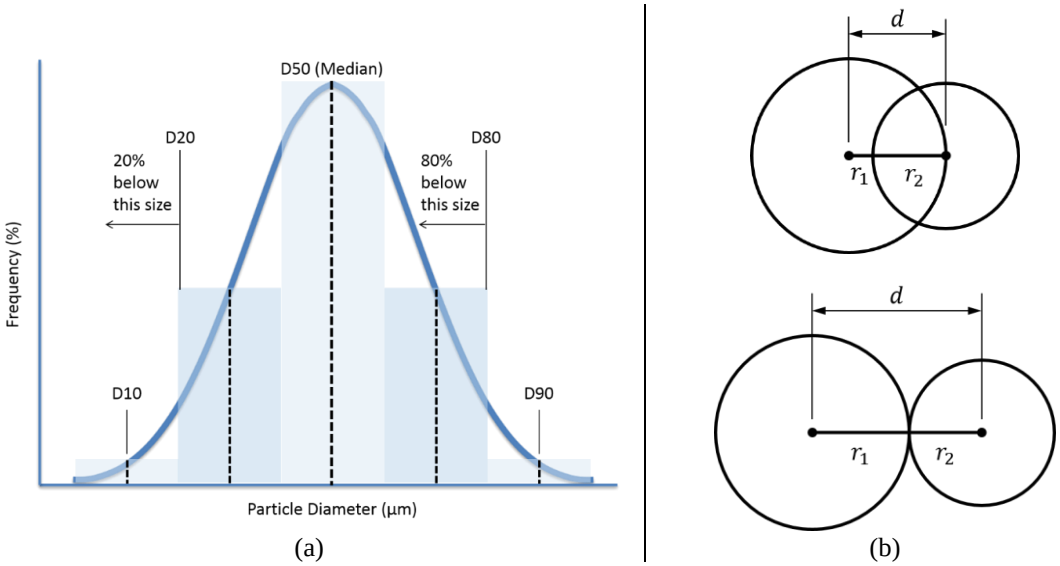

Figure 3.9. (a) Approximate particle size discrete probability distribution of CNP and FGP MPLs and (b) overlapping conditions between two adjacent carbon agglomerate particles.

characterization techniques such as SEM and FIB-SEM are incapable of differentiating between the carbon and PTFE particles [94], the PTFE particles' behavior and intended location can be inspired by the GDL manufacturing process. During the sintering step, the temperature exceeds the melting point of the PTFE that enables coalescence of adjacent PTFE particles and uniform re-distribution into narrow pore spaces (smallest pores) between carbon particle agglomerates; a crucial step for imparting homogeneous surface characteristics. Furthermore, a non-destructive monochromatic nano-scale X-ray computed tomography (NXCT) visualization technique is developed in our group for 3D phase-segregated reconstruction of MPL nano-porous structure. In this technique, a low-energy X-ray is utilized to measure the mass attenuation coefficients of carbon and PTFE phases, which is higher for PTFE compared to carbon as a consequence of their different effective atomic numbers, which in turn provides an opportunity to distinctively visualize the solid phases of the material. Using this technique, it is discovered that PTFE is indeed situated in conglomerated regions distributed randomly within connected domains of carbon particle agglomerates, hence, acting as a porous binder for carbon particles [181].

In the present model, the PTFE agglomerates are small cylindrical graphite particles of fixed length and diameter extracted from material datasheet and PTFE particle size distribution characterization data, *cf*. Figure 3.8. Inspired by the manufacturing process, the PTFE reconstruction is implemented by randomly distributing cylindrical PTFE particle agglomerates with the volume Ω_T derived in Eq. (3-11) within the narrow pore spaces between the carbon agglomerates, namely, *PTFE agglomerate space* with the volume percentage VP_{TS}. To distinguish the *PTFE agglomerate space*, first, loosely packed solid spheres within a certain range of diameters are randomly distributed in the void spaces of the pre-existing carbon agglomerate structure through a series of steps utilizing a multi-sized random loose sphere packing method. The intent of spheres distribution is to restrict spreading of PTFE particles into pores comparatively larger than the PTFE particle size. The diameter of the small pores which are in the same order as the PTFE agglomerates should be excluded from the range of solid sphere diameters. Next, the process continues by inverting the domain structure such that the carbon agglomerates and solid spheres are transformed into void space and the remaining void space converts to *PTFE agglomerate space* to prepare for the PTFE agglomerate generation. Stemmed from the fact that the

PTFE is a highly porous agglomerate structure, estimating the volume fraction of the solid spheres VP_{SS_T} should satisfy the condition that VP_{TS} is considerably greater than Ω_T. Thereafter, the PTFE structure is implemented by randomly distributing the PTFE overlapping particles in agglomeration with each other and with the pre-existing structure. In the last step, the carbon agglomerates and PTFE structures are merged into a complete MPL solid structure with the remaining domain volume being assigned as pore space.

v. MPL Design Tool Algorithm

The algorithm flowchart of the proposed MPL microstructural modeling framework which is extensively described in subsections i to iv is diagrammatically illustrated in Figure 3.10. The MPL design tool algorithm was implemented in GeoDict using the input parameters extensively introduced in the introduction of section 3.2.1 and listed in Table 3.2. The validated framework is expected to become a reliable and versatile tool for hypothetical MPL materials design and prototyping assignments to reduce the cost and time of the design cycle.

3.2.2. Model Validation

MPL virtual reconstruction requires thorough model validation to ensure accurate representation of the real structural characteristics. For instance, an MPL with a given porosity can have a variety of possible particle arrangements with different PSD and tortuosity, which leads to different transport properties. Therefore, concise quantitative validation of the MPL model structural characteristics should be conducted to satisfy the measured MPL porosity, thickness, basis weight, and PSD. As part of the quantitative validation, the pore shape, size, and connectivity of the MPL need to be characterized via MIP experiment where the method is extensively introduced in sections 2.1, MIP experiment methodology, and section 3.1, the methodology to extract the MPL-specific MIP PSD data [133]. As a qualitative validation, a collection of SEM images is captured to compare the detailed structure of the real MPL with that of the virtually reconstructed model.

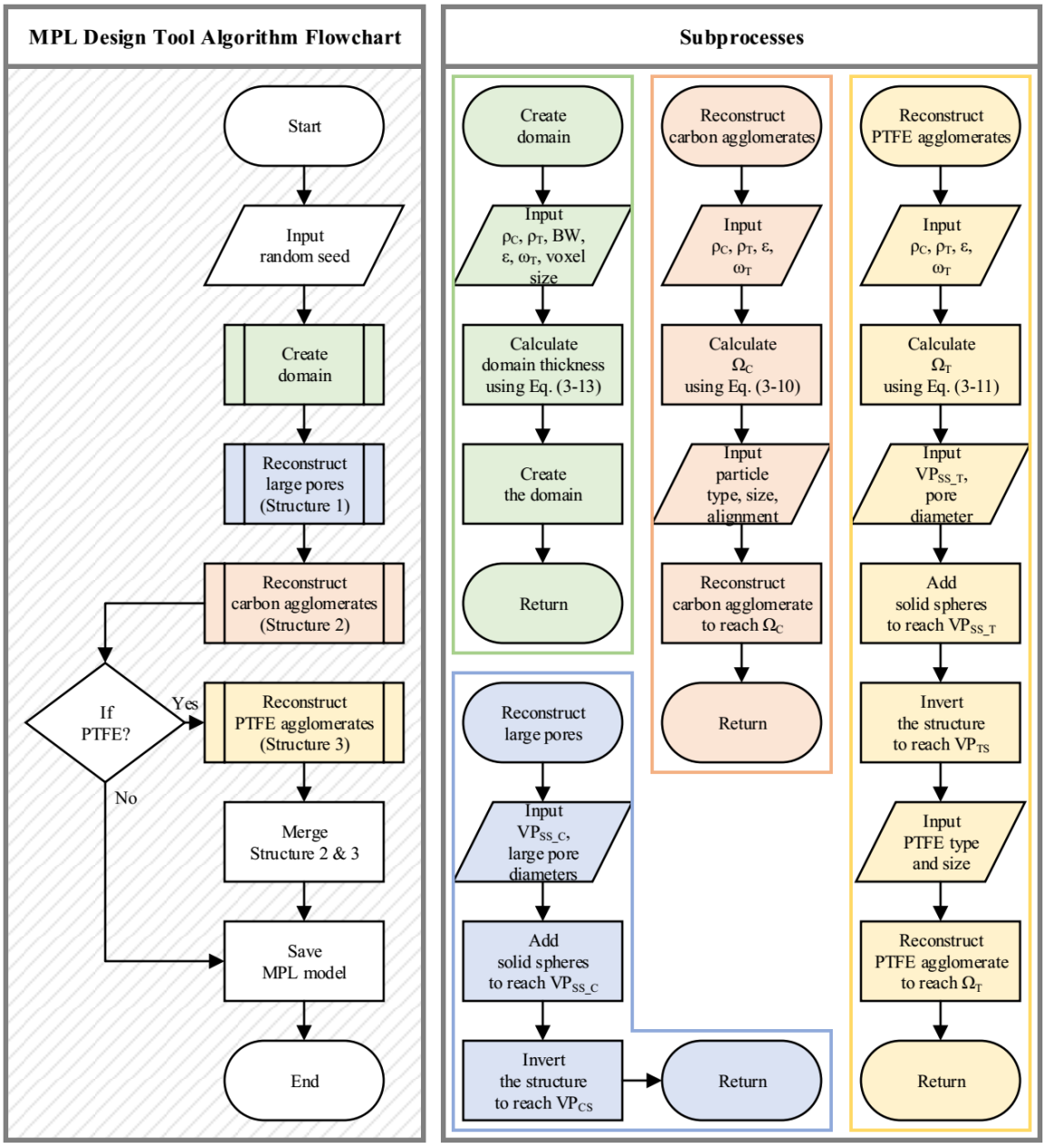

Figure 3.10. The MPL design tool algorithm flowchart (left-side block) and its subprocesses (right-side block). Subprocesses color coding: - Create domain in green, - Reconstruct large pores in blue, - Reconstruct carbon agglomerates in orange, and - Reconstruct PTFE agglomerates in yellow.

As a qualitative validation, the surface views of the stochastic reconstructed models for the CNP MPL with D50 ≈ 40 nm and porosity of 62% and the FGP MPL with D50 ≈ 8 µm and porosity of 70% are compared to measured SEM images in Figure 3.11. As observed in the SEM image of the CNP MPL with D50 ≈ 40 nm, *cf.* Figure 3.11(a), the MPL consists of carbon nanoparticle agglomerates with isotropic alignment, which are roughly of spherical shape with equal size, and PTFE, which is less visible. Due to non-uniform distribution of particles, the solid structure forms an intricate network of pores and

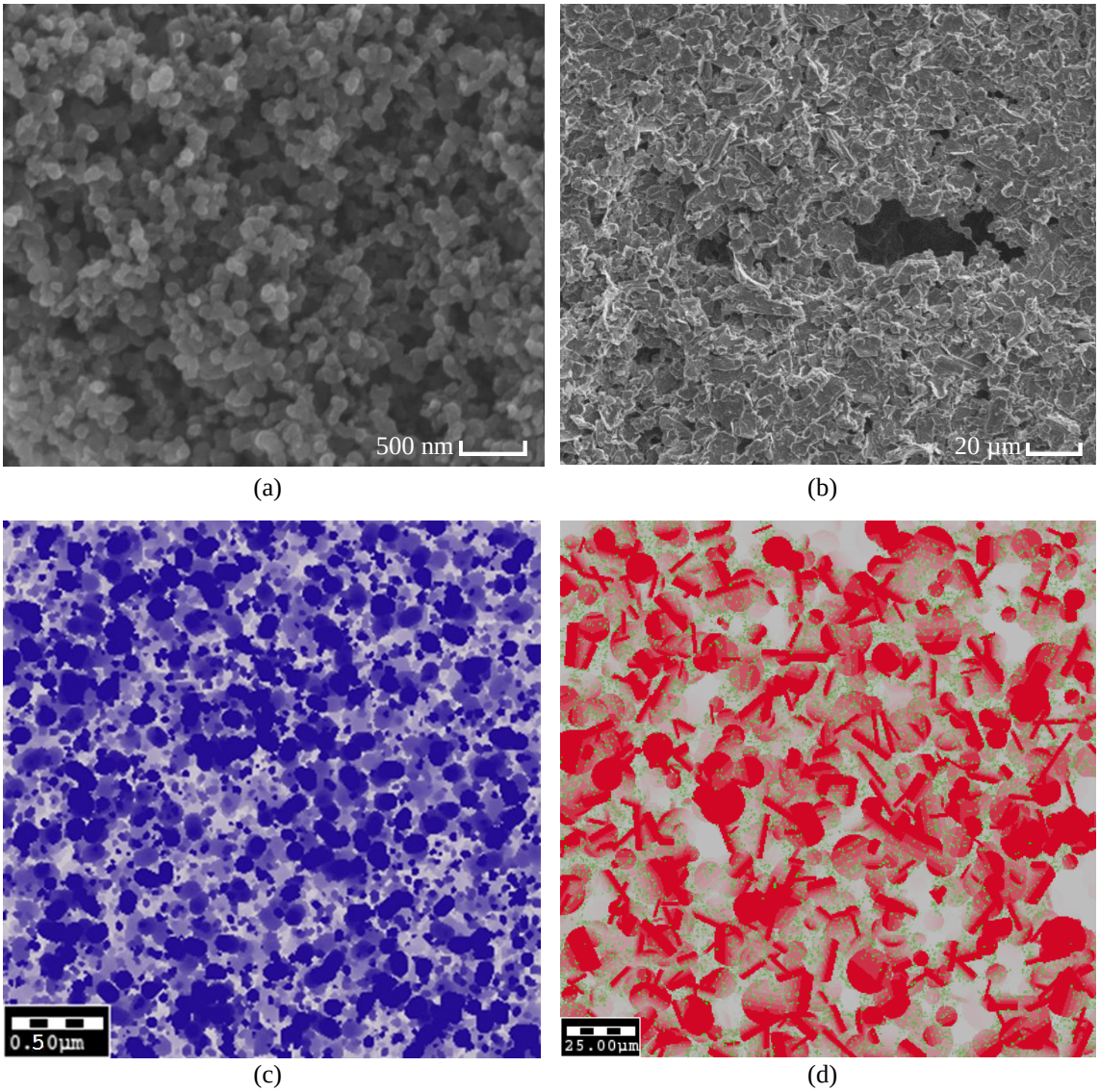

(a) (b)

(c) (d)

Figure 3.11. Back-scattered surface view SEM image of (a) a CNP MPL with D50 ≈ 40 nm and porosity of 62% and (b) an FGP MPL with D50 ≈ 8 µm and porosity of 70% compared to their respective stochastic reconstructed models (c) and (d) where carbon and PTFE are in blue color in (c) and flake graphite and PTFE are in red and green colors, respectively, in (d).

Table 3.3. Simulated porosity of the virtually reconstructed CNP MPL with D50 ≈ 40 nm and FGP MPLs with D50 ≈ 8 and 23 µm compared with their respective MIP-measured MPL porosities.

MPL Porosity (%)	CNP MPL (D50 ≈ 40 nm)	FGP MPL (D50 ≈ 8 µm)	FGP MPL (D50 ≈ 23 µm)
Measured	61.6	56.6	70.5
Modeled	60.8	54.2	68.9
Error	1.3	4.2	2.3

agglomerates with approximate median particle size of 40 nm. By comparing with the stochastic reconstructed model in Figure 3.11(c), these specifications are effectively addressed in the stochastic model. The characteristics of the FGP MPL with D50 ≈ 8 µm which consists of roughly circular disc-shaped graphite particles and PTFE with predominant alignment of the graphite particles in the in-plane (x, y) direction are in good agreement with the stochastic reconstructed model, *cf.* Figure 3.11(b) and (d). The obtained images demonstrate the accuracy of the reconstructed MPL models.

In order to quantitatively validate the pore structure of the MPL models, the MIP-based and FIB-SEM-based pore structure characterization techniques are elaborated in the following subsections in detail.

i. MIP-based Pore Structure Characterization

The stochastic model MPL porosities for the CNP MPL with D50 ≈ 40 nm and FGP MPLs with D50 ≈ 8 and 23 µm are in good agreement with MIP-measured porosities with less than 5% error as summarized in Table 3.3. As a further validation, the MIP-measured porosity of the CNP MPL are in good agreement with the corresponding results obtained by FIB-SEM pore structure characterization conducted in subsection 3.2.2ii as well as the characterization study reported by our group in [94].

The reconstructed MPL PSD is analyzed via a simulated intrusion porosimetry method with the top and bottom faces in contact with a virtual non-wetting fluid reservoir by closely mimicking the MIP experiment as elaborated in subsection 2.2.2 [133]. As a further quantitative validation, Figure 3.12 compares the simulated PSD data of CNP MPL with D50 ≈ 40 nm and FGP MPLs with D50 ≈ 8 and 23 µm with the MIP-measured data of the corresponding MPL-coated Kapton films. In the figures, the Kapton film CVF is also included with pore volume observed at very small and very large pore sizes within the

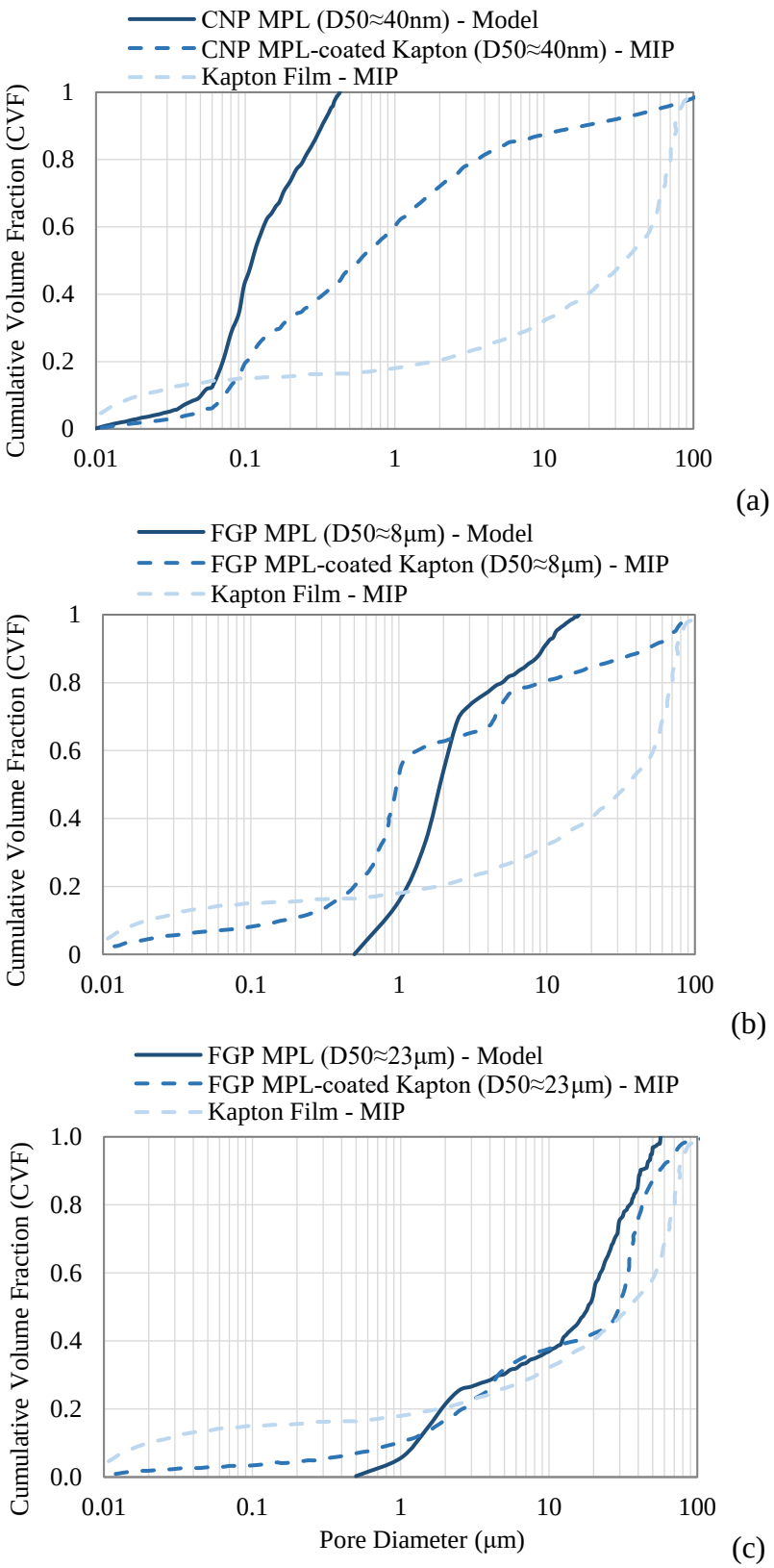

Figure 3.12. Simulated cumulative PSD of (a) CNP MPL with D50 ≈ 40 nm, (b) FGP MPL with D50 ≈ 8 µm, and (c) FGP MPL with D50 ≈ 23 µm compared to measured MIP PSD data of the corresponding MPL-coated Kapton film.

measured range, which is due to the aforementioned Kapton film edge effect. A portion of the perceived MPL pore volume at these pore sizes may therefore be associated with Kapton rather than the MPL material itself. As can be seen, the overall trends of the pore size distributions are in good agreement between simulated and measured PSD data with a small deviation in which the discrepancy is explained by the Kapton effect.

ii. FIB-SEM-based Pore Structure Characterization

To further validate the stochastic microstructural CNP MPL model with D50 ≈ 40 nm, a customized 3D morphological MPL characterization framework, which was previously developed by our group featuring a customized FIB-SEM imaging reconstruction technique [94], is employed in this work to calculate and analyze the PSD of the pure CNP MPL structure coated on a Kapton® polyimide film. The method includes iterative focused ion beam (FIB) milling, scanning electron microscopy (SEM), 3D reconstruction, and material property simulations to accurately investigate the MPL microstructure, porosity, pore size distribution, and the effective transport properties in the final step. This morphological characterization technique requires minimal sample preparation before characterization and effectively reproduces the original structure.

The FIB-SEM reconstruction framework starts with Ga^+ ion milling which makes it possible to capture a set of serial cross-sectional images with minimum preparation of the sample and subsequently less damage caused by sample cutting. Combining the ion milling of the structure with high-resolution cross-sectional SEM imaging will give high quality volumetric information of the CNP MPL structure, which is used for 3D reconstruction of the target volume [94,96]. The two beams have a coincident angle of 52º which is schematically shown in Figure 3.13(a) with the FEI Helios NanoLab™ 650 FIB-SEM system shown in Figure 3.13(b). The encouraging feature of the developed imaging technique is to take high-resolution images of successive slices for 3D rendering. An optimized milling current of 10 pA at 30 kV is chosen to prevent Ga^+ ion deposition and damage of the area of interest.

The manual screening approach is used to choose the most appropriate region of interest for FIB milling and subsequent SEM imaging, intended to be representative of the overall average structure of the CNP MPL sample. Then, the selected specimen is coated with platinum prior to milling away the surrounding area that is a useful approach to prevent the risk of damage of the structure. To this end, a 1 µm thickness platinum coating is deposited over the target volume to prevent the ion damage. The next step to prepare the target volume for ion milling is called trenching, *i.e.*, milling away the surrounding volume of the specimen to reduce the side effects of shadowing artifacts and horizontal gradients. Thus, trenching is performed with high current beam in the surrounding area far from the specimen to lower currents while becoming closer to the specimen. The obtained FIB/SEM MPL images of the platinum deposited and trenched structure for the CNP MPL sample are shown in Figure 3.14 and Figure 3.15.

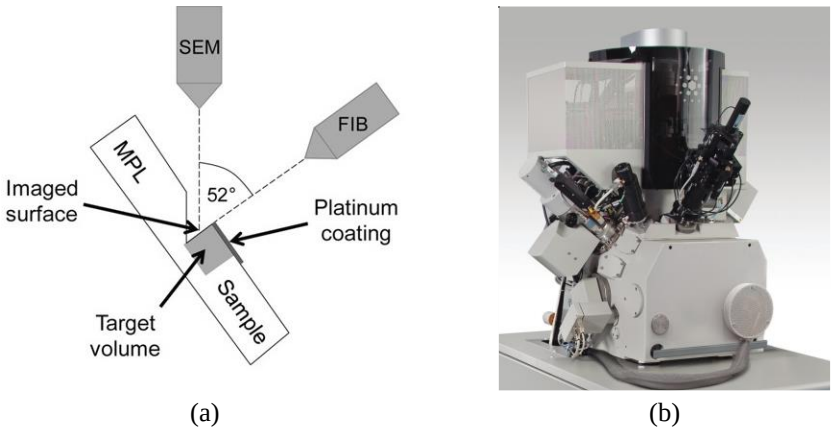

(a) (b)

Figure 3.13. (a) A schematic view of the coincident angle between the FIB and SEM beams in (b) the FEI Helios NanoLab™ 650 FIB-SEM system.

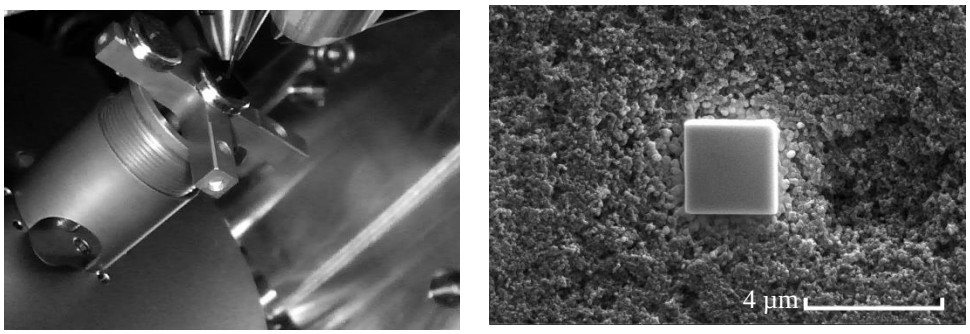

(a) (b)

Figure 3.14. (a) The FIB and SEM beams and the coincident angle of 52° and (b) the platinum deposited onto the specimen surface.

Serial cross-sectional micrographs of the CNP MPL sample are obtained by successive milling of the structure with 10 nm step size for 100 slices at 10 pA and 30 kV. It is followed by capturing high resolution SEM images with 65kx magnification of the milled surfaces to reconstruct the CNP MPL microstructure with 1 μm^3 dimensions. Figure 3.16 illustrates a raw image of the milled CNP MPL structure captured by SEM. It should be mentioned that previous studies proved that the effect of sectioning step size and direction is negligible on the overall reconstructed structure properties [94,182].

Image processing is the key step to create a precise quantification of the CNP MPL microstructure after capturing the raw images of the cross-sectional milled MPL structures. The main steps in the image processing protocol include image alignment, stretching or angle correction caused by the coincident angle between the FIB and SEM beams which is

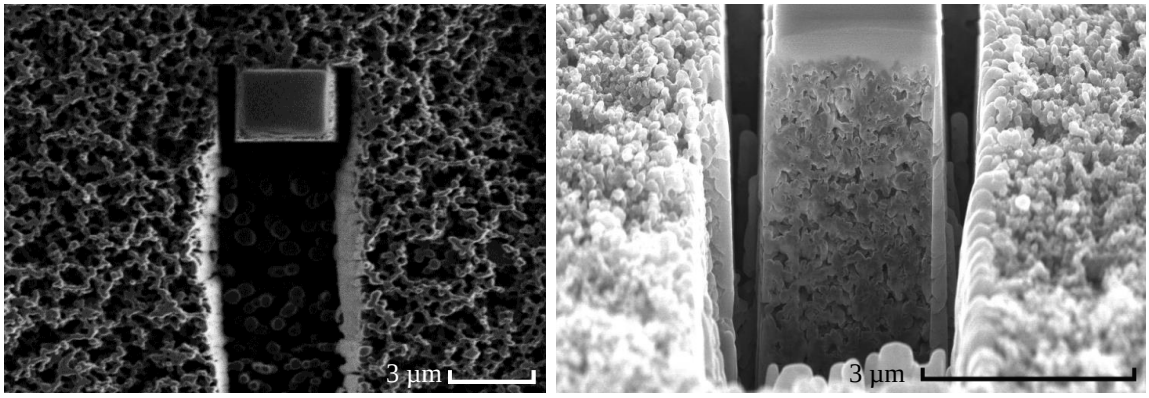

(a) (b)

Figure 3.15. (a) FIB and (b) SEM images of the trenched surface of the CNP MPL with D50 ≈ 40 nm.

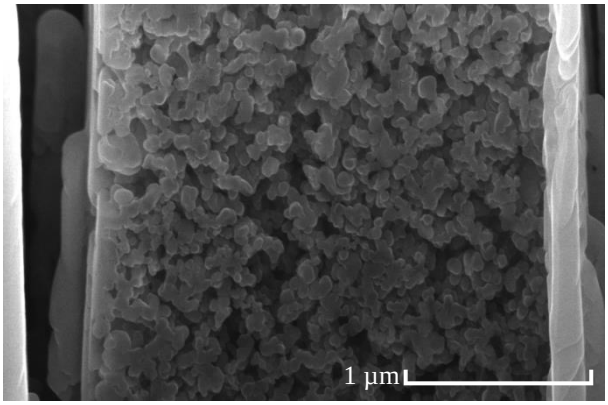

Figure 3.16. Raw SEM image of the CNP MPL microstructure with D50 ≈ 40 nm.

problematic for the SEM images, and cropping. Figure 3.17 illustrates the image processing steps for the MPL sample captured by FIB-SEM imaging technique. Alignment is the first step of image processing which is required due to small changes in the SEM beam viewing-angle leading to beam shift and image displacement in the successive images. The misalignment can be recognized by a marker; an un-milled structure at the corner of the raw images. Stretching is the next step, where the variation between the viewing angle and the cross-sectional view is corrected by multiplication of the vertical side by $1/sin52°$. In the last step, the final domain is cropped representing the average internal structure of the CNP MPL. Despite the advantage of serial cross-sectional imaging, horizontal gradients and shadowing artifacts are inevitably observed in the raw images and ultimately decreases the accuracy of image segmentation. Therefore, filtering is another process step to improve

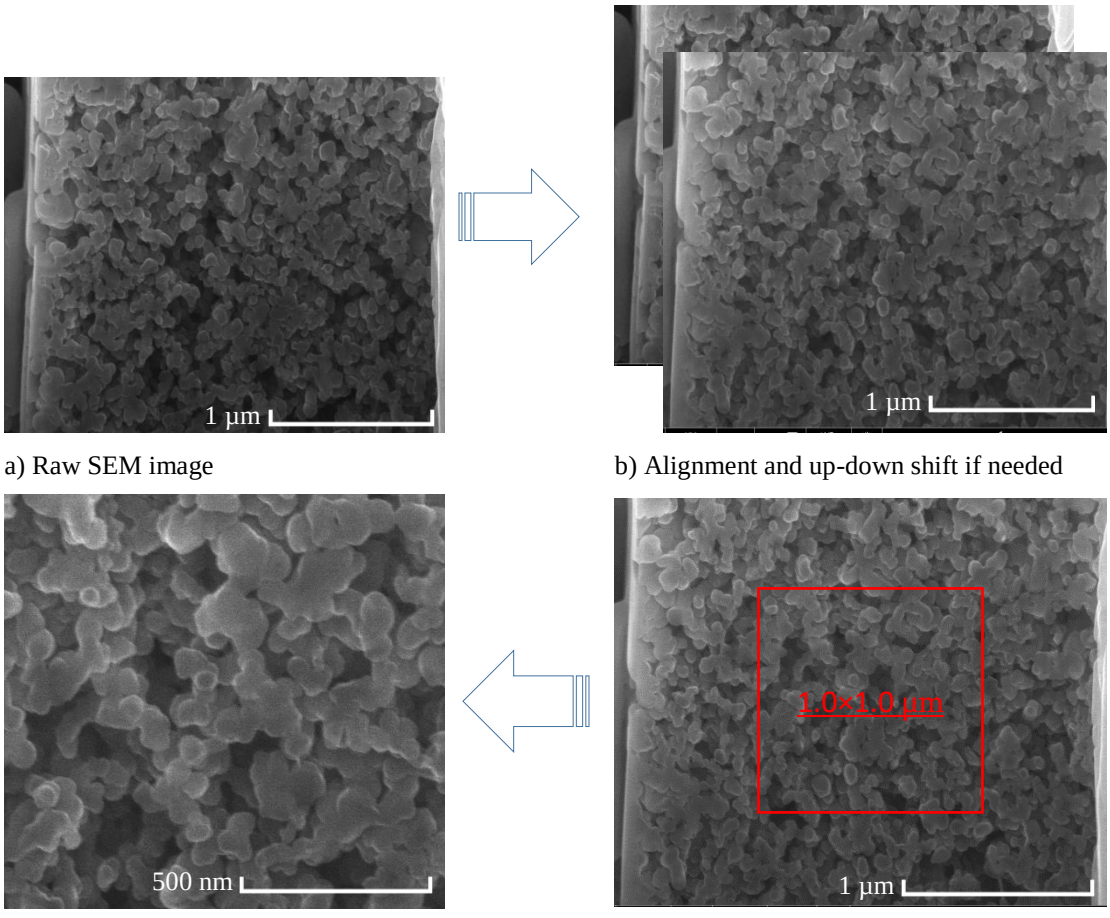

a) Raw SEM image

b) Alignment and up-down shift if needed

d) Cropped image

c) Stretching and cropping

Figure 3.17. Image pre-processing steps of the FIB-SEM image stack for the CNP MPL with D50 ≈ 40 nm.

this which is considered before segmentation of the sliced images. A segmentation procedure is conducted in the next step to transform each voxel to a binary format representing pore and solid phases of the images. A schematic view of the procedure is illustrated in Figure 3.18, where the solid phase is observed as blue agglomerate particles and the remaining part is the void space. The solid phase of the CNP MPL comprises of both carbon nanoparticles and PTFE. The two solid phases are difficult to distinguish in the captured FIB-SEM images and datasets where the focus is primarily on the pore phase, thus, distinguishing the solid phases is beyond the scope of the present work. The most commonly employed method to segment the voxel/pixel-based dataset is thresholding. The segmentation is performed by tracking the changes between two consecutive images to

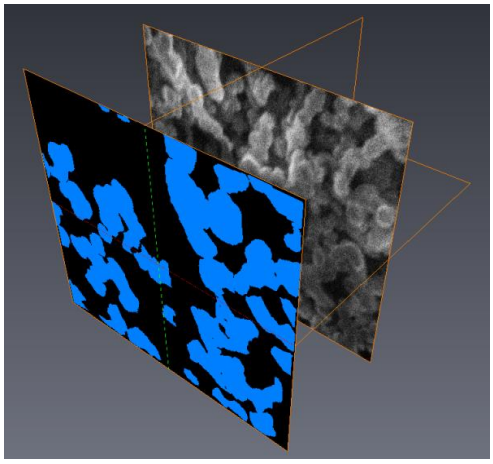

Figure 3.18. Segmentation of the cropped images of CNP MPL captured by FIB-SEM imaging technique.

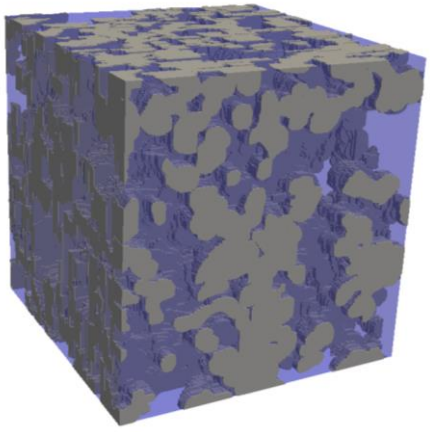

Figure 3.19. Segmented 3D reconstructed CNP MPL with D50 ≈ 40 nm with the porosity of 58%.

differentiate the solid phase from the pore space. The technique is based on identifying the solid phase contours using the brightness gradient within each image. The stack of 2D segmented images is combined in 3D to obtain a reconstructed volume (1 μm^3) of the microstructure. The resulting structures for the CNP MPL is illustrated in Figure 3.19.

The 3D reconstructed CNP MPL model as a binarized solid-pore digital image is utilized as a computational domain for calculation of pore size distribution by means of Euclidean distance transform (EDT) [107]. By applying the EDT, the binarized MPL reconstructed image, which consists of either solid voxel (0 value) and pore voxel (1 value), is converted into Euclidean distance map in which each pore voxel PV has a value corresponding to distance to the nearest solid voxel SV by utilizing the distance function as follows:

$$|d(PV, SV)| = \sqrt{(PV_x - SV_x)^2 + \left(PV_y - SV_y\right)^2 + (PV_z - SV_z)^2} \qquad (3\text{-}15)$$

where $PV = (PV_x, PV_y, PV_z)$ and $SV = (SV_x, SV_y, SV_z)$ are the coordinates of the pore and solid voxels, respectively. By applying Eq. (3-15) to all pore voxels, the Euclidean distance map is formed. The process is continued by finding the coordinates and the value of the local maxima in the Euclidean distance map which represents the center and radius of the pores, respectively [130,183].

In this study, FEI Helios NanoLab^{TM} 650 dual beam FIB-SEM system is utilized for high-resolution nano-tomography of the CNP MPL sample with D50 ≈ 40 nm. Figure 3.20 depicts the calculated CVF PSD data of the FIB-SEM reconstructed CNP MPL model as well as MIP-measured data compared to the stochastic CNP MPL model as a further validation of the MPL stochastic modeling framework which demonstrates a good agreement between the data. Note that pores larger than 1 µm in the MIP-measured PSD data are neglected to have a reasonable comparison with that of the FIB-SEM model due to micro-scale domain size (1×1×1 μm^3) in the FIB-SEM MPL microstructural reconstruction technique. As a recall, selecting the representative volume element (RVE) as the entire microstructure is typically too large to allow detailed micro-scale simulations. Alternatively, an RVE is selected as a micro-scale domain in the MPL material that is

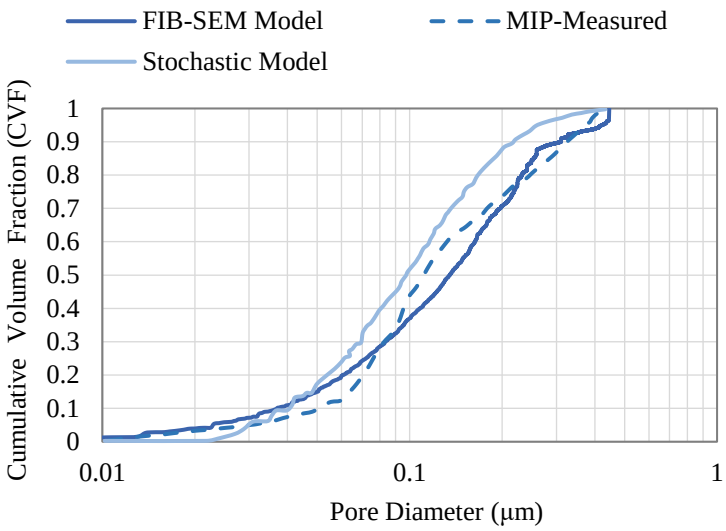

Figure 3.20. Cumulative PSD of the reconstucted CNP MPL (D50 ≈ 40 nm) model for the developed stochastic modeling framework compared to the developed FIB-SEM reconstruction technique using FEI Helios NanoLab™ 650 system as well as MIP-measured data (excluding large pores).

statistically representative of the entire sample's microstructure and represents the macroscale properties of the sample with a desired accuracy.

3.3. Results and Discussion

Microstructural MPL models are stochastically reconstructed and validated using the algorithm described in section 3.2.1 for CNP and FGP MPLs in different median particle sizes in which the stochastic approach is employed to represent the random nature of the MPLs under study. The anisotropic effective transport properties of the MPLs are simulated using the methodologies thoroughly explained in subsection 2.2.3 with the results elaborated in section 4.3.

3.4. Summary

In the present work, a comprehensive MPL stochastic microstructural modeling framework was developed to reconstruct the MPL structure by distinguishing between carbon or graphite particles and PTFE for different MPL compositions. The capabilities of the developed framework included reconstruction of MPL with different pore morphology compositions, *i.e.*, particle type, size, thickness, PTFE content, and the number of MPLs,

to study the influence of MPL morphology on GDL transport properties. The MPLs under study were conventional CNP MPL with median particle size of 40 nm and FGP MPLs with median particle sizes of roughly 8, 18, and 23 μm as promising alternatives for next-generation fuel cells. An extensive qualitative and quantitative validation was conducted for MPLs under study with measured SEM images, porosity, pore, and particle size distributions. Considering that the MPL is not a stand-alone layer, a technique was developed in this section to extract the MPL MIP PSD data of an MPL-coated Kapton film. In addition, a customized 3D morphological MPL characterization framework developed by our group featuring a customized FIB-SEM imaging reconstruction technique was employed in this work to further validate the CNP MPL pore structure. The validated modeling framework is a reliable well-established algorithm for design and prototyping assignments of hypothetical materials for next-generation fuel cells. Given the significant challenges associated with measurement of MPL transport properties, the numerical modeling is a compelling approach to obtain a comprehensive understanding of MPL transport properties which is addressed in this thesis.

Chapter 4.

Gas Diffusion Layer Characterization and Microstructural Modeling

In general, the GDL is a bi-layer graded porous structure which has two distinct layers, *i.e.*, an MPL coated on a macro-porous GDL substrate. Understanding the correlation between the MPL real pore morphology composition and MPL-coated GDL transport properties provides important information for material optimization and fuel cell design. Hence, the focus of this chapter is to stochastically reconstruct MPL-coated GDLs using single- and multi-pore-scale approaches where the GDL substrate and MPL microstructural modeling frameworks are established in Chapter 2 and Chapter 3, respectively, and to numerically model their transport properties. Furthermore, a parametric study is conducted to investigate the effect of MPL composition on MPL and MPL-coated GDL transport properties, *i.e.*, effective diffusivity, permeability, and thermal and electrical conductivities. In closing, the developed MPL and MPL-coated GDL microstructural modeling framework in this work, is expected to become a reliable tool for MPL and GDL design and prototyping assignments and can substantially reduce the time and cost of the MEA and fuel cell design cycles.

This chapter is structured as follows. Firstly, the MPL-coated GDL manufacturing process steps as well as qualitative and quantitative characterization of pore morphology and structure for single-layer MPLs coated on an AvCarb EP40T GDL substrate is described in section 4.1. Section 4.2 establishes pore-scale model approaches to stochastically reconstruct the MPL-coated GDLs under study. In section 4.2.2, a qualitative and quantitative microstructural validation is conducted for pore size distribution, porosity, and SEM images. In the last section, section 4.3, the effects of MPL particle type and size on the MPL and MPL-coated GDL transport properties, *i.e.*, effective diffusivity, permeability, and thermal and electrical conductivities, are investigated and the results are thoroughly elaborated.

4.1. GDL Morphology and Pore Structure Characterization

Commercially available MPLs are carbon-based materials normally composed of small-scale carbon powder and hydrophobic agent agglomerates. In conventional MPL-coated GDL manufacturing, *cf*. Figure 3.1, upon MPL deposition onto the GDL substrate, which is mostly a wet-coating process, the MPL forms a distinct layer on the GDL substrate with no clear interface [110]. It is due to likely penetration of several orders of magnitude smaller MPL agglomerates into comparatively larger open pores of the GDL substrate, thus, forming an uneven MPL-penetrated layer profile. The porous nature of the resulting MPL-coated GDL architecture is complex in terms of inherently different pore structures of the GDL substrate, as characterized in section 2.1, and MPL, as characterized in section 3.1, as well as the way they are connected [133]. Understanding the optimum MPL thickness and penetration profile which significantly influences the pore distribution throughout the GDL and consequently enhances mass transport, strength, and durability of a cell is a critical challenge. It is reported in the literature that the penetration profile is highly affected by MPL design parameters such as carbon powder and hydrophobic agent specifications (type, size, and density) and their loadings as well as MPL slurry and GDL manufacturing (MPL deposition, drying, and sintering techniques) [11,184,185]. Hence, they may exhibit different penetration behaviors, *i.e.*, partial, in-depth, or no penetration into the substrate. For instance, different MPL carbon powder types can induce significant differences in morphological and microstructural and consequently physical characteristics of the resulting MPL-coated GDLs [11,164]. The optimized MPL thickness controlled by carbon particle loading as well as the MPL penetrated profile can considerably improve the flow of reactants, by-products, and electrons throughout the GDL.

As a qualitative characterization, tracing several commercially available MPL-coated GDL cross-sectional SEM images with a sample image illustrated in Figure 4.1 verifies that the majority of the conventional MPL materials coated on a GDL substrate is present as a discrete layer on top of the GDL substrate with a minor degree of penetration into the substrate forming a compact composite-like architecture. The MPL-penetrated region at the MPL-substrate interface is predominantly associated with filling of open non-planar features at the surface of the GDL substrate, such as void spaces between the fibers.

As a result, the GDL substrate architecture is modified by lessening the volume of the macropores and consequently make the IP and TP MPL-coated GDL physical characteristics more uniform. Consequently, the GDL substrate and MPL-coated GDL are quite dissimilar in terms of morphology and pore structure, however, their morphological and microstructural characteristics are interdependent. It is worth noting that the MPL ink penetration is restricted by the hydrophobic properties of the PTFE-treated GDL substrate; thereby, the MPL-penetrated layer cannot be adjusted without significant changes in the fabrication procedure [17].

As a quantitative characterization, the measured DVF PSD data of a GDL substrate compared with an MPL-coated GDL achieved upon MPL deposition is depicted in Figure 4.2[12] adapted from an open literature to highlight the noticeably smaller and more homogeneous GDL microstructure pore sizes than that of the substrate [11]. Moreover, the CVF data of the two microstructures in micro, meso, and macropores ranges are tabulated in the figure. By analyzing the data, it is perceived that the MPL deposition results in a notable increase in the micropores volume associated with forming small spaces at the interfaces of the carbon fibers, carbon particles, and PTFE; but a dramatic decrease in the mesopores and macropores volumes of the substrate referred to filling these pores with MPL particles. Thereby, a more even GDL microstructure pore size distribution and accordingly more uniform IP and TP GDL physical characteristics are achieved.

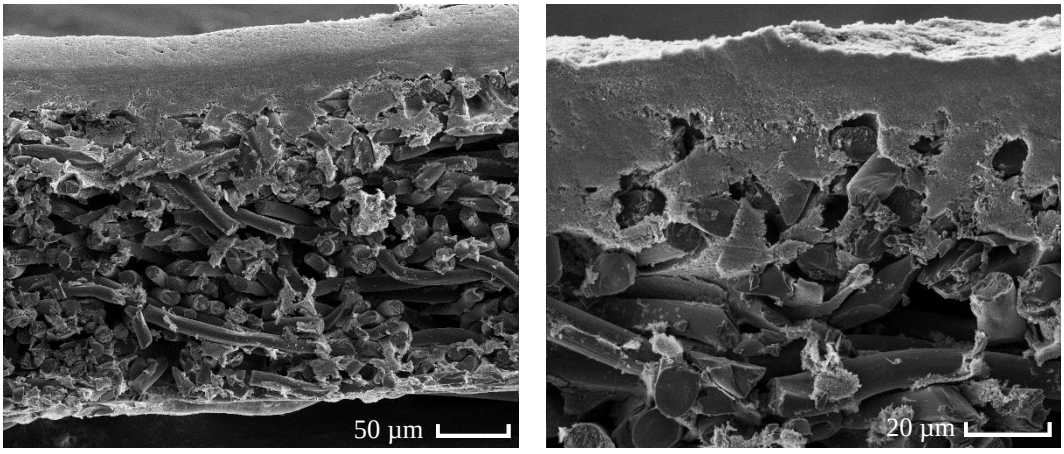

Figure 4.1. Cross-sectional view SEM image of a GDL (CNP MPL-coated GDL).

[12] Reprinted from [11] with minor modifications with permission from Elsevier.

To implement a reliable model of the FGP MPL-coated GDL, a characterization study is conducted in this work to investigate the effect of FGP MPL particle size on the GDL porosity and thickness and thereby MPL penetration profile into the GDL substrate. In Figure 4.3, MIP-measured porosity of five different MPL-coated GDL samples coated with FGP MPLs with 2, 6, 8, 11, and 23 µm median particle sizes in 30 and 60 g m^{-2} MPL loadings are compared to that of the AvCarb EP40T GDL substrate. The MPL-coated GDL porosity in the figure shows a linearly decreasing trend from about 81% for the GDL substrate to 77% and 73% for the MPL-coated GDL with 30 g m^{-2} and 60 g m^{-2} MPL loadings, respectively, independent of the MPL median particle size. It is observed that the MPL-coated GDL porosity, which is mostly influenced by the GDL substrate large pores, is approximately the same irrespective of the MPL median particle size for both MPL loadings. This means that the MPL penetration into the GDL substrate, which is associated with filling of open non-planar features at the surface of the GDL substrate, is fairly

	Micropores pores < 50 nm	Mesopores 50 nm < pores < 7 µm	Macropores pores > 7 µm
GDL substrate CVF	7%	42%	51%
MPL-coated GDL CVF	33%	39%	28%

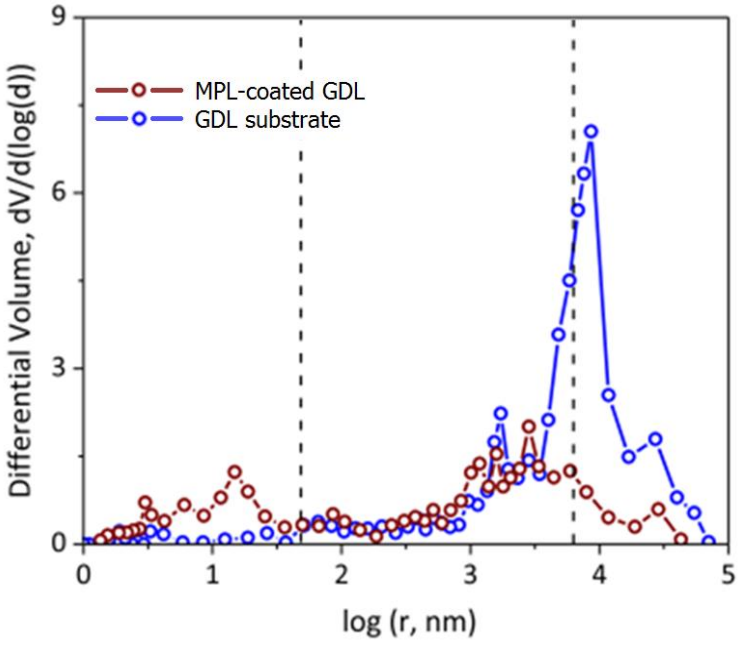

Figure 4.2. Graphical differential volume fraction illustration of a carbon paper GDL susbtrate compared with an MPL-coated GDL along with tabulated cumulative volume fraction data in different pore size ranges [11].

independent of the MPL particle size. Furthermore, the measured GDL thicknesses under 200 psi compression pressure are depicted in Figure 4.4 as a function of MPL median particle sizes and loadings. In agreement with the porosity data, the GDL thickness is practically independent of the particle size. The significant thickness increase between 30 and 60 g m^{-2} MPL loadings combined with the measured porosities emphasize the fact that most of the MPL sits as a discrete layer on top of the GDL substrate with marginal penetration into the GDL substrate. In addition, more details on the MPL-substrate interaction is essential to have a reliable MPL-coated GDL model implementation that can be inspired from cross-sectional SEM images.

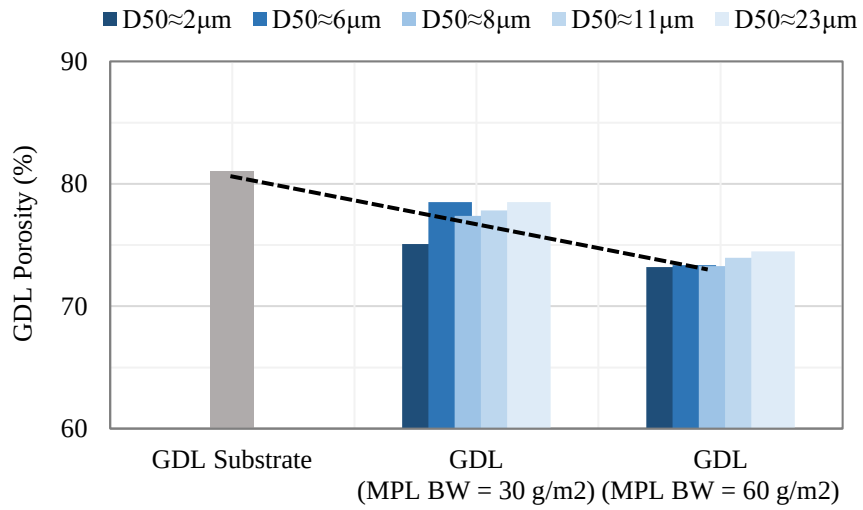

Figure 4.3. MIP-measured MPL-coated GDL porosity (%) with 0, 30, and 60 g m^{-2} MPL loading for flake graphite particle MPLs with different median particle sizes.

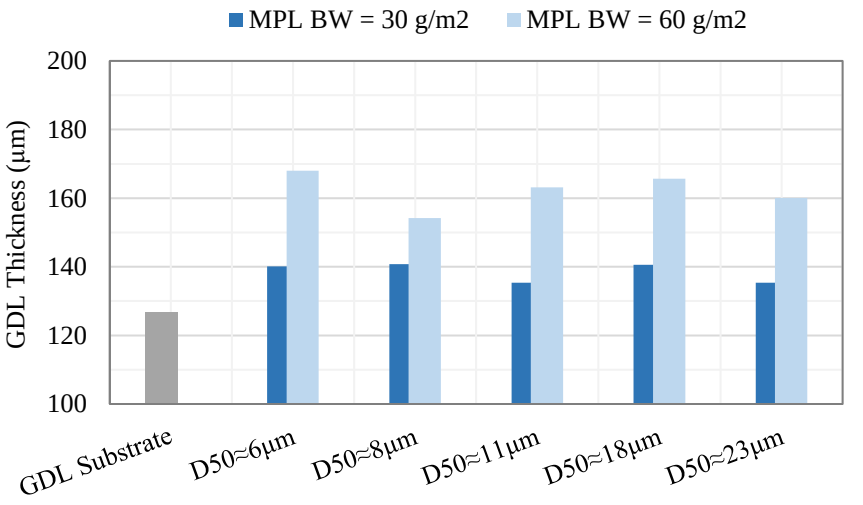

Figure 4.4. Measured GDL thickness under 200 psi compression with 30 and 60 g m^{-2} MPL loading for flake graphite particle MPLs with different median particle sizes.

4.2. Numerical Formulation

4.2.1. GDL Stochastic Microstructural Modeling

In order to develop an accurate MPL-coated GDL reconstruction design tool, detailed information on the porous medium structure is required. Inspired by the MPL-coated GDL characterization, *cf.* section 4.1, the MPL-coated GDL generally consists of a GDL substrate and a coated MPL as a discrete layer on top of the substrate with a certain degree of penetration. To precisely model the full GDL as a computational grid for GDL transport properties simulation, the individually reconstructed GDL substrate and MPL structures should be combined in a way in which the challenges associated with MPL penetration and the difference in their pore size ranges are resolved. By analyzing the GDL SEM images, *cf.* Figure 3.2, it is realized that the thickness of the MPL-penetrated layer, which is associated with filling of open non-planar features at the surface of the substrate, does not have a uniform pattern along the surface. In this work, the average of the penetration thickness pattern is considered as the penetration thickness h_{pen} which is a factor of the MPL thickness as follows:

$$h_{pen} = k_{pen} h_{MPL} \tag{4-1}$$

where h_{MPL} is the MPL thickness derived from Eq. (3-13) and $0 < k_{pen} < 1$ is the relative penetration with no penetration being 0 and full penetration being 1.

The MPL-coated GDLs studied in this work are single-layer MPLs coated on an AvCarb EP40T GDL substrate. The MPLs include CNP MPL with median particle size of 40 nm and FGP MPLs with median particle sizes of roughly 8, 18, and 23 μm. The pore size range of the FGP MPLs (mesopores to macropores) is roughly on the same order as that of the GDL substrate (macropores) as characterized in detail in sections 2.1 and 3.1. Thus, a low-resolution single-pore-scale model is able to reconstruct the porous structure of the FGP MPLs coated on GDL substrate. The process steps are graphically illustrated in Figure 4.5. The MPL-coated GDL reconstruction process starts with (1) cropping the bottom of reconstructed GDL substrate structure to the considered MPL-penetrated layer

thickness. In the next step, (2) voxels are embedded to the top of the structure to meet the MPL thickness followed by (3) overlaying with the reconstructed FGP MPL model. The final steps are to (1') crop the top of the original reconstructed GDL substrate structure for the considered MPL-penetrated layer thickness and (4) add it to the bottom of the overlaid reconstructed FGP MPL model. Note that all reconstruction process steps are conducted in the TP direction.

On the contrary, the pore size range of the CNP MPL (micropores) and the GDL substrate (macropores) differ by two or three orders of magnitude, as characterized in detail in sections 2.1 and 3.1. Therefore, the provision of a single-pore-scale stochastic model is not feasible to resolve the microporous structure of the CNP MPL and accurately model a sufficiently large domain of the macroporous GDL substrate [109]. Hence, two multi-pore-scale MPL-coated GDL reconstruction approaches are proposed. The first approach is the homogeneous multi-pore-scale MPL-coated GDL model which is composed of a high-resolution model (voxel length: 20 nm) to resolve the porous structure of the CNP MPL and a low-resolution model (voxel length: 0.5 µm) to reconstruct the GDL in which the MPL is added as a homogeneous porous medium on the reconstructed macroporous GDL

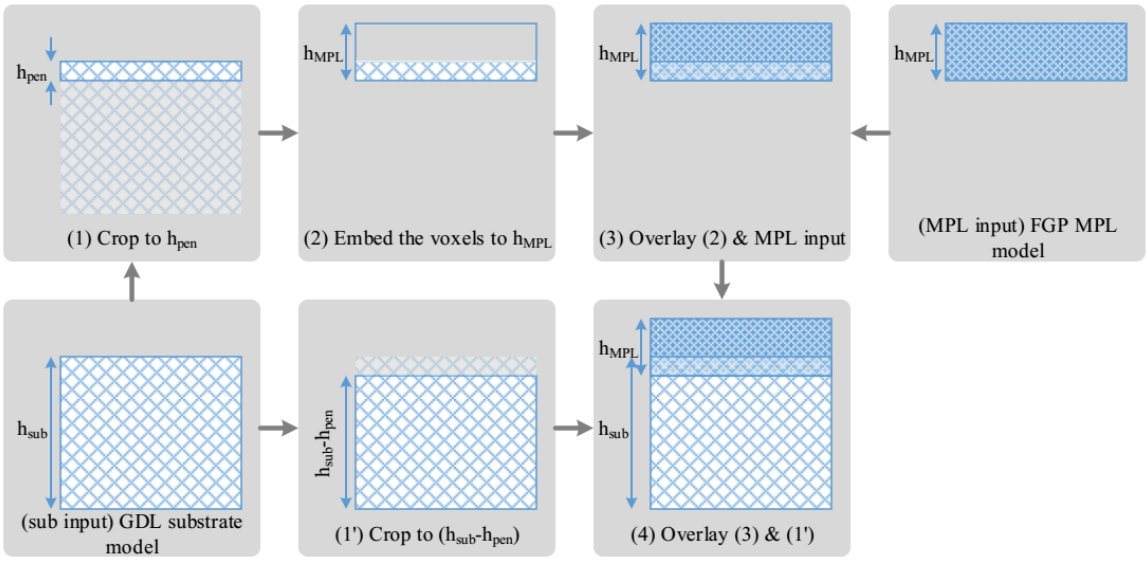

Figure 4.5. Graphicall illustration of the process steps for low-resolution single-pore-scale MPL-coated GDL model.

substrate with an MPL-penetrated layer thickness, *cf.* Figure 4.6(a). The alternative approach is the network resistance model graphically depicted in Figure 4.6(b) in which the low-resolution GDL substrate and the high-resolution CNP MPL are stochastically reconstructed as individual layers followed by simulation of their transport properties. Thereafter, the overall MPL-coated GDL resistive properties in the IP and TP directions are calculated as follows:

$$R_{IP} = (R_{MPL}^{-1} + R_{sub}^{-1})^{-1} \tag{4-2}$$

$$R_{TP} = R'_{MPL} + R'_{sub} \tag{4-3}$$

where $R_{MPL} = 1/D_{IP,MPL}A_{MPL}$, $R_{sub} = 1/D_{IP,sub}A_{sub}$, $R'_{MPL} = h_{MPL}/D_{TP,MPL}$, and $R'_{sub} = h_{sub}/D_{TP,sub}$ for the case of MPL-coated GDL effective diffusivity property. The network resistance model does not take into consideration the MPL penetration into the GDL substrate and its compounded diffusion resistance which results in higher GDL gas diffusivity compared to the homogeneous model, as a sensitivity study will be elaborated later in section 4.3.1. Therefore, the homogeneous multi-pore-scale model is the preferable framework for full GDL simulations.

In this study, the simulations conducted for the CNP MPL-coated GDL are based on the homogeneous multi-pore-scale approach where the MPL is treated as a homogeneous porous medium added to the macroporous GDL substrate model in which the MPL intrudes to the substrate by the penetration coefficient. To follow this idea, the modeled MPL properties using a high-resolution reconstructed microstructure are considered as an input for the low-resolution MPL-coated GDL model to calculate the GDL transport properties. The reconstructed GDL is a rectangular cuboid computational domain composed of cubic voxels where each voxel serves as either solid material (carbon fiber, binder, or PTFE) or void space (GDL substrate pores) or homogeneous porous medium (MPL) with specified simulated MPL properties. The process of adding the CNP MPL to the GDL substrate is implemented using the same approach as for the FGP MPL-coated GDL model, *cf.* Figure 4.5.

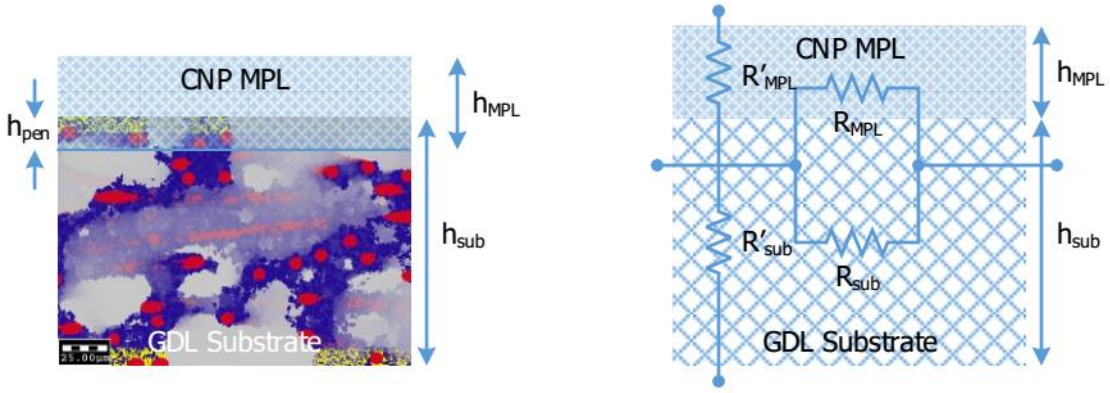

(a) (b)

Figure 4.6. Schematic illustration of (a) homogeneous multi-scale and (b) network resistance multi-pore-scale model of an MPL-coated GDL (CNP MPL coated on an Avcarb EP40T GDL substrate).

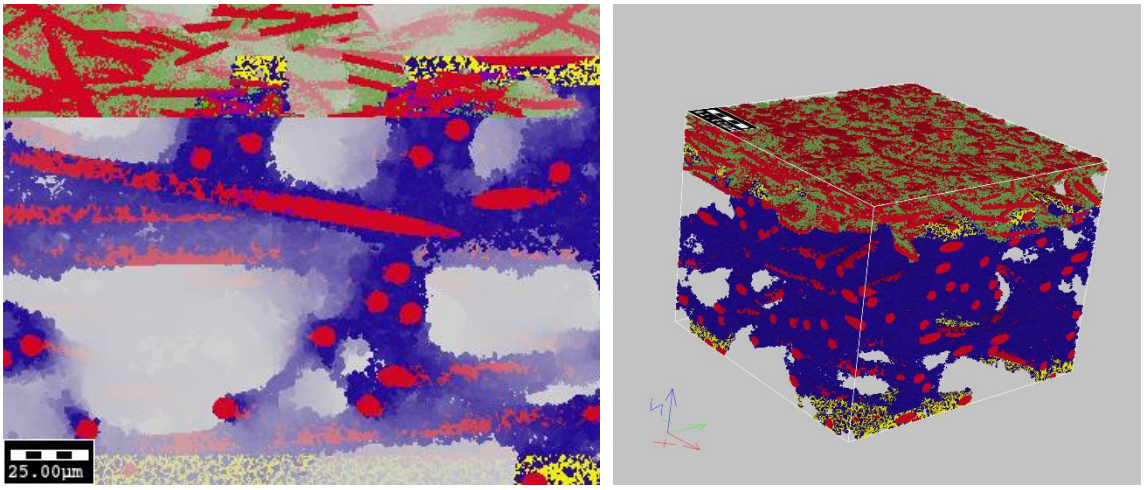

Figure 4.7. 2D and 3D views of the reconstructed GDL model for 60 g m^{-2} FGP MPL (graphite particles in red and PTFE in green) with D50 ≈ 23 µm coated on AvCarb EP40T GDL substrate (carbon fibers in red, binder in blue, and PTFE in yellow).

4.2.2. Model Validation

Figure 4.7 depicts the 2D and 3D views of the reconstructed model for 60 g m^{-2} FGP MPL with D50 ≈ 23 µm coated on AvCarb EP40T GDL substrate. In the figure, the FGP MPL is coated on GDL substrate with 20 µm MPL-penetrated layer thickness with the overall GDL porosity of 74%. Figure 4.8 illustrates the experimental and simulated CVF of a GDL substrate compared with a GDL on which 60 g m^{-2} FGP MPL with D50 ≈ 8 or 23 µm is coated on AvCarb EP40T GDL substrate. Note that, to reconstruct the MPL-coated GDL, the GDL reconstruction with different MPL-penetrated layer thicknesses is

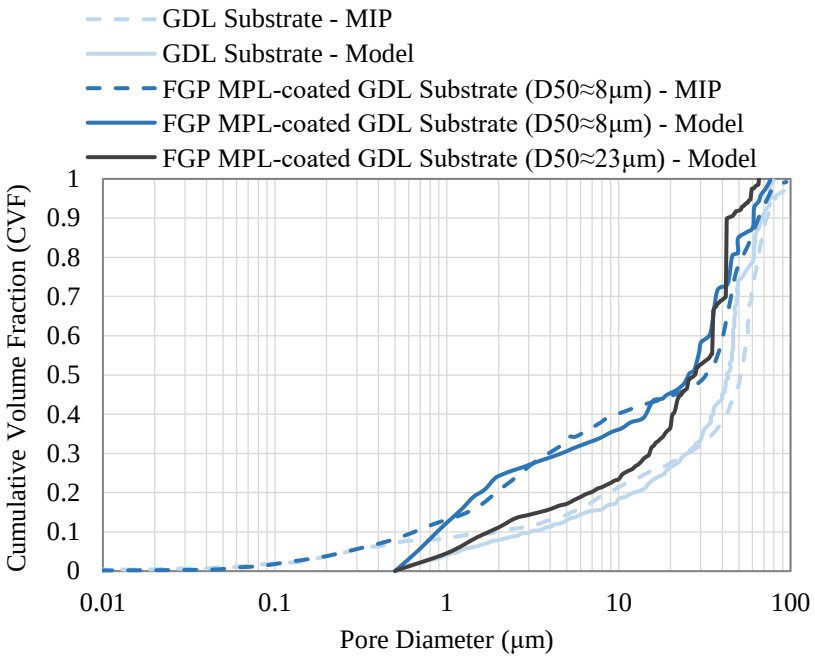

Figure 4.8. Simulated cumulative PSD data of AvCarb EP40T GDL substrate and 60 g m^{-2} FGP MPL with D50 ≈ 8 or 23 µm coated on GDL substrate compared to measured MIP PSD data of the corresponding GDL substrate and FGP MPL-coated GDL with D50 ≈ 8 µm.

exercised through which the optimum GDL thickness, porosity, and pore size distribution is achieved. As a result, 20 µm MPL-penetrated layer thickness is considered for 60 g m^{-2} MPL coated on AvCarb EP40T GDL substrate for FGP and CNP MPLs; representing a reasonable planar (average) reconstruction of non-planar MPL filling of the open surface GDL substrate. The simulated PSD in Figure 4.8 is in good agreement with the MIP-measured data for the GDL substrate as well as the FGP MPL-coated GDL with D50 ≈ 8 µm. By coating the MPL on GDL substrate, the CVF data of the GDL is shifted to the left compared with the GDL substrate due to the added smaller pores. Moreover, the MPL marginal penetration into the GDL substrate results in a slight decrease in the number of larger pores in the GDL.

4.3. Results and Discussion

In this section, the effect of MPL structure (particle type and size) on transport properties of MPLs and MPL-coated GDLs under study, *i.e.*, effective diffusivity, tortuosity, permeability, and thermal and electrical conductivities, are investigated in detail. The three principal directions of transport properties are considered in both through-

plane (TP; *z*) and in-plane (IP; *x* and *y*) directions. The simulated data reported here are the average transport properties of ten stochastic structures and the variability is indicated by 95% confidence intervals. Given that the delicate MPL layer is not a stand-alone layer and the high uncertainties and cost are associated with MPL transport property measurements, numerical modeling is a compelling approach to obtain comprehensive understanding of these properties. This modeling approach thus serves as a bridge between the MPL real pore morphology composition and MPL-coated GDL transport properties for material optimization and fuel cell design.

4.3.1. Effective Diffusivity

Figure 4.9(a) and (b) illustrate the simulated IP and TP tortuosity and effective diffusivity of the CNP MPL model with D50 ≈ 40 nm and FGP MPL models with D50 ≈ 8, 18, and 23 μm. The simulated FGP MPLs' tortuosity and diffusivity reveal the preferential IP particle orientation of the MPLs which results in IP-oriented connected pores and consequently lower tortuosity and enhanced diffusivity capabilities compared with the TP direction. As mentioned in the FGP MPL pore structure characterization in section 3.1, an increasing porosity trend is observed with the MPL particle size from porosity of ~56% with D50 ≈ 8 μm to ~70% with D50 ≈ 23 μm. Similarly, large pores associated with the effective particle spacing of the MPL microstructure shows an unambiguously increasing trend with the FGP MPL graphite particle size, thus, a decreasing tortuosity tendency. Therefore, an increasing trend is exhibited in the effective diffusivity in all three principal directions by increasing the FGP median particle size from D50 ≈ 8 μm to 23 μm. The findings demonstrate that the particle size adjustment enables precise control over the effective MPL pore size, tortuosity, and consequently effective diffusivity.

To simulate diffusion in MPL porous media, determining the porous medium pore size range offers an opportunity to understand which diffusion type has the dominant effect on the overall gas reactant diffusion transport. As noted in subsection 2.2.3ii, the contribution of each type of diffusion, *i.e.*, bulk diffusion D_{bulk} and Knudsen diffusion D_{Kn}, to the overall diffusion is described by the Knudsen number. The mean free path of

the key GDL gas reactants such as hydrogen, nitrogen, and oxygen is estimated in the range of 65-75 nm at atmospheric temperature and pressure conditions. Hence, the gas reactant transport through bulk diffusion is dominant where the diameter of the pores is generally two orders of magnitude higher than the gas reactant mean free path ($Kn \ll 1$ in pore diameters > ~10 µm), whereas in pores with diameters less than one-tenth of the mean free path ($Kn \gg 1$ in pore diameters < ~10 nm), the Knudsen diffusion becomes dominant. For any other pore diameters between the above limits, both diffusion types are taken into effect. The relationship used for mixed diffusion for which $Kn \approx 1$ is a series network resistance model known as the Bosanquet equation [139,140]. Therefore, the bulk diffusion is considered as the dominant diffusion through the relatively large pores of the FGP MPLs (pore diameters > ~10 µm) whilst the combination of Knudsen and bulk diffusion (Bosanquet equation) are taken into account in the effective gas diffusion mechanism through the CNP MPL pores (~50 nm < pore diameters < ~10 µm).

Given that the porosity of the CNP MPL ($\varepsilon \approx 62\%$) is higher than that of the FGP MPL with D50 ≈ 8 µm ($\varepsilon \approx 56\%$) and their approximately equivalent IP tortuosity values of ~2, the comparatively lower IP diffusivity of CNP MPL (~60%) can be attributed to the higher contribution of Knudsen diffusion to the overall diffusion, whereas it is mainly influenced by bulk diffusion in FGP MPLs, *cf.* Figure 4.9. With the same scenario as the above, TP diffusivity of the CNP MPL is slightly lower than that of the FGP MPL with D50 ≈ 8 µm, whilst, the CNP MPL is ~50% less tortuous which is associated with the contribution of Knudsen effect. The higher diffusivity values for FGP MPL with D50 ≈ 8, 18, and 23 µm compared with CNP MPL are likely favorable for PEFCs operating at high current density conditions where oxygen diffusion rates are important in the context of GDL design.

The simulated IP and TP effective diffusivity of the CNP MPL is also compared to available literature data [32,94] in Figure 4.9. The isotropic particle distribution of the CNP MPL results in approximately the same tortuosity and consequently the same diffusivity of ~0.12 in both IP and TP directions. The simulated TP diffusivity is in reasonable agreement with our group's previously reported data obtained using the FIB-SEM characterization technique [94]. The TP diffusivity is also compared to the measured data in [32] where an

MPL coated on SolviCore carbon paper GDL substrate was measured using a Loschmidt cell apparatus with an oxygen-nitrogen gas mixture. Using a series resistance network, the MPL TP diffusion was estimated to be $1.54\pm0.22\times10^{-6}$ m^2 s^{-1} which is equivalent to an effective diffusivity of 0.073±0.01 for the calculated porosity of 64%. The difference between the diffusivity of the present model and the measured data in [32] may be associated with ignoring the resistance of the MPL-penetrated layer into the GDL substrate in their MPL-coated GDL resistance network analysis.

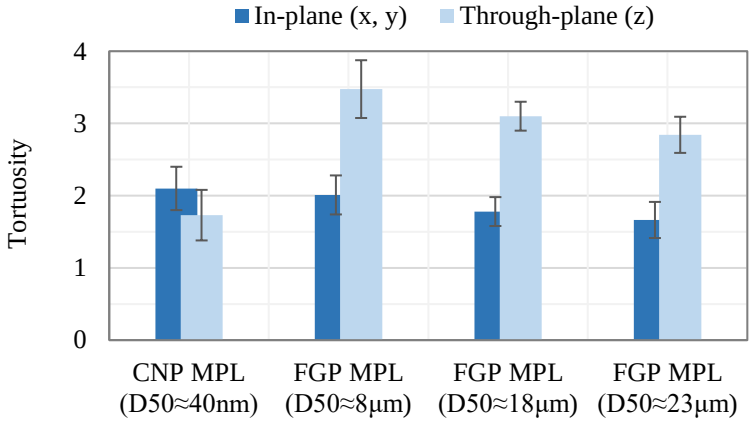

(a)

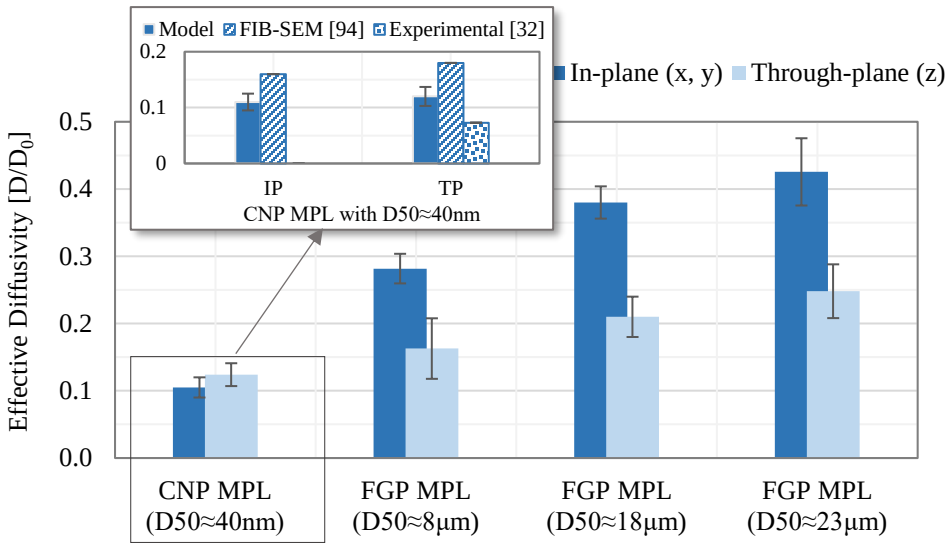

(b)

Figure 4.9. Simulated IP and TP (a) tortuosity and (b) effective diffusivity of the CNP MPL stochastic model with D50 ≈ 40 nm and FGP MPL models with D50 ≈ 8, 18, and 23 µm. Comparison is made in (b) with FIB-SEM characterization data [94] and experimental data [32].

In order to better understand the effect of adding MPL to the GDL substrate, Figure 4.10(a) and (b) illustrate the simulated IP and TP tortuosity and effective diffusivity of the corresponding full GDLs with 60 g m^{-2} MPL loading coated on an AvCarb EP40T GDL substrate. The results demonstrate that the average effective diffusivity of the MPL-coated GDL for CNP MPL with D50 ≈ 40 nm and FGP MPLs with D50 ≈ 8, 18, and 23 μm compared to the bare GDL substrate is substantially reduced by ~58% (from 0.62 to ~0.26) in the TP direction whereas only by ~18% in the IP direction. The TP gas diffusion pathways are narrowed down along the diffusion direction with a steep TP tortuosity increase of 2.2x due to the presence of the MPL, while in the IP direction, the main diffusion pathways of the GDL substrate remain intact except for the MPL-penetrated layer at the top with a slight IP tortuosity increase of 1.1x, *cf.* Figure 4.10(a). Note that, 20 μm MPL-penetrated layer thickness is considered for 60 g m^{-2} MPL coated on AvCarb EP40T GDL substrate for CNP and FGP MPLs.

In Figure 4.10, the simulated TP effective diffusivity of the FGP MPL-coated GDLs is increased slightly with particle size from D50 ≈ 8 μm to 23 μm as a result of higher MPL porosity, larger pore size, and reduced tortuosity. The slight decrease in the FGP MPL TP tortuosity with increasing particle size, *cf.* Figure 4.9, has a direct effect on the full GDL tortuosity drop by ~30%. The more tortuous TP diffusion pathway is likely exacerbated by the reduced volume of macropores within the GDL substrate in the MPL-penetrated layer. It should be noted that the highest TP diffusion resistance is observed in the MPL-penetrated layer within the top portion of the GDL substrate by analyzing the simulated concentration field; thereby, the net MPL penetration into the GDL substrate plays an important role for the overall diffusion coefficient. Regarding the IP diffusivity, even though the IP tortuosity of FGP MPLs has a mild decreasing trend with particle size, *cf.* Figure 4.9, the IP tortuosity and subsequently IP diffusivity of the full GDL remains approximately unchanged. This is owing to a largely retained IP diffusion pathway in the GDL substrate. In addition, the CNP MPL has the lowest MPL diffusivity attributed to the contribution of Knudsen diffusion despite the fact that FGP MPL with D50 ≈ 8 μm has the highest MPL tortuosity, *cf.* Figure 4.9. Nevertheless, the lowest full GDL TP diffusivity is associated with the FGP MPL-coated GDL with D50 ≈ 8 μm due to the highest tortuosity value of 3.6 in the TP direction.

The pore size range of the FGP MPLs (mesopores to macropores) is roughly on the same order as that of the GDL substrate (macropores). Thus, a single low-resolution pore-scale model (voxel length: 0.5 μm) is able to reconstruct the porous structure of the FGP MPLs coated on GDL substrate as the process steps are thoroughly elaborated in section 4.2.1. A sensitivity study is conducted to verify the negligible contribution of Knudsen diffusion on the overall effective diffusivity of GDL substrate coated with FGP MPLs. In this study, a 4x higher resolution FGP MPL with D50 ≈ 8 μm is modeled and the diffusivity of the GDL substrate coated with the FGP MPL is simulated using the Bosanquet approximation. The result reveals ~12% lower diffusivity compared to the low-resolution model where bulk diffusion is the only contributor of the overall diffusion.

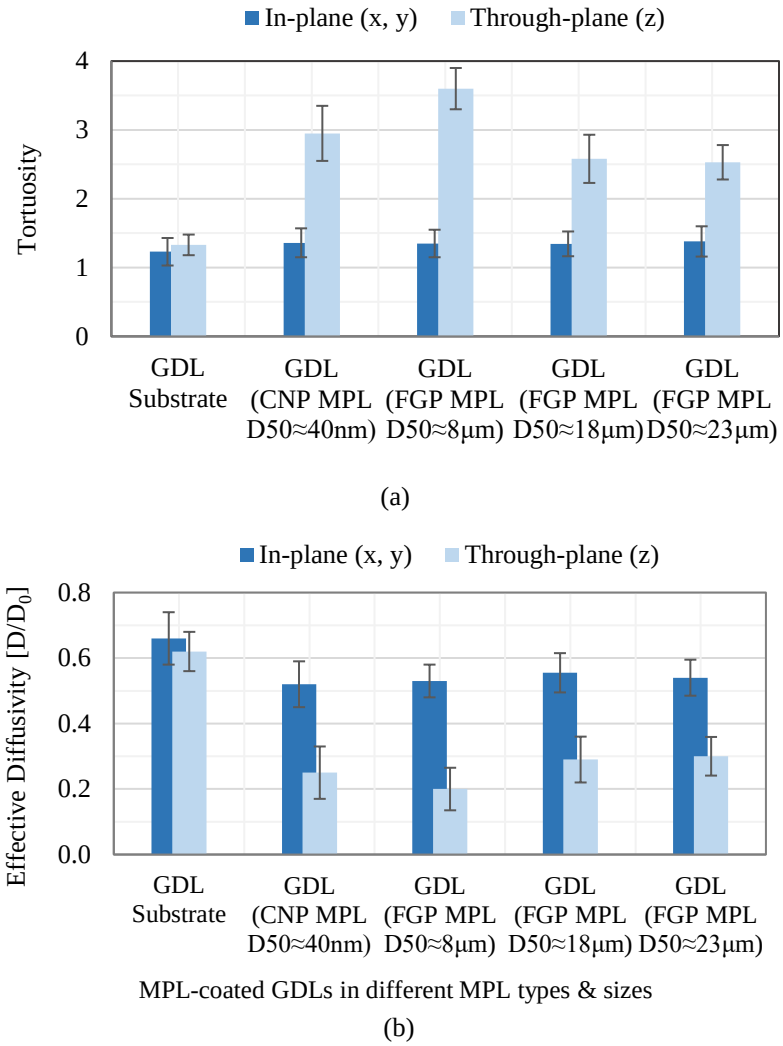

Figure 4.10. Simulated IP and TP (a) tortuosity and (b) effective diffusivity of an Avcarb EP40T GDL substrate with and without MPL coating with different MPL particle types and sizes.

On the contrary, the pore size range of the CNP MPL (micropores) and the GDL substrate (macropores) differ by two or three orders of magnitude. Therefore, the provision of a single-resolution stochastic model is not feasible to resolve the microporous structure of the CNP MPL and accurately model a sufficiently large domain of the macroporous GDL substrate. Hence, two multi-pore-scale MPL-coated GDL reconstruction approaches were proposed. The first approach is the homogeneous multi-pore-scale model and the alternative approach is the network resistance model as extensively discussed in section 4.2.1. For the sake of comparison, the simulated IP and TP effective diffusivity of the CNP MPL-coated GDL using the two approaches are compared and validated with measured data in Figure 4.11. The network resistance model is observed to slightly overestimate the GDL diffusion properties compared to the homogeneous model and measured data, which stems from the fact that the network resistance model neglects the MPL penetration into the GDL substrate and its compounded diffusion resistance. Hence, the homogenous modeling approach is generally recommended for diffusion simulation.

4.3.2. Permeability

Figure 4.12 illustrates the simulated IP and TP permeability of the CNP MPL with D50 ≈ 40 nm and FGP MPLs with D50 ≈ 8, 18, and 23 µm and their respective MPL-coated GDLs compared with the results of the AvCarb EP40T GDL substrate model. First

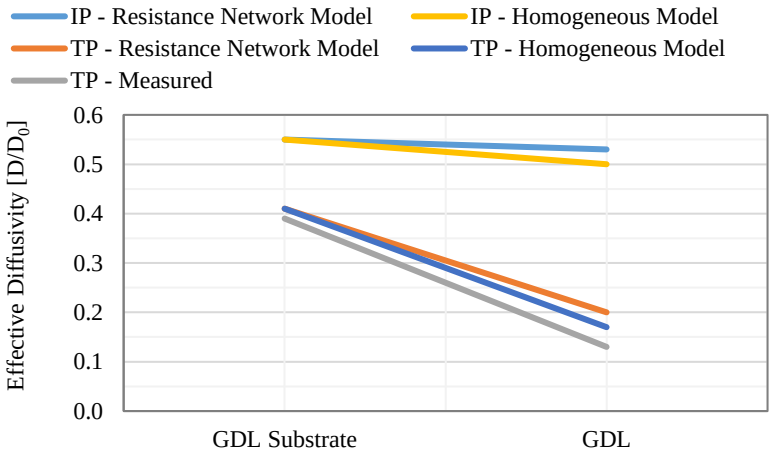

Figure 4.11. Simulated IP and TP diffusivity of the CNP MPL-coated GDL with macro-homogeneous and resistance network models compared with that of the GDL substrate and measured data.

of all, the trends and observations demonstrate that the MPL permeability (between 10^{-13} and 10^{-12} m^2) is lower than that of the GDL substrate (~10^{-11} m^2) owing to the MPLs' smaller pores, lower porosity, and higher PTFE loading. This sharp reduction is most notable for the CNP MPL (~10^{-13} m^2) having two orders of magnitude lower permeability due to its fine pore structure and consequently the contribution of Knudsen effects as extensively elaborated in subsection 2.2.3iii. Likewise, the CNP MPL has considerably lower gas permeability and hence higher flow resistance relative to the FGP MPLs. Second, the IP and TP permeability of the FGP MPLs increases with particle size due to their larger overall pore size and porosity which reduces the flow resistance. It is worth noting that the IP permeabilities are twice the TP ones due to the preferential particle alignment in the *xy*-plane and larger connected pathways for the flow.

Third, the IP and TP simulated permeabilities of the MPL-coated GDLs are substantially reduced compared to that of the bare GDL substrate as shown in Figure 4.12. As expected, the reduction in the TP permeability, which is mainly attributed to addition of the substantially low-porosity and small pore size MPLs to the bare GDL substrate, is much more significant than in the IP directions where the high permeability of the GDL substrate prevails. Due to such low permeability MPLs, the MPL becomes the convective

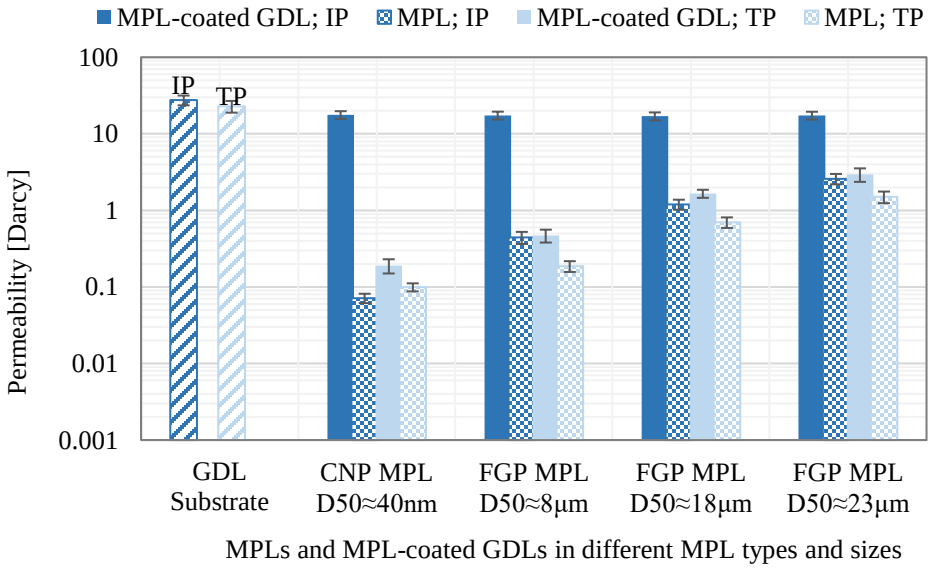

Figure 4.12. Simulated IP and TP permeability of AvCarb EP40T GDL substrate model compared with CNP MPL with D50 ≈ 40 nm and FGP MPLs with D50 ≈ 8, 18, and 23 µm and their respective MPL-coated GDL models.

TP transport limiting layer in the MPL-coated GDLs, which is of particular importance for liquid water transport and water management in the MEA. Fourth, the TP permeability of the full GDL is also observed to be highly sensitive to the MPL structure, where the MPL adds a sizable flow resistance for the GDL. Hence, the trends of the TP permeability curves of the MPL-coated GDLs are, in general, in accordance with those of the MPLs. The CNP MPL-coated GDL has the lowest TP permeability, two orders of magnitude lower than that of the GDL substrate and the TP permeability increases considerably with particle size for the FGP MPL-coated GDLs. Finally, with the same analysis as the GDL IP diffusivity, it is observed that the IP GDL permeability is independent of MPL particle size as the GDL substrate carries most of the in-plane flow and the MPL-penetrated layer thickness is limited relative to the GDL substrate thickness.

Several comprehensive mathematical models such as the widely known Kozeny–Carman method have been developed to estimate the gas permeability of porous media based on the pore characteristics, *i.e.*, porosity, tortuosity, and mean pore size [11,186]. However, such a model has not yet been developed to precisely estimate the GDL gas permeability, given its relatively complex pore structure. Moreover, these models only represent the contributions of the GDL substrate and do not consider the addition of the MPL. Thus far, due to uncertainties in MPL gas permeability mathematical models and lack of accurate experimental data, MPL permeability simulations such as the ones reported here could conceivably bridge this knowledge gap and be used for material optimization and fuel cell design.

4.3.3. Conductivity

i. Electrical Conductivity

The ohmic losses due to electronic conduction in a fuel cell are a combination of the internal electrical resistances, which are related to the intrinsic (bulk) characteristics of each individual cell component, and the interfacial electrical resistances, due to the differences in the structural, morphological, and chemical properties of the cell components in contact. The electron transport pathways in the transition region between the catalyst layer and GDL substrate are complex due to morphological and structural dissimilarity

between the two; thereby, the interfacial electrical resistance is generally high. To this end, coating the MPL on the GDL substrate surface facing the catalyst layer results in filling the macroscale pores and building up more direct and additional electron-carrying pathways between the two, thus reducing the interfacial contact resistance. However, the MPL introduces additional bulk electrical resistance that needs to be accounted for.

The IP and TP effective electrical conductivity, σ_{eff}, of the MPLs and MPL-coated GDLs under study are estimated by simulation of steady-state electrical conduction in the solid phase of the microstructural models with data shown in Figure 4.13. Note that, 20 µm MPL-penetrated layer thickness is considered for 60 g m^{-2} MPL coated on AvCarb EP40T GDL substrate for CNP and FGP MPLs. First of all, the isotropic particle distribution in the CNP MPL results in approximately equal electrical conductivity in both IP and TP directions whereas the preferential IP particle orientation of the FGP MPLs leads to enhanced IP electrical conductivity, roughly twice the value in the TP direction. Second, a lower electrical conductivity is observed in the CNP MPL compared to the FGP MPL with D50 ≈ 8 µm which can be explained by the smaller particle size, decreased number of contact points between particles, and higher porosity of the CNP MPL ($\varepsilon \approx 62\%$) compared to the FGP MPL with D50 ≈ 8 µm ($\varepsilon \approx 56\%$). Third, within the FGP MPLs category, an

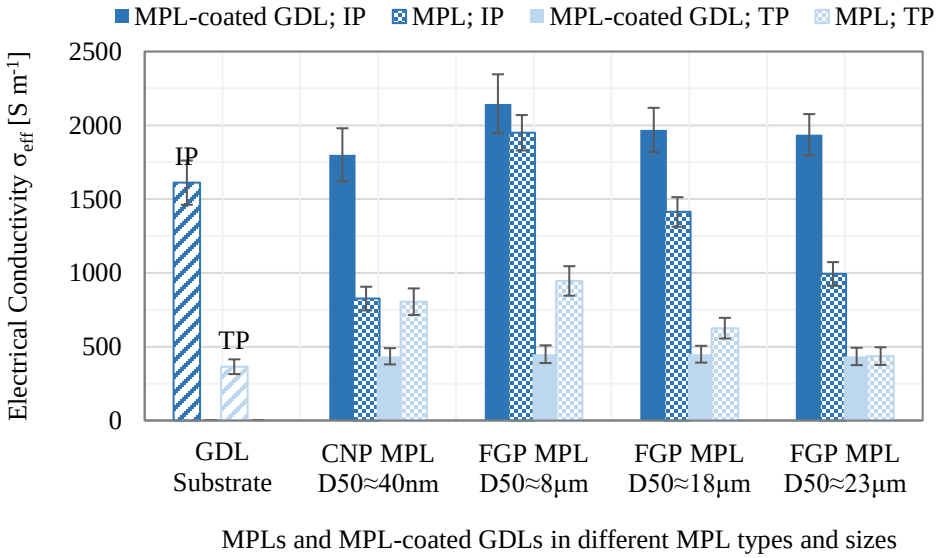

Figure 4.13. Simulated IP and TP electrical conductivity of Avcarb EP40T GDL substrate model compared with CNP MPL with D50 ≈ 40 nm and FGP MPLs with D50 ≈ 8, 18, and 23 µm and their respective MPL-coated GDL models.

increasing pore size trend associated with the effective particle spacing of the MPLs microstructure is observed as anticipated with the MPL particle size from porosity of ~56% with D50 ≈ 8 µm to ~70% with D50 ≈ 23 µm. Thus, the electron transport pathways and consequently the electrical conductivity is found to decrease with increasing particle size.

Furthermore, the MPL-coated GDLs have roughly 20% higher IP and TP electrical conductivity than the bare GDL substrate for all MPL types under study. This is attributed to the higher TP conductivity of the MPLs compared to the substrate and the MPL/substrate overlap in the penetration region. Moreover, the MPL-coated GDLs exhibit approximately 5x higher electrical conductivity in the IP direction than in the TP direction due to the anisotropic GDL substrate fiber alignment that also coincides with the particle alignment in the FGP MPLs which results in more direct pathways for electron transport in the IP direction. Finally, it is concluded that the type and size of carbon particles making up the MPL influences the electron transport capabilities of the MPL-coated GDL.

ii. Thermal Conductivity

Heat transfer in PEFC GDLs is dominated by conduction, which occurs through solid phase, fluid phase, and interconnected fibers and particles. The temperature gradient, which is a strong function of the cell components' thermal conductivities, is a critical parameter that impacts both water and heat transport mechanisms, and consequently the performance and durability of the cell. Therefore, detailed thermal analysis and subsequently accurate knowledge on thermal conductivity of cell components, particularly the GDL, is crucial. The GDL thermal conductivity is generally represented by effective thermal conductivity, *i.e.*, a thermo-physical property that takes the contribution of each species' thermal conductivity into effect.

The simulated IP and TP effective thermal conductivity, K_{eff}, of the MPLs and MPL-coated GDLs under study are illustrated in Figure 4.14, in general, with the same trend as effective electrical conductivity. With the same logic as electrical conductivity results; approximately equal thermal conductivity in both IP and TP directions in the CNP MPL compared to FGP MPLs with enhanced IP electrical conductivity roughly twice the value in the TP direction; lower thermal conductivity in the CNP MPL compared to the

FGP MPL with D50 ≈ 8 µm; and decrease in thermal conductivity of FGP MPLs with increasing particle size are observed.

Furthermore, it is observed that the thermal conductivity of the MPL-coated GDLs is significantly higher than that of the bare GDL substrate for all MPL types under study with ~70% and ~140% increases in the TP and IP directions, respectively. This finding is in contrast to the mild increasing trend of electrical conductivity in the MPL-coated GDLs which is the key difference between the two conductivities. This is ascribed to the higher values of the local thermal conductivities of MPL structure components in contrary to their local electrical conductivities. As mentioned in section 2.2.3iv, the flake graphite particles' thermal conductivity is roughly 2.5x higher than the thermal conductivity of amorphous carbon, whereas their electrical conductivity is approximately 3x lower than the electrical conductivity of amorphous carbon. In addition, the pore space and PTFE are not electrically conductive and considered as passive phases while their local thermal conductivities are considered as 0.25 W m^{-1} K^{-1} for PTFE and 0.03 W m^{-1} K^{-1} for air in the pore space. Moreover, the MPL-coated GDLs exhibit approximately 3x higher thermal conductivity in the IP direction than in the TP direction with the same logic as the trend of electrical conductivity observations.

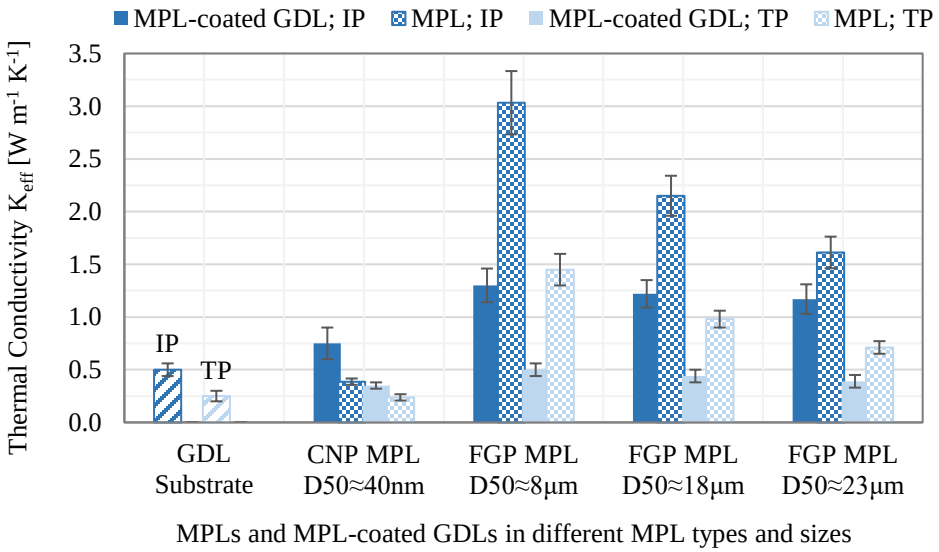

Figure 4.14. Simulated IP and TP thermal conductivity of Avcarb EP40T GDL substrate model compared with CNP MPL with D50 ≈ 40 nm and FGP MPLs with D50 ≈ 8, 18, and 23 µm and their respective MPL-coated GDL models.

It is worth mentioning that a vast majority of thermal analyses in the literature have been greatly simplified and restricted to simple model representations. In many analyses, thermal conductivity has been predicted by combining series and parallel models and/or by taking the mean geometric average of the thermal conductivities of solid and liquid phases [187]. Only a few modeling studies have considered the thermal conductivity of the GDL [108] as anisotropic and parametrically investigated its impact on polarization behavior under different operating conditions, which is a prominent contribution of this thesis.

4.4. Summary

In this chapter, single-layer MPLs coated on an AvCarb EP40T GDL substrate for MPLs under study were stochastically reconstructed utilizing single- or multi-pore-scale approaches inspired by manufacturing and characterization data. Note that the GDL substrate and MPL microstructural modeling frameworks were established in Chapter 2 and Chapter 3, respectively. The process steps for microstructural reconstruction of FGP MPL-coated GDL using low-resolution single-pore-scale approach were elaborated at length. For the CNP MPL-coated GDL microstructural modeling, two multi-pore-scale approaches were proposed, *i.e.*, the homogeneous multi-pore-scale and network resistance approaches. The homogeneous multi-scale model was found to be the preferable framework for full GDL simulations where the CNP MPL is treated as a homogeneous porous medium added to the macroporous GDL substrate model in which the MPL intrudes into the substrate by the penetration coefficient. In order to verify the developed microstructural modeling framework, a detailed qualitative and quantitative validation was conducted for SEM images, porosity, and pore size distribution.

A parametric study was conducted to investigate the effect of MPL composition on MPLs and MPL-coated GDLs transport properties, *i.e.*, effective diffusivity, permeability, and thermal and electrical conductivities in both through-plane (TP; z) and in-plane (IP; x and y) directions. The microstructural modeling framework developed in this work serves as a bridge between the MPL real pore morphology composition and MPL as well as MPL-coated GDL transport properties. An increasing trend is exhibited in the simulated MPL effective diffusivity in all three principal directions by increasing the median particle size

which demonstrates that the particle size adjustment enables precise control over the effective MPL pore size, tortuosity, and consequently effective diffusivity. Moreover, the higher diffusion through relatively large pores of FGP MPLs, where bulk diffusion is dominant, compared with CNP MPLs, where a combination of Knudsen and bulk diffusion are taken into effect, are likely favorable for PEFCs operating at high current density conditions where oxygen diffusion rates are important in the context of GDL design. In addition, the values of the simulated effective diffusivity of the MPL-coated GDLs for all MPLs under study compared to the bare GDL substrate is substantially reduced in the TP direction whereas slight decrease is observed in the IP direction. The TP gas diffusion pathways are narrowed down due to the presence of the MPL with a steep TP tortuosity increase, while in the IP direction, the main diffusion pathways of the substrate remain intact except for the MPL-penetrated layer. By analyzing the simulated concentration field, the highest TP diffusion resistance is observed in the MPL-penetrated layer, thereby, the net MPL penetration into the substrate plays an important role for the overall diffusion coefficient which is neglected in the pure MPL transport property measurements in the literature. Given that the delicate MPL layer is not a stand-alone layer and the high uncertainties and cost are associated with MPL transport property measurements, our developed numerical modeling framework is a superior approach to obtain comprehensive understanding of pure MPL properties. Furthermore, a lower trend is observed in the simulated MPL permeability than that of the GDL substrate owing to the MPLs' smaller pores, lower porosity, and higher PTFE loading. Due to such low-permeability MPLs, the MPL becomes the convective TP transport limiting layer in the MPL-coated GDLs, which is of particular importance for liquid water transport and water management in the MEA. At the end, it is worth mentioning that a vast majority of transport properties obtained from theoretical and analytical models in the literature have been greatly simplified and restricted to simple model representations in which the relatively complex GDL substrate pore structure as well as the contribution of the MPL coated on GDL substrate are underestimated. For instance, thermal conductivity has been predicted by combining series and parallel models and/or by taking the mean geometric average of the thermal conductivities of solid and liquid phases. Thus far, the developed modeling framework

could conceivably bridge this knowledge gap which provides advantageous information for material optimization and fuel cell design; a prominent contribution of this thesis.

Chapter 5.

Conclusions and Future Work

5.1. Thesis Conclusions

This thesis aimed to develop a comprehensive 3D GDL stochastic microstructural modeling framework to retrieve the heterogeneous GDL microstructure, which was used as a domain for numerical computation of transport properties, as a reliable and flexible tool to correlate between the GDL composition, real pore morphology, and transport properties. The developed modeling framework was a collection of stochastic processes which describe the probability distributions of the porous media constituents and aim to encompass all the details of the GDL porous media. Inspired by the GDL manufacturing and real pore morphology characterization in this stochastic modeling framework, the 3D digital realizations of GDL substrate; consisting of graphitized carbon fiber, carbonized binder, and hydrophobic agent; as well as MPL; consisting of carbon agglomerates and hydrophobic agent; are obtained. The modeling framework is followed by establishing pore-scale model approaches to stochastically reconstruct MPL-coated GDLs where the algorithm flowcharts of GDL substrate and MPL microstructural modeling frameworks are briefly described in the GDL Substrate Design Tool Algorithm and MPL Design Tool Algorithm subsections, respectively.

The reliability of the modeling framework was examined by extensive qualitative and quantitative validation for the existing materials with measured characterization data where the validation algorithm flowchart was thoroughly described in the Model Validation subsection. Thereupon, the framework was demonstrated as a robust algorithm for design and prototyping assignments of hypothetical materials for next-generation fuel cells. The modeling framework was utilized in this thesis to study the effects of PTFE loading and liquid water saturation on the GDL substrate anisotropic transport properties for both gas and liquid phases. With regards to the PTFE loading, the simulated results demonstrated an important trade-off between enhanced hydrophobicity and reduced gas diffusivity and permeability which must be considered and optimized in the GDL substrate

design and manufacturing processes. The presence of liquid water was determined to act as a barrier to gas diffusion and affected the gas phase porosity of the GDL substrate. Interestingly however, liquid water was also found to reduce the thermal resistance between the fibers and significantly increase the effective thermal conductivity. The new saturation dependent correlations proposed for these transport properties are therefore an important contribution of this work, as previous empirical correlations were either nonexistent (thermal conductivity) or shown to be inaccurate in the critical through-plane direction (diffusivity). Furthermore, a parametric study was conducted to investigate the effect of MPL pore morphology composition, *i.e.*, MPL particle type and size, on the MPL and MPL-coated GDL transport properties. The trends demonstrated that the MPL particle size adjustment enables precise control over the effective MPL pore size, tortuosity, and consequently effective diffusivity. Moreover, the higher diffusion through MPLs with relatively larger pores were observed which are likely favorable for PEFCs operating at high current density conditions where oxygen diffusion rates are important in the context of GDL design. In addition, the highest TP diffusion resistance was observed in the MPL-penetrated layer, thereby, the net MPL penetration into the substrate plays an important role for the overall diffusion coefficient which is underestimated in the MPL transport property experimental studies in the literature. It is also worth mentioning that the transport properties of theoretical and analytical models in the literature have been simplified to simple model representations in which the relatively complex GDL substrate pore structure as well as the contribution of the MPL coated on GDL substrate are underestimated. It was further concluded that the MPL becomes the convective TP transport limiting layer in the MPL-coated GDLs, which is of particular importance for liquid water transport and water management in the MEA.

Referring to the literature, the superiority of the developed framework was demonstrated as a feasible, cost- and time-effective technique in material optimization and design cycle with iterative nature compared to experimental and tomographic techniques. It was also demonstrated as a reliable framework for 3D realization of the GDL porous material which closely resembles that of the actual material compared to analytical and empirical techniques. The developed framework was well-suited to capture the stochastic behavior of the GDL porous structure by providing multiple realizations of the material

and hence mathematically parameterize the structure, hence, combined with the time and cost advantages makes it a comprehensive framework to characterize, manipulate, and optimize the structure. The developed validated stochastic modeling framework can be used as a versatile and reliable framework for 3D realizations of GDL porous material structure and understanding the correlation between the GDL morphology and transport properties. This paves the way for design and development of improved GDL materials with desired transport properties in modern PEFCs.

5.2. Future Work

The following research directions can be considered as the future work of this thesis:

- The developed modeling framework can be extended to further understand the transport properties of other types of GDLs such as carbon cloth GDLs, metallic GDLs, GDLs with curved fibers, GDLs with alternative hydrophobic agents, and other various novel MPL and GDL architectures.

- The developed modeling framework can be extended to model other MEA constituents, *i.e.*, catalyst layers, to understand the correlation between the microstructure and transport properties for design and prototyping of low Pt-loading highly active catalyst layers. It could also be adopted for other types of electrochemical cells such as electrolyzers and flow batteries.

- In PEFCs operating under high current density conditions, the GDL plays a crucial role in the overall water management to prevent significant losses related to liquid water saturation. Thereby, the effect of liquid water on the capillary pressure and relative transport properties of MPL-coated GDLs can be studied by the developed modeling framework in modern GDLs.

- The compression pressure has a significant effect on the overall MPL-coated GDL thermal resistance, and it can be further studied using the developed modelling framework.

- The iterative microstructural reconstruction process of GDL diagrammatically illustrated in Figure 2.17 can be optimized to a more computationally efficient modeling framework with least amount of iterations using machine learning algorithms in the concept of artificial intelligence.

References

[1] U.S. Department of Energy, Energy Effic. Renew. Energy. (2015). hydrogenandfuelcells.energy.gov.

[2] J. Larminie, A. Dicks, Fuel Cell Systems Explained, 2nd ed., 2003.

[3] M.M. Mench, Fuel Cell Engines, John Wiley and Sons Inc., New Jersey, 2008.

[4] DOE Technical Targets for Fuel Cell Systems and Stacks for Transportation Applications | Department of Energy, (2020). https://www.energy.gov/eere/fuelcells/doe-technical-targets-fuel-cell-systems-and-stacks-transportation-applications (accessed February 6, 2020).

[5] Fuel Cell Technical Team Roadmap, United States Driving Research and Innovation for Vehicle efficiency and Energy sustainability (U.S. DRIVE) technical team, U.S. Department of Energy, 2017.

[6] J. Marcinkoski, J. Spendelow, A. Wilson, D. Papageorgopoulos, P. Reviewed, R. Ahluwalia, B. James, C. Houchins, J. Moton, DOE Hydrogen and Fuel Cells Program Record Record - Fuel Cell System Cost, 2015. https://www.hydrogen.energy.gov/pdfs/15015_fuel_cell_system_cost_2015.pdf.

[7] J. Marcinkoski, J. Spendelow, A. Wilson, D. Papageorgopoulos, DOE Hydrogen and Fuel Cells Program Record - Fuel Cell System Cost, 2017. http://mechanismsrobotics.asmedigitalcollection.asme.org/article.aspx?doi=10.1115/1.4036738.

[8] Path to hydrogen competitiveness: a cost perspective; Hydrogen Council with analytical support from McKinsey & Company, 2020. https://hydrogencouncil.com/wp-content/uploads/2020/01/Path-to-Hydrogen-Competitiveness_Full-Study-1.pdf.

[9] Hydrogen scaling up : A sustainable pathway for the global energy transition, 2017. https://hydrogencouncil.com/wp-content/uploads/2017/11/Hydrogen-scaling-up-Hydrogen-Council.pdf.

[10] T. Sutharssan, D. Montalvao, Y.K. Chen, W.C. Wang, C. Pisac, H. Elemara, A review on prognostics and health monitoring of proton exchange membrane fuel cell, Renew. Sustain. Energy Rev. 75 (2017) 440–450. https://doi.org/10.1016/j.rser.2016.11.009.

[11] A. Ozden, S. Shahgaldi, X. Li, F. Hamdullahpur, A review of gas diffusion layers for proton exchange membrane fuel cells—With a focus on characteristics, characterization techniques, materials and designs, Prog. Energy Combust. Sci. 74 (2019) 50–102. https://doi.org/10.1016/j.pecs.2019.05.002.

[12] A. Suzuki, T. Hattori, R. Miura, H. Tsuboi, N. Hatakeyama, H. Takaba, M.C. Williams, A. Miyamoto, Porosity and Pt content in the catalyst layer of PEMFC: Effects on diffusion and polarization characteristics, Int. J. Electrochem. Sci. 5 (2010) 1948–1961.

[13] D.P. Wilkinson, J. Zhang, R. Hui, J. Fergus, X. Li, Proton Exchange Membrane Fuel Cells; Materials Properties and Performance, CRC Press, Taylor & Francis Group, LLC, 2010.

[14] EG&G Services, I. Prsons, Science applications International Corporation, Fuel Cell Handbook, Fifth edit, 2000.

[15] A. Thomas, G. Maranzana, S. Didierjean, J. Dillet, O. Lottin, Thermal and water transfer in PEMFCs: Investigating the role of the microporous layer, Int. J. Hydrogen Energy. 39 (2014) 2649–2658. https://doi.org/10.1016/j.ijhydene.2013.11.105.

[16] R. Omrani, B. Shabani, Gas diffusion layer modifications and treatments for improving the performance of proton exchange membrane fuel cells and electrolysers: A review, Int. J. Hydrogen Energy. 42 (2017) 28515–28536. https://doi.org/10.1016/j.ijhydene.2017.09.132.

[17] U. Pasaogullari, C.-Y. Wang, K.S. Chen, Two-Phase Transport in Polymer Electrolyte Fuel Cells with Bilayer Cathode Gas Diffusion Media, J. Electrochem. Soc. 152 (2005) A1574. https://doi.org/10.1149/1.1938067.

[18] J. Benziger, J. Nehlsen, D. Blackwell, T. Brennan, J. Itescu, Water flow in the gas diffusion layer of PEM fuel cells, J. Membr. Sci. 261 (2005) 98–106. https://doi.org/10.1016/j.memsci.2005.03.049.

[19] R. Flückiger, F. Marone, M. Stampanoni, A. Wokaun, F.N. Büchi, Investigation of liquid water in gas diffusion layers of polymer electrolyte fuel cells using X-ray tomographic microscopy, J. Electrochim. Acta. 56 (2011) 2254–2262. https://doi.org/10.1016/j.electacta.2010.12.016.

[20] J.T. Gostick, M.W. Fowler, M.D. Pritzker, M. a. Ioannidis, L.M. Behra, In-plane and through-plane gas permeability of carbon fiber electrode backing layers, J. Power Sources. 162 (2006) 228–238. https://doi.org/10.1016/j.jpowsour.2006.06.096.

[21] M. V. Williams, E. Begg, L. Bonville, H.R. Kunz, J.M. Fenton, Characterization of Gas Diffusion Layers for PEMFC, J. Electrochem. Soc. 151 (2004) A1173. https://doi.org/10.1149/1.1764779.

[22] V. Gurau, M.J. Bluemle, E.S. De Castro, Y.M. Tsou, T.A. Zawodzinski, J.A. Mann, Characterization of transport properties in gas diffusion layers for proton exchange membrane fuel cells, J. Power Sources. 165 (2007) 793–802. https://doi.org/10.1016/j.jpowsour.2006.12.068.

[23] J. Ihonen, M. Mikkola, G. Lindbergh, Flooding of Gas Diffusion Backing in PEFCs, J. Electrochem. Soc. 151 (2004) A1152. https://doi.org/10.1149/1.1763138.

[24] M. V. Williams, H.R. Kunz, J.M. Fenton, Influence of Convection Through Gas-Diffusion Layers on Limiting Current in PEM FCs Using a Serpentine Flow Field, J. Electrochem. Soc. 151 (2004) A1617. https://doi.org/10.1149/1.1789791.

[25] N. Zamel, X. Li, Effective transport properties for polymer electrolyte membrane fuel cells - With a focus on the gas diffusion layer, Prog. Energy Combust. Sci. 39 (2013) 111–146. https://doi.org/10.1016/j.pecs.2012.07.002.

[26] J. Sole, Investigation of water transport parameters and processes in the gas diffusion layer of PEM fuel cells, Virginia Tech, 2008. http://scholar.lib.vt.edu/theses/available/etd-05042008-161055/.

[27] B. Ramos-Alvarado, J.D. Sole, A. Hernandez-Guerrero, M.W. Ellis, Experimental characterization of the water transport properties of PEM fuel cells diffusion media, J. Power Sources. 218 (2012) 221–232. https://doi.org/10.1016/j.jpowsour.2012.05.069.

[28] Y. Wang, K.S. Chen, Elucidating two-phase transport in a polymer electrolyte fuel cell, Part 1: Characterizing flow regimes with a dimensionless group, Chem. Eng. Sci. 66 (2011) 3557–3567. https://doi.org/10.1016/j.ces.2011.04.016.

[29] J.P. Owejan, T.A. Trabold, M.M. Mench, Oxygen transport resistance correlated to liquid water saturation in the gas diffusion layer of PEM fuel cells, Int. J. Heat Mass Transf. 71 (2014) 585–592. https://doi.org/10.1016/j.ijheatmasstransfer.2013.12.059.

[30] D.R. Baker, C. Wieser, K.C. Neyerlin, M.W. Murphy, The Use of Limiting Current to Determine Transport Resistance in PEM Fuel Cells, ECS Trans. 3 (2019) 989–999. https://doi.org/10.1149/1.2356218.

[31] U. Beuscher, Experimental Method to Determine the Mass Transport Resistance of a Polymer Electrolyte Fuel Cell, J. Electrochem. Soc. 153 (2006) A1788. https://doi.org/10.1149/1.2218760.

[32] C. Chan, N. Zamel, X. Li, J. Shen, Experimental measurement of effective diffusion coefficient of gas diffusion layer/microporous layer in PEM fuel cells, Electrochim. Acta. 65 (2012) 13–21. https://doi.org/10.1016/j.electacta.2011.12.110.

[33] C. Quick, D. Ritzinger, W. Lehnert, C. Hartnig, Characterization of water transport in gas diffusion media, J. Power Sources. 190 (2009) 110–120. https://doi.org/10.1016/j.jpowsour.2008.07.093.

[34] G.S. Hwang, a. Z. Weber, Effective-Diffusivity Measurement of Partially-Saturated Fuel-Cell Gas-Diffusion Layers, J. Electrochem. Soc. 159 (2012) F683–F692. https://doi.org/10.1149/2.024211jes.

[35] J.H. Rohling, J. Shen, C. Wang, J. Zhou, C.E. Gu, Photothermal deflection measurement of effective gas diffusion coefficient of a porous medium, Eur. Phys. J. Spec. Top. 153 (2008) 111–113. https://doi.org/10.1140/epjst/e2008-00405-9.

[36] N. Zamel, N.G.C. Astrath, X. Li, J. Shen, J. Zhou, F.B.G. Astrath, H. Wang, Z.S. Liu, Experimental measurements of effective diffusion coefficient of oxygen-nitrogen mixture in PEM fuel cell diffusion media, Chem. Eng. Sci. 65 (2010) 931–937. https://doi.org/10.1016/j.ces.2009.09.044.

[37] J.H. Rohling, J. Shen, C. Wang, J. Zhou, C.E. Gu, Determination of binary diffusion coefficients of gases using photothermal deflection technique, Appl. Phys. B Lasers Opt. 87 (2007) 355–362. https://doi.org/10.1007/s00340-007-2595-9.

[38] M.S. Ismail, T. Damjanovic, D.B. Ingham, M. Pourkashanian, A. Westwood, Effect of polytetrafluoroethylene-treatment and microporous layer-coating on the electrical conductivity of gas diffusion layers used in proton exchange membrane fuel cells, J. Power Sources. 195 (2010) 2700–2708. https://doi.org/10.1016/j.jpowsour.2009.11.069.

[39] G. Xu, J.M. Lamanna, J.T. Clement, M.M. Mench, Direct measurement of through-plane thermal conductivity of partially saturated fuel cell diffusion media, J. Power Sources. 256 (2014) 212–219. https://doi.org/10.1016/j.jpowsour.2014.01.015.

[40] E. Sadeghi, N. Djilali, M. Bahrami, A novel approach to determine the in-plane thermal conductivity of gas diffusion layers in proton exchange membrane fuel cells, J. Power Sources. 196 (2011) 3565–3571. https://doi.org/10.1016/j.jpowsour.2010.11.151.

[41] P. Teertstra, G. Karimi, X. Li, Measurement of in-plane effective thermal conductivity in PEM fuel cell diffusion media, Electrochim. Acta. 56 (2011) 1670–1675. https://doi.org/10.1016/j.electacta.2010.06.043.

[42] J.H. Chun, K.T. Park, D.H. Jo, J.Y. Lee, S.G. Kim, E.S. Lee, J.-Y. Jyoung, S.H. Kim, Determination of the pore size distribution of micro porous layer in PEMFC using pore forming agents under various drying conditions, Int. J. Hydrogen Energy. 35 (2010) 11148–11153. https://doi.org/10.1016/j.ijhydene.2010.07.056.

[43] O.S. Burheim, H. Su, S. Pasupathi, J.G. Pharoah, B.G. Pollet, Thermal conductivity and temperature profiles of the micro porous layers used for the polymer electrolyte membrane fuel cell, Int. J. Hydrogen Energy. 38 (2013) 8437–8447. https://doi.org/10.1016/j.ijhydene.2013.04.140.

[44] L.M. Pant, S.K. Mitra, M. Secanell, Absolute permeability and Knudsen diffusivity measurements in PEMFC gas diffusion layers and micro porous layers, J. Power Sources. 206 (2012) 153–160. https://doi.org/10.1016/j.jpowsour.2012.01.099.

[45] G. Unsworth, N. Zamel, X. Li, Through-plane thermal conductivity of the microporous layer in a polymer electrolyte membrane fuel cell, Int. J. Hydrogen Energy. 37 (2012) 5161–5169. https://doi.org/10.1016/j.ijhydene.2011.12.012.

[46] G. Karimi, X. Li, P. Teertstra, Measurement of through-plane effective thermal conductivity and contact resistance in PEM fuel cell diffusion media, J. Electrochim. Acta. 55 (2010) 1619–1625. https://doi.org/10.1016/j.electacta.2009.10.035.

[47] a. Tamayol, M. Bahrami, Analytical determination of viscous permeability of fibrous porous media, Int. J. Heat Mass Transf. 52 (2009) 2407–2414. https://doi.org/10.1016/j.ijheatmasstransfer.2008.09.032.

[48] M.M. Tomadakis, T. Robertson, Viscous permeability of random fiber structures: comparison of electrical and diffusional estimates with experimental and analytical results., J. Compos. Mater. 39 (2005) 163–168.

[49] Bruggeman DAG., Calculation of various physics constants in heterogenous substances I: dielectricity constants and conductivity of mixed bodies from isotropic substances, Ann. Der Phys. 24 (1935) 636–664.

[50] M.M. Mezedur, M. Kaviany, M. Moore, Effect of pore structure, randomness and size on effective mass diffusivity, AICHEJ. 48 (2002) 15–24.

[51] J.H. Nam, M. Kaviany, Effective diffusivity and water-saturation distribution in single- and two-layer PEMFC diffusion medium, Int. J. Heat Mass Transf. 46 (2003) 4595–4611. https://doi.org/10.1016/S0017-9310(03)00305-3.

[52] M.M. Tomadakis, S.V. Sotirchos, , AIChE J. 39 (2004) 397..pdf, AICHEJ. (2004) 397.

[53] P.K. Das, X. Li, Z.S. Liu, Effective transport coefficients in PEM fuel cell catalyst and gas diffusion layers: Beyond Bruggeman approximation, J. Appl. Energy. 87 (2010) 2785–2796. https://doi.org/10.1016/j.apenergy.2009.05.006.

[54] A. Bejan, D.A. Nield, Convection in Porous Media, third ed., Springer, 2006.

[55] M. Kaviany, Principles of heat transfer in porous media, second ed., Springer, 1995.

[56] J. Bear, Dynamics of fluids in porous media, Dover Publications, New York, 1972.

[57] M. Van Genuchten, Closed form equation for predicting the hydraulic conductivity of unsaturated soils, Am. J. Soil Sciience Soc. 44 (1980) 892–898.

[58] H. Looyenga, Dielectric constants of heterogeneous mixtures, Physica. 31 (1965) 401–406.

[59] Z. Zeng, R. Grigg, A Criterion for Non-Darcy Flow in Porous Media, Transp. Porous Media. 63 (2006) 57–69. https://doi.org/10.1007/s11242-005-2720-3.

[60] Z. Abdulagatova, I.M. Abdulagatov, V.N. Emirov, Effect of temperature and pressure on the thermal conductivity of sandstone, Int. J. Rock Mech. Min. Sci. 46 (2009) 1055–1071.

[61] Z. Hashin, S.A. Shtrikman, A variational approach to the theory of the effective magnetic permeability of multi-phase materials., J. Appl. Phys. 33 (1962) 3125–3131.

[62] E. Sadeghi, M. Bahrami, N. Djilali, Analytic determination of the effective thermal conductivity of PEM fuel cell gas diffusion layers, J. Power Sources. 179 (2008) 200–208. https://doi.org/10.1016/j.jpowsour.2007.12.058.

[63] Y. Shi, J. Xiao, S. Quan, M. Pan, R. Yuan, Fractal model for prediction of effective thermal conductivity of gas diffusion layer in proton exchange membrane fuel cell, J. Power Sources. 185 (2008) 241–247. https://doi.org/10.1016/j.jpowsour.2008.07.010.

[64] U. Pasaogullari, P.P. Mukherjee, C.-Y. Wang, K.S. Chen, Anisotropic Heat and Water Transport in a PEFC Cathode Gas Diffusion Layer, J. Electrochem. Soc. 154 (2007) B823. https://doi.org/10.1149/1.2745714.

[65] C.J. Bapat, S.T. Thynell, Effect of anisotropic thermal conductivity of the GDL and current collector rib width on two-phase transport in a PEM fuel cell, J. Power Sources. 179 (2008) 240–251. https://doi.org/10.1016/j.jpowsour.2007.12.033.

[66] H. Sadeghifar, M. Bahrami, N. Djilali, A statistically-based thermal conductivity model for fuel cell Gas Diffusion Layers, J. Power Sources. 233 (2013) 369–379. https://doi.org/10.1016/j.jpowsour.2013.01.086.

[67] T.E. Springer, Characterization of Polymer Electrolyte Fuel Cells Using AC Impedance Spectroscopy, J. Electrochem. Soc. 143 (1996) 587. https://doi.org/10.1149/1.1836485.

[68] H. Ostadi, P. Rama, Y. Liu, R. Chen, X.X. Zhang, K. Jiang, Influence of threshold variation on determining the properties of a polymer electrolyte fuel cell gas diffusion layer in X-ray nano-tomography, Chem. Eng. Sci. 65 (2010) 2213–2217. https://doi.org/10.1016/j.ces.2009.12.019.

[69] J. Becker, R. Flückiger, M. Reum, F.N. Büchi, F. Marone, M. Stampanoni, Determination of Material Properties of Gas Diffusion Layers: Experiments and Simulations Using Phase Contrast Tomographic Microscopy, J. Electrochem. Soc. 156 (2009) B1175. https://doi.org/10.1149/1.3176876.

[70] J.P. James, H.-W. Choi, J.G. Pharoah, X-ray computed tomography reconstruction and analysis of polymer electrolyte membrane fuel cell porous transport layers, Int. J. Hydrogen Energy. 37 (2012) 18216–18230. https://doi.org/10.1016/j.ijhydene.2012.08.077.

[71] R. Thiedmann, F. Fleischer, C. Hartnig, W. Lehnert, V. Schmidt, Stochastic 3D Modeling of the GDL Structure in PEMFCs Based on Thin Section Detection, J. Electrochem. Soc. 155 (2008) B391. https://doi.org/10.1149/1.2839570.

[72] Y. Wang, S. Cho, R. Thiedmann, V. Schmidt, W. Lehnert, X. Feng, Stochastic modeling and direct simulation of the diffusion media for polymer electrolyte fuel cells, Int. J. Heat Mass Transf. 53 (2010) 1128–1138. https://doi.org/10.1016/j.ijheatmasstransfer.2009.10.044.

[73] M.M. Daino, S.G. Kandlikar, 3D phase-differentiated GDL microstructure generation with binder and PTFE distributions, Int. J. Hydrogen Energy. 37 (2012) 5180–5189. https://doi.org/10.1016/j.ijhydene.2011.12.050.

[74] V.P. Schulz, J. Becker, A. Wiegmann, P.P. Mukherjee, C.-Y. Wang, Modeling of Two-Phase Behavior in the Gas Diffusion Medium of PEFCs via Full Morphology Approach, J. Electrochem. Soc. 154 (2007) B419. https://doi.org/10.1149/1.2472547.

[75] G. Inoue, T. Yoshimoto, Y. Matsukuma, M. Minemoto, Development of simulated gas diffusion layer of polymer electrolyte fuel cells and evaluation of its structure, J. Power Sources. 175 (2008) 145–158. https://doi.org/10.1016/j.jpowsour.2007.09.014.

[76] N. Zamel, X. Li, J. Shen, J. Becker, A. Wiegmann, Estimating effective thermal conductivity in carbon paper diffusion media, Chem. Eng. Sci. 65 (2010) 3994–4006. https://doi.org/10.1016/j.ces.2010.03.047.

[77] M. El Hannach, E. Kjeang, Stochastic Microstructural Modeling of PEFC Gas Diffusion Media, J. Electrochem. Soc. 161 (2014) F951–F960. https://doi.org/10.1149/2.1141409jes.

[78] J.T. Gostick, M. a. Ioannidis, M.W. Fowler, M.D. Pritzker, Pore network modeling of fibrous gas diffusion layers for polymer electrolyte membrane fuel cells, J. Power Sources. 173 (2007) 277–290. https://doi.org/10.1016/j.jpowsour.2007.04.059.

[79] P.K. Sinha, C.-Y. Wang, Pore-network modeling of liquid water transport in gas diffusion layer of a polymer electrolyte fuel cell, Electrochim. Acta. 52 (2007) 7936–7945. https://doi.org/10.1016/j.electacta.2007.06.061.

[80] P.K. Sinha, C.-Y. Wang, Liquid water transport in a mixed-wet gas diffusion layer of a polymer electrolyte fuel cell, Chem. Eng. Sci. 63 (2008) 1081–1091. https://doi.org/10.1016/j.ces.2007.11.007.

[81] P.K. Sinha, P.P. Mukherjee, C.-Y. Wang, Impact of GDL structure and wettability on water management in polymer electrolyte fuel cells, J. Mater. Chem. 17 (2007) 3089. https://doi.org/10.1039/b703485g.

[82] B. Markicevic, a. Bazylak, N. Djilali, Determination of transport parameters for multiphase flow in porous gas diffusion electrodes using a capillary network model, J. Power Sources. 171 (2007) 706–717. https://doi.org/10.1016/j.jpowsour.2007.06.053.

[83] a. Bazylak, V. Berejnov, B. Markicevic, D. Sinton, N. Djilali, Numerical and microfluidic pore networks: Towards designs for directed water transport in GDLs, Electrochim. Acta. 53 (2008) 7630–7637. https://doi.org/10.1016/j.electacta.2008.03.078.

[84] K.-J. Lee, J.H. Nam, C.-J. Kim, Pore-network analysis of two-phase water transport in gas diffusion layers of polymer electrolyte membrane fuel cells, Electrochim. Acta. 54 (2009) 1166–1176. https://doi.org/10.1016/j.electacta.2008.08.068.

[85] K.-J. Lee, J.H. Nam, C.-J. Kim, Steady saturation distribution in hydrophobic gas-diffusion layers of polymer electrolyte membrane fuel cells: A pore-network study, J. Power Sources. 195 (2010) 130–141. https://doi.org/10.1016/j.jpowsour.2009.06.076.

[86] T. Koido, T. Furusawa, K. Moriyama, An approach to modeling two-phase transport in the gas diffusion layer of a proton exchange membrane fuel cell, J. Power Sources. 175 (2008) 127–136. https://doi.org/10.1016/j.jpowsour.2007.09.029.

[87] G. Luo, Y. Ji, C.-Y. Wang, P.K. Sinha, Modeling liquid water transport in gas diffusion layers by topologically equivalent pore network, Electrochim. Acta. 55 (2010) 5332–5341. https://doi.org/10.1016/j.electacta.2010.04.078.

[88] R.T. White, A. Wu, M. Najm, F.P. Orfino, M. Dutta, E. Kjeang, 4D in situ visualization of electrode morphology changes during accelerated degradation in fuel cells by X-ray computed tomography, J. Power Sources. 350 (2017) 94–102. https://doi.org/10.1016/j.jpowsour.2017.03.058.

[89] R.T. White, F.P. Orfino, M. El Hannach, O. Luo, M. Dutta, A.P. Young, E. Kjeang, 3D printed flow field and fixture for visualization of water distribution in fuel cells by X-ray computed tomography, J. Electrochem. Soc. 163 (2016) F1337–F1343. https://doi.org/10.1149/2.0461613jes.

[90] D. Cheng, S. Ye, E. Gyenge, Reactive Sensor for Investigation of Gas Diffusion Layer Hydrophobicity in PEM Fuel Cells, Electrochem. Solid-State Lett. 11 (2008) B148. https://doi.org/10.1149/1.2932055.

[91] V. Berejnov, D. Sinton, N. Djilali, Structure of porous electrodes in polymer electrolyte membrane fuel cells: An optical reconstruction technique, J. Power Sources. 195 (2010) 1936–1939. https://doi.org/10.1016/j.jpowsour.2009.10.050.

[92] Z. Fishman, J. Hinebaugh, A. Bazylak, Microscale Tomography Investigations of Heterogeneous Porosity Distributions of PEMFC GDLs, J. Electrochem. Soc. 157 (2010) B1643. https://doi.org/10.1149/1.3481443.

[93] Z. Fishman, A. Bazylak, Heterogeneous Through-Plane Porosity Distributions for Treated PEMFC GDLs I. PTFE Effect, J. Electrochem. Soc. 158 (2011) B841. https://doi.org/10.1149/1.3594578.

[94] A. Nanjundappa, A.S. Alavijeh, M. El Hannach, D. Harvey, E. Kjeang, A customized framework for 3-D morphological characterization of microporous layers, Electrochim. Acta. (2013). https://doi.org/10.1016/j.electacta.2013.04.103.

[95] E. a. Wargo, V.P. Schulz, a. Çeçen, S.R. Kalidindi, E.C. Kumbur, Resolving macro- and micro-porous layer interaction in polymer electrolyte fuel cells using focused ion beam and X-ray computed tomography, Electrochim. Acta. 87 (2013) 201–212. https://doi.org/10.1016/j.electacta.2012.09.008.

[96] E. a. Wargo, a. C. Hanna, a. Çeçen, S.R. Kalidindi, E.C. Kumbur, Selection of representative volume elements for pore-scale analysis of transport in fuel cell materials, J. Power Sources. 197 (2012) 168–179. https://doi.org/10.1016/j.jpowsour.2011.09.035.

[97] Y. Yin, T. Wu, P. He, Q. Du, K. Jiao, Numerical simulation of two-phase cross flow in microstructure of gas diffusion layer with variable contact angle, Int. J. Hydrogen Energy. 39 (2014) 15772–15785. https://doi.org/10.1016/j.ijhydene.2014.07.162.

[98] W.R. Campaigne, P.W. Fieguth, Frozen-state hierarchical annealing, IEEE Trans. Image Process. 22 (2013) 1486–1497. https://doi.org/10.1109/TIP.2012.2233482.

[99] L.M. Pant, Stochastic Characterization and Reconstruction of Porous Media, University of Alberta, 2016.

[100] P.P. Mukherjee, C.Y. Wang, Q. Kang, Mesoscopic modeling of two-phase behavior and flooding phenomena in polymer electrolyte fuel cells, J. Electrochim. Acta. 54 (2009) 6861–6875. https://doi.org/10.1016/j.electacta.2009.06.066.

[101] J. Hinebaugh, J. Gostick, A. Bazylak, Stochastic modeling of polymer electrolyte membrane fuel cell gas diffusion layers – Part 2: A comprehensive substrate model with pore size distribution and heterogeneity effects, Int. J. Hydrogen Energy. 42 (2017) 15872–15886. https://doi.org/10.1016/j.ijhydene.2017.04.269.

[102] A. Nabovati, J. Hinebaugh, A. Bazylak, C.H. Amon, Effect of porosity heterogeneity on the permeability and tortuosity of gas diffusion layers in polymer electrolyte membrane fuel cells, J. Power Sources. 248 (2014) 83–90. https://doi.org/10.1016/j.jpowsour.2013.09.061.

[103] S. Didari, A. Asadi, Y. Wang, T.A.L. Harris, Modeling of composite fibrous porous diffusion media, Int. J. Hydrogen Energy. 39 (2014) 9375–9386. https://doi.org/10.1016/j.ijhydene.2014.04.011.

[104] Numerical Evaluation of Effective Gas Diffusivity – Saturation Dependence of Uncompressed and Compressed Gas Diffusion Media in PEFCs V. P. Schulz, (n.d.).

[105] K. Schladitz, S. Peters, D. Reinel-Bitzer, A. Wiegmann, J. Ohser, Design of acoustic trim based on geometric modeling and flow simulation for non-woven, J. Comput. Mater. Sci. 38 (2006) 56–66. https://doi.org/10.1016/j.commatsci.2006.01.018.

[106] N. Zamel, X. Li, J. Becker, A. Wiegmann, Effect of liquid water on transport properties of the gas diffusion layer of polymer electrolyte membrane fuel cells, Int. J. Hydrog. Energy. 36 (2011) 5466–5478. https://doi.org/10.1016/j.ijhydene.2011.01.146.

[107] M. El Hannach, R. Singh, N. Djilali, E. Kjeang, Micro-porous layer stochastic reconstruction and transport parameter determination, J. Power Sources. 282 (2015) 58–64. https://doi.org/10.1016/j.jpowsour.2015.02.034.

[108] N. Zamel, J. Becker, A. Wiegmann, Estimating the thermal conductivity and diffusion coefficient of the microporous layer of polymer electrolyte membrane fuel cells, J. Power Sources. 207 (2012) 70–80. https://doi.org/10.1016/j.jpowsour.2012.02.003.

[109] J. Becker, C. Wieser, S. Fell, K. Steiner, A multi-scale approach to material modeling of fuel cell diffusion media, Int. J. Heat Mass Transf. 54 (2011) 1360–1368. https://doi.org/10.1016/j.ijheatmasstransfer.2010.12.003.

[110] M. Mathias, J. Roth, J. Fleming, W. Lehnert, A. Opel, A.G. Global, A. Propulsion, Diffusion media materials and characterisation, in: Handbook of Fuel Cells-Fundamentals, Technology and Applications, John Wiley and Sons, Ltd., 2003.

[111] S. Park, J.W. Lee, B.N. Popov, Effect of carbon loading in microporous layer on PEM fuel cell performance, J. Power Sources. 163 (2006) 357–363. https://doi.org/10.1016/j.jpowsour.2006.09.020.

[112] Z. Fishman, A. Bazylak, Heterogeneous Through-Plane Distributions of Tortuosity, Effective Diffusivity, and Permeability for PEMFC GDLs, J. Electrochem. Soc. 158 (2011) B247. https://doi.org/10.1149/1.3524284.

[113] J.D. Fairweather, P. Cheung, D.T. Schwartz, The effects of wetproofing on the capillary properties of proton exchange membrane fuel cell gas diffusion layers, J. Power Sources. 195 (2010) 787–793. https://doi.org/10.1016/j.jpowsour.2009.08.032.

[114] G. Lin, T. Van Nguyen, Effect of Thickness and Hydrophobic Polymer Content of the Gas Diffusion Layer on Electrode Flooding Level in a PEMFC, J. Electrochem. Soc. 152 (2005) A1942. https://doi.org/10.1149/1.2006487.

[115] G.G. Park, Y.J. Sohn, T.H. Yang, Y.G. Yoon, W.Y. Lee, C.S. Kim, Effect of PTFE contents in the gas diffusion media on the performance of PEMFC, J. Power Sources. 131 (2004) 182–187. https://doi.org/10.1016/j.jpowsour.2003.12.037.

[116] R. Schweiss, C. Meiser, T. Damjanovic, I. Galbiati, N. Haak, SIGRACET Gas Diffusion Layers for PEM Fuel Cells, Electrolyzers, and Batteries, 2016. https://www.researchgate.net/publication/295859224_SIGRACETR_Gas_Diffusion_Layers_for_PEM_Fuel_Cells_Electrolyzers_and_Batteries_White_Paper.

[117] N. Erdman, D.C. Bell, R. Reichelt, Scanning Electron Microscopy in Springer Handbook of Microscopy, Springer, 2019. https://doi.org/10.1007/978-3-030-00069-1.

[118] S. Nasrazadani, S. Hassani, Modern analytical techniques in failure analysis of aerospace, chemical, and oil and gas industries in Handbook of Materials Failure Analysis, Elsevier Ltd, 2016. https://doi.org/10.1016/B978-0-08-100117-2.00010-8.

[119] S.P. Rigby, P.I. Chigada, J. Wang, S.K. Wilkinson, H. Bateman, B. Al-Duri, J. Wood, S. Bakalis, T. Miri, Improving the interpretation of mercury porosimetry data using computerised X-ray tomography and mean-field DFT, Chem. Eng. Sci. 66 (2011) 2328–2339. https://doi.org/10.1016/j.ces.2011.02.031.

[120] A. Arvay, E. Yli-Rantala, C.H. Liu, X.H. Peng, P. Koski, L. Cindrella, P. Kauranen, P.M. Wilde, A.M. Kannan, Characterization techniques for gas diffusion layers for proton exchange membrane fuel cells - A review, J. Power Sources. 213 (2012) 317–337. https://doi.org/10.1016/j.jpowsour.2012.04.026.

[121] H. Giesche, Mercury porosimetry: A general (practical) overview, Part. Part. Syst. Charact. 23 (2006) 9–19. https://doi.org/10.1002/ppsc.200601009.

[122] Mercury intrusion porosimetry theory, Micrometrics Instrum. Corp. (2020).

[123] M.J. Martínez, S. Shimpalee, J.W. Van Zee, a. V. Sakars, Assessing Methods and Data for Pore-Size Distribution of PEMFC Gas-Diffusion Media, J. Electrochem. Soc. 156 (2009) B558. https://doi.org/10.1149/1.3080653.

[124] X. Wang, H. Zhang, J. Zhang, H. Xu, X. Zhu, J. Chen, B. Yi, A bi-functional micro-porous layer with composite carbon black for PEM fuel cells, J. Power Sources. 162 (2006) 474–479. https://doi.org/10.1016/j.jpowsour.2006.06.064.

[125] V.V. Chetlur, H.S. Dhillon, Coverage analysis of a vehicular network modeled as cox process driven by poisson line process, IEEE Trans. Wirel. Commun. 17 (2018) 4401–4416. https://doi.org/10.1109/TWC.2018.2824832.

[126] G. Last, M. Penrose, Lectures on the Poisson Process, IMS Textbook by Cambridge University Press, 2017. https://doi.org/10.1017/9781316104477.

[127] A.G. Yiotis, M.E. Kainourgiakis, G.C. Charalambopoulou, A.K. Stubos, Microscale characterisation of stochastically reconstructed carbon fiber-based Gas Diffusion Layers; Effects of anisotropy and resin content, J. Power Sources. 320 (2016) 153–167. https://doi.org/10.1016/j.jpowsour.2016.04.096.

[128] Inverse Transform Method, (n.d.). http://www.columbia.edu/~ks20/4404-Sigman/4404-Notes-ITM.pdf.

[129] L. Yi, Simulation Studies of the Packing of Multi-Sized Particle Systems, The University of New South Wales, 2012.

[130] M.M. Roozbahani, R. Borela, J.D. Frost, Pore size distribution in granular material microstructure, Materials (Basel). 10 (2017) 1–21. https://doi.org/10.3390/ma10111237.

[131] L. Burtseva, B.V. Salas, R. Romero, F. Werner, Multi-Sized Sphere Packings : Models and Recent Approaches, (2015) 1–21.

[132] P. Soille, Morphological Image Analysis: Principles and Applications, Sens. Rev. 20 (1999). https://doi.org/10.1108/sr.2000.08720cae.001.

[133] Z. Tayarani-Yoosefabadi, D. Harvey, J. Bellerive, E. Kjeang, Stochastic microstructural modeling of fuel cell gas diffusion layers and numerical determination of transport properties in different liquid water saturation levels, J. Power Sources. 303 (2016) 208–221. https://doi.org/10.1016/j.jpowsour.2015.11.005.

[134] N. Zamel, Transport Properties of the Gas Diffusion Layer of PEM Fuel Cells, University of Waterloo, 2011.

[135] F. Barbir, PEM Fuel Cells: Theory and Practice, 2nd ed., Elsevier Inc, 2013. https://doi.org/10.1016/b978-0-12-387710-9.00007-2.

[136] H. Wu, Mathematical Modeling of Transient Transport Phenomena in PEM Fuel Cells, University of Waterloo, 2009.

[137] J.D. Anderson, Computational Fluid Dynamics, The Basics with Applications, 2nd ed., McGraw-Hill Inc., 2010. https://doi.org/10.1017/CBO9780511780066.

[138] K.H. Clifford, S.W. Webb, Gas transport in Porous Media, Springer, 2006.

[139] R. Krishna, J.M. van Baten, Investigating the validity of the Bosanquet formula for estimation of diffusivities in mesopores, Chem. Eng. Sci. 69 (2012) 684–688. https://doi.org/10.1016/j.ces.2011.11.026.

[140] W.G. Pollard, R.D. Present, On gaseous self-diffusion in long capillary tubes, Phys. Rev. 73 (1948) 762–774. https://doi.org/10.1103/PhysRev.73.762.

[141] K.S. Spiegler, Diffusion of gases across porous media. 5, 529 – 532., Ind. Eng. Chem. Fundam. 5 (1966) 529–532.

[142] G. Karniadakis, A. Beskok, N. Aluru, Microflows and Nanoflows: Fundamentals and Simulation, Springer, 2005.

[143] Fraunhofer ITWM, Fraunhofer ITWM, Http//Www.Geodict.Com/Userguide.Php, Date Accessed, Dec. 5th, 2012. (n.d.). http://www.geodict.com/userguide.php.

[144] M.S. Ismail, D. Borman, T. Damjanovic, D.B. Ingham, M. Pourkashanian, On the through-plane permeability of microporous layer-coated gas diffusion layers used in proton exchange membrane fuel cells, Int. J. Hydrogen Energy. 36 (2011) 10392–10402. https://doi.org/10.1016/j.ijhydene.2010.09.012.

[145] W. Kast, C.R. Hohenthanner, Mass transfer within the gas-phase of porous media, Int. J. Heat Mass Transf. 43 (2000) 807–823. https://doi.org/10.1016/S0017-9310(99)00158-1.

[146] P.J.A.M. Kerkhof, A modified Maxwell-Stefan model for transport through inert membranes: The binary friction model, Chem. Eng. J. Biochem. Eng. J. 64 (1996) 319–343. https://doi.org/10.1016/S0923-0467(96)03134-X.

[147] L. Wu, M.T. Ho, L. Germanou, X.J. Gu, C. Liu, K. Xu, Y. Zhang, On the apparent permeability of porous media in rarefied gas flows, J. Fluid Mech. 822 (2017) 398–417. https://doi.org/10.1017/jfm.2017.300.

[148] R.D. Hazlett, , Transp. Porous Media, 20,21 1995, Transp. Porous Media. 20 (1995) 21.

[149] M. Hilpert, C. Miller, Pore-morphology-based simulation of drainage in totally wetting porous media. , 24:243–255, 2001., Adv.Water Resour. 24 (2001) 243–255.

[150] J.T. Gostick, M.W. Fowler, M. a. Ioannidis, M.D. Pritzker, Y.M. Volfkovich, a. Sakars, Capillary pressure and hydrophilic porosity in gas diffusion layers for polymer electrolyte fuel cells, J. Power Sources. 156 (2006) 375–387. https://doi.org/10.1016/j.jpowsour.2005.05.086.

[151] M. Mortazavi, K. Tajiri, Effect of the PTFE content in the gas diffusion layer on water transport in polymer electrolyte fuel cells (PEFCs), J. Power Sources. 245 (2014) 236–244. https://doi.org/10.1016/j.jpowsour.2013.06.138.

[152] C. Lim, C.Y. Wang, Effects of hydrophobic polymer content in GDL on power performance of a PEM fuel cell, Electrochim. Acta. 49 (2004) 4149–4156. https://doi.org/10.1016/j.electacta.2004.04.009.

[153] M. Khandelwal, M.M. Mench, Direct measurement of through-plane thermal conductivity and contact resistance in fuel cell materials, J. Power Sources. 161 (2006) 1106–1115. https://doi.org/10.1016/j.jpowsour.2006.06.092.

[154] E. Sadeghi, N. Djilali, M. Bahrami, Effective thermal conductivity and thermal contact resistance of gas diffusion layers in proton exchange membrane fuel cells. Part 1: Effect of compressive load, J. Power Sources. 196 (2011) 246–254. https://doi.org/10.1016/j.jpowsour.2010.06.039.

[155] H. Meng, C.Y. Wang, Electron transport in PEFCs, J. Electrochem. Soc. 151 (2004) A358–A367.

[156] J.G. Pharoah, K. Karan, W. Sun, On effective transport coefficients in PEM fuel cell electrodes: Anisotropy of the porous transport layers, J. Power Sources. 161 (2006) 214–224. https://doi.org/10.1016/j.jpowsour.2006.03.093.

[157] M. Acosta, C. Merten, G. Eigenberger, H. Class, R. Helmig, B. Thoben, H. Müller-Steinhagen, Modeling non-isothermal two-phase multicomponent flow in the cathode of PEM fuel cells, J. Power Sources. 159 (2006) 1123–1141. https://doi.org/10.1016/j.jpowsour.2005.12.068.

[158] L. Hao, P. Cheng, Pore-scale simulations on relative permeabilities of porous media by lattice Boltzmann method, Int. J. Heat Mass Transf. 53 (2010) 1908–1913. https://doi.org/10.1016/j.ijheatmasstransfer.2009.12.066.

[159] E. Dana, F. Skoczylas, Experimental study of two-phase flow in three sandstones . II . Capillary pressure curve measurement and relative permeability pore space capillary models e d, Int. J. Multiph. Flow. 28 (2002) 1965–1981.

[160] E.C. Kumbur, K.V. Sharp, M.M. Mench, On the effectiveness of Leverett approach for describing the water transport in fuel cell diffusion media, J. Power Sources. 168 (2007) 356–368. https://doi.org/10.1016/j.jpowsour.2007.02.054.

[161] K. Li, Interrelationship between Resistivity Index, Capillary Pressure and Relative Permeability, Transp. Porous Media. 88 (2011) 385–398. https://doi.org/10.1007/s11242-011-9745-6.

[162] J.P. Owejan, T. a. Trabold, D.L. Jacobson, D.R. Baker, D.S. Hussey, M. Arif, In situ investigation of water transport in an operating PEM fuel cell using neutron radiography: Part 2 – Transient water accumulation in an interdigitated cathode flow field, Int. J. Heat Mass Transf. 49 (2006) 4721–4731. https://doi.org/10.1016/j.ijheatmasstransfer.2006.07.004.

[163] O. Burheim, P.J.S. Vie, J.G. Pharoah, S. Kjelstrup, Ex situ measurements of through-plane thermal conductivities in a polymer electrolyte fuel cell, J. Power Sources. 195 (2010) 249–256. https://doi.org/10.1016/j.jpowsour.2009.06.077.

[164] W.M. Yan, C.Y. Hsueh, C.Y. Soong, F. Chen, C.H. Cheng, S.C. Mei, Effects of fabrication processes and material parameters of GDL on cell performance of PEM fuel cell, Int. J. Hydrogen Energy. 32 (2007) 4452–4458. https://doi.org/10.1016/j.ijhydene.2007.02.003.

[165] D. Ye, E. Gauthier, J.B. Benziger, M. Pan, Bulk and contact resistances of gas diffusion layers in proton exchange membrane fuel cells, J. Power Sources. 256 (2014) 449–456. https://doi.org/10.1016/j.jpowsour.2014.01.082.

[166] G. Bin Jung, W.J. Tzeng, T.C. Jao, Y.H. Liu, C.C. Yeh, Investigation of porous carbon and carbon nanotube layer for proton exchange membrane fuel cells, Appl. Energy. 101 (2013) 457–464. https://doi.org/10.1016/j.apenergy.2012.08.045.

[167] W.-M. Yan, D.-K. Wu, X.-D. Wang, A.-L. Ong, D.-J. Lee, A. Su, Optimal microporous layer for proton exchange membrane fuel cell, J. Power Sources. 195 (2010) 5731–5734. https://doi.org/10.1016/j.jpowsour.2010.03.041.

[168] A. Bottino, G. Capannelli, A. Comite, C. Costa, A.L. Ong, Microporous layers based on poly(vinylidene fluoride) and sulfonated poly(vinylidene fluoride), Int. J. Hydrogen Energy. 40 (2015) 14690–14698. https://doi.org/10.1016/j.ijhydene.2015.08.099.

[169] S.B. Park, Y. Park, Fabrication of gas diffusion layer (GDL) containing microporous layer using flourinated ethylene prophylene (FEP) for proton exchange membrane fuel cell (PEMFC), Int. J. Precis. Eng. Manuf. 13 (2012) 1145–1151. https://doi.org/10.1007/s12541-012-0152-x.

[170] R. Hiesgen, I. Wehl, K.A. Friedrich, M. Schulze, A. Haug, A. Bauder, A. Carreras, X.Z. Yuan, H. Wang, Atomic Force Microscopy Investigation of Polymer Fuel Cell Gas Diffusion Layers before and after Operation, ECS Trans. 28 (2010) 79–84. https://doi.org/10.1149/1.3496615.

[171] T. Kitahara, H. Nakajima, K. Okamura, Gas diffusion layers coated with a microporous layer containing hydrophilic carbon nanotubes for performance enhancement of polymer electrolyte fuel cells under both low and high humidity conditions, J. Power Sources. 283 (2015) 115–124. https://doi.org/10.1016/j.jpowsour.2015.02.115.

[172] F. Lapicque, M. Belhadj, C. Bonnet, J. Pauchet, Y. Thomas, A critical review on gas diffusion micro and macroporous layers degradations for improved membrane fuel cell durability, J. Power Sources. 336 (2016) 40–53. https://doi.org/10.1016/j.jpowsour.2016.10.037.

[173] A. Ozden, S. Shahgaldi, J. Zhao, X. Li, F. Hamdullahpur, Assessment of graphene as an alternative microporous layer material for proton exchange membrane fuel cells, Fuel. 215 (2018) 726–734. https://doi.org/10.1016/j.fuel.2017.11.109.

[174] A. Ozden, S. Shahgaldi, X. Li, F. Hamdullahpur, A graphene-based microporous layer for proton exchange membrane fuel cells: Characterization and performance comparison, Renew. Energy. 126 (2018) 485–494. https://doi.org/10.1016/j.renene.2018.03.065.

[175] A.T. Najafabadi, M.J. Leeuwner, D.P. Wilkinson, E.L. Gyenge, Electrochemically Produced Graphene for Microporous Layers in Fuel Cells, ChemSusChem. 9 (2016) 1689–1697. https://doi.org/10.1002/cssc.201600351.

[176] D. Spernjak, J. Fairweather, R. Mukundan, T. Rockward, R.L. Borup, Influence of the microporous layer on carbon corrosion in the catalyst layer of a polymer electrolyte membrane fuel cell, J. Power Sources. 214 (2012) 386–398. https://doi.org/10.1016/j.jpowsour.2012.04.086.

[177] P. Kuchenbecker, M. Gemeinert, T. Rabe, Inter-laboratory study of particle size distribution measurements by laser diffraction, Part. Part. Syst. Charact. 29 (2012) 304–310. https://doi.org/10.1002/ppsc.201000026.

[178] G. Eshel, G.J. Levy, U. Mingelgrin, M.J. Singer, Critical Evaluation of the Use of Laser Diffraction for Particle-Size Distribution Analysis, Soil Sci. Soc. Am. J. 68 (2004) 736–743. https://doi.org/10.2136/sssaj2004.0736.

[179] Malvern Instruments Limited, Laser Diffraction Analyzer - Mastersizer 3000, 2013.

[180] F.A.L. Dullien, Porous media: fluid transport and pore structure., 1979.

[181] M. Andisheh-Tadbir, F.P. Orfino, E. Kjeang, Three-dimensional phase segregation of micro-porous layers for fuel cells by nano-scale X-ray computed tomography, J. Power Sources. 310 (2016) 61–69. https://doi.org/10.1016/j.jpowsour.2016.02.001.

[182] H. Ostadi, P. Rama, Y. Liu, R. Chen, X.X. Zhang, K. Jiang, 3D reconstruction of a gas diffusion layer and a microporous layer, J. Memb. Sci. 351 (2010) 69–74. https://doi.org/10.1016/j.memsci.2010.01.031.

[183] F.H. She, K.L. Tung, L.X. Kong, Calculation of effective pore diameters in porous filtration membranes with image analysis, Robot. Comput. Integr. Manuf. 24 (2008) 427–434. https://doi.org/10.1016/j.rcim.2007.02.023.

[184] M. Han, J.H. Xu, S.H. Chan, S.P. Jiang, Characterization of gas diffusion layers for PEMFC, Electrochim. Acta. 53 (2008) 5361–5367. https://doi.org/10.1016/j.electacta.2008.02.057.

[185] O.M. Orogbemi, D.B. Ingham, M.S. Ismail, K.J. Hughes, L. Ma, M. Pourkashanian, Through-plane gas permeability of gas diffusion layers and microporous layer: Effects of carbon loading and sintering, J. Energy Inst. 91 (2018) 270–278. https://doi.org/10.1016/j.joei.2016.11.008.

[186] D. Froning, J. Yu, G. Gaiselmann, U. Reimer, I. Manke, V. Schmidt, W. Lehnert, Impact of compression on gas transport in non-woven gas diffusion layers of high temperature polymer electrolyte fuel cells, J. Power Sources. 318 (2016) 26–34. https://doi.org/10.1016/j.jpowsour.2016.03.102.

[187] J.J. Baschuk, X. Li, A general formulation for a mathematical PEM fuel cell model, J. Power Sources. 142 (2005) 134–153. https://doi.org/10.1016/j.jpowsour.2004.09.027.